THE PRODUCTION OF ACETYLENE BY A CARBON ARC

A THESIS PRESENTED FOR THE
DEGREE OF DOCTOR OF PHILOSOPHY
IN CHEMICAL ENGINEERING
IN THE
UNIVERSITY OF CANTERBURY

by
P.G. WILES
1979

ADDENDA

1. Unless otherwise stated, 'current density' refers to anode current density.

2. Section 6.3.5. The high speed photography suggests that the mean arc column length is of the order of 2 cm. Higham and Meek[109] have measured the voltage gradient in a hydrogen arc of 20 cm length (electrode effects minimal), at 1 atmosphere and of 100-300 A. After about 3 μs the arc was found to reach steady state conditions whereupon the voltage gradient was found to be 30-35 V cm^{-1} for currents of 230-250 A respectively. This is an upper value for this work, since pure hydrogen has the highest voltage gradient of any gas[111]. Once carbon vapour diffuses into the hydrogen arc column the voltage gradient will be expected to be reduced. Therefore 20 V cm^{-1} is a likely mean (conservative) value for the plasma voltage gradient. The total plasma voltage drop is therefore estimated to be 40 V, as stated in the text.

3. Section 7.4.1. Blix and Guile[110] use a drag coefficient of 0.63 for the movement of an arc column through a perpendicular magnetic field. Perry[116] provides values close to 1.0 for the flow of turbulent fluids over a solid cylinder. If a value of C_D of 0.63 is used rather than 0.2 then the estimated arc expansion velocities are:- 250 and 380 ms^{-1} respectively. These values are still of order 0.5 mm μs^{-1} as previously estimated. (The velocity depends on $\sqrt{C_D}$ and its variations are relatively insignificant when compared to those from variations in arc diameter and gas density)

Additional References

109. Higham, F.B. & Meek, F.M.; Voltage gradients in long gaseous spark channels. Proc. Phys. Soc., 63B, 641, 1949.

110. Blix, E.D. & Guile, A.E.; Column control in the magnetic depletion of a short arc. Brit. J. Appl. Phys. 16, 857, 1965.

111. Suits, C.G.; High pressure arcs in common gases in free convection. Phys. Rev. 55, 561, 1939.

112. Siegel, R. & Howell, J.R.; Thermal radiation transfer, McGraw-Hill, 1972, p.721.

113. Huddlestone, R.H. & Leonard, S.L.; Plasma diagnostic techniques, Academic Press, p.308.

114. Touloukian et al.; Thermophysical properties of matter - the TPRC data series, volume 10, Thermal Diffusivity IFI-Plenum, New York 1973, p.21.

115. Kreith, F.; Principles of heat transfer, 2nd ed. Intertext, 1965, p596.

116. Perry, J.H.; The Chemical Engineering Handbook 4th ed. McGraw-Hill, 5-60.

ACKNOWLEDGEMENTS

The author is most grateful to Dr John Abrahamson for his supervision of this project. John's interest, patience and stimulating ideas over the past five years have made him an ideal supervisor. Without this supervision many of the significant results presented in this thesis would not have been possible.

The demands made on the technical staff by this project, have been severe. Their skills and competence cannot be faulted. The practical help given by Dr Clive Davies has been very much appreciated. The help Mr Trevor Berry has given has been very valuable, often working with equipment pushed to its operating limits. The use of the electron microscope facilities of the Mechanical Engineering Department is gratefully acknowledged. The help given in their use by Dr Brian Rhodes and Mr Mike Flaws has been most important.

The author wishes to thank the Chemistry Department for the use of various pieces of equipment, the Physics Department for the use of the microdensitometer and the Christchurch Public Hospital, Clinical Services Department, for the use of their electron microscope.

The Mineral Resources Subcommittee of the University Grants Committee provided a grant for this project which the author is most grateful for.

The author would like to thank the Head of Department, Professor Miles Kennedy for his interest in this work and for taking care of the author's financial needs.

Finally, the author wishes to thank Mrs C. McEntee for the task of transforming a large untidy collection of notes into this thesis.

TABLE OF CONTENTS

		Page
ABSTRACT		1
SUMMARY		2
1.	INTRODUCTION	4
1.1	Previous Work	4
1.1.1	Baddour's Work	4
1.1.2	The Avco Work	6
1.2	Conclusions from Previous Work	7
1.3	Abrahamson's Reactor	7
1.4	Ward's Reactor	9
1.5	Objects of Study	9
2.	ENERGY AND MASS BALANCES OVER WARD'S REACTOR	12
2.1	Summary	12
2.2	Overall Energy Balance	12
2.2.1	Experimental Method	12
2.2.2	Results and Discussion of Results	14
2.2.2.1	Reactor Heat Flow Data	17
2.3	The Prequench Gas Specific Enthalpy and Temperature	19
2.4	Mass Balances	20
2.4.1	Previous Work	20
2.4.2	Analysis of Gas Samples by Chromatography	21
2.4.3	Carbon Usage	22
2.4.4	Results and Discussion of Results	24
2.4.4.1	Gas Analysis	24
2.4.4.2	Hydrogen Purity	25
2.4.4.3	Detection of New Compounds in Reactor Gas	25
2.4.4.4	Nitrogen-Hydrogen Mixture Feed Gas	27
2.4.4.5	Carbon Balance	27

		Page
3.	THE ABLATION OF CARBONACEOUS MATERIALS	30
3.1	Summary	30
3.2	Experimental	30
3.2.1	The Measurement of the Anode Feed Rate	30
3.2.1.1	Background	30
3.2.1.2	New Feed Systems	32
3.2.2	The Electrical Current Contact	35
3.2.3	Joining Anode Sections	35
3.2.4	Current Measurement	37
3.2.5	Coal Core Anodes	37
3.2.5.1	Low Current Testing of 7.94 mm Coal Core Anodes	37
3.2.6	Cathodes Used in Ward Reactor	38
3.2.7	Power Supply Voltage	38
3.3	Constraints on the Investigation of Carbon Ablation, With the Present (Ward) Reactor	39
3.3.1	Current and Power	39
3.3.2	Materials	39
3.4	Results	40
3.4.1	The Ablation of 7.94 mm Anodes	40
3.4.2	The Ablation of Graphite and Graphite-Coal Anodes of Differing Diameters	42
3.4.3	The Relationship between Ablation per Unit Area and Current Density	42
3.5	The Ablation of Graphite at High Current Density in the Kiloampere Range	45
3.6	The Resistive Heating of Graphite Electrodes	46
3.6.1	The Radial Temperature Gradient in Graphite Conductors	46
3.6.2	Commercial Considerations	48
3.7	Cathode Ablation	48

		Page
4.	CARBON DEPOSITION WITHIN THE REACTOR	51
4.1	Types of Deposit	51
4.2	Conclusions	55
5.	THE ADDITION OF METHANE AS A SUPPLEMENTARY FEED GAS	56
5.1	Summary	56
5.2	Experiment to Attempt Methane Pyrolysis	56
5.3	Conclusions	59
6.	QUENCH DESIGN AND QUENCH PROCESSES (Graphite Gasification and Acetylene Formation)	60
6.1	Summary	60
6.2	Process Development	60
6.2.1	Ward's Quenches	60
6.2.2	This Work	61
6.2.3	Multi-Tubed Quench	61
6.2.4	Fluidised Bed Quench	63
6.2.4.1	Operation of the Spouted Bed Quench	64
6.2.4.2	Analysis of Heat Transfer in the Spout Tube	67
6.2.4.3	An Estimate of the Breakdown of Acetylene in the Spout Tube	69
6.2.4.4	Quenching Rate Required in a Commercial Quench	72
5.2.4.5	Quenching Rates Likely in Liquid Spray Systems	73
6.3	The Prequench Gas Composition and the Formation of Acetylene	75
6.3.1	Categorizing the Gas Composition	75
6.3.2	Theoretical Equilibrium Gas Compositions	76
6.3.3	Comparison of Equilibrium and Typical Reactor Gas Compositions	78
6.3.4	Delayed Acetylene Breakdown Due to Induction	79
6.3.5	The Action of Atomic Hydrogen in Graphite Gasification	79

		Page
6.3.6	Avco Isotope Mixing Experiments	83
6.4	Conclusions on the Formation and Preservation of Acetylene	85
7.	DYNAMIC BEHAVIOUR OF THE HIGH CURRENT HYDROGEN ARC	87
7.1	Summary	87
7.2	Procedure	87
7.3	Observations	88
7.3.1	The Voltage Waveform	88
7.3.2	The Current Waveform	88
7.3.3	High Speed Photographs	91
7.3.4	Arc Attachment Spot Temperatures	95
7.3.4.1	Measurement of Spot Temperatures	98
7.3.4.2	Spot Cool-down Rate	99
7.3.5	Cathode Spot Current Density	100
7.4	Modelling of Observed Waveforms	101
7.4.1	Arc Loop Expansion	101
7.4.2	Voltage and Current Discontinuities	103
7.4.3	Arc Voltage Less Than Minimum Steady State	105
7.5	Rate of Arc Attachment Movement	107
7.6	Bulk Surface or Arc Attachment Ablation	107
7.7	Conclusions	110
8.	SPECTROSCOPY OF THE CARBON-HYDROGEN ARC	112
8.1	Summary	112
8.2	Procedure	112
8.2.1	Films	112
8.2.2	Film Calibration	113
8.2.3	Space and Time Averaging	115
8.3	Identification of Spectral Features	115
8.3.1	Visible Region	115
8.3.2	Ultraviolet region	116

		Page
8.4	Quantitative Interpretation of Spectra	116
8.4.1	Electron Concentration	121
8.4.2	Plasma Temperature	123
8.4.3	Impurity Concentration in Plasma	126
8.4.4	Molecular Temperature	127
8.4.4.1	C_2 Vibrational Temperature	127
8.4.4.2	C_2 Rotational Temperature	128
8.5	The Radiative Energy Balance	136
8.5.1	Procedure	136
8.5.2	Individual Components of the Emitted Radiation	136
8.5.2.1	Atomic Carbon	136
8.5.2.2	Atomic Hydrogen	136
8.5.2.3	Hydrogen Bremnstrahlung Radiation	137
8.5.2.4	Hydrogen Recombination Radiation	137
8.5.2.5	C_2 Molecular Radiation	139
8.5.2.6	The Total Volumetric Emission	139
8.5.2.7	Anode Tip Radiation	140
8.5.3	Moving Plasma Exposure Probability	140
8.5.3.1	The Anode	141
8.5.3.2	The Plasma	141
8.5.3.3	Hydrogen Balmer/Anode Spectral Intensity Ratios	142
8.5.3.4	The Plasma-Slit Coincidence Probability	143
8.5.4	The Total Radiation Balance	143
8.6	Optically Thick H_α	143
8.7	Particulate Carbon Loss from the Anode	144
8.7.1	Carbon Arc in Air	144
8.7.2	Carbon Arc in Hydrogen	145
8.7.2.1	Radiation Profiles About Anode Tip	145
8.7.3	Quantitative Estimate of Particulate Radiation	149

		Page
8.8	Total Plasma Radiation Loss	151
8.9	Conclusions	151
9.	CONCLUSIONS AND RECOMMENDATIONS	153
9.1	Ablation	153
9.2	Coal Anodes	153
9.3	Graphite Sublimation Temperature in Hydrogen	154
9.4	Arc Dynamics	154
9.5	Reactor Design	154
9.6	Spectroscopy	155
9.7	Stockton Coal	155
REFERENCES		156
APPENDICES		162
I	Spectroscopic Data	162
II	The Radiative Heat Loss from the Anode	163
III	Carbon Fibre Layers on Arc Electrodes - I Their Properties and Cool-Down Behaviour (published Carbon 16, 341, 1978).	167
IIIa	Supplement to "Carbon Fibre Layers on Arc Electrodes - I"	176
IIIa.1	Circumstantial Evidence	176
IIIa.2	Looking for Whisker Growth After Arc Cutoff - (an attempt)	178
IIIa.2.1	Experimental	179
IIIa.2.2	Results and Discussion	182
IV	The Sublimation Temperature of Graphite	188
V	The Free Vaporization of Graphite	192
VI	Structure of Carbon Fibres Found on Carbon Arc Anodes (Proceedings of 14th Biennial Conference on Carbon, 1979, p.254)	196

LIST OF FIGURES

		Page
1	Consumable Anode Reactors	5
2	Abrahamson Reactor	8
3	Ward Reactor	10
4	Multi-tubed Quench Design	15
5	Thermal Response of Ward Reactor	16
6	Gas Chromatograph Analysis	23
7	Design of Anode Feed	33
8	Sliding Anode Current Contact	36
9	Ablation Rate of 7.9 mm Anodes	41
9a	Ablation Rate of Graphite Anodes - Various Diameters	43
10	Ablation Rate of Graphite versus Current Density	44
11	Thermal Constraints on Carbon Conductors	49
12	Carbon Deposition versus C/H Ratio	52
13	Carbon Deposition versus Hydrogen Flow	54
14	Carbon Deposits in Reactor and Quench Tubes	58
15	Design of Fluidised Bed Quench	65
16	Cooling Curve for Spouted Quench	70
17a,b,c,d	Arc Voltage Waveforms	89
18a,b,c,d	Arc Current Waveforms	90
19	High Speed Photograph of Arc Blow-out Mode	92
20	High Speed Photograph of Anode Spot Motion	93
21	Anode Spot Movement onto Coal Core Vent Hole	94
22	Detailed Side View of Anode Attachment	96
23a,b	Anode and Cathode Particle Loss	97
24	Vaporization Rate of Carbon	109
25	Visible Carbon-Hydrogen Arc Spectrum	117 118
26a,b,c	Ultraviolet Carbon-Hydrogen Arc Spectrum	119 120
27	Relative Profiles of H Balmer Lines	122

		Page
28a,b,c,d	Rotational-Vibrational Spectrum of C_2 Swan Bands	129,130,131 132
29	Vibrational Temperature Plot for C_2	133
30	Rotational Temperature Plot for C_2	135
31a,b,c,d	Radiation Profiles at Anode Tip	147,148
A1	Thermopile Temperature Profile of Anode	165
A2	Switching-Delay Circuit for Standard Arc	180
A3	Power Supply for Standard Arc	181
A4	Anode Surface Whisker Growth Experiment	183
A5a,b	Microdensitometer Profiles of Standard Anode Tip - Hot and Cold.	184,185
A6	Arrhenius Plot of Carbon Vaporization Rates	189

LIST OF PLATES

		Page
1	Colour Photographs of High Intensity Carbon-Hydrogen Arc	146
A1	SEM Micrographs of Cathode Whisker Deposits	177

LIST OF TABLES

		Page
1	Gas Analysis for Carbon Balances	28
2	Carbon Balances	29
3	Gas Cooling Rate in Spout Tube	69
4	Theoretical Hydrocarbon Equilibrium Compositions - Single Phase	77
5	Theoretical Hydrocarbon Equilibrium Compositions - Two Phase	78
6	Electron Concentrations	123
7	Recombination Radiation Data	138
8	Hydrogen Spectral and Anode Spectral Data for Slit Probability	142

ABSTRACT

This study continues the work with the reactor built by Ward[1] for the production of acetylene by ablating carbon at the tip of a graphite anode with a high intensity D.C. arc, into a hydrogen atmosphere. This study attempts to combine data sought for the technical evaluation of a commercial process with an understanding of the conditions existing at the anode tip region and in the high temperature gas stream of the reactor. From this an insight as to how the carbon is ablated and how acetylene is formed and preserved in the reactor is obtained.

Note addenda front and back.

SUMMARY

The Ward reactor has been modified so that runs of one hour duration are now possible. It was found that 20-30 minutes of reactor operation were required for thermal steady state to be obtained. Energy balances can now be obtained.

In a comprehensive gas analysis, ten compounds have been detected as reaction products. Three of these have not been specifically identified, but are believed to be substituted C_3 and C_4 alkynes. A satisfactory mass balance is now obtainable over the Ward reactor.

The ablation rates of four different types of carbon anodes have been investigated with diameters varying from 5.1 - 9.5 mm and currents of 130 - 300 A D.C. Included in these tests were 9.5 mm graphite rods drilled out and packed with a 6.35 mm core of Stockton No. 2 coal. Contrary to Ward's results, for a given anode diameter, the ablation rate is found to depend linearly on the arc current. Tests carried out with a 5000 A A.C. power supply with 25.4 mm diameter AGSR graphite rods show that electrode rupture is a serious limitation to a viable industrial acetylene process using an ablating anode.

A spouted bed acetylene quench of novel design has been designed, built and successfully tested.

Methane has been introduced into the reactor with the aim of pyrolysing it to acetylene. In most tests, soot rapidly blocked the reactor outlet. Mixing and thermal constraints appear to limit progress for methane conversion.

The dynamics of the arc has been examined by high speed photography (3200 fps) and oscilloscope observations of the voltage and current waveforms. The waveforms are found to be highly transient, with a mean repetition rate of 3 kHz. Voltages up to twice the open circuit potential are observed and are associated with rapid voltage spikes (300 V rise in < 2 μs). For a nominal current of 200 A, the anode arc attachment is found to be about 0.7 mm in diameter. The attachment movement on the anode tip is probably controlled by local impurities, and is assumed to have a velocity of the order 300 ms^{-1}. The plasma behaviour has been tentatively explained in terms of the phenomena of "anode hash" and magnetic blow-out.

The temperature profile along the shank of the anode, back from the tip has been obtained by comparison with the radiance of the standard arc. The tip brightness temperature is estimated to be 3950 ± 50 K. The brightness temperatures of the anode and cathode attachments appear to be about 200 K higher.

The spectrum of the carbon-hydrogen plasma from 240 - 660 nm has been obtained. The significant spectral lines identified are the hydrogen Balmer series, the C_2 (Swan) bands and several C^o and C^+ lines. However, expected bands from CH and C_3 were not detected. The spectral features present enabled the plasma temperature, electron concentration and to some extent the composition to be obtained. A plasma radiation balance was attempted so that an upper limit could be placed on the likely concentration of carbon crystallites above the anode surface.

The appendices include a copy of a publication which reports the existence of carbon whiskers on the anode attachment of the Standard Arc (11A current). Also included is a debate which attempts to reject the hypothesis that liquid carbon can exist at one atmosphere.

1. INTRODUCTION

1.1 Previous Work

Two previous processes[14,15,102] have been reported in which it was attempted to ablate (vaporise) a carbonaceous electrode as the anode of a D.C. arc. The carbon rich vapour produced at the electrode tip was allowed to react with the surrounding hydrogen atmosphere at a high temperature (> 2000 K) so that acetylene was the principal product formed. The hot gas mixture had to be cooled by some means which was more rapid than the acetylene decomposition rate.

1.1.1 Baddour's Work

Baddour and workers[14, 15] used a ¼" or 3/8" graphite anode placed on the axis of a graphite tube of about 1" I.D., see Fig. (1). The anode was placed in front of the tube such that the tip was just inside the entrance. The arc was struck from the tip (anode) to the inner wall of the tube (cathode). Magnetic arc rotation was used to uniformly heat the gases (H_2 or CH_4) the carbon vapour was to react with. The product gas was withdrawn through the end of the hollow cathode. This feature appears to be the major difficulty in any possible industrial application of a reactor of this type. Since reaction is taking place inside the cathode tube, carbon deposition may gradually block the tube up. At the tube entrance the wandering cathode arc attachment may erode the tube away. For a semi-continuous operation the cathode tube would have to be fed to balance the loss and, at the same time, consume the deposition, and allow the gases to be quenched at the cathode end. These requirements would be very difficult if not impossible to meet with this design.

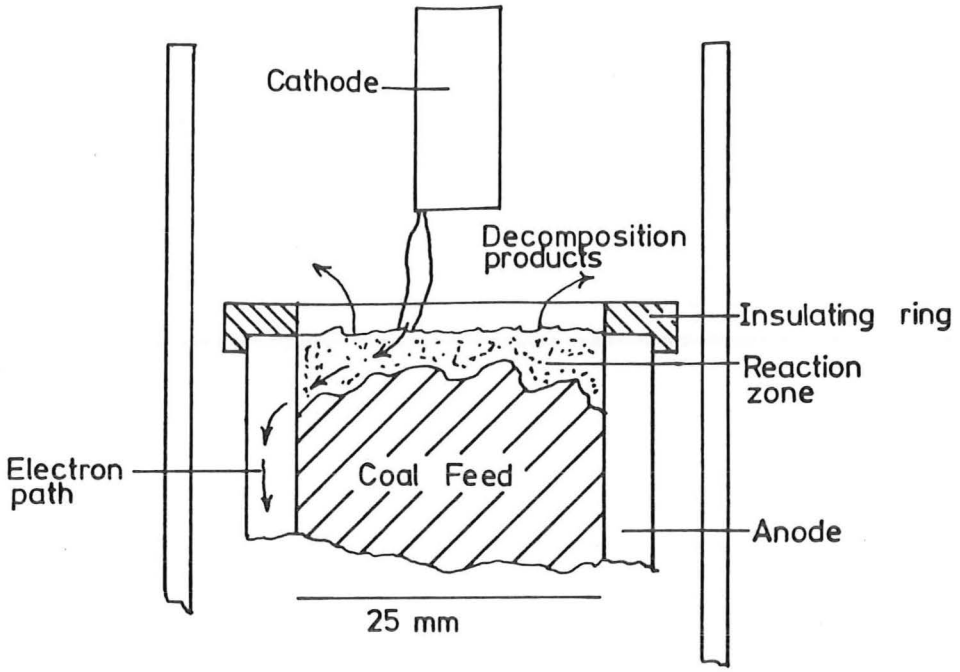

Avco Consumable Anode Reactor

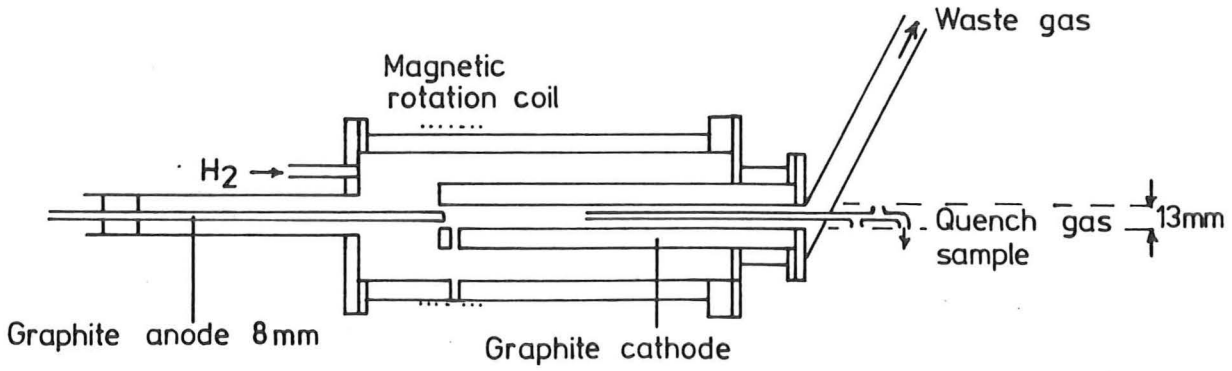

Baddour Consumable Anode Reactor

Figure 1.

Baddour obtained much valuable data on the ablation rate of graphite anodes. The ¼" D electrode ablations were measured from 150-350A (current densities of 4.5-11 A mm^{-2}) and 3/8" electrodes, 150-500A (2-7 A mm^{-2}). For both diameters and up to the maximum current densities used, the ablation rate varied linearly with current (although with considerable scatter).

1.1.2 The Avco Work

Avco Corporation were awarded a contract by the U.S. Office of Coal Research in 1966, to devise a process in which coal could be converted to acetylene.[102] Their initial scheme is shown in Fig. (1). Crushed, dried coal was pushed up a tube by a ram. An arc was allowed to wander over the surface of this exuding mass. The coal surface was an anode of a D.C. arc. A 25 mm rod of coal was used with a current of about 900 A (2 A mm^{-2} and 40 kW). The coal was fed at the rate the surface coal was pyrolyzed (*not at the rate it was ablated*). The unreacted material (char, ash etc.) was allowed to fall over the side. The atmosphere surrounding the coal was hydrogen, which served as a quench gas. Avco managed to obtain 4% acetylene in the product gas and a conversion of 16% of the coal to acetylene. Avco abandoned the process and went on to develop a more successful process whereby very finely crushed coal was poured through a magnetically rotated arc. Even at the end of the investigation the final process could only convert the volatile content of the dry coal (about 35% depending on the coal) to acetylene. Any commercial plant would have to find a use for coal char amounting to 2/3 of the feedstock.

In the consumable anode process, Avco found the reaction (or gasification zone) was about 10 mm below the char surface. Microscopic examination showed that a significant amount of soot was deposited in the

char pores as the gas escaped between the char particles.

1.2 Conclusions from Previous Work

A number of conditions in the Avco consumable anode process must be avoided if higher yields are to be achieved. As far as possible all the carbon in the coal must be vaporized. The acetylene formation reactions must be allowed to proceed without subsequent decomposition on hot carbon surfaces. As high a current density as possible should be used in ablating the electrode tip, so that the fraction of power lost, as radiation, should be minimised. Any reactor design should not include features which could not be commercialized, (e.g. Baddour's cathode arrangement). It is beyond the scope of this work to investigate how a suitable coal could be formed into a conductive rod to supply the anode of the arc. (Davies[103] has made significant progress in the screw extrusion of low ash, high swelling coal.)

1.3 Abrahamson's Reactor

Abrahamson[4] designed and built a reactor consisting of a vertical 1/8" graphite anode, fed from beneath, a horizontal tungsten cathode, and surrounded by a cylindrical graphite shell, see Fig. (2). The graphite shell was designed to be heated by convection-conduction from the plasma and radiation from the electrodes. Abrahamson found a linear dependence between ablation rate and current (10-50 A, (1-6 A mm^{-2}) up to 4 kW).

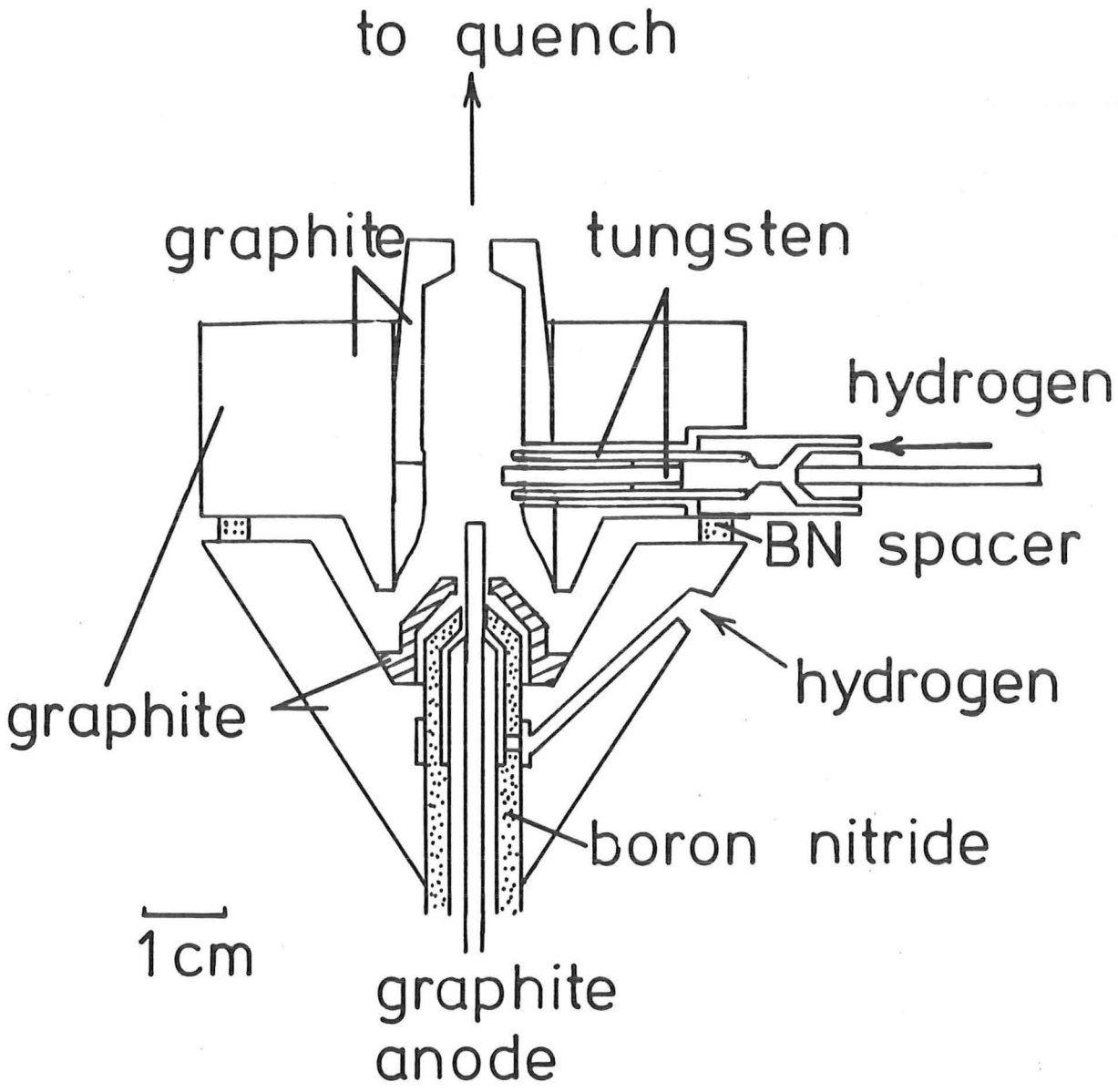

4 kW Arc Reactor.

Figure 2.

1.4 Ward's Reactor

As a scale-up of Abrahamson's reactor, Ward[1] designed, built and successfully operated a reactor of similar concept but capable of ablating (5/16") 7.94 mm graphite (AGSR Union Carbide) anodes with up to 250 A, and a power of 20 kW. Abrahamson's single horizontal tungsten cathode was replaced with three symmetrically placed horizontal graphite cathodes. Ward experienced considerable difficulty operating with this arrangement. He finally achieved satisfactory operation with only one cathode. This has been retained for all subsequent work, see Fig. (3). A number of Ward's experiments were concerned with evolving a cathode design which controlled the build-up of carbon on its tip. He achieved a moderately satisfactory design in which additional hydrogen was introduced coaxially around the cathode tip.

Ward found that his ablation rates rose exponentially with current (100-250 A). This contrasted with both Abrahamson's and Baddour's work, where a linear dependence was found. This was potentially highly significant because by operating at the highest possible current density it would be possible to greatly reduce the energy cost of ablating a given mass of carbon, resulting in acetylene at the lowest specific cost.

1.5 Objective of Study

It was one of the major aims of this work to confirm or refute these conflicting results. Furthermore, reliable ablation rates at the highest possible current density should be striven for. The ablation rates of non-graphitized carbons should be investigated as well as graphite tubes packed with ground and dried coal.

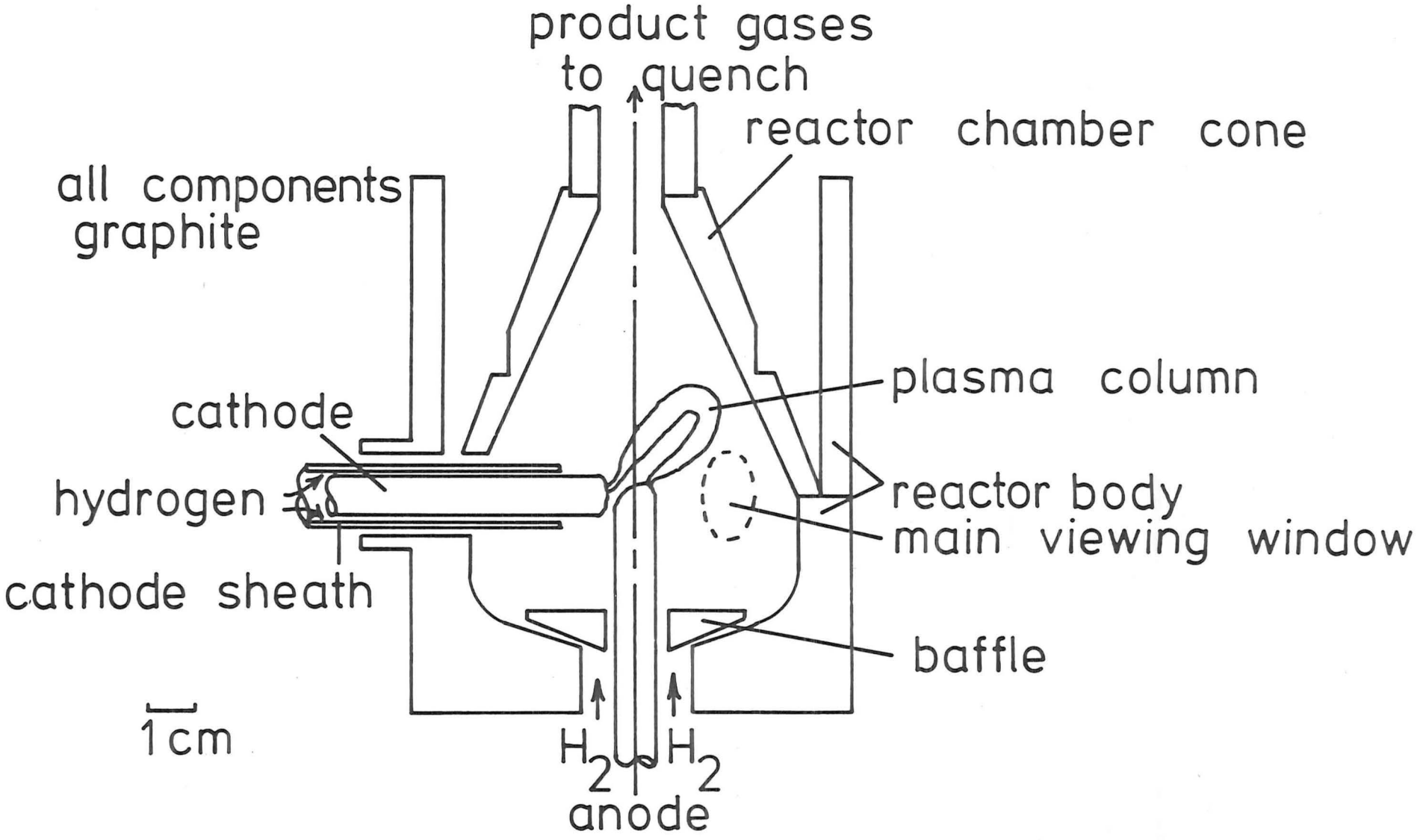

Core of 30 kW Arc Reactor. Figure 3.

Ward used a gas cooler (quench) which consisted of a water-jacketed copper tube (¼" or 5/16" I.D. by 25 cm long). It was expected that this simple device would be unsuitable on a commercial scale plant. Therefore, some other quench capable of scaling to industrial operation, should be devised and if possible tested.

In spite of both Abrahamson's and Ward's endeavours, very little was known about the chemistry and physics of the carbon-hydrogen arc reactor, to the extent that neither could obtain carbon balances. Abrahamson proposed that his 'missing' carbon left the system as crystallites too small to be trapped by most filters. Major gaps in understanding concerned; how the arc behaved, how and in what form the carbon is ablated, what species are present in the plasma, what temperatures are involved, and how is the acetylene formed and preserved?

Ward suffered the additional handicap that he could not feed in sufficient anode to run his reactor until thermal steady state had been reached. Abrahamson concluded his acetylene concentrations were the result of a high temperature gas phase equilibrium in which solid carbon (soot etc.) was an insignificant participant. Ward was unable to confirm or refute this model. If confirmed, this would be an important basis for understanding the reactions and predicting the product gas from a commercial process.

2. ENERGY AND MASS BALANCES OVER WARD'S REACTOR

2.1 Summary

Ward[1] was unable to run his reactor long enough to reach thermal equilibrium. By extending the anode feed from 0.3 m to 1 m, runs of sufficient length were obtained such that a satisfactory balance between the input electrical power and reactor and quench cooling streams was achieved.

Satisfactory carbon balances were obtained by weighing before and after the various reactor components and by measuring the product gas composition by gas chromatography.

2.2 Overall Energy Balance

2.2.1 Experimental Method

Ward's maximum running time appears to be limited to about 10 minutes. This was due to the anode feed capacity of only one 0.3 m graphite rod. A new feed tube was fitted which could drive up to 1 m of anode. With this it was hoped that sufficient running time could be obtained to reach thermal steady state. To facilitate the reaching of steady state, the inner graphite reactor block was pruned to about 2/3 of its former mass.

The reactor lid which closes the top of the reactor and to which the quench is bolted, was found to be unsatisfactorily cooled. The effect of this was that the quench cooling stream carried away part of the reactor heat loss. This would have provided Ward with some unreliable data. (His prequench gas enthalpies and temperatures would be too high.) A new lid was made, which provided more space for insulation at the top of the reactor. In addition a spiral cooling coil was soldered internally to the lid.

The reactor and quench cooling water flows were separately measured on metric 14 Rotameters. The accuracy of these was limited by fluctuations in the mains water pressure during use to ±5%.

The temperature rise in each stream was measured by Ward, using 5 copper/constantan thermocouples in series and glued into the water lines. This was retained for the quench cooling stream. The temperature rise in the reactor cooling stream was measured by a single copper/constantan thermocouple. The junctions were insulated from the copper tubing by two layers of PTFE tape, and secured by several more layers of tape. These were then wrapped in a 2 cm layer of cotton wool to ensure good thermal insulation from the environment. The quench gas and water outlet temperatures were measured by two additional copper/constantan thermocouples, attached in the above described manner. The reference junctions of these two thermocouples were maintained in an ice bath. All the thermocouples' signals were recorded on a Philips sampling recorder. The temperatures could be measured to an accuracy of ±2%.

Ward estimated the electrical power input by reading the arc voltmeter and ammeter, separately, and multiplying the two values. Because of the constantly varying values of each, it is unlikely that very reliable data were obtained.

Initially the current and voltage were recorded separately on charts. Often the traces were so 'messy' that the signals were probably only reliable to ±10%. An analogue multiplier, (Teledyne Philbrick 4452), was used to provide a direct output signal which was proportional to the instantaneous power. (This device has a frequency response which is flat to 50 kHz and -3 dB at 400 kHz, so that reasonable accuracy can be expected in spite of the highly transient waveforms supplied to it (see Fig. 17). The multiplier output voltage was recorded in place of the arc voltage. The arc current, power and voltage could be

obtained with expected accuracies of ±3%, ±5% and ±6% respectively.

2.2.2 Results and Discussion of Results

It was found that about 20-25 minutes of reactor operation were required for the reactor cooling water temperature rise to stabilize, see Fig. 5. The arc power cannot be maintained constant for more than a few minutes, for two reasons. As the cathode is burnt up the arc gap increases, so that the current decreases with time until the operator manually nudges the cathode forward again. Secondly, the arc power always is a maximum at start-up. This is believed to be due to the fact that the conductors are cold and have least resistance, and the magnetic saturation characteristics of the saturable reactor cores (power/supply) are temperature dependent. (It should be noted that the total resistance across the reactor terminals is only 0.32 Ω with a 250 A arc, with electrode resistance of 1/10 of this.)

For the majority of runs, the multi-tubed cross-flow quench was used, see Fig. 4. This was an efficient gas cooler to the extent that the product gas normally left the quench less than 10 K above the outlet cooling water temperature. The typical heat loss in the product gas stream would be for a flow of 30 litres min^{-1} consisting of 95 mole % H_2 and 5 mole % C_2H_2 and ($Cp\ H_2$ = 28.6 J mol^{-1} K^{-1}, $Cp\ C_2H_2$ = 44.1 J mol^{-1} K^{-1}) equal to 7.2 W. This is insignificant when compared to a power input of at least 6 kW.

The power required to produce 1.1 x 10^{-3} mole of C_2H_2 per second would be: (ΔH_f^o = 226 kJ $mole^{-1}$) 250 W. Included in the power required for chemical reaction must be an allowance for the O_2 impurity in the H_2 feed. This varied widely, but a typical value of up to 1% O_2 is likely. ΔH_f^o for CO is -110.5 kJ $mole^{-1}$ (almost all the O_2 appears as CO[2]. CO is favoured over H_2O at equilibrium above 1300 K and at 1 Bar, so that the product gas would contain 2% CO.) The formation of 4.5 x 10^{-4}

Figure 4.

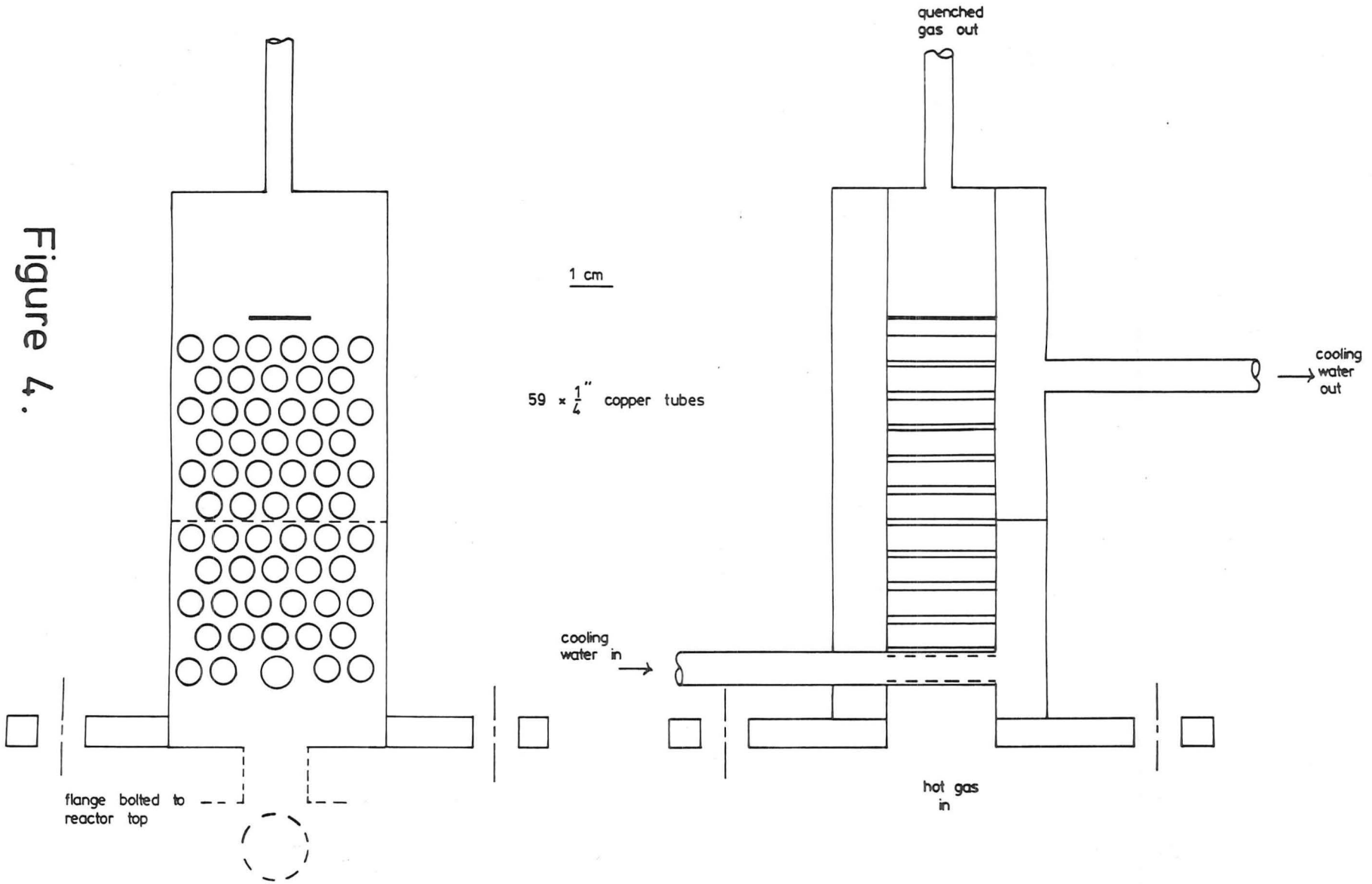

Design of Multi-Tubed Quench.

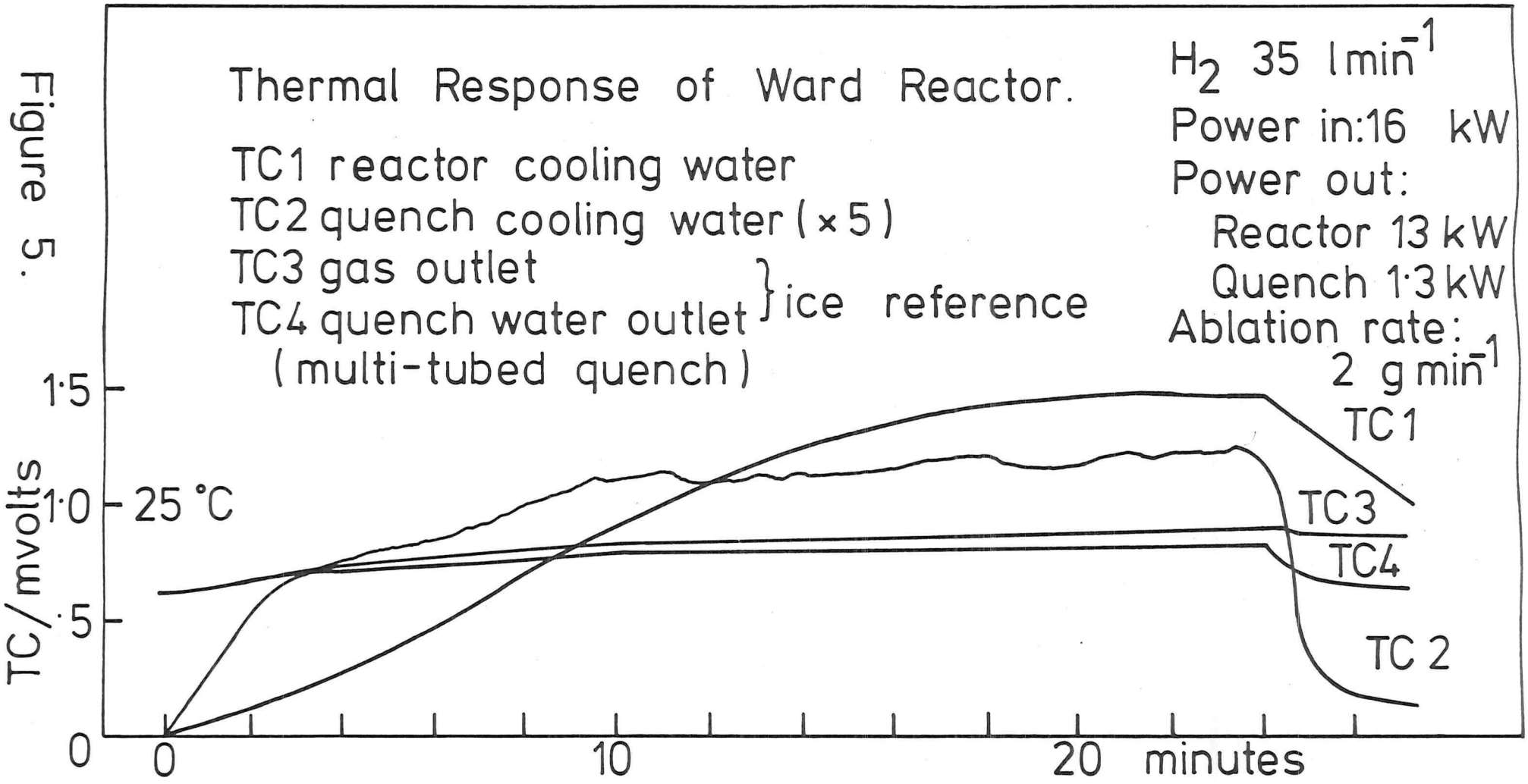
Thermal Response of Ward Reactor.
TC1 reactor cooling water
TC2 quench cooling water (×5)
TC3 gas outlet
TC4 quench water outlet
(multi-tubed quench)
} ice reference
H2 35 l min-1
Power in: 16 kW
Power out:
Reactor 13 kW
Quench 1·3 kW
Ablation rate:
2 g min-1
TC1
TC3
TC4
TC2
25 °C
TC/mvolts
1·5
1·0
·5
0
0
10
20 minutes

Figure 5.

moles of CO per second will supply 50 W. Heat losses from the external surfaces of the reactor and quench are considered to be negligible as almost the entire surface is covered either externally or internally by cooling coils which are within 30 K of ambient temperature.

2.2.2.1 Reactor heat flow data (typical examples): Reactor Run 1.12.77, 9.5mm anode coal core multi-tube quench

Mean ablation rate was 2.5 ± 0.2 g min^{-1} H_2 35 ± 2 ℓ min^{-1}

Input power 12 ± 1.5 kW (150 ± 30 A)

(± 1 kW random error + ± 0.5 calibration error)

150 V open circuit

Reactor cooling water - 7.2 ± 0.7 kW

(The run was terminated at the 22nd minute when the cathode was fully consumed. At that time the reactor cooling temperature difference was still rising very slightly.)

Quench cooling water -1.6 ± 0.2 kW

Heat of reaction (C_2H_2) -0.3 ± 0.1 kW

O_2 (0.25%) (CO) +0.012 kW

Discrepancy = 2.9 ± 2.5 kW

Reactor Run 6.10.77. Run lasted 25 minutes, with steady state reached at the 23rd minute.

9.5 mm anode - coal core multi-tube quench

Mean ablation rate 2.0 ± 0.2 g min^{-1}

Input power 9 ± 1 kW 160 ± 15 A

(150 V open circuit) 33 ℓ min^{-1} H_2

Reactor cooling water -6.9 ± 0.6 kW

Quench cooling water -1.6 ± 0.2 kW

Heat of reaction (C_2H_2) -0.25 ± 0.1 kW

O_2 (4%!) +0.25 ± 0.2 kW

Discrepancy = 0.5 ± 2.1 kW

The discrepancy is well within the expected uncertainty.

Reactor Run 8.8.75. 24-minute run

200 V open circuit multi-tube quench

Input power 16 ± 2 kW (80 V & 200 A)

(estimated from voltage record and ammeter readings during run).

7.95 mm graphite anode

Mean ablation rate 3.6 ± 0.5 g min^{-1}

Total hydrogen flow = 35 ℓ min^{-1}

Reactor cooling water -13.3 ± 1 kW

(steady state reached at 22nd minute).

Quench cooling water -1.3 ± 0.2 kW

Heat of reaction (C_2H_2) -0.25 ± 0.1 kW

O_2 concentration in feed H_2 - unknown

Discrepancy = 1.2 ± 3.3 kW

The thermocouple response curves for this run are shown in Fig. 5. It should be noted that the quench heat load varies erratically because it is related to the arc power (which influences the gas temperature) and the current (which determined the ablation rate, which influences the mass flow rate into the quench). These two inter-related quantities vary for reasons given in section 2.2.2. The outlet gas temperature when using the multi-tubed cross flow quench is within 1 or 2 K of the water outlet temperature at the start of the run. The exhaust temperature gradually increases during the run as soot deposits on the tubes, reducing the overall heat transfer coefficient.

The quench water temperature can be seen to 'stabilise' after 11 minutes while the reactor water temperature continues to rise for another 11 minutes. This provides good evidence that the two streams are satisfactorily thermally isolated.

2.3 The Prequench Gas Specific Enthalpy and Temperature

The quench cooling load was almost independent of arc power, over the range 7.5 kW to 15 kW. For a hydrogen flow rate of 35 ± 3 $\ell\ min^{-1}$ the quench load was 1.2 ± 0.3 kW. The quench heat load is dependent on the hydrogen flow rate.

Run	Power	Gas flow rate	Quench
9.10.75	7.5 ± 0.5 kW	33 $\ell\ min^{-1}$ H_2	1.1 ± 0.1 kW
18.9.74	7.5 ± 0.5 kW	52 $\ell\ min^{-1}$ H_2	2.0 ± 0.2 kW

The mixed mean specific enthalpy of the prequench gases can be defined as the ratio of the quench heat load to the total gas mass flow rate out of the reactor.

For run of 9.10.75:

$$\text{The } H_2 \text{ mass flow rate} = \frac{2 \times 33 \pm 2}{22 \times 60}\ g\ s^{-1}$$

$$= 0.05 \pm 0.004\ g\ s^{-1}$$

$$\text{The nett carbon flow rate} = \frac{1.9 \pm 0.3}{60}\ g\ s^{-1}$$

$$= 0.03 \pm 0.002\ g\ s^{-1}$$

$$\text{Total mass flow} = 0.08 \pm 0.006\ g\ s^{-1}$$

$$\text{The Specific Enthalpy} = \frac{1100 \pm 100}{0.08 \pm 0.006}\ J\ g^{-1}$$

(not counting chemical enthalpy) $= 13.7 \pm 2\ kJ\ g^{-1}$

For run of 18.9.74:

$$\text{The } H_2 \text{ mass flow rate} = 0.079 \pm 0.002\ g\ s^{-1}$$

$$\text{The nett carbon flow rate} = 0.017 \pm 0.002\ g\ s^{-1}$$

$$\text{Total mass flow} = 0.096 \pm 0.004\ g\ s^{-1}$$

$$\text{The Specific Enthalpy} = \frac{2000 \pm 200}{0.096 \pm 0.004}\ J\ g^{-1}$$

$$= 21 \pm 3\ kJ\ g^{-1}$$

The mean heat capacities (Cp) of H_2 and C_2H_2 were obtained by integrating the polynomial functions given in Touloukian[3], over the temperature range 300 to 2000 K.

Mean Cp H_2 = 15.47 J g^{-1} K^{-1} = 30.94 J mol^{-1} K^{-1}

Mean Cp C_2H_2 = 3.48 J g^{-1} K^{-1} = 90.48 J mol^{-1} K^{-1}

The average Cp for 9.10.75 is:

$$15.5 \times 0.625 + 3.5 \times 0.375 = 11 \pm 1 \text{ J } g^{-1} K^{-1}$$

hence the prequench temperature can be estimated.

$$\frac{\text{H mixed mean}}{\text{Cp mean}} \quad \frac{\text{J } g^{-1}}{\text{J } g^{-1} K^{-1}} = \frac{13.7 \pm 2 \text{ K J } g^{-1}}{11 \pm 1 \text{ J } g^{-1} K^{-1}}$$

above ambient = 1250 ± 300 K

T absolute = 1250 ± 300 + 300

= 1550 ± 300 K

The average Cp for 18.9.74 is:

$$15.5 \times 0.82 + 3.5 \times 0.18 = 13.3 \pm 1 \text{ J } g^{-1} K^{-1}$$

$$T = \frac{21{,}000 \pm 300}{13.3 \pm 1} + 300$$

$$= 1880 \pm 400 \text{ K}$$

2.4 Mass Balances

2.4.1 Previous Work

Abrahamson assumed that all of the carbon inflow to his reactor was converted to acetylene, soot or deposited carbon. He analysed the product gas samples for acetylene by wet chemical means. He could only account for an average of about 70% of the carbon inflow.

Ward arranged for his gas samples to be analysed by gas chromatography for: C_2H_2, CO, C_2H_4, C_2H_6, CH_4, and CO_2. He claimed he was able to close the carbon balance but had some difficulty in explaining the presence of oxygen in the product gas (mostly in the form of CO). (It should be noted that above about 180 A, Ward's carbon ablation rates became increasingly doubtful (see Fig. 9, p.41). Therefore his instantaneous carbon balances above 180 A would become increasingly doubtful.) Reasons for Ward's erroneous ablation results are discussed in section 3.2.1.1.

2.4.2 Analysis of Gas Samples by Chromatography

Marchio[4] reports that acetylene-hydrocarbon mixtures can be effectively separated by using a 6 feet by 3/16 inch aluminium column of an equal mixture of Porapak N and R.

Initially the N + R column was fitted in the oven of a Varian 90-P3 chromatograph, fitted with a thermal conductivity detector. Externally across the sample and reference gas outlets, was fitted a 12 feet by ¼ inch column of 5A molecular sieve. It was hoped that an oven temperature could be chosen that allowed good separation of CH_4, CO_2, C_2H_4, C_2H_6, and C_2H_2 by the N + R column and then the H_2, N_2, O_2, CO and CH_4 by the molecular sieve column. This was unsatisfactory and was finally abandoned when it was found that temperature programming was necessary for the N + R column in order to elute the higher hydrocarbons. The N + R column was fitted to a Varian 1520 chromatograph. The column was temperature programmed: 40°C isothermal for 2 minutes, 10°C per minute up to 160°C, and isothermal for 15 minutes. Either a flame ionisation (FID) or a thermal conductivity detector (TC) could be used. (FID was useful for detecting very low concentrations of hydrocarbons.) The molecular sieve column was transferred to the oven of the 90-P3 chromatograph and operated at 40°C. The TC detectors in the two

instruments were fitted with Gow - Mac WX filaments. When run under identical conditions, the two systems gave responses which were equivalent to within ±2%. The TC detectors were calibrated with the following gases: O_2, N_2, CO_2, CH_4 and C_2H_2. The response was found to be linear over the range tested of 2.5 µl to 4 ml. (Peak area was estimated by using the product of peak height and width at half height.) Calibrations for the individual gases were obtained to an expected accuracy of ±5%. In practice the gas composition would have an overall uncertainty of ±10% due to contamination of many samples with varying amounts of air. A typical hydrocarbon analysis using a thermal conductivity detector is shown in Figure 6.

Gas samples were taken from the reactor exhaust gas line immediately above the quench, via a short side arm fitted with a silicone rubber septum. Samples were drawn into 1 ml or 5 ml Precision Sampling Corporation 'Pressure Lok' syringes.

2.4.3 Carbon Usage

The anode feed rate was measured by the methods described in chapter 3. Except for the sections close to the threaded joints, it was assumed that the rods were of constant mass per unit length. The anode rods, cathode assembly, reactor chamber core, baffle, and exhaust tube were all weighed before and after a run. (See diagram of reactor core, Figure 3, section (1.4) for details). Some carbon was always deposited on the bottom half of the reactor body. Because of the difficulty in removing and reassembling this section the carbon deposit was not weighed regularly. It was estimated to be (20 ± 5)% of the total deposited carbon. (The total deposited carbon was normally about 30% of the total ablated carbon.) The soot deposited on the quench tubes was not normally weighed, but was measured to be about 1% of the total ablated carbon.

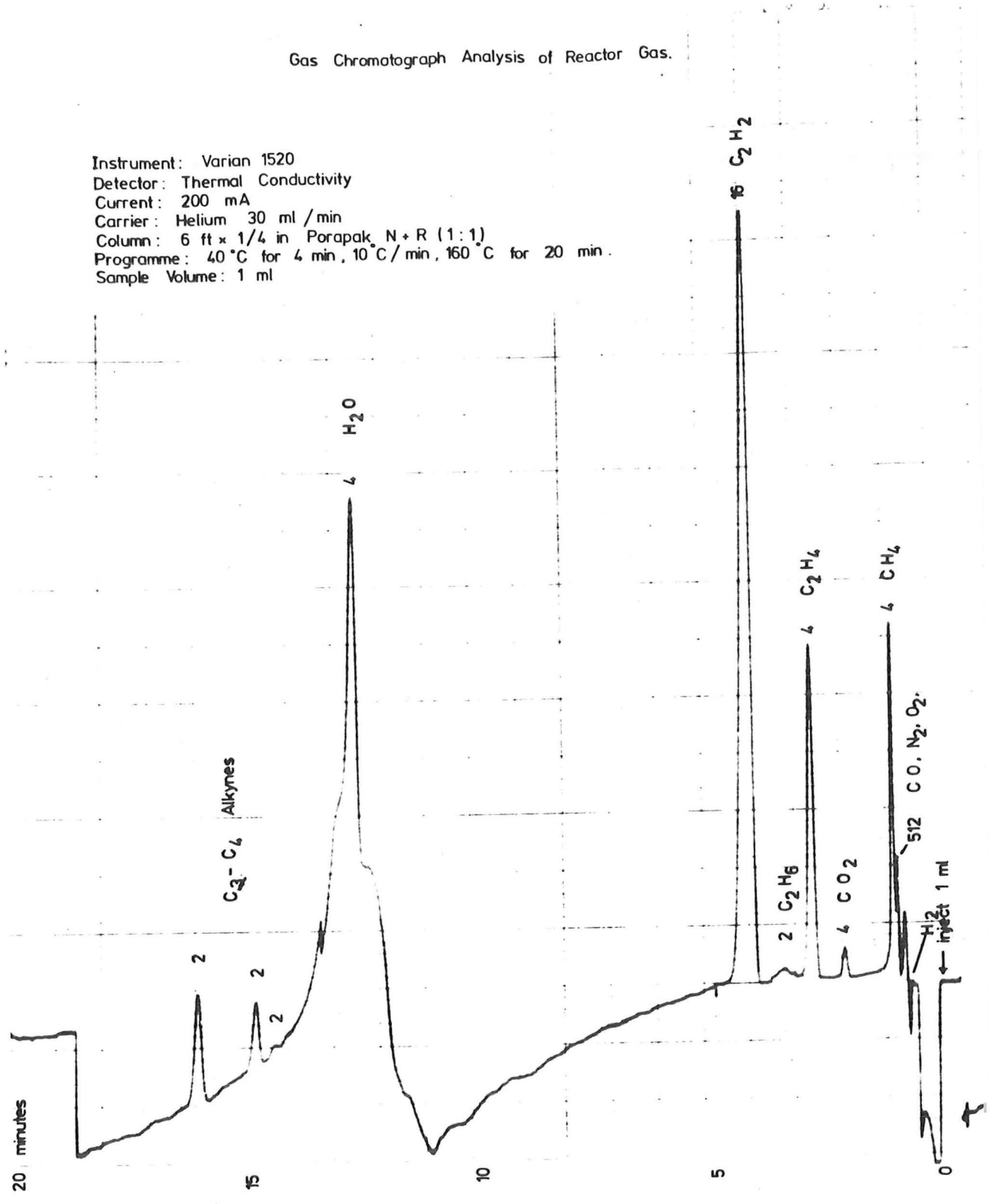
Gas Chromatograph Analysis of Reactor Gas.
Instrument: Varian 1520
Detector: Thermal Conductivity
Current: 200 mA
Carrier: Helium 30 ml / min
Column: 6 ft × 1/4 in Porapak N + R (1 : 1)
Programme: 40 °C for 4 min, 10 °C / min, 160 °C for 20 min.
Sample Volume: 1 ml
C_2H_2
16
H_2O
4
C_3 - C_4 Alkynes
2
2
2
C_2H_6
2
C_2H_4
4
CO_2
4
CH_4
4
512 CO, N_2, O_2,
H_2
inject 1 ml
20 minutes
15
10
5
0

Figure 6.

Likewise, the mass of soot collected in the glass cyclone thimble was not normally weighed. In spot checks it was very much less than 1 gram and was considered negligible.

It was assumed that a constant fraction of the ablated carbon was redeposited throughout the run for a given hydrogen flow rate. (This may not be so. Ward's data shows that typically between 10% to 15% of the ablated carbon was deposited, with some values as high as 30%. In all cases the C/H mass ratio was close to 1. This requires a low hydrogen flow rate (20-30 ℓ min^{-1}) because his currents were generally low. His runs were up to 10 minutes. For a run of 30 minutes and a hydrogen flow of 51 ℓ min^{-1} (about the maximum possible) and C/H mass = 0.25, 20% of the carbon was redeposited. A large number of runs at about 40 ℓ min^{-1} of hydrogen, consistently gave values of 25-30% carbon redeposited.) Fig. 13. It was also observed that if the reactor was run for less than 1-2 minutes then the material deposited on the reactor core was soft black soot. If, however, the run was longer, then a layer of a hard, tough, grey form of carbon was deposited. Clearly this change was dependent on the wall temperature, but it is not known if the fraction of carbon being deposited was significantly altered.

2.4.4 Results and Discussion of Results

2.4.4.1 Gas analysis: The chromatograph procedure described in (2.4.2)gave very reliable results. The gas sampling suffered from the ingress of variable amounts of air to most samples. 'Pressure Lok' syringes are ideal when new, but after some use their reliability falls drastically. (It is important to note that the reactor itself, after flushing out with H_2, and running, has essentially no air in it. This is established from the lack of CN molecular radiation in the arc spectrum, see Figure 25.

Water vapour was present in the reactor gas, but was not quantitatively analysed for. At the reactor temperatures involved, any oxygen present would favour the formation of CO rather than H_2O.

2.4.4.2 Hydrogen Purity: The reactor was run with industrial grade hydrogen, made locally and supplied by New Zealand Industrial Gases. The company 'attempts' to supply a product with less than 0.1% O_2 and 0.1% N_2 and a limit on the H_2O dewpoint. Both Abrahamson[5] and Ward[1] accepted these values. It was found that many cylinders have free water in them. Very much more seriously, the oxygen concentration varied enormously from 0.05% to 4%. The average value would be about 0.5% O_2. Since the discovery of the excessive O_2 impurity, all new cylinders were checked before use Cylinders with more than 1% O_2 were rejected. (Almost all cylinders met the 0.1% N_2 specification). It is suggested that Ward's CO measurements can be explained by these observations.

2.4.4.3 Detection of New Compounds in Reactor Gas: Using the flame ionisation detector and comparing the components of the reactor gas with Town gas and Rockgas, it was established that no C_3 or larger alkanes or simple alkenes were produced with a detectable limit of about 1 ppm by volume. However four new components were discovered. One was identified as benzene. The normal benzene concentration was too low to be detected by the TC detector, the typical concentrations being probably in the range 0.001% - 0.01% v/v.

Plasma-arc devices operated by other workers[6,7,8,9] have produced trace amounts of the following four compounds:-

		Mass number
Diacetylene	$-C \equiv C - C \equiv C-$	50
Vinyl-acetylene	$\overset{\vert}{C} = \overset{\vert}{C} - \overset{\vert}{C} \equiv C -$	52
Methyl-acetylene	$-\overset{\vert}{C} - C \equiv C-$	40
Allene	$-\overset{\vert}{C} = C = \overset{\vert}{C}-$	40

	Hüels[6]	Du Pont[7]	Westinghouse[8]	Hoechst[10]	Valibekov + Bolotov[9]
C_2H_2	14.5	15.2	8.7	20.9	2.1
C_2H_4	0.9	3.0	0.8	1.1	1.5
C_2H_6	0.04	<0.01			0.6
C_3H_4) methyl	0.4	0.2		) 0.26	
C_3H_4) allene		0.04		)	
C_4H_2	0.6	0.7	0.2	0.43	0.15
C_4H_4	0.1			0.17	0.3
C_6H_6	0.3			0.085	

Typical results for the Ward reactor would be: C_2H_2 6.5%, C_2H_4 0.4%, C_2H_6 ~<0.01%, CH_4 0.1%, combined total of three unknown peaks ~0.1%(21.4.78), C_6H_6 <0.01%.

An attempt was made to collect one of these unknown peaks after passing through the TC detector. The contents of the sample tube were analysed by a mass spectrometer by Girardin[11]. His report showed that a peak corresponding to a mass number of 52 was significantly raised. It can be tentatively concluded that vinyl acetylene is one of the reactor products.

Further investigation into the identification of the three unknown compounds has not been attempted. In terms of mass consumption of carbon, they are significant; being the third largest consumer of carbon (not including CO). Commercially, trace quantities of higher alkynes tend to polymerize out in pipe lines. The risk of explosions from the highly unstable products has to be met[7].

2.4.4.4 Nitrogen-hydrogen mixture feed gas: One run was attempted with a gas feed of 7 ± 2 ℓ min^{-1} of N_2 at the cathode, plus a mixture of 24 ± 2 ℓ min^{-1} and 11 ± 1 ℓ min^{-1} of H_2 and N_2 respectively, fed in via the anode. The gas composition during the first part of the run contained 4% C_2H_2 and approximately 9% of HCN. HCN was confirmed by turning off the H_2 flow after the 9th minute, and waiting 1 minute before taking a new sample. The C_2H_2 concentration was now almost zero and the new component had also dropped to almost zero. This confirmed the presence of HCN and rejected the possibility of $(CN)_2$ being formed. No other new peaks were observed on the chromatograph trace. These results appear to be consistent with data published by Nikolov and Petrov[12].

2.4.4.5 Carbon Balance: The results of gas analyses for seven runsare presented in Table 1. The carbon balances for the above seven runs are presented in Table 2. Supplementary run data is also included The instantaneous carbon deposition rate within the reactor has the largest experimental uncertainty. This was assessed as being as large as ±30%. All carbon balances are well within the uncertainties.

Table 1: Gas Analyses for Carbon Balances

Gas Species/% v/v

Run No.	CH_4	C_2H_2	C_2H_4	C_2H_6	C_3C_4	C_6H_6	CO	CO_2	H_2 by difference	Total hydrogen flow to reactor/g hr^{-1}
1	0.16	7.4	0.53	-	0.05	trace	-	trace	91.86	220
2	0.2	6.4	0.66	trace	0.1	-	-	trace	92.64	220
3	~0.15	6.9	0.54	-	~0.15	-	~0.15	-	92.11	220
4	0.28	7.5	0.75	trace	~0.05	-	~0.54	~0.01	90.876	202
5	0.21	6.35	0.69	0.10	-	-	1.06	0.021	92.52	220
6	-	5.4	0.43	trace	-	-	0.11	trace	94.06	220
7	-	5.6	0.5	-	-	-	-	-	93.9	160

All components subject to experimental uncertainty of ±10%.

Table 2: Carbon Balances

Run No.	Duration of run	Instantaneous anode ablation rate	Mean % of total carbon vaporised deposited in reactor	Rate of carbon deposition	Rate of Carbon loss in gases leaving reactor	% carbon vaporised converted to acetylene	Carbon unaccounted for as % carbon vaporised	Carbon to hydrogen mass ratio based on carbon vaporised	Energy to produce unit mass acetylene $(SER)_a$
	Min.	g hr^{-1}	%	g hr^{-1}	g hr^{-1}	%	%	-	kWhr kg^{-1}
1	6	384 ± 5%	(28 ± 5)	107 ± 30	216 ± 50	(51.5 ± 10)	(16 ± 37)	1.7	116
2	4	419 ± 5%	(31 ± 5)	130 ± 30	282 ± 50	(60.76± 10)	(1.6 ± 30)	1.86	78.4
3	4½	343 ± 5%	(35 ± 5)	120 ± 30	207 ± 47	(53.4 ± 10)	(4.5 ± 34)	1.55	121
4	11	292 ± 5%	(27 ± 5)	79 ± 20	211 ± 35	(61.9 ± 10)	(0.8 ± 31)	1.45	71.4
5	9½	240 ± 5%	(26 ± 5)	62 ± 20	206 ± 32	(70.0 ± 10)	(-12 ± 36)	1.08	76.9
6	8	205 ± 10%	(20.5±5)	42 ± 10	157 ± 30	(70.1 ± 10)	(3.0 ± 32)	0.92	121.9
7	11	175 ± 10%	(27*± 5)	47 ± 10	112 ± 27	(41.6 ± 10)	(9.0 ± 33)	1.6	131.3

* estimated

	Mean current	Anode dia.	Anode H_2	Cathode H_2 (litres per minute)
1	270 ± 30	5/16"	32 ± 2	13 ± 2
2	290 ±	5/16"	32 ± 2	13 ± 2
3	280 ±	5/16-1/8"	32 ± 2	13 ± 2
4	210 ± 30	5/16"	32 ± 2	8 ± 2
5	230 ± 30	3/8"	32 ± 2	13 ± 2
6	230	3/8-¼ coal	32 ± 2	13 ± 2
7	205 ± 20	3/8-¼ coal	24 ± 2	8 ± 2

3. THE ABLATION OF CARBONACEOUS MATERIALS

3.1 Summary

From an engineering interest, one of the most significant areas of investigation has been to examine how much carbon can be ablated for a given current and power; and to establish the scaling laws between the significant parameters. To this end both Abrahamson[5] and Ward put a great deal of effort. It is very significant to note that Abrahamson, using 1/8" graphite anodes, found a linear function of ablation rate with current, but Ward[1] found an exponential function for 5/16" anodes (but used rather greater currents). Both Abrahamson and Ward confined their ablation studies to Union Carbide AGSR graphite rods.

This work attempts to rationalize this conflict. The ablation of three different carbons has been investigated. Anodes of diameters varying between 5·08 mm and 9.5 mm have been ablated. In addition, 9.5 mm anodes drilled out and packed with a 6.35 mm core of -72 BS mesh No. 2 Stockton coal, have been successfully run in the reactor.

3.2 Experimental

3.2.1 The Measurement of the Anode Feed Rate

3.2.1.1 Background: Abrahamson[5] fed his 1/8" (3.2 mm) anodes into his reactor by a rubber friction wheel driven by a variable speed D.C. motor. The current through the armature was varied by a variac to control the speed. The variac voltage was calibrated in terms of the anode drive velocity. So long as the frictional drive system did not slip, reliable results should have been possible.

Ward[1] fed his 5/16" (7.94 mm) anodes by a piston driven by a pressurised oil supply. A hydraulic pump provided a supply of high pressure oil which was returned through a throttling valve back to the pump. A bleed-off was taken from the high pressure line, via a fine needle valve and a rotameter to the piston assembly to drive the anode.

The position of the steel rotameter ball was calibrated for various anode velocities. The pump unit was operated long enough to reach constant temperature before a run, so that the supply of oil to the rotameter, hopefully had a constant temperature and hence viscosity. Ward's system had a number of problems associated with it:-

a) Was the viscosity of the oil through the rotameter constant?

b) No written copy of the feed rate data was obtained, making subsequent reanalysis of the data impossible.

c) Since the oil flow rate was small, 2-50 cm^3 min^{-1} and the oil viscosity reasonably large, a very closely fitting rotameter ball was used. The response time for this system to reach a steady value for a change in flow rate would have been several seconds. This would have made it very difficult to record the ablation rate and current at the same instant.

It should be noted that both Abrahamson and Ward attempted to measure the instantaneous rate of feed. This could be dangerous particularly in the case of Ward's device because the arc-electrode system is seldom at steady state. Rather, the anode is either slowly accumulating in the arc zone or diminishing. It is only safe to measure the average ablation rate over some time interval (e.g. 60 s) or fixed element of rod (e.g. 1 cm) and check that conditions have been maintained relatively steady in the previous and subsequent intervals. Abrahamson selected readings for which ablation rates appeared to remain steady over a period of a few seconds.

3.2.1.2 New feed systems: A hydraulic system was used since it provided a fully enclosed device, which eliminated dangerous gas leaks from the reactor. The anode was driven by a piston in a 1.57 cm bore brass tube from a pressurised reservoir. The reservoir was partly filled with oil and pressurised up to 7 bar from a nitrogen cylinder. Two anode drive tubes were built; one, 1 m long, and another 3 m long, providing up to almost 1 m and 3 m of anode feed respectively. The rate of feed was adjusted by a needle valve between the pressure reservoir and the drive tube.

The feed rate was determined with an additional tube (1 m long) and piston, identical in bore to the drive tubes. In place of the anode, a 6 mm D stainless steel rod was attached to the piston. This rod, 1.2 m long, emerged from the top end of the 'displacement' tube via an O-ring seal. The displacement tube assembly was fitted in the oil line between the needle valve and the drive tube. When oil was admitted to the top of the displacement tube, the piston and rod moved down, transferring oil to the anode drive tube. In this way, the movement of the displacement rod corresponded exactly with the movement of the anode, see Figure 7. The movement of the displacement rod was transferred to a rotary shaft via a sprocket and chain. Fixed to the shaft was a disc with equally spaced radial slots. These slots were used to make and break a light beam which activated the event marker on the Yokogawa strip chart recorder.

When the 3 m drive tube was used a four port reversing valve was used to reverse the flow of oil in the displacement cylinder.

This system had three problems associated with it. By far the most important was that nitrogen dissolved slightly in the oil. Bubbles were released in the displacement and drive tubes, resulting in jerky operation unless repeated purging and dismantling were carried out. The displacement of oil resulted in the 1:1 movement of the pistons only in the downwards movement of the displacement piston.

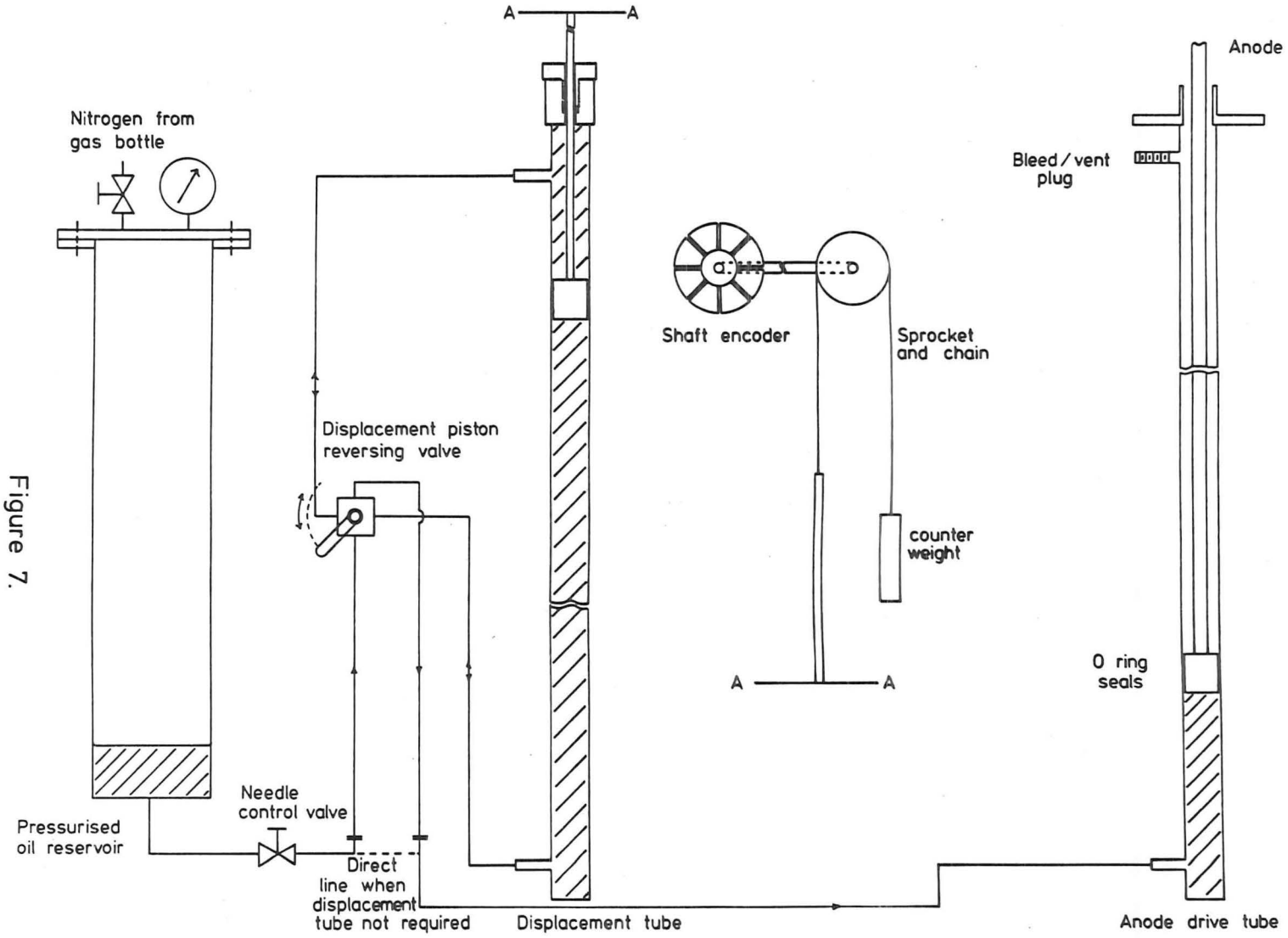

Figure 7.

Design of Anode Drive and Feed Rate Measuring System. (not to scale)

With a limit of 7 bar from the oil supply, the friction was sufficient to produce poor control at the highest ablation velocities investigated.

For the bulk of the results to be presented, a simplified and more direct measurement system was used. The 1 m drive tube was supplied with oil directly from the pressurised reservoir via the needle control valve. The anode rods had small circumferential grooves (approx. 0.25 mm deep) machined at regular intervals (2, 3 or 4 cm) depending on the experimental conditions to be used. When the arc was operating, the grooves could be readily seen on the screen of the projected arc image, as they approached the electrode tip. A convenient line was ruled across the screen and with the assistance of Dr C.E. Davies, the recorder event marker was manually activated as each groove coincided with the reference mark. In addition, a stopwatch was used to check that the recorder chart was operating at the correct speed during runs. (It was found with another recorder also with a digitally derived chart drive system, that the level of radio interference during arc operation was sufficient to seriously upset the calibrated speed). No disagreement was ever detected with the Yokogawa recorder.

All feed rate systems used to date have assumed that the graphite rods are of constant diameter and constant density. This would have been particularly important for Abrahamson's work, as the 1/8" rods are significantly oversize and often have inclusions on their surface, making their cross-section non-circular. He used only those which just passed through a hole gauge, 3.2 mm diameter. Weighing a number of 5/16" (7.94 mm) and 3/8" (9.53 mm) graphite rods, showed that they had a mass per unit length of 0.796 ± 1% g cm^{-1} and 1.24 ± 1.5% g cm^{-1} respectively. For anodes of 6.35 mm and 5.08 mm and drilled out (annular) anodes a density of 1670 kg m^{-3} was used. With the technique described, the rate of anode consumption could be measured to ± 5%.

3.2.2 The Electrical Current Contact

It is fundamental to this reactor concept that the moving anode rod at its upper end must carry the entire arc current. At some point the current must be supplied by a sliding contact. Ward used a tungsten tube of 5/16" internal (nominal) bore. A section of one side was machined away and replaced with a tungsten section which could be held in place by a spring, so as to provide sufficient contact pressure against the moving anode to produce an adequately low contact resistance. The upper end of the tungsten tube reached within 5 cm of the arc. The anode temperature immediately above the contact was assumed by Ward to be sufficient to necessitate the use of this refractory metal.

A new contact had to be made to accommodate 9.53 mm rods. New contacts (9.53 mm and 7.94 mm), Figure 8, were machined out of bars of copper. Longitudinal slots were machined so that the anode hydrogen flow sweeping past could provide additional cooling. Contact pressure was obtained using Ward's system, except a graphite block was used instead of the tungsten section. No trouble was experienced with either contact. From the tar deposit on top of the 9.53 mm contact (after coal runs), it appears the top reached no more than 400^{o}C.

3.2.3 Joining Anode Sections

Ward's feed system could only drive 1½ 7.94 mm rods (about 0.4 m travel maximum). This necessitated a joint between two graphite rods. Ward, after considerable experimentation found a 3/16" W threaded joint was satisfactory. This has too low a root diameter and is very easily broken. A No. 1 BA thread has been found to be more satisfactory. Up to six sections have been screwed end to end and run in the reactor without significant trouble. The 9.53 mm rods were joined using a 5/16" UNF thread. Care is always needed to ensure the thread is centred along the axis of the rod, otherwise failure may occur when being loaded through the current contact.

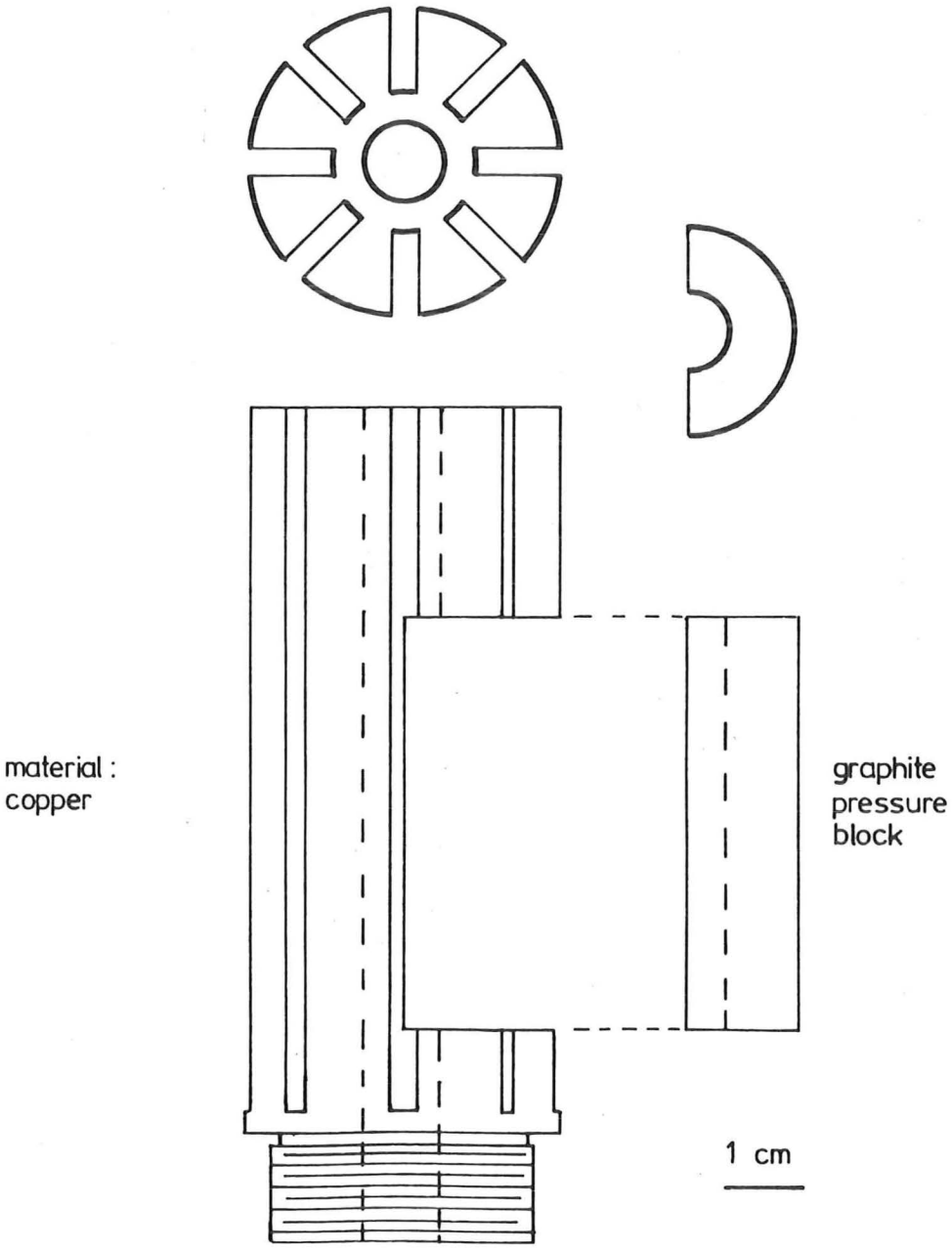

400 Amp. Sliding Anode Current Contact.

Figure 8.

3.2.4 Current Measurement

An Avo 0.00025 Ω shunt resistor provides a voltage signal of sensitivity 4 A mV^{-1} which was recorded by a Toa chart recorder. A current record is produced with an expected accuracy of better than ± 5%. An additional shunt (Yokogawa 0.000166 Ω) is used to display on a panel meter the current during operation. It should be noted that the recorder chart displays an 'average' current, as the recorder has a time constant of approximately one second.

3.2.5 Coal Core Anodes

The 7.94 mm and 9.53 mm graphite rods were drilled axially for about 90% of their lengths with 4.8 mm and 6.35 mm holes respectively. Dried and ground (-72 BS mesh) coal (No. 2 Stockton and one sample of Ohai) was vacuum-packed into the hollow rods by Dr C.E. Davies[13]. If required the rods were then threaded and grooved in the usual way.

3.2.5.1 Low current testing of 7.94 mm coal core anodes: A 7.94 mm x 0.3 m anode packed with No. 2 Stockton coal was placed in the 'Standard Arc' device built by the author[104]. A standard 3.18 mm graphite cathode was used. An arc of 35 - 40 A in a nitrogen atmosphere was struck onto the coal cored tip. A few particles of coal were initially ejected combined with some volatile matter. The arc attachment burnt around the graphite annulus for a few minutes until it had burnt away, exposing the coked core. At this stage it could be seen that the arc attachment jumped onto the coked core fleetingly. It was concluded that the coal core could be made to carry the arc current. It was also significant that with the extreme heating of the tip, large slugs of swelling coal did not shoot out.

An additional experiment was carried out using a rod (7.94 mm) of partially graphitised carbon (Union Carbide grade CMG). This has a somewhat higher resistivity than the standard Union Carbide AGSR graphite

rods. It was expected that the increased resistivity of the annulus would help make the arc attachment favour the coke core. This experiment terminated suddenly after 1-2 minutes with an explosion. The entire rod had ruptured. Investigation showed that the CMG material has a lower porosity than the AGSR; this coupled with the increased ohmic heating of the rod, produced gas pressures within, that led to the observed result.

From this experience, all coal cored anodes (AGSR) used in the high current reactor had small holes (No. 60) drilled through the wall every 10 mm to vent excess pressure.

Ohai coal was found to be unsatisfactory as there was no sticking of the particles.

3.2.6 Cathodes Used in Ward Reactor

All reactor runs in this work were carried out with a single cathode. Ward's final cathode design[1] was used throughout, except for some minor changes. A ¼" UNF thread was used for securing the graphite rod to the copper conductor. A 7.94 mm graphite rod was used, with only the threaded end passing through the BN collar, being machined down to 6.3 mm. For high current runs (> 250 A), up to 3 cm of rod was allowed to extend beyond the sheath, see Figure 3. This was necessary in order to provide a useful life of approximately 15 minutes burning. In all cathodes, a hydrogen flow of 10 ± 3 litres per minute was used.

3.2.7 Power Supply Voltage

All the ablation results were obtained with the reactor power supply set at 200 V open circuit. With this arrangement the 3-phase supply is balanced between the three saturable reactors. It was discovered that Ward used an open circuit voltage of 150 V. In this condition most of the load is drawn from 2 phases, and the saturable reactors are unbalanced. It is not known whether the unsymmetrical waveform of the

current supply being used, could have any influence on the ablation results he obtained. See figure in addenda.

3.3 Constraints on the Investigation of Carbon Ablation, with the Present (Ward) Reactor

3.3.1 Current and Power

Ward investigated the ablation of 7.94 mm graphite rods over the current range 100 - 220 A. (This corresponds to a current density of 2 - 4.5 A mm^{-2}.) Ward's results[1] showed a non-linear increase in ablation for an increase in current. Any commercial process would exploit this 'effect'. Therefore it was vital that ablation should be investigated to the largest possible current and current density.

The maximum capability of Ward's power supply is unknown. However, an average current of 400 A and power of 25 kW is obtainable with some in reserve. With the extreme current and voltage transients which are now known to exist (section 7.3), diode failure at higher ratings is a serious possibility.

At 16 kW (250 - 300 A), about 10 minutes of reactor operation can be achieved before significant melting of the ceramic insulation occurs. This period was reduced to 5 minutes at 24 kW (300 - 350 A). At the highest ratings investigated in this work, a maximum running time of 5 - 7 minutes was considered safe, otherwise serious structural failure could not be dismissed.

3.3.2 Materials

The smallest diameter rods that can be satisfactorily joined (by threading) appears to be 7.94 mm. For this reason, anodes smaller than 7.94 mm were not extensively investigated. To achieve high current densities (up to 15 A mm^{-2}), short sections of 7.94 mm rods were turned down to 6.35 mm and 5.08 mm diameter for testing. The investigation of anodes of greater than 9.53 mm diameter was not considered to be useful,

because of the low current densities obtained. (A 12.7 mm rod would have been limited to a maximum of less than 3 A mm^{-2}). Current densities greater than 15 A mm^{-2} could not be conveniently investigated because the anode velocity was so great (> 5 mm s^{-1}) that control by the operator was extremely difficult. (Intermediate current densities were investigated by appropriate current settings and by drilling out the core of the rods.)

In addition to graphite, two other grades of carbon were tested. The highest resistivity (GA) grade (coked petroleum coke) was important because of its possible similarity to an extruded coked coal anode. The ability of the GA grade to pass the necessary current and its ablation compared to the AGSR grade graphite was observed.

3.4 Results

3.4.1 The Ablation of 7.9 mm Anodes

The experimental dataare shown in Figure 9. The ablation of three different carbon materials are compared. Ward's results are also plotted. It can be seen that above about 180 A, Ward's results depart significantly and increasingly from the results of this work. This work establishes the linear relationship between current and ablation rate for a fixed anode diameter. This is in agreement with the results of Abrahamson[5] and Baddour and Iwasyk[14, 15].

It can be seen that there is significant scatter in the experimental results. This is accounted for by small accumulations or depletions of the anode in the arc zone during the measuring intervals. The precise geometry of the anode tip relative to the cathode tip and the arc gap, may have slight effects on the ablation due to changes in the radiation losses. It can be seen that there is no difference between the ablation of AGSR graphite and CMG partial graphite However GA grade coke appears to have a slightly greater rate of ablation compared to the other

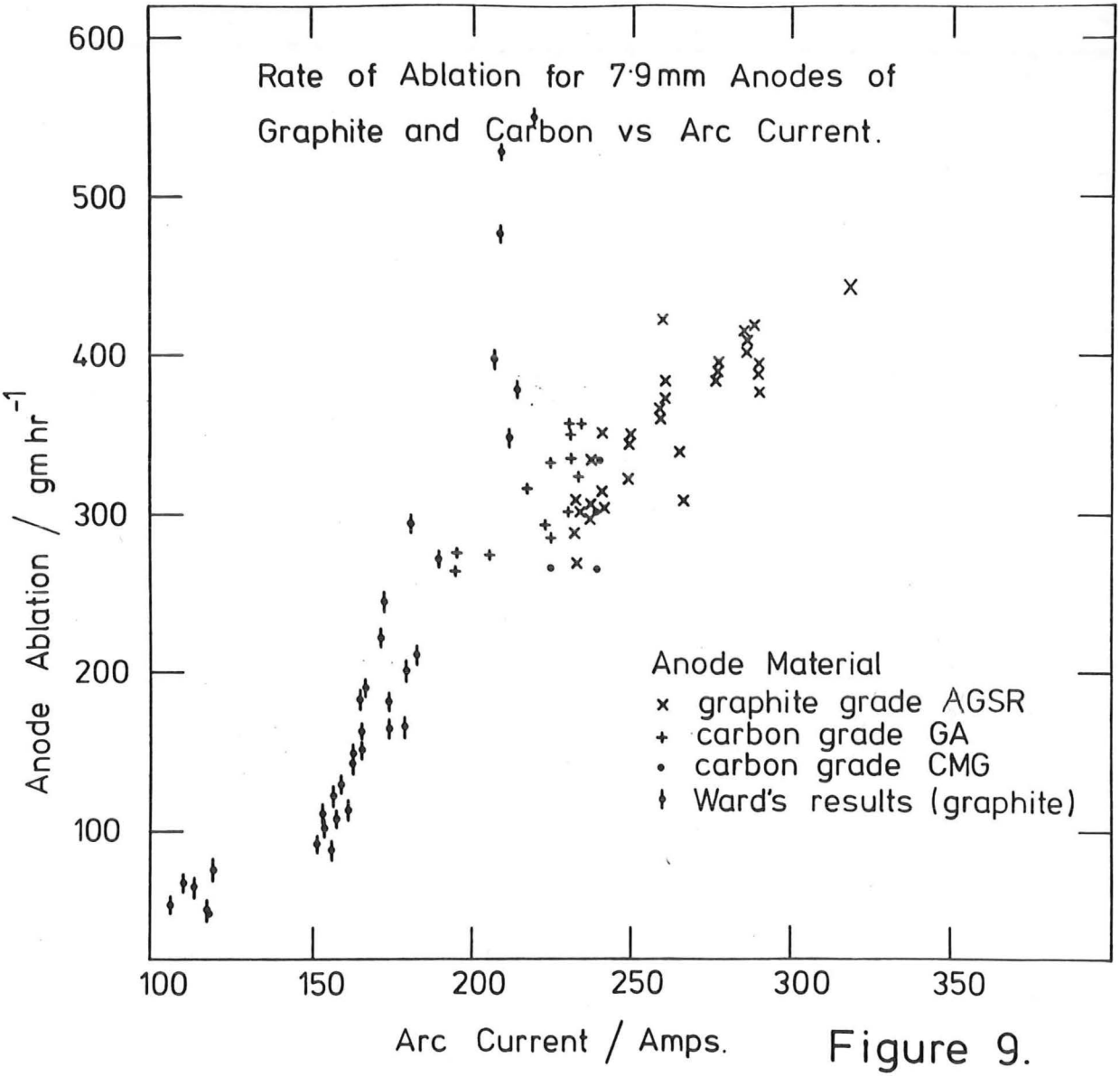
Rate of Ablation for 7·9mm Anodes of Graphite and Carbon vs Arc Current.
Anode Ablation / gm hr^{-1}
600
500
400
300
200
100
100
150
200
250
300
350
Arc Current / Amps.
Anode Material
× graphite grade AGSR
+ carbon grade GA
• carbon grade CMG
Ward's results (graphite)

Figure 9.

two materials. This is expected because the increased resistive heating and lower thermal conductivity mean that less of the anode voltage drop is required to supply the anode axial conduction.

3.4.2 The Ablation of Graphite and Graphite/Coal Anodes of Differing Diameters

These results are shown in Figure 9a. Again a linear trend is apparent although there is considerable scatter. The reason why the data points for solid 9.5 mm anodes tend to be so scattered is not known. It should be noted that a number of coal cored data points fall well above the general ablation trend. This is due to chunks of coal being ejected from the tip without being ablated in the correct manner. Otherwise the coal core data points fall among the general experimental scatter.

3.4.3 The Relationship between Ablation per Unit Area and Current Density

The plotting of ablation per unit area against current density, more usefully relates anodes of differing diameters to each other. This plot is probably the most useful for engineering scale-up purposes. The data for graphite and graphite-coal anodesare shown in Figure 10. (It should be noted that this graph uses the data of Figure 9a, and relates it in terms of per unit anode tip area.) The data of Abrahamson[5] can be seen to fit well with this work. It is tempting to produce a straight line fit through all the data points, however the uniform steady state thermal ablation model investigated by Dr C.E. Davies[16] shows this would be an over-simplification. Davies[16] has shown theoretically that a large anode should have a greater ablation rate per unit area than a smaller diameter anode for the same current density. This amounts to about 20% between 9.53 mm and 3.2 mm anodes. This effect appears to be demonstrated between Abrahamson's data (3.2 mm) and the 9.5 mm and 7.9 mm anodes of this work.

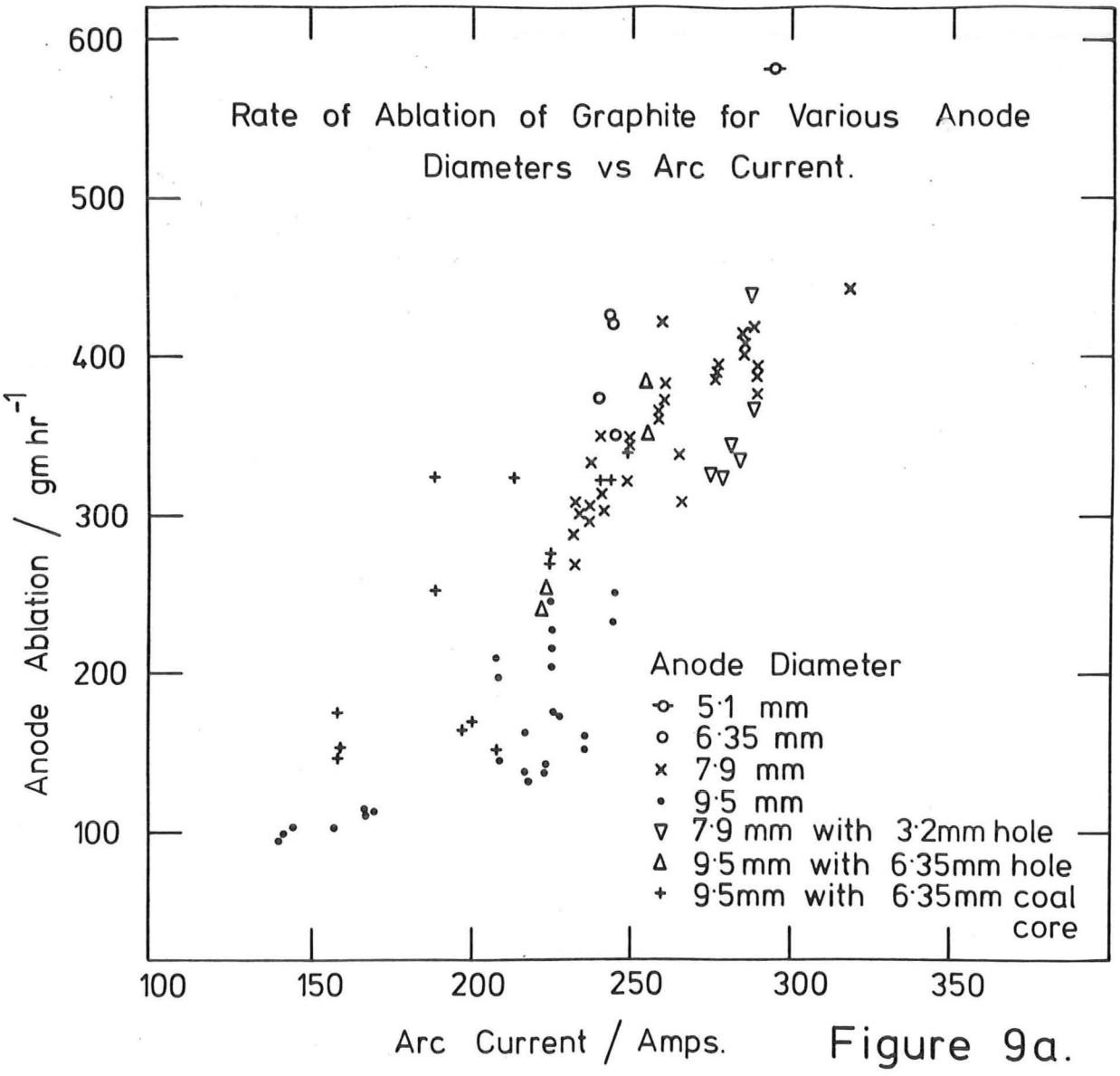
Rate of Ablation of Graphite for Various Anode Diameters vs Arc Current.
Anode Ablation / gm hr⁻¹
600
500
400
300
200
100
100
150
200
250
300
350
Arc Current / Amps.
Anode Diameter
5·1 mm
6·35 mm
7·9 mm
9·5 mm
7·9 mm with 3·2mm hole
9·5mm with 6·35mm hole
9·5mm with 6·35mm coal core

Figure 9a.

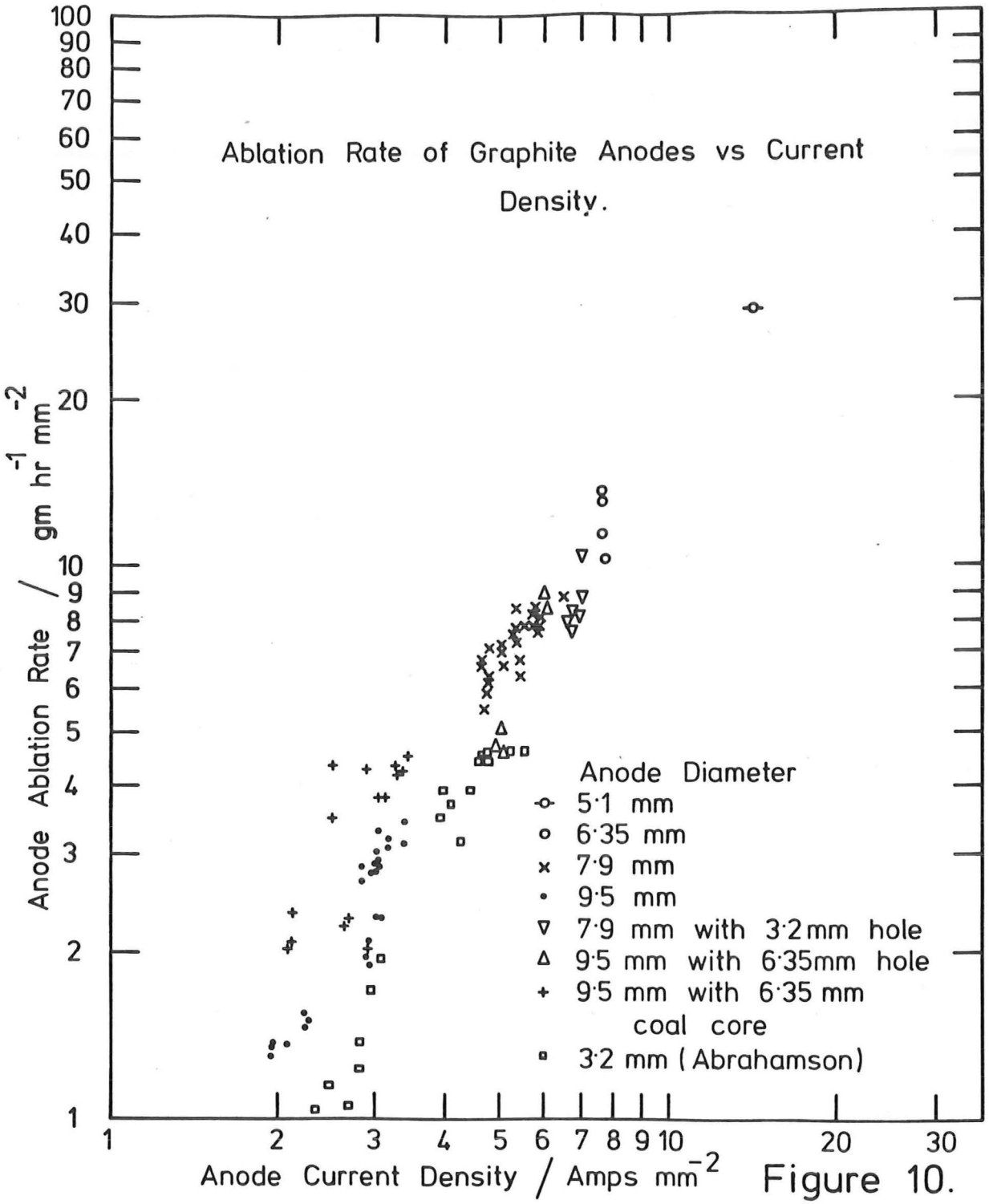
Ablation Rate of Graphite Anodes vs Current Density.
Anode Ablation Rate / gm hr^{-1} mm^{-2}
Anode Current Density / Amps mm^{-2}
Anode Diameter
5·1 mm
6·35 mm
7·9 mm
9·5 mm
7·9 mm with 3·2mm hole
9·5 mm with 6·35mm hole
9·5 mm with 6·35 mm coal core
3·2 mm (Abrahamson)

Figure 10.

3.5 The Ablation of Graphite of High Current Density in the Kiloampere Range

The ablation studies carried out in the Ward[1] reactor are limited to about 400 A D.C. Alloy Steel of Christchurch have a 3-phase (A.C., note) arc electric furnace which can provide 6 kA per phase. A number of tests were carried out using this facility to estimate the ablation rate of 25.4 mm and 19.05 mm graphite rods in air.

Most of the tests ended after periods ranging between 20 s and 80 s, with the explosive rupturing of the electrode. It was significant to note that examination of the fragments showed that almost all split in half longitudinally, and that the central core (about 5 mm in diameter) had vaporized, see ref. 13. An attempt to record the surface temperature of an electrode with an optical pyrometer, showed that just prior to rupturing it was off the scale set at 3000°C. Equally spaced holes were drilled every 25.4 mm through the electrodes, so as to serve as reference points for the ablation measurements. It was significant to notice that jets of vapour could be seen issuing from the holes during operation.

The most reliable ablation test was one of 82 seconds with a 25.4 mm electrode at an average current of 3 kA. Length ablated was 60 mm.

current density	=	6 A mm^{-2}
mass ablated	=	52 x 10^{-3} kg in 82 s
rate of ablation	=	2280 g hr^{-1}
ablation rate/area	=	4.5 g hr^{-1} mm^{-2}

The plot of Figure 10 predicts for 6 A mm^{-2}, 6.5 gm hr^{-1} mm^{-2} should be ablated for the DC arc in hydrogen. Bearing in mind that the AC electrode is an anode for one half of each cycle and the considerable experimental uncertainty involved, these values appear to give further justification to the current density correlation (Figure 10) for the purposes of engineering scale-up.

3.6 The Resistive Heating of Graphite Electrodes

It seemed obvious that the Alloy Steel run electrodes failed due to resistive heating. Failure occurred when the vapour pressure of carbon species, or the pressure of trapped gases, exceeded the bursting strength of the material. The observation that the electrode core had 'vanished' suggests that the electrode axis had reached, or was very close to the carbon sublimation temperature. This is also supported by the observation of jets of vapour from the radial holes.

3.6.1 The Radial Temperature Gradient in Graphite Conductors

If a uniform graphite rod, carrying a steady uniformly distributed current is considered, it will be assumed that heat loss from the surface is solely by radiation and that no longitudinal temperature gradient exists (a section some distance from either the electrode tip or current contact is considered).

Carslaw and Jaeger[17] provide a solution for uniform heat production in a cylinder, given by:

$$T_o - T_r = I^2 \Omega \frac{r^2}{4K} \qquad (1)$$

where T_o is the axis temperature in K

T_r is the temperature at radius r

Ω is the resistivity in Ωm

r is the radius in m

I is current density A m^{-2}

$\dot{i}$ is the total current in A

K is the thermal conductivity in W m^{-1} K^{-1}

A heat balance over a length of rod ℓ establishes the surface temperature for a conductor of radius r:

$$i^2 \omega = 2\pi r \ell \varepsilon \sigma T_s^4 \qquad (2)$$

where ω is the resistance of rod length ℓ

T_s is the surface temperature

$\Omega = \omega \frac{\pi r^2}{\ell}$ = resistivity in Ωm

$$i^2 \frac{\Omega \ell}{\pi r^2} = 2\pi r \ell \varepsilon \sigma T_s^4$$

expressing i in terms of current density I ($W\ m^{-2}$) (for scale-up the current density is the important parameter.):

$$I^2 r \Omega = 2 \varepsilon \sigma T_s^4 \qquad (3)$$

Substituting T_s in (3) for T_r in (1)

$$T_o - \sqrt[4]{\frac{I^2 r \Omega}{2 \varepsilon \sigma}} = \frac{I^2 \Omega r^2}{4K}$$

i.e. T_o = axis temperature = radial ΔT + surface T

$$= \frac{I^2 \Omega r^2}{4K} + \sqrt[4]{\frac{I^2 r \Omega}{2 \varepsilon \sigma}}$$

Typical properties of a high quality graphite are:

emissivity = 1.0

$\Omega = 1 \times 10^{-5}\ \Omega m$

$K = 30\ W\ m^{-1}\ K^{-1}$ at 3500 K[27]

$I = 7\ A\ mm^{-2}$ (total current = 3170 A)

$= 7 \times 10^6\ A\ m^{-2}$

$r = 12 \times 10^{-3}$ m

$\sigma = 5.8 \times 10^{-8}\ W\ m^{-2}\ K^{-4}$

then: $T_o = 588 + 2668 = 3256$ K

Although this value is 600 K below the likely sublimation temperature, it should be noted that the radial temperature gradient is significant and that it depends on I^2 and r^2. Also there is considerable uncertainty in Ω and K for the material in the 3000+ K region.

3.6.2 Commercial Considerations

The Alloy Steel experiments revealed that high temperature strength is a limiting parameter in scale-up considerations. A coked coal electrode would have properties not nearly as satisfactory as those of AGSR graphite. The mechanical strength would possibly be at least an order of magnitude less. The resistivity would be one or more orders of magnitude greater (except possibly at the electrode tip). Davies[13] measured values of resistivity of the tips of the packed coal electrode cores. His lowest values are about 1×10^{-4} Ωm (an order of magnitude higher than AGSR). The thermal conductivity is likely to be lower, and considerable pressures will be developed within the coke pores by trapped gases. A plot of axis temperature for various current densities and resistivities against electrode diameter may help to reveal limitations on the process. Figure 11 shows that only relatively small diameter electrodes are possible (1 or 2 cm), and that very low current densities are required (of order 1 A mm^{-2}). These constraints necessitate the use of large numbers of energy inefficient reactors to process a given amount of material[13]. On this basis alone, the prospects of a commercial process look most unlikely.

3.7 Cathode Ablation

Ward[1] investigated the deposition or ablation of carbon on the graphite cathode. He concluded with his final cathode design that carbon build-up could be controlled by a suitable flow of hydrogen (10-20 ℓ min^{-1})

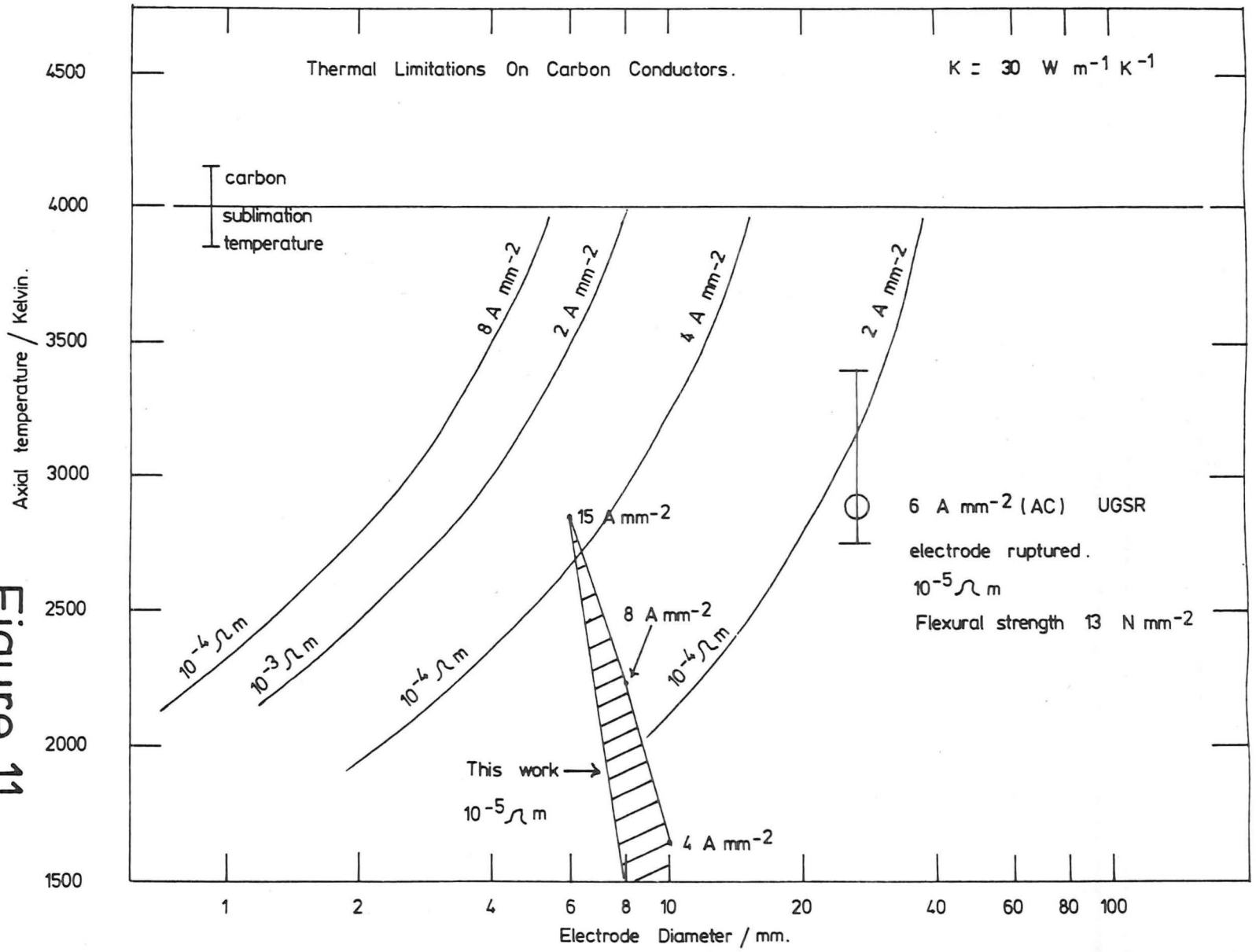
Thermal Limitations On Carbon Conductors.
K = 30 W m⁻¹ K⁻¹
carbon
sublimation
temperature
8 A mm⁻²
2 A mm⁻²
4 A mm⁻²
2 A mm⁻²
10⁻⁴ Ω m
10⁻³ Ω m
10⁻⁴ Ω m
10⁻⁴ Ω m
15 A mm⁻²
8 A mm⁻²
4 A mm⁻²
This work
10⁻⁵ Ω m
6 A mm⁻² (AC) UGSR
electrode ruptured.
10⁻⁵ Ω m
Flexural strength 13 N mm⁻²
Axial temperature / Kelvin.
4500
4000
3500
3000
2500
2000
1500
1
2
4
6
8
10
20
40
60
80
100
Electrode Diameter / mm.

Figure 11.

from the cathode sheath. He also noted that, 'if too high a current is drawn, rapid erosion of the cathode soon resulted'. His results may be influenced by his lower operating voltage (150 V O.C. compared with this work, 200 V O.C.), which required a slightly smaller arc gap. However at 230-250 A or greater the 7.9 mm cathode in this work always had a nett erosion. Below 230 A Ward's conclusions are generally supported with the addition that the precise placing of cathode tip with respect to the ablating anode tip is important. Above 250 A, cathode ablation is an important factor in reactor operation as it often limited the running time. To maximise the operating time the cathode was extended up to 3 cm beyond the sheath, (the maximum that could be fitted with the present reactor design). Cathode ablation rates up to 0.35 gm min^{-1} were measured at currents of 280 A (0.57 kA cm^{-2}). Mentel[18] provides data on ablation of 6.15 mm graphite cathodes, in an argon atmosphere.

Mentel's data extends down to 1 kA cm^{-2} where the ablation loss is 5 mg cm^{-2} s^{-1}. At 0.57 kA cm^{-2} the ablation measured in this work is 12 mg cm^{-2} s^{-1} (in hydrogen). This is at least 2 or 3 times Mentel's results. This difference is probably accounted for by the reactivity of of carbon in hydrogen, different heating rates of the hydrogen ion current compared with the argon ion current at the cathode attachment, and the different convective heat losses along the electrodes.

4. CARBON DEPOSITION WITHIN THE REACTOR

4.1 Types of Deposit

Three types of soot have been observed on the inner graphite chamber after reactor operation.

If the reactor was run for only a few seconds (i.e. the walls were not allowed to warm up), then a soft lampblack-like film was found to cover the inner graphite chamber.

If the reactor reached 'working temperature', then a hard, relatively tough, greyish, relatively uniform and smooth layer was found. This material appeared to have a coefficient of expansion greater than the ATJ graphite surface it was deposited on. This pyrolytic layer, when cold, was usually cracked and had partially pulled itself away from the parent deposition surface. Often, the whole upper chamber core could be restored by prizing the deposit out in one piece. It is believed that this material is deposited at about 2000^{o}C. This appears to be consistent with the data assembled by Palmer[19]. (It is interesting to note that the Avco researchers[102] report these two distinct deposits in their final plasma-arc coal reactor. Removal was effected by turning off the coal and hydrogen flows and inject steam into the reactor, before the hard pyrolytic deposit could form. This operation was repeated on a cyclic basis, and was their solution to the build-up of deposits in their process.) The total mass of this deposit was usually 20-30% of the ablated graphite. When the fraction of carbon redeposited is plotted against C/H ratio, the highly scattered points, surprisingly show little tendency to increase with increasing 'richness' in the vapour phase, see Figure 12. This may imply the deposition is a surface or surface catalysed process. If the percentage of carbon redeposited is plotted against the combined hydrogen flow rate

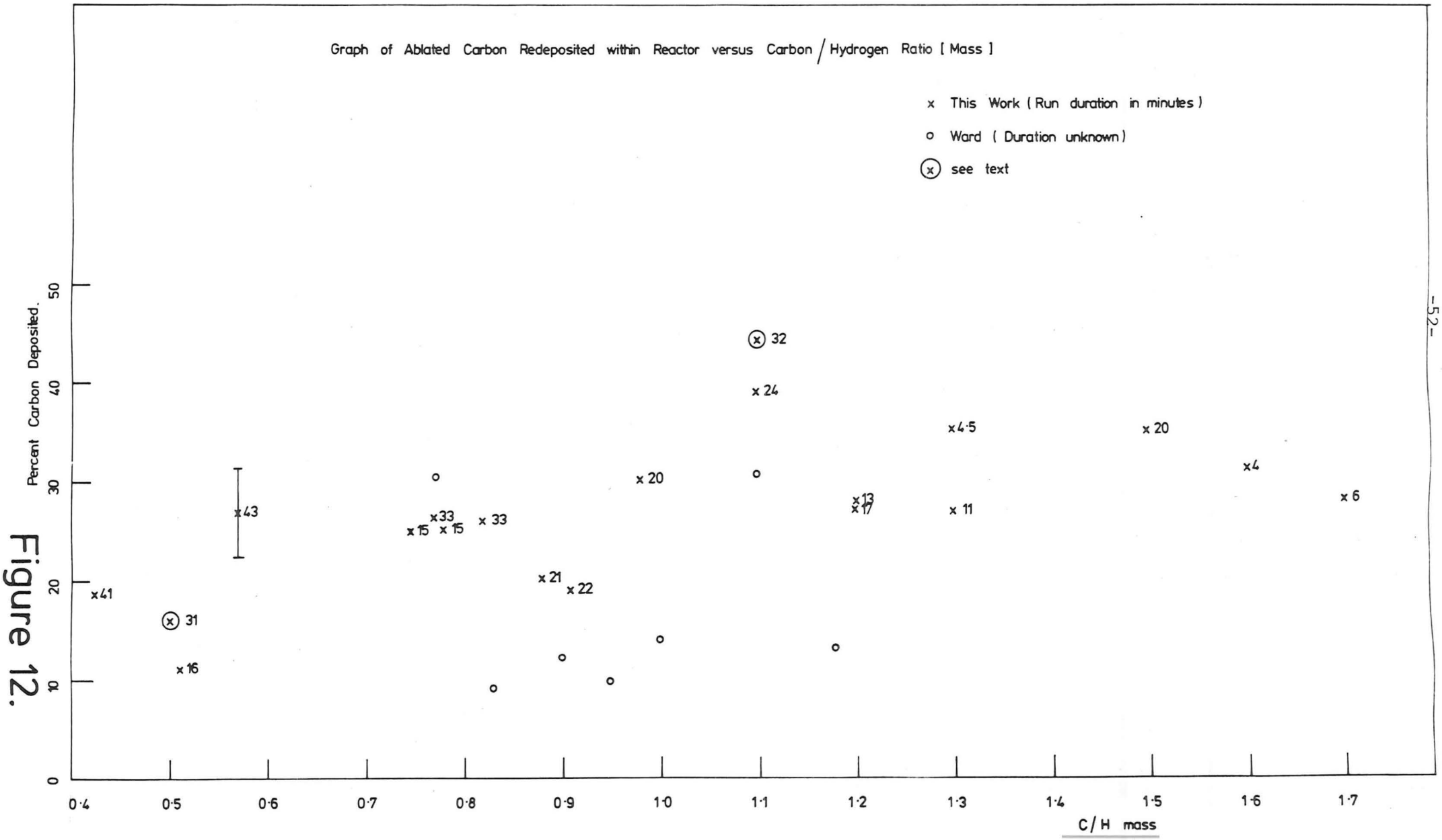
Graph of Ablated Carbon Redeposited within Reactor versus Carbon / Hydrogen Ratio [Mass]
x This Work (Run duration in minutes)
o Ward (Duration unknown)
(x) see text
Percent Carbon Deposited.
0
10
20
30
40
50
0·4
0·5
0·6
0·7
0·8
0·9
1·0
1·1
1·2
1·3
1·4
1·5
1·6
1·7
C / H mass
x41
(x) 31
x16
x43
x15
x33
x15
x33
x21
x22
x20
(x) 32
x24
x4·5
x13
x17
x11
x20
x4
x6

Figure 12.

into the reactor, (Figure 13), then once again a high degree of scatter is seen. The general observation is that the fraction of carbon deposited falls considerably with flow rate. Indeed low flow rates (less than 30 $\ell\ s^{-1}$ or so) resulted in 40% or more of carbon being deposited. This was not a useful regime for operation, so that the maximum C/H ratio investigated was constrained by this. The pair of data points marked by circlesclearly show this. They were consecutive runs of the same duration (31 and 32 minutes), with the same current and anode diameter. The hydrogen flow was increased from 20 to 40 $\ell\ min^{-1}$. The fraction deposited fell by a factor of five. The scatter on the graph shows some other variable is important, and is more or less random. This is probably the arc-electrode geometry. This varies greatly both during and between runs. The carbon vapour plume may be thus directed at times towards the chamber wall. Indeed it was usually found that the pyrolytic deposit was thickest opposite the cathode side of the chamber. In addition this area was discoloured, suggesting interaction with the extremities of the arc.

It was noted in section (6.3.5) that the residence time at 40 $\ell\ min^{-1}$ is approximately 10 ms, and that this is sufficient time for atomic hydrogen to diffuse to the chamber walls. It is reasonable to conclude that if the residence time is allowed to be too great (much over 10 ms for this reactor geometry) the atomic hydrogen concentration can fall to an insufficient level to sustain a homogeneous gas phase. The result is gross carbon deposition. In fact at low flow rates (long residence times) the wall deposit changes from a hard smooth deposit to a more gross coke like accumulation (and if allowed to continue would before long, block up the chamber).

The third type of wall deposit was a feather type of coke which grew out from the surface. This generally grew when attempts were made to

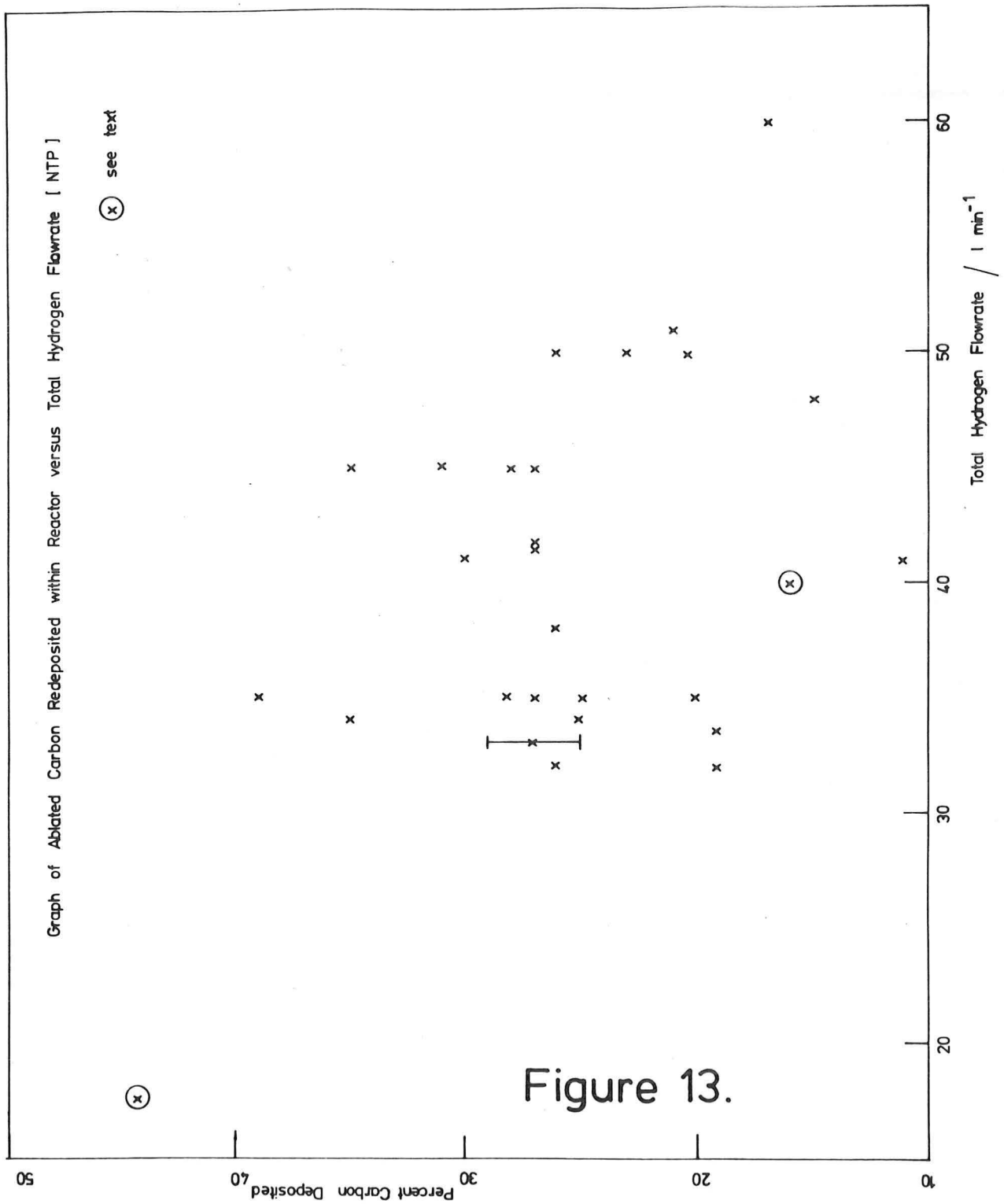
Graph of Ablated Carbon Redeposited within Reactor versus Total Hydrogen Flowrate [NTP]
see text
Percent Carbon Deposited
10
20
30
40
50
Total Hydrogen Flowrate / l min⁻¹
20
30
40
50
60

Figure 13.

introduce significant quantities of methane into the reactor. After a minute or two this grew sufficiently to block the chamber outlet. A photograph is shown in Figure 14.

4.2 Conclusions

It can be concluded that an optimal reactor chamber geometry would be one meeting two criteria:-

a) The chamber is large enough so that the arc or anode vapour plume cannot reach the wall before being mixed with the bulk hydrogen.

b) The residence time is sufficiently small to prevent appreciable amounts of atomic hydrogen to diffuse to the walls. It should be noted that these two criteria require high gas velocities in the chamber. This may be such that arc blow-out occurs. This would place an additional constraint on the design and efficiency of a possible process.

(See section (9.5) for a partial solution.)

5. THE ADDITION OF METHANE AS A SUPPLEMENTARY FEED GAS

5.1 Summary

The proposal was to improve the thermal efficiency (and economics) of the reactor by using 'excess' sensible heat for the cracking of methane. The optimal point of feed for the methane was to be determined.

Four different feed points were tried. In all cases unsatisfactory operation resulted.

5.2 Experiments to Attempt Methane Pyrolysis

The first and simplest process attempted was to utilize the plasmatron cracking process[20].

In this process a high temperature gas stream and the cold methane are contacted at the entrance of a tubular reactor of suitable residence time (1-3 ms), and then the products are quenched.

The hot gas outlet of the Ward reactor was to supply the thermal energy. The methane (about 10 mole % of the reactor flow) was introduced into the hot gases via two 4.5 mm diameter ports set opposite one another. The reaction took place in a 20 mm diameter graphite tube 100 mm long. To the top of this section was bolted the multi-tubed quench (or the fluidised bed quench). The results of these experiments were that either a great deal of soot was produced and/or most of the methane passed unreacted.

The first fundamental problem was to mix the two gas streams. This is extremely difficult because the Reynolds number of reactor gases at the point of mixing is of the order of 100. This implies that laminar flow conditions prevail. Indeed, it was found that a shell of carbon formed at the interface where the hot and two cold gas streams meet; one on each side of the exhaust tube. This

effectively kept the two streams separated for most of the reaction length. To try to improve penetration of the methane into the hot gas, the mixing point was modified to greatly increase its velocity. The methane was fed in through six equally spaced radial holes of 0.5 mm diameter. This gave little improvement.

It was obvious that there was insufficient thermal energy to achieve the desired reactions. (Plasmatron devices operating on hydrogen or hydrogen/argon mixtures produce a gas stream at or close to sonic velocity at temperatures of 5000 K or more, with high specific enthalpies, including large amounts of dissociational energy). It has been established that the mixed mean reactor outlet temperature is close to 1800 K (section 2.3). In an adiabatic reactor under the imposed conditions, it seemed impossible to achieve a useful process. The next approach tried was to introduce the methane via the cathode sheath. This had several potential advantages. The methane would be premixed with about two volumes of hydrogen before entering the reactor. It was expected that this would help suppress soot formation[21]. Also, the methane would be introduced into the hottest region of the arc. This technique failed because massive deposits of carbon built up on the cathode. After a few minutes of operation during which some methane was being converted to acetylene, the acetylene concentration would suddenly fall to an insignificant level and could not be restored by turning the methane off. It was found that the inside (and in particular the upper part of the reactor chamber) was heavily fouled with a feather-like coke, and that a plug had formed, obstructing the outlet exhaust tube. See photographs of deposits in figure 14. As argued in section (6.4), this porous deposit had the apparent ability to destroy the single phase equilibrium gas compositions, as the gas was forced through it. Obviously this was a self-sustaining catastrophic process as all the carbon fed into or ablated in the reactor was building up in the top of the chamber. The reactor was always shut down after this

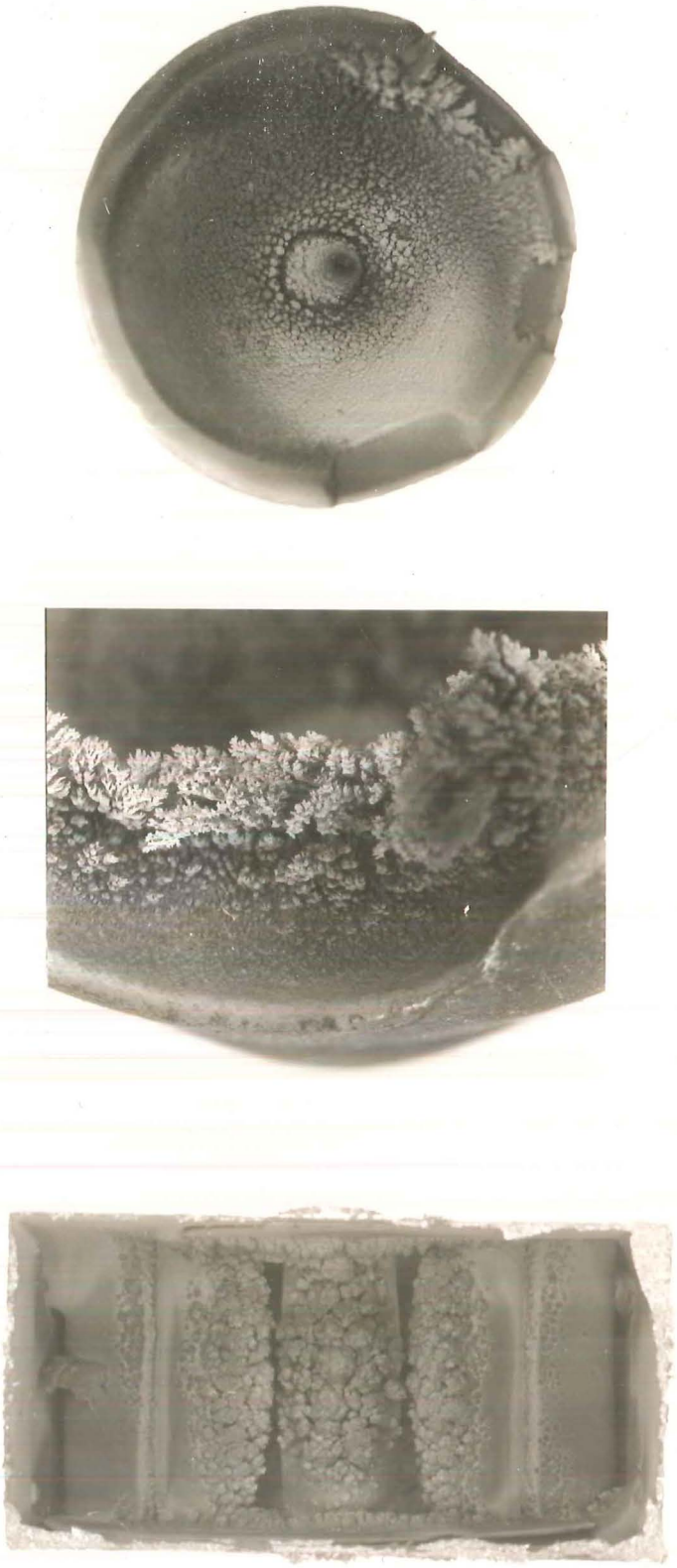

Figure 14 Carbon deposits after methane addition.
Top: Blockage of reactor outlet.
Middle: Detail of 'feather coke' on reactor cone.
Bottom: Fouling on quench tubes.

drop in acetylene concentration was observed.

This phenomena plagued all further attempts to feed methane successfully into the reactor. Methane was added to the anode hydrogen stream with the above result.

The final attempt was to feed the methane up the centre of the anode. This was expected to ensure as far as possible, severe cracking of the methane. This was readily done by drilling an axial hole along the anodes and fitting a sliding O-ring seal below the current contact, so that the normal anode hydrogen flow could be maintained.

It was interesting to find that the arc could be run with gas issuing from the anode centre. However the feed of the anode was difficult to control. The ablation rate was greatly reduced if all the anode was to be consumed, and not just the side nearest the cathode. This resulted from two effects. The anode tip was being cooled, so that the carbon vapour pressure at the tip was diminished. Also the increased vertical gas velocity caused the arc to lengthen and possibly to be cooled, effectively causing an increase in arc voltage and a drop in current. Again the above sooting problems were present.

5.3 Conclusions

All likely places for the addition of a supplementary pyrolysis gas were examined with little success. It was concluded that with the limitations imposed by the Ward reactor a useful process for the cracking of natural gas could not be achieved.

6. QUENCH DESIGN AND QUENCH PROCESSES

(Graphite gasification and acetylene formation)

6.1 Summary

Ward's[1] shell and tube quench was found to be deficient in design and heat transfer capacity.

A new quench was built which consisted of 60 closely packed tubes in a cross flow configuration. A fluidised bed quench of novel design was built also. Both devices performed relatively satisfactorily.

Comparison of the gas analysis results of the quenched gas with the theoretical gas phase compositions at equilibrium before quenching, shows relatively good agreement. This provides strong support for Abrahamson's 'supercooled equilibrium' theory[5]. Atomic hydrogen appears to be important for acetylene formation and stabilization.

6.2 Process Development

6.2.1 Ward's Quenches

Ward operated two quench devices. Each consisted of a copper tube 0.38 m long surrounded by a water jacket. The two devices only differed in the diameter of the central copper tube (9.53 mm and 6.35 mm). Ward presents results of the typical thermal response of the reactor system during an 8 minute run. (Presumably this is about the longest run that his anode feed would allow.) The gas temperature at the quench outlet starts off at 15^{o}C and rises until at the 8th minute it is 80^{o}C and still rising steeply. Ward does not record which quench was used or any information of arc power or hydrogen flow rates, for the response curves presented. Ward also records that the acetylene concentration fell to less than half its initial value during the run.

6.2.2 This Work

It was found that when operating with a gas flow of 40-50 ℓ min^{-1} and power of about 15 kW, that the gas outlet temperature reached at least 250^{o}C, after about 13 minutes of operation. During one such run, the weld securing the central heat transfer tube to the bottom flange broke, spraying water directly into the reactor. It was probable that the cause of failure was due to differential expansion of the central heat transfer tube relative to the external jacket. It was obvious that any shell and tube device of this design would suffer from differential expansion problems, particularly where high heat fluxes were encountered. (It was subsequently found that between 0.5 - 1 kW could be transferred across a quench tube 10 mm diameter and 8 cm long. With an average heat flux of up to 400 kW m^{-2} on the water side, Krieth[22] shows that this is well into the nucleate boiling region (with forced convection). This would result in a significant rise in the heat transfer tube temperature (10 - 20^{o}C could be expected). This would result in differential expansion and the above failure. In spite of the limitations of the Ward quenches, they had the advantages of being of the simplest design and that any carbon deposits found in them could be easily removed.

6.2.3 Multi-tubed Quench

The maximum Reynolds number that could be expected in either of the Ward shell and tube quenches is of the order of one hundred. The flow throughout the quench tube is therefore laminar. It would be expected that the greatest cooling rates of the bulk gas stream would occur if the gas stream was highly turbulent or if the single laminar gas stream could be broken into a number of subsidiary laminar streams which could be cooled separately.

The multi-tubed quench was designed with 60 2.5 cm long copper tubes, 59 of which were 6.35 mm O.D. in a triangular configuration. The clearance between the tubes was 2 mm. (This was the smallest spacing it was considered safe to use, without the space between tubes being filled with soot.) (Differential expansion was unlikely to be a problem with tubes only 2.5 cm long). The central tube at the gas inlet must take the full blast of the hot reactor gas. It was vital that nucleate or film boiling should not be allowed to occur on this tube. For this reason the full water flow was directed through this tube, and to minimise the pressure drop the tube diameter was increased to 7.94 mm O.D. A diagram of the device is shown in Figure 4.

It was hoped that fouling of the tubes would not seriously impair its performance during a run, and that cleaning of the 50 or more inaccessible tubes would not be too difficult afterwards.

In operation the multi-tubed quench exceeded expectations. Under any conditions of normal operation the gas outlet temperature never rose more than 10 K above the quench water outlet temperature. The thermal response is shown in Figure 5. During a long run of 30-40 minutes, up to 1.5 g of carbon would be deposited on the tubes. This was removed by flushing with a large flow of water and some scraping of the front tubes.

It was noted that the acetylene concentrations were now more stable than with the Ward devices. The acetylene concentration always passed through a maximum shortly after startup (still) but having settled down could generally be maintained. (Some of the reasons for the maximum C_2H_2 concentration at startup are given in section (2.2.2)). It was also found that the maximum acetylene concentration appeared to be limited not by the quench, but by the maximum ablation rate. (Concentrations of 10-12% C_2H_2 were obtained at currents of 300 A and 45 ℓ min^{-1} of H_2).

6.2.4 Fluidised Bed Quench

Industrially, a tubed quench is unlikely to be satisfactory due to soot fouling. Traditionally plasma arc devices have used a water spray (or liquid hydrocarbon) to quench the gases. (A hydrocarbon quench will not be considered because of future availability limitations.) A water quench is an efficient process but increasingly suffers from effluent treatment specifications. It was throught that a fluidised bed device may be a satisfactory alternative. The main requirements for such a device are: a sufficiently fast cooling rate, a gas outlet temperature of no more than 300^{o}C, and a minimal pressure drop (when scaled to a commercial size). Some facility for heat recovery was an additional incentive.

Three basic designs were considered. Elliot[23] suggested a shallow bed. The distributor plate would consist of a number of narrow parallel slots. The bed depth would be 3 - 6 cm. Cooling fins could be immersed in the bed. The distributor plate could be prevented from melting by making it integral with the cooling fins. This idea was rejected because the distributor slots had to be so narrow (~0.25 mm) that they would get blocked up with soot and fragments of anode which are ejected.

Forbes[24] designed a spouted bed device, which eliminated the above problem. A hot gas is simply shot into a deep (15 - 25 cm) cylindrical bed of crushed coke particles. Heat transfer is in two stages. The entrained particles in the central spout are heated by the cooling gas. The hot particles then circulate to the wall where they descend, transferring heat to the external cooling coils. The only potential problem that could be foreseen was when scaled up to commercial size an excessively deep bed may be required. This may result in an unsatisfactory pressure drop.

Squires[25, 26] suggested a modification to the Forbes design, to utilize the fast fluidisation phenomenon. This consisted of including a central spout tube to the Forbes design. This is shown in Figure 15. Bed particles are entrained into the high velocity hot gas stream in the gap between the bottom of the fluidised bed chamber and the bottom of the spout tube. Very intense mixing occurs in the spout, with the hot particles and cooled gas emerging at the top of the tube. The solids/gas ratio in the spout can be controlled by adjustment of the clearance at the base of the spout. As the density of the solids plus gas in the spout is relatively low, the overall pressure drop could be kept low on scale-up, even if the external bed was deep (> 1 m). The diameter of the spout tube was chosen after a series of tests with cold gas. It was found that satisfactory operation was obtained when the spout diameter was equal to the bottom hole diameter.

For experimental operation a thermocouple was fitted such that the temperature at the spout outlet could be recorded. A second thermocouple was placed in the annulus about 1 cm above the bottom of the spout tube. This was sheathed in an open ended glass tube so that the junction just protruded but was unable to contact the metal walls. The glass tube also ensured the thermocouple projected to the correct depth. The lower thermocouple measured the cooling occurring in the main bed (between the particles and the external wall), and/or whether there was any tendency for the hot gas to bypass the spout tube. A torch bulb was placed in the upper part of the chamber so that the material issuing from the spout could be observed.

6.2.4.1 Operation of the spouted bed quench: The reactor was supplied with a stream of nitrogen, while the bed chamber was charged with crushed coke (0.25 - 0.5 mm diameter), to within 4-5 cm of the top of the spout; (about 1 ℓ). The filling port was then closed and the hydrogen flow to the reactor was turned up while the nitrogen was turned down and finally off. The reactor was run in the usual way. The coke/gas mixture generally

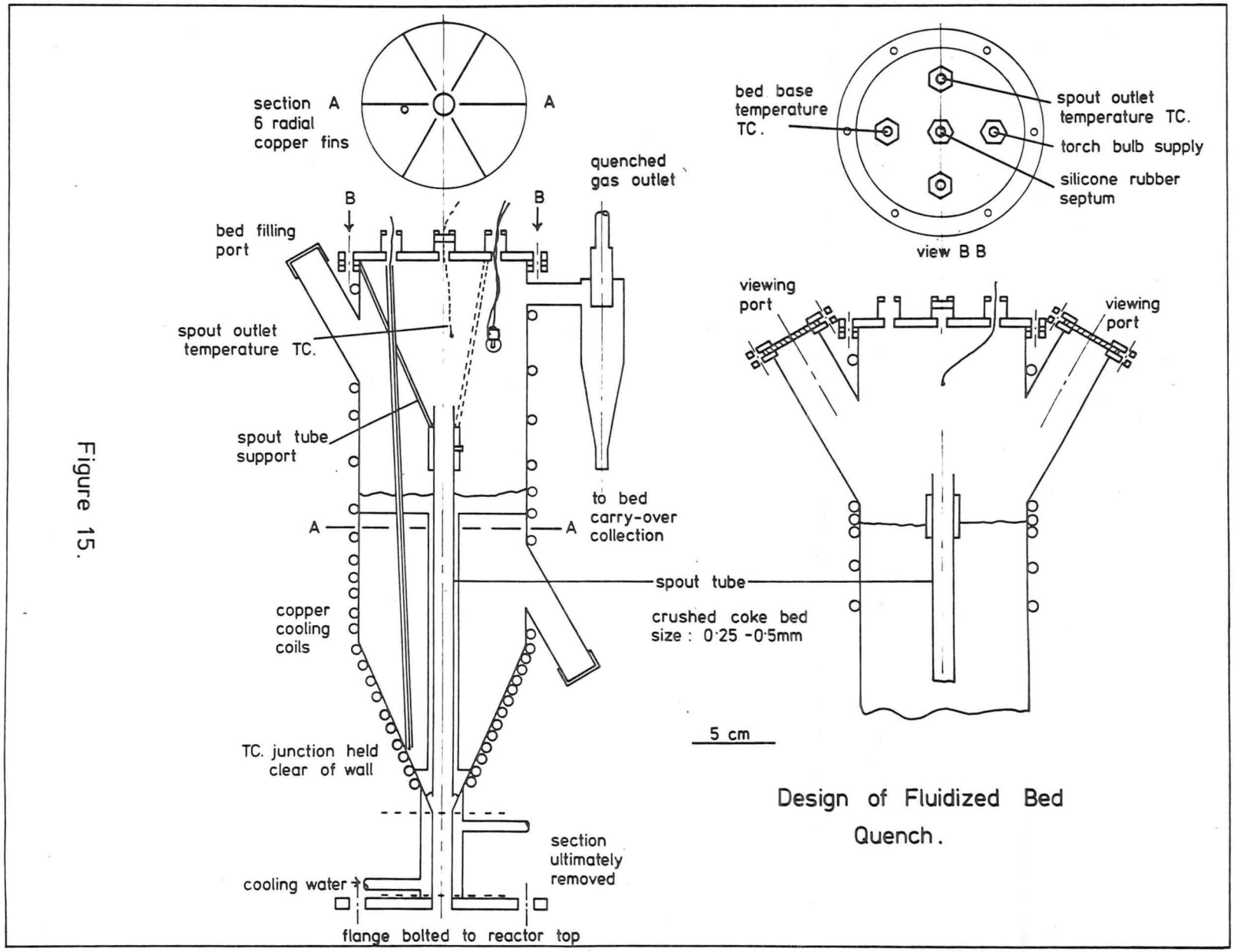

Figure 15.

Design of Fluidized Bed Quench.

emerged from the spout tube as a steady stream. Occasionally slight pulsations were observed. No visible sign was observed of light from the arc region. At the end of the run, the hydrogen flow was maintained for about five minutes to help cool the reactor. The flow was then smoothly changed back to nitrogen. Once the hydrogen had been flushed out, the flange between the fluidised bed and reactor top was unbolted and a thin piece of sheet metal was inserted. The nitrogen flow was then turned off.

After each run a proportion of the bed was found to have fallen into the reactor chamber. When operating techniques were perfected and the hydrogen flowrate was at least 45 $\ell\ min^{-1}$, this amounted to no more than a few percent of the total bed and presented no real problems. (A potential problem was that a short may occur between the cathode and the graphite chamber, if particles bridged the small gap.)

The crushed coke was the only bed material tried in the quench. It had the obvious advantage of being almost pure carbon and so not complicating the chemistry. The size distribution could be easily altered. However the cooling rate is dependent (for a given solids/gas mass ratio), on the heat transfer area per kilogram of particles. This very strongly favours very small particles, but they would be easily swept out of the bed chamber. A compromise is required between particle size and density. SiC and WC are at least twice as dense as coke, while their thermal conductivities are in the order of one hundred times greater[27]. Whether the use of such materials is justified is not known. Lack of resources has prevented investigation. (The attrition of the coke would be a problem on a commercial scale. Metal carbides, being extremely hard, are unlikely to be affected.)

Initial runs showed that with a quench heat load of 1 ± 0.1 kW, the spout outlet temperature stabilized at 130 - 145°C with the base of the bed some 50°C cooler. These results were incorrectly assumed to be very encouraging. The original Forbes quench had a water jacketed section of 6.5 cm to lead the gases into the bed. It was assumed that negligible cooling took place in this section and that a low cooling rate would enable significant amounts of the acetylene to break down.

Removal of the water cooled section drastically increased the bed and spout temperatures. It was now obvious that previously it was not a true fluidised bed quench and probably 0.5 kW was transferred to the jacket. The spout and bed base temperatures were respectively 260°C and 165°C and rising steeply after 7 minutes running.

The quench was modified by fitting 6 radial copper fins which projected almost the full annular thickness of the bulk bed. Satisfactory operation was now obtained. With a quench heat load of 1 ± 0.1 kW, the spout and bed base temperatures were stable at 250 ± 10°C and 115 ± 15°C respectively.

It was significant to find that there was no noticeable change in the exhaust gas compositions between the spouted bed and the multi-tubed quenches. This would suggest that the final gas compositions obtained are independent of the quenching process, and that the quenched gas is directly related in composition to the hot gas composition.

6.2.4.2 Analysis of heat transfer in the spout tube: If it is assumed that the coke particles enter the spout tube at a uniform temperature of 115°C and leave the spout in thermal equilibrium with the gas stream at 250°C, then the mass ratio of coke/gas can be estimated. (It will be assumed that no heat is transferred across the spout tube wall). Then a heat balance between the gas and particles gives:-

$$\dot{m}_{coke}\, C_{p\ coke}\, \Delta T_{coke} = \dot{m}_{reaction\ gas}\, C_{p\ reaction\ gas}\, \Delta T_{gas}$$

The values of $C_{p\ coke} = 12.6\ kJ\ kg^{-1}\ K^{-1}$

$C_{p\ reactor\ gas} = 15\ kJ\ kg^{-1}\ K^{-1}$

$\Delta T_{coke} = 135\ K$

$\Delta T_{reactor\ gas} = 1800 - 523\ K = 1277\ K$

Hence $\dot{m}_{coke}/\dot{m}_{reactor\ gas} \simeq 11/1$

If the coke particles are considered to be spheres of 0.3 mm diameter and that they are uniformly distributed in the spout gas stream, with all the heat transfer resistance being within the particle, then Paterson's solution[28] can be used to investigate the thermal equilibrium assumption. The cooling rate curve can also be obtained. (The thermal diffusivities of coke[114] and hydrogen[115] are $3 \times 10^{-7}\ m^2\ s^{-1}$ and $1.3 \times 10^{-3}\ m^2\ s^{-1}$ respectively, so it is reasonable to assume that the system is similar to particles in a well-stirred fluid. Thermal diffusivities were estimated at 1500 K.)

The ratio of heat capacities of the particle to the fluid

$$= \frac{11}{1} \times \frac{12.6}{15} = 9.2 \simeq 10$$

and $\tau = \frac{\kappa t}{a^2}$ = dimensionless time

$$= \frac{\text{diffusivity of coke} \times \text{time}}{(\text{particle radius})^2}$$

$$= \frac{3 \times 10^{-7}\ t}{(\frac{0.3}{2} \times 10^{-3})^2} = 13.3\ t$$

if T' is the fluid temperature at time t, and

T_o is the fluid temperature at t = 0, and

the initial particle temperature = 0,

then the tabulated solution in Table 3 is:

if $T_o = T_{gas} - T_{cold\ particle} = 2000\ K - 400\ K = 1600\ K$

F = fraction of heat transferred at time t

Table 3

Gas Cooling Rate in Spout Tube

τ	t/s	T'/T_o	T'	T gas	F
10^{-8}	7.7×10^{-10}	0.996	1594	1994	4.4×10^{-3}
10^{-7}	7.7×10^{-9}	0.990	1584	1984	0.011
10^{-6}	7.7×10^{-8}	0.967	1547	1947	0.036
10^{-5}	7.7×10^{-7}	0.902	1443	1843	0.108
10^{-4}	7.7×10^{-6}	0.737	1179	1579	0.289
10^{-3}	7.7×10^{-5}	0.451	722	1122	0.604
10^{-2}	7.7×10^{-4}	0.203	325	725	0.877
10^{-1}	7.7×10^{-3}	0.100	160	560	0.99
> 1		0.091			

If the mean gas velocity in the spout is considered to be the exhaust velocity (250°C, 70 ℓ min^{-1} and 1 cm diameter), then the residence time in a tube 20 cm long will be 13 ms (neglecting volume of coke). Even with the crude velocity approximation it can be seen that in 1 ms about 90% of the heat transfer has occurred, so that it is reasonable to assume that the particles are in equilibrium with the gas stream at the spout exit.

The cooling rate at t = 0 is approximately given by:

$$\left(\frac{dT}{dt}\right)_{t=0} = \frac{1994 - 1984}{7.7\times10^{-10} - 7.7\times10^{-9}} = -1.4 \times 10^{9} \text{ K s}^{-1}$$

The cooling curve data for the spout gas stream from Table 3 is plotted in Figure 16.

6.2.4.3 An estimate of the breakdown of acetylene in the spout tube: The thermal decomposition of acetylene is very well described by a second order rate equation over the range 700 K to 2500 K[19].

$$\left(\frac{\partial C_{C_2H_2}}{\partial t}\right)_{T,P} = -K\, e^{-E/T}\, C_{C_2H_2}^{\ 2}$$

The overall reaction $C_2H_2 \rightarrow H_2 + C_{solid}$ has a negligible volume change of reaction. However the concentration of C_2H_2 will change dramatically during the cooling.

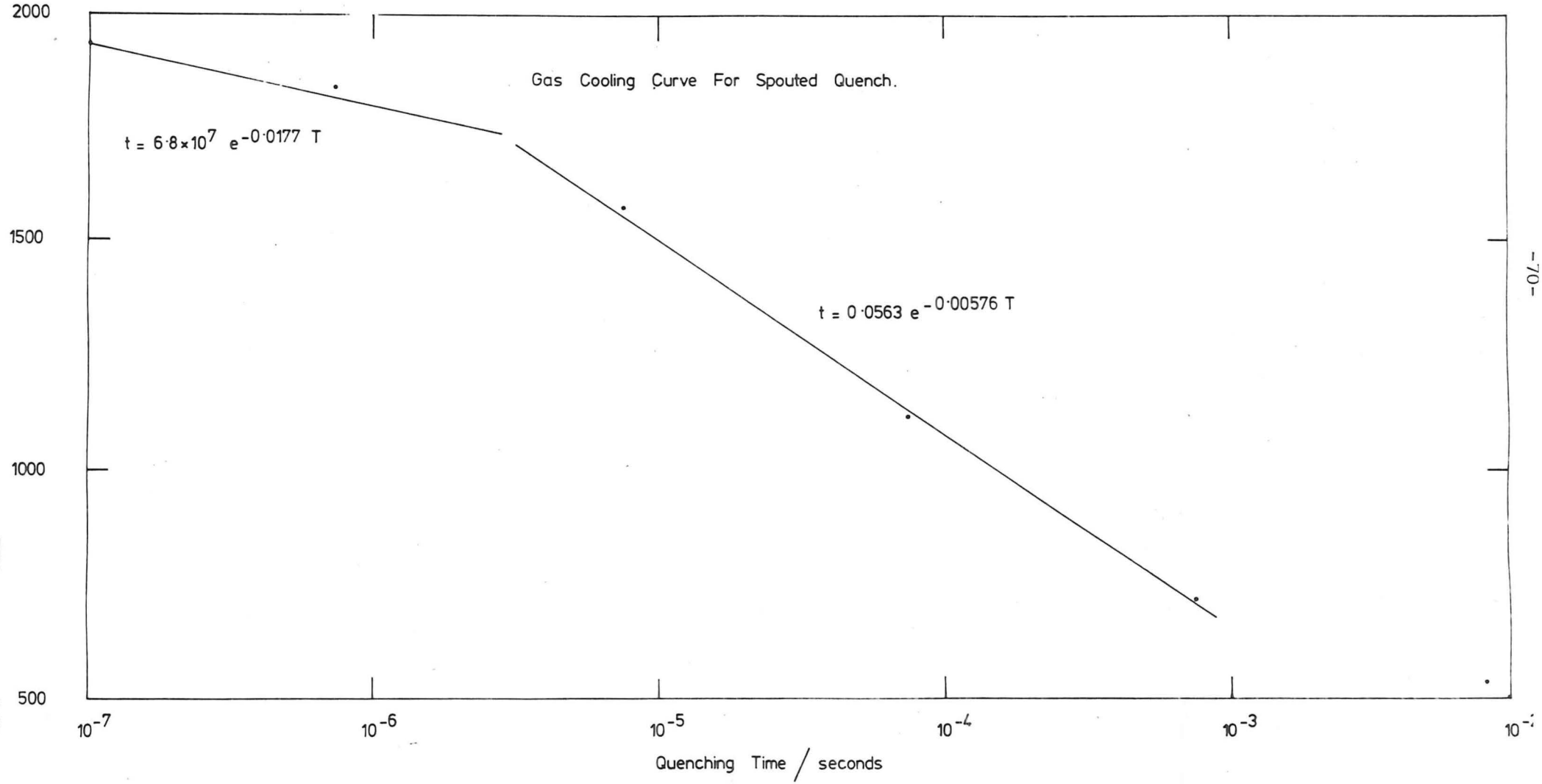
Gas Cooling Curve For Spouted Quench.
t = 6·8×10^7 e^-0·0177 T
t = 0·0563 e^-0·00576 T
Gas Temperature / kelvin
2000
1500
1000
500
10^-7
10^-6
10^-5
10^-4
10^-3
Quenching Time / seconds

Figure 16.

$$C_{C_2H_2} = \left(\frac{n}{V}\right) = \frac{p}{RT}$$

for an ideal gas where p is the C_2H_2 partial pressure if the partial pressure is expressed in terms of the mole fraction of C_2H_2 (x) and the total pressure (p_o), then

$$C_{C_2H_2} = \frac{x\, p_o}{RT}$$

$$\left(\frac{\partial C_{C_2H_2}}{\partial t}\right)_{T,P} = \frac{p_o}{RT}\,\frac{\partial x}{\partial t}$$

substituting

$$\frac{p_o}{RT}\,\frac{\partial x}{\partial t} = -K\, e^{-E/T} \left(\frac{x\, p_o}{RT}\right)^2$$

hence

$$\frac{dx}{dt} = -K\, e^{-E/T}\, \frac{x^2\, p_o}{RT}$$

Using the experimental Arrhenius plot given in [19], $K = 4.4 \times 10^{13}$ cm^3 mole^{-1} s^{-1} and $E = 20936$ K.

The gas cooling data will be used by fitting two exponential curves to it. From 2000 K to 1700 K

$$t = 6.8 \times 10^{7}\, e^{-0.0177\, T}$$

and from 1700 K to 500 K

$$t = 0.0563\, e^{-5.76 \times 10^{-3}\, T}$$

and so $dt = -1.2 \times 10^{6}\, e^{-0.0177\, T}\, dT$ 2000 - 1700 K

and $dt = -3.2 \times 10^{-4}\, e^{-5.76 \times 10^{-3}\, T}\, dT$ 1700 - 500 K

Using P = 1 atmosphere, $R = 82.05$ atm cm^3 mole^{-1} K^{-1}, if the initial mole fraction of C_2H_2 is 0.1, then

$$\int_{0.1}^{x} \frac{dx}{x^2} = \int_{2000}^{1700} \frac{1}{82.05} \times 1.2 \times 10^{6} \times 4.4 \times 10^{13}\, \frac{e^{-\left(\frac{20936}{T} \times 0.0177\, T\right)}}{T}\, dT$$

integrating the R.H.S. numerically by the trapezoidal rule:

$$\{-\frac{1}{x} + \frac{1}{0.1}\} = 6.4 \times 10^{17} \{-2.1 \times 10^{-20}\}$$

$$-\frac{1}{x} = -10 - 0.013$$

$$x = \frac{1}{10.013} = 0.09987$$

and:-

$$\int_{0.09987}^{x} \frac{dx}{x^2} = \int_{1700}^{500} \frac{1}{82.05} \times 3.2 \times 10^{-4} \times 4.4 \times 10^{13} \frac{e^{-(\frac{20936}{T} + 5.76 \times 10^{-3} T)}}{T} dT$$

$$= 1.7 \times 10^{8} \{-4.6 \times 10^{-11}\}$$

$$\{-\frac{1}{x} + \frac{1}{0.09987}\} = -7.7 \times 10^{-3}$$

$$x = 0.09980$$

Hence well under 1% of the available C_2H_2 is lost, which is in general agreement with experimental results.

6.2.4.4 Quenching rate required in a commercial quench: If it is specified that at least 90% of the available acetylene must be preserved and that the cooling curve is exponential with respect to time (t), then the minimum initial quenching rate can be calculated. (This is probably the simplest cooling model; using a single linear resistance.)

Conditions: Initial temperature 2000 K

Final " 500 K

Initial C_2H_2 mole fraction 0.1

Final " " " 0.09

Cooling curve $T = a\, e^{-bt}$

then $$\frac{dT}{dt} = -a\, b\, e^{-bt} = -bT$$

substituting this in the rate equation viz.:

$$bT \frac{dx}{dT} = \frac{KP_o}{R} \frac{x^2}{T} e^{-E/T}$$

and so:- $$\int_{0.1}^{0.09} \frac{dx}{x^2} = \int_{2000}^{500} \frac{KP_o}{R\,b} \frac{e^{-E/T}}{T^2}\, dT$$

integrating and solving for b:-

$$b \geqslant 662\ s^{-1}$$

and the cooling curve is $T = 2000\ e^{-662t}$ and so the initial quenching rate has to be at least $-662 \times 2000\ K\ s^{-1} = -1.3 \times 10^6\ K\ s^{-1}$.

6.2.4.5 Quenching rates likely in liquid spray systems: Conventional acetylene manufacturing processes have used either a water or hydrocarbon spray quench[29, 30]. The rate of evaporation of liquid drops is limited by mass transfer at high gas temperatures[31].

A comparison should be made of the likely cooling rates possible with water drops, to the rates predicted above (where mass transfer is not present).

If water is sprayed into the base of the spout tube instead of coke particles, then the gas stream will be primarily cooled by evaporation of the drops. The velocity of the 2000 K gas at the spout entrance is approximately 4 5 m s^{-1}.

The drop Reynolds Number is $\frac{V_\infty D}{\nu}$ where V_∞ is the upstream gas velocity, D is the drop diameter, and ν is the kinematic viscosity of the hot gas.

$$Re = \frac{4\ 4\ m\ s^{-1} \times 1 \times 10^{-4}\ m}{2.5 \times 10^{-3}\ m^2\ s^{-1}} \simeq 2$$

The mass transfer number B for evaporation is given by:

$$B = \frac{Cp\Delta T}{L}$$

where Cp is the specific heat capacity of the hot gas (section 2.3), ΔT is the temperature difference between the hot gas and the evaporating drop and L is the latent heat of vaporisation of water.

$$B = 14 \text{ kJ kg}^{-1} \text{ K}^{-1} \times \frac{2000 - 400 \text{ K}}{2250 \text{ kJ kg}^{-1}} \quad (31) = 10$$

Under conditions of intense evaporation the drop evaporisation rate is given by (31) to be:-

$$\dot{m} = -(2D\pi \, k/c) \ln(1 + B)$$

where $\dot{m}$ is the rate of evaporation of a single drop in kg s^{-1}

D is the drop diameter, m

k is the thermal conductivity of the hot gas, kW m^{-1} K^{-1}

C is the specific heat capacity of the hot gas, kJ kg^{-1} K^{-1}

$$\dot{m} = 2\pi \times 1 \times 10^{-4} \times \frac{5 \times 10^{-4}}{14} \times \ln 11 \text{ kg s}^{-1}$$

$$= 5.4 \times 10^{-8} \text{ kg s}^{-1}$$

The mass of a water drop of diameter 1×10^{-4} m is 5.2×10^{-10} kg.

If the same mass ratio of water to gas is used as in the spouted bed (10:1), then each drop cools 5.2×10^{-11} kg of gas.

An enthalpy balance gives the gas cooling rate:

$$m_{gas} \quad Cp_{gas} \quad \frac{dT}{dt} \text{ gas} = \dot{m}_{drop} \, L_{drop}$$

$$\frac{dT}{dt} \text{ gas} = \frac{5.4 \times 10^{-8}}{5.2 \times 10^{-11}} \times \frac{2250}{14}$$

$$= 1.7 \times 10^{5} \text{ K s}^{-1}$$

For the same mass coolant to gas ratio, this is 4 orders of magnitude smaller than the initial quenching rate calculated above. It can be concluded that a particulant quench has the advantages over water sprays of very much higher initial cooling rates and does not produce a liquid effluent treatment problem.

6.3 The Prequench Gas Composition and the Formation of Acetylene

6.3.1 Categorizing the Gas Composition

In the previous sections it was estimated that the gas was cooled sufficiently rapidly that a negligible fraction of the acetylene had time to decompose. It will be tentatively assumed that the other final constituents are similarly quenched. Both Abrahamson and Ward used the mean specific enthalpy at the quench inlet to describe the composition of the product gas. Abrahamson's specific enthalpies lay in the range 20 - 40 MJ kg^{-1} (corresponding to temperatures of 2000 - 3000 K). Ward's results lay in the range 12 - 25 MJ kg^{-1} (temperatures of 1600 - 2500 K). (It should be noted that Ward's values are probably too large, because of inadequate thermal isolation between the reactor body and quench). The specific enthalpies covered in this work lay in the range 10 - 15 MJ kg^{-1} (1400 - 2000 K), which are only about half the values Abrahamson obtained.

Abrahamson investigated the acetylene concentration over a very wide mass C/H ratio range of 0.3 - 3.5; while Ward covered the range 0.8 - 3.5. (Ward's C/H ratios are suspect in the higher values because of his faulty carbon ablation rates. They are more likely to extend to ratios of 2 or 2.5.) This work covers the restricted range of 0.5 - 1.7.

Both Abrahamson and Ward considered two significant theories of acetylene formation. The first was that complete equilibrium existed between the carbon and hydrogen in the prequench gas including soot and ablated graphite particles. This theory was proposed by Plooster and Reed[32], who passed hydrogen over graphite heated to 2500 - 2900 K. Contact times were at least 0.1 s.

Abrahamson found no basis for a two phase equilibrium, and instead proposed that gas phase reactions were fast, such that solid carbon, (if present), effectively played no part. Ward considered both theories and found what he considered to be some evidence for both. Ward considered the initial acetylene concentrations (which were always the highest in each run), to be not inconsistent with a single phase equilibrium. Acetylene concentrations obtained for 'steady-state' operation showed a maximum of 6% C_2H_2, which he considered to be close to two phase equilibrium concentrations (at 3000 K).

6.3.2 Theoretical Equilibrium Gas Compositions

Both Abrahamson and Ward made extensive use of the thermodynamic equilibrium tables calculated by Duff and Bauer[33] (covering single and two phase systems), and the tables calculated by Lieberman and Mark[34] (single phase only). These data will continue to be assumed to be reliable for conclusions drawn in this work. Oxygen will be assumed to be absent. The single and two phase compositions are presented in Tables 3 and 4, at the lowest prequench temperature, (1400 K), and the highest, (2000 K). Duff and Bauer conveniently table compositions for the single phase case with the molar C/H ratio of 0.1. (C/H mass = 1.2, which is close to typical reactor operating conditions).

Between 1400 and 2000 K the equilibrium concentrations of radicals are negligible ($H < 0.001$). Therefore the recombination of radicals during quenching would be expected to have an insignificant effect on the gas composition.

Table 4

Theoretical Hydrocarbon Equilibrium Compositions
Single Phase

C/H molar = 0.1 Pressure = 1 bar

Composition by mole fraction

Component	Temperature 1400 K	1700 K	2000 K
Acetylene	0.01	0.07	0.08
Ethylene	0.006	0.003	6×10^{-4}
Ethane	1×10^{-4}	1×10^{-5}	5×10^{-7}
Methane	0.16	0.03	0.004
Benzene	0.007	6×10^{-4}	2×10^{-6}
Propane)) Butane)	$< 10^{-7}$	$< 10^{-7}$	$< 10^{-7}$
Methyl acetylene	1×10^{-4}	4×10^{-4}	1×10^{-4}
Vinyl acetylene	5×10^{-6}	4×10^{-5}	1×10^{-5}
Diacetylene	1×10^{-5}	7×10^{-4}	0.001
H	4×10^{-6}	2×10^{-4}	0.001
CH	-	-	-
CH_2	2×10^{-6}	5×10^{-5}	3×10^{-4}
C_2H	2×10^{-8}	3×10^{-7}	1.3×10^{-4}
CH_3	4×10^{-5}	2×10^{-4}	3×10^{-4}

(blank denotes $< 10^{-8}$) (remainder H_2)

Table 5
Theoretical Hydrocarbon Equilibrium Compositions
Two Phase
(Solid Carbon Present) 1 bar

Component	Temperature	
	1400 K	2000 K
Acetylene	5×10^{-6}	0.001
Ethylene	3×10^{-6}	6×10^{-6}
Ethane	4×10^{-8}	-
Methane	0.004	4×10^{-4}
Benzene	-	-
H	6×10^{-6}	0.002
CH_3	1×10^{-6}	3×10^{-5}
C_2H	-	1×10^{-6}
CH_2	3×10^{-7}	3×10^{-5}
Methyl acetylene	-	8×10^{-6}
Diacetylene	-	6×10^{-8}

6.3.3 Comparison of Equilibrium and Typical Reactor Gas Compositions

The typical reactor product gas composition is:- (in volume fraction)

C_2H_2	0.06
C_2H_4	0.005
C_2H_6	0.0001
CH_4	0.0015
C_6H_6	~0.0001

Total unidentified C_3 and C_4 alkynes 0.0005. It is obvious that with the exception of CH_4, the two phase equilibrium cannot account for the experimental results. Conversely good agreement is found for the single phase equilibrium, with the exception of CH_4. Palmer's[19] correlation of the first order decomposition data for methane can be used to estimate the likely loss of methane during quenching. If this data is

used with the cooling rates used for acetylene breakdown it can be shown that like acetylene a negligible fraction of methane is likely to be lost. Therefore, if the single phase is accepted, the low measured methane concentrations cannot be accounted for by preferential breakdown during quenching.

6.3.4 Delayed Acetylene Breakdown Due to Induction

Various studies[35, 36] investigating the decomposition of acetylene in shock tubes, have reported that an induction period is required before the breakdown of acetylene can begin. This time delay was found to be in the order of 10 - 100 μs (2000 - 1500 K). The approximate residence time in the arc reactor, from the anode tip to the mouth of the exhaust tube is 10 ms. Since this period is much greater than the induction period, it cannot explain the preservation of acetylene in the reactor.

6.3.5 The Action of Atomic Hydrogen in Graphite Gasification

An important clue to the reaction of high temperature graphite and hydrogen is obtained by doing an energy balance on the hydrogen feed and the plasma power dissipation. If the plasma voltage drop is 40 V (out of a total of 70 - 80 V), and the current is 200 A, then 8 kW is available to heat the hydrogen gas stream. The hydrogen mass flow rate is about 50×10^{-6} kg s^{-1}. The mixed mean specific enthalpy of this gas is 160 MJ kg^{-1}. Examination of the enthalpy tables for equilibrium hydrogen shows that this condition is met at 3750 K, where the gas composition is $x_{H_2} = 0.33$, $x_H = 0.67$, $x_{H^+} = 1 \times 10^{-8}$. It is concluded that there is sufficient energy available to produce an atmosphere mostly of atomic hydrogen. If the diffusivity of atomic hydrogen in molecular hydrogen at 4000 K is of the order 0.02 m^2 s^{-1} [37], then in the available residence time of 10 ms, the atomic hydrogen is estimated to be able to diffuse using the relation $x = \sqrt{2Dt}$ (from Kinetic Theory and Fick's Second Law in one dimension); a distance of

($x = \sqrt{2 \times 0.02 \times 0.01}$) 0.02 m. This is about the mean radius of the conical top of the chamber. With very rapid diffusion and the vigorous motion of the plasma column, it seems reasonable that the upper section of the reactor chamber is filled with atomic hydrogen.

(It now seems clear that the reactor wall heat loss is controlled by the diffusion and recombination of atomic hydrogen. About 2 kW is radiated from the anode, (p 166) and no more than 2 kW from the cathode. Only 1 kW of the total gas enthalpy reaches the quench, leaving something of the order of 7 kW of heat of recombination to be lost on wall or particle collisions). If this high mole fraction of atomic hydrogen is required for acetylene formation and survival then some important implications are revealed for industrial scale-up. The mean gas specific enthalpy must be maintained on scale-up. Therefore the mean plasma power dissipation must be scaled in proportion to the hydrogen flow rate. However as the arc chamber volume increases, its volume/surface area ratio increases so that with a constant gas residence time a smaller fraction of atomic hydrogen is lost by wall collisions. Alternatively, a larger fraction of atomic hydrogen would survive to reach the quench. Some gains in the thermal efficiency of the process may be realizable on scale-up but would require considerable experimental work.

Balooch and Olander[38] have convincingly demonstrated, in a molecular beam experiment, that graphite is only gasified by atomic hydrogen and not by molecular hydrogen (over the temperature range 400 K - 2200 K).

Three distinct phases of reaction were observed. Below 800 K, methane is the sole product. Above 1000 K acetylene is the only hydrocarbon produced. Between 800 K and 1000 K, they found that no gasification occurred, but that recombination of atomic hydrogen took

place on the graphite surface. In addition, it was found that the total reaction rate (with respect to atomic hydrogen) depended on the crystal orientation (basal or prism plane), the H atom collision rate (partial pressure), and the probability the H atoms will chemically bind to the graphite surface. This sticking probability was found to be independent of temperature, and was found to be 0.02 and 0.006 for the prism and basal planes respectively. The data was best fitted by molecular hydrogen having zero sticking probability (i.e. no part in the graphite reactions).

At 4000 K, the JANAF tables[39] show that the heats of reaction of graphite with atomic hydrogen are:-

$$2C_{Gr} + 2H \rightarrow C_2H_2 \quad \Delta H - 243 \text{ kJ mole}^{-1}$$

$$2H \rightarrow H_2 \quad \Delta H - 462 \text{ kJ mole}^{-1}$$

In addition the heat of vaporisation of graphite is:-

$$C_{Gr} \rightarrow C_n \quad \Delta H + 23 \text{ MJ kg}^{-1}$$

All at 4000 K

Clarke and Fox[40] investigated the reaction of graphite filaments in hydrogen. They found that up to 3000 K (depending on the pressure) that the filament mass loss rate was a surface reaction dependent on the atomic hydrogen partial pressure. Above 3000 K (1 bar) the mass loss rate became dominated by free carbon ablation, so that the reaction with atomic hydrogen was no longer a bulk surface reaction. It will be assumed that the bulk of the gasification reaction takes place on the surface of graphite particles ejected from the ablating anode at about 4000 K. Since the particle temperature is almost the same as the mean gas temperature, negligible heat will be transferred by atom collisions. (The atomic hydrogen-particle collisions which are fully inelastic (i.e. stick) are destined to react anyway). Therefore the

heat transfer to the ablating particle is determined by the competing acetylene and recombination reactions. Using the kinetic results of Balooch and Olander, for 4000 K, the rates of acetylene formation and atomic hydrogen recombination are in the ratio of 15:1. (Methane production is four orders of magnitude less). Heat transfer to an ablating-reacting graphite particle is dominated by the acetylene reaction. For every 2 kg of graphite converted to acetylene an additional 1 kg of carbon can be vaporised.

If a 25 μm diameter particle of graphite is ejected from the anode surface then its survival time depends on either being gasified by atomic hydrogen attack or by encountering the wandering arc attachment. Such a particle has a surface area of 2×10^{-9} m^2 and a mass of 1.6×10^{-11} kg.

Using Balooch and Olanders' value of the gas collision rate per m^2 per second, times the sticking probability:-

$$\text{reaction rate} = \frac{\eta\, p}{(2\pi\, m_H\, kT)^{\frac{1}{2}}}$$

where η is the atomic hydrogen sticking probability mean value = 0.01

p is the equilibrium partial pressure at 3750 K of atomic hydrogen, and is 66,000 N m^{-2}

m_H is the mass of the hydrogen atom (1.7×10^{-27} kg)

k is the Boltzmann's constant, J K^{-1}

T is the gas temperature (4000 K)

Then the reaction rate = 2.5×10^{25} $\frac{\text{atoms atomic hydrogen}}{m^2\ s}$

= 42 moles m^{-2} s^{-1}

Power released per m^2 of graphite reacted to acetylene is 42 moles m^{-2} s^{-1} x $\frac{243}{2}$ kJ $mole^{-1}$ = 5100 kW m^{-2}.

The energy required to vaporise the particle of 1.6×10^{-11} kg is $\frac{1}{3} \times 23$ MJ $kg^{-1} \times 1.6 \times 10^{-11}$ kg $= 1 \times 10^{-4}$ J. Assuming the surface area remains constant, then sufficient energy can be supplied in:

$$\frac{1 \times 10^{-4}}{2 \times 10^{-9} \times 5 \times 10^{6} \text{ m}^2 \times \text{W m}^{-2}} \text{ J} = 0.01 \text{ s}$$

During 10 ms the particle is likely to be entrained in the arc attachment about 30 times. Therefore gasification by direct chemical attack is not significant for the destruction of the larger graphite particles. However atomic hydrogen attack may be important for the binder particles (10 - 100 nm diameter).

(It is possibly significant to note that if the predicted rate of atomic hydrogen gasification at 4000 K is 42 moles H m^{-2} s^{-1}, and that typically the reactor is producing acetylene at the rate of 7×10^{-3} moles s^{-1}, then only 3.5 cm^2 of surface area is required. For an 8 mm diameter anode, this is 7 times the superficial electrode tip area, or 2.5 times the tip area plus the area of one half a diameter back from the tip).

6.3.6 Avco Isotope Mixing Experiments

In the course of the Avco developmental work[102], a number of experiments were performed with a plasmatron type of reactor. Hydrogen was used to provide the high enthalpy gas stream. To be 'reacted' with the hot hydrogen was a cold quench stream of acetylene diluted with either argon or more hydrogen. The original aim was to add sufficient cold inert gas,that when mixed, the gas reactions were frozen (or quenched). The acetylene fraction was adjusted so that the outlet concentration was the same as that of the coal pyrolysis reactor. The ratio of hot H_2 to cold dilution gas was the same as that also used in the coal pyrolysis reactor. In this way it was possible to find out how much acetylene was

lost through poor quenching; whether the quench gas was participating in the reactions; and what reactions, if any, were taking place in the final milliseconds of reaction. It was initially determined that hydrogen dilution was vastly superior to argon, for the same molar flow rate. With hydrogen dilution, 90% of the acetylene was preserved, as against 45% with argon. When the dilution hydrogen was replaced with deuterium it was found that not only had the D_2 entered the acetylene but that the product was statistically mixed in deuterium. It made little difference whether the plasmatron and quench gases were interchanged for H_2 and D_2. This suggests that some kind of equilibrium is involved, possibly with the C_2H radical.

viz. $C_2H_2 + D_2 \leftrightarrow C_2H, C_2D, H, D, H_2, D_2, C_2D_2$

However, substitution of 5% of the acetylene with $^{13}C_2H_2$ showed that the C≡C bond was reactive and that the isotopes were in statistical equilibrium. This implied that <u>all</u> the bonds were reactive in the C_2H_2 molecule immediately prior to being finally frozen.

This implies that an equilibrium is involved, involving probably:

C_2H_2, C_2H, CH, C, H_2, H

It is significant to note that the product gas from the final Avco coal arc reactor has some similarities with the gas from the Ward reactor. Avco's typical composition is:

C_2H_2	11.2 % vol.
C_2H_4	1.0
CH_4	1.8
CO	5.1
CO_2	0.1
C_4H_2	0.1
C_3H_4	0.1

C_3H_6	0.05
C_4H_4	0.05
H_2O	6.0

The CO, CO_2 and H_2O fractions are due to the much higher levels of oxygen introduced in the coal. Examining the hydrocarbon concentrations it can be seen that there is no possibility of a two phase equilibrium, but a single phase equilibrium is a real possibility. It is suggested that the hydrogen arc is a rich source of atomic hydrogen. It is possible that, for the acetylene decomposition studies, argon is a poor 'quench' gas because it allows the rapid removal of H atoms by three body collisions. This would suggest that the gas mixture should be kept free of large non-acetylenic molecules and soot particles (and precursors) until the gas composition is truly frozen.

6.4 Conclusions on the Formation and Preservation of Acetylene

It is concluded that the graphite is gasified in the vicinity of the anode surface by a combination of atomic hydrogen attack and arc attachment heating. It is tempting to suggest that the low methane concentrations (relative to single phase equilibrium) are a result of the preferential kinetics in the graphite gasification. Once the gaseous products move away from the anode they are diluted by the surrounding gas stream which has a large molar excess of atomic hydrogen. This effectively prevents any possibility of carbon (soot) formation because of immediate regasification by atomic hydrogen. Thus it is possible to establish a semi-single phase equilibrium.

This is supported by the experimental observation that when the reactor is run with an additional methane feed, that sooting almost immediately starts and accumulates as a porous plug of carbon blocking the mouth of the graphite exhaust tube. As soon as this occurs the

acetylene concentration drops to an insignificant (IR absorption) value. This loss of acetylene is not recovered by running the reactor normally on hydrogen only. It seems that the porous plug of carbon acts as an atomic hydrogen filter (by allowing surface recombination of radicals). Once the excess atomic hydrogen is removed the system can rapidly (~ 1 ms) change to the two phase system, where the C_2H_2 concentration is only 0.1% by volume at 2000 K. Therefore it seems important that the concentration of atomic hydrogen should be maintained at least until immediately prior to quenching. (If the second order rate of decomposition data for acetylene is used it is found that at 2500 K the concentration of acetylene can drop from 10% to 1% in less than 2 ms).

7. DYNAMIC BEHAVIOUR OF THE HIGH CURRENT HYDROGEN ARC

7.1 Summary

Voltage and current waveforms of the arc show that its behaviour is highly transient. The arc undergoes an abrupt switching action (<2 μs) at an average rate of 3 kHz. Transient voltages up to twice the open circuit supply voltage are observed. High speed motion pictures (3200 fps) are not fast enough to show detail of arc column movement, but show details of the behaviour of the anode and cathode attachments. The anode and cathode arc attachments appear to have temperatures about 200 K above the bulk electrode tip temperatures. The measured ablation rates can be accounted for by thermal vaporization.

7.2 Procedure

The voltage across the reactor electrical terminals was connected via a x10 probe to a Tektronix 7313 storage oscilloscope. Sweep speeds used were 200 μs/div. and 20 μs/div. The current waveform was obtained by connecting the oscilloscope across the current shunt resistor (0.00025 Ω), which provides a sensitivity of 4A/mV. The oscilloscope was used in differential mode to reduce problems of earth loops and small offset voltages possibly associated with them. Initial results produced a signal of 'complete noise', out to the fastest sweep speed the oscilloscope could store. A 2 pole low pass Butterworth filter[41] with a cut-off frequency of 100 kHz (-12 dB/octave) was fitted between oscilloscope and shunt resistor. Results were slightly better but still largely noise.

Finally, an 8 pole Butterworth filter[41] (-48 dB/octave) with a cut-off frequency of 100 kHz was fitted. With this filter, meaningful signals (100 μs/div) could be obtained. Simultaneous voltage and current waveforms could not be obtained because the use of two storage oscilloscopes was not available.

High speed motion pictures were obtained using a Beckman & Whitley camera, set to run at its maximum rate (3200 frames per second). The camera was placed as close as possible to the reactor window. Excessive light intensity was controlled by using Kodak Double X negative film type 7222 (200 ASA), an aperture of f22 and an 8x neutral density filter. For some of the runs the anode was split axially in half (one half being used), so that a better view of the area between the electrodes could be obtained.

7.3 Observations

7.3.1 The Voltage Waveform

The voltage waveforms show a series of 'exponentially' falling spikes (Figs. 17 a, b, c, d). The time between spikes varied widely, from 20 μs to 2 ms. During periods of the order of 100 μs or more after the spike decay a 'steady state' arc appears to operate with a voltage of 60 ± 10 V.

The peak voltages of the spikes vary from 150 to 400 V. It should be noted that the maximum supply voltage is ordinarily 200 V. The voltage rise time is extremely short, <1 μs. When the arc is at steady state, the arc voltage can collapse again (relatively slowly over 20-30 μs) to between +30 and -20 V. Voltages around zero or negative values appear to favour the largest spike voltages (at least 350 V).

7.3.2 The Current Waveform

The current waveforms obtained are very similar to the voltage waveforms, Figures 18 a,b,c,d. From this similarity it will be assumed that the discontinuities and rapidly decaying spikes are related in time to the same events.

The peak height of the current spikes reach 400 A but their true maxima may be greater than this, since they will be attenuated by

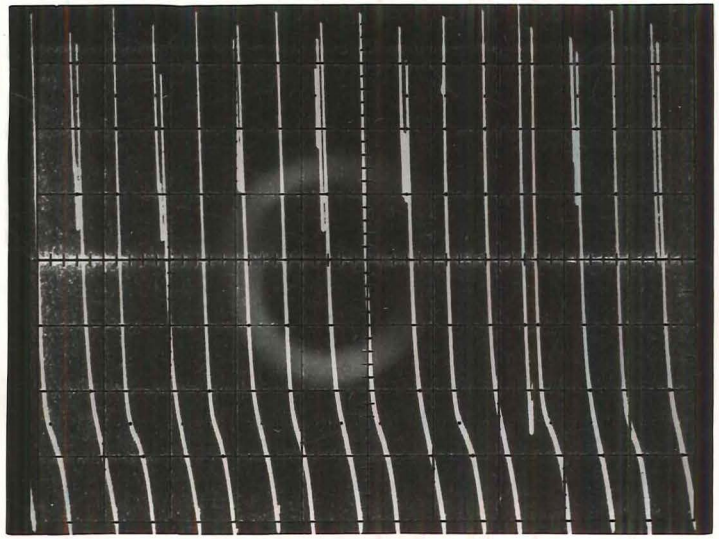

a

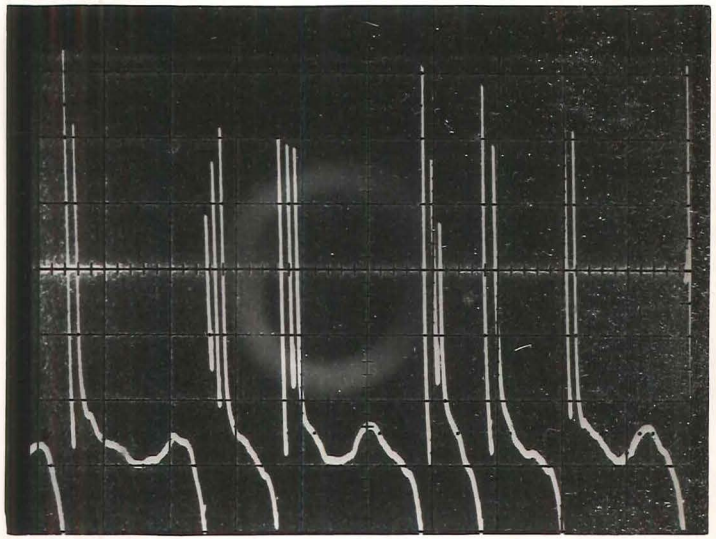

b

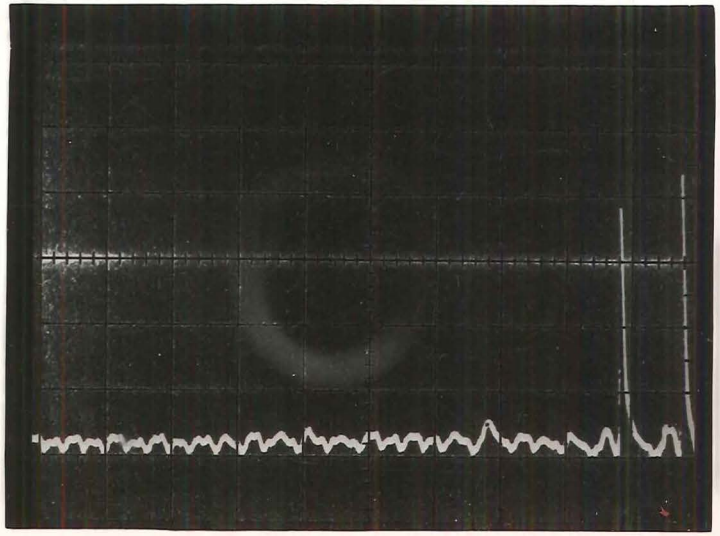

c

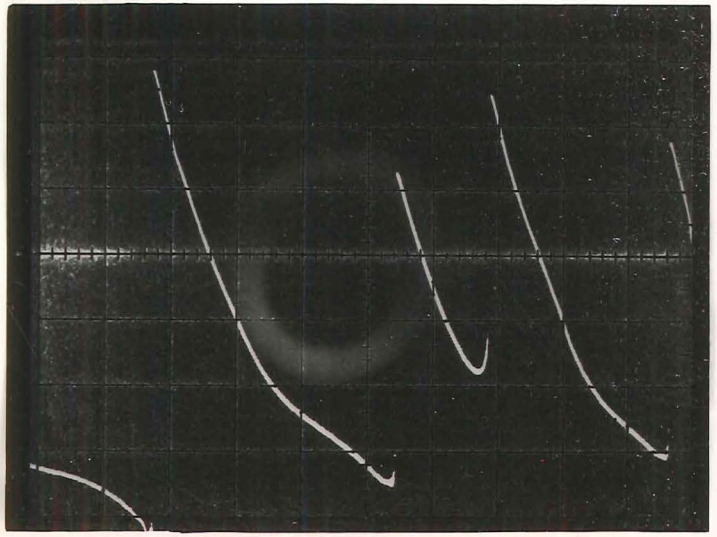

d

Figure 17 : Arc voltage wave-forms. 50 V per division vertical. a,b,c 200 us per division horizontal d 20 us per division horizontal. (voltage zero is bottom line)

Figure 18 : Arc current waveforms.
100 kHz cut off low pass filter (-48 dB per octave) 80 A per division vertical.
a,b,c 100 us per division horizontal
d 20 us per division horizontal.
(current zero is third line up)
Note similarity with voltage waveforms.

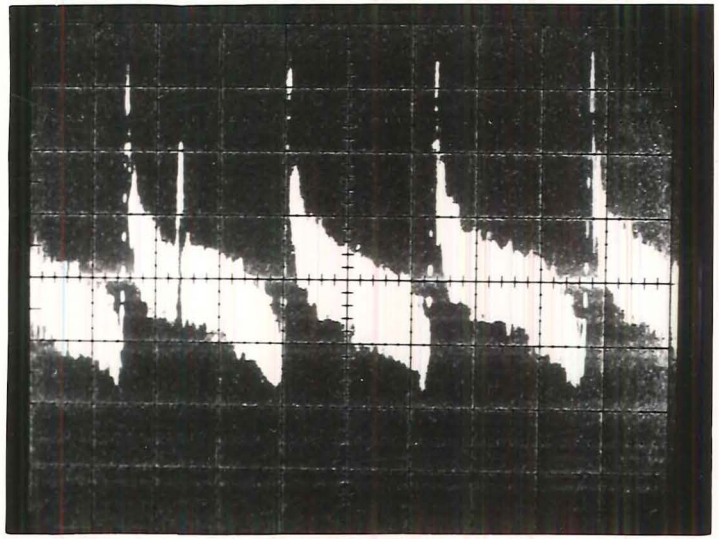

a

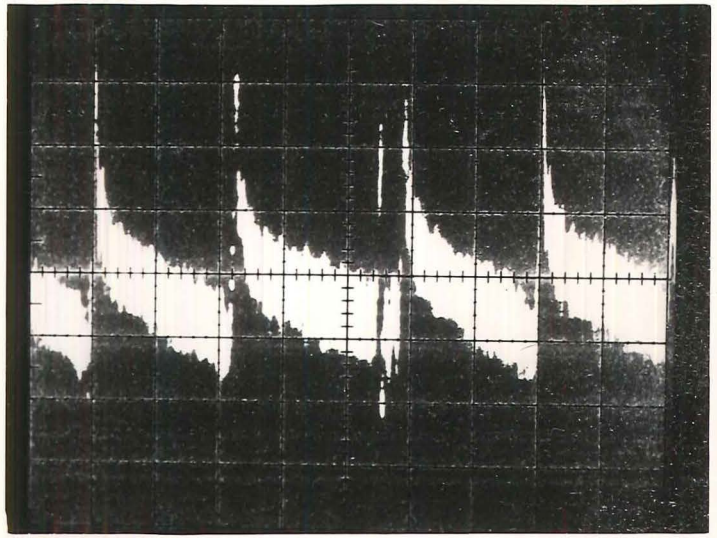

b

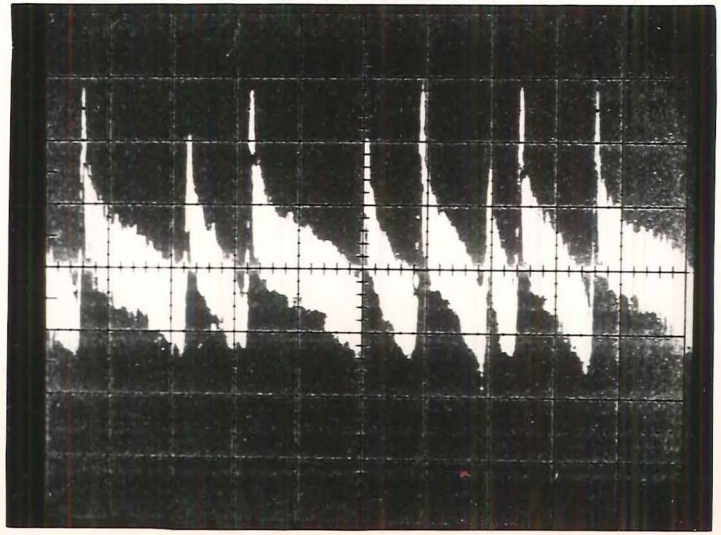

c

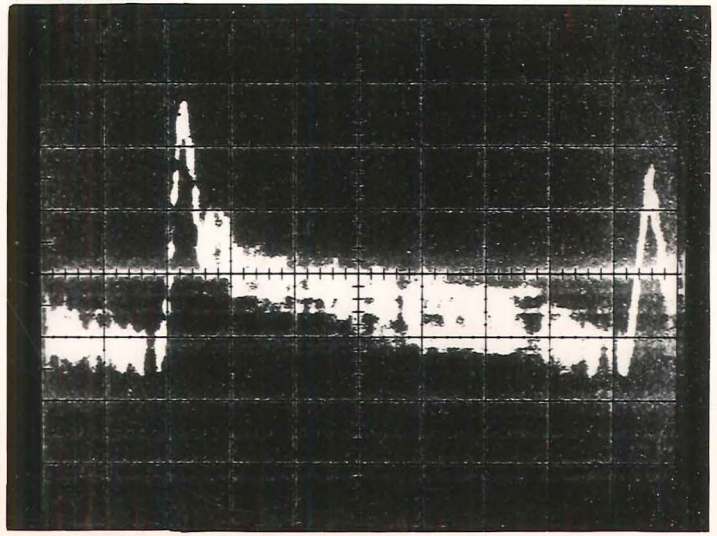

d

the sharp cut-off 100 kHz filter. The steady state current is about 120 A for this particular setting of the saturable reactor cores. Like the voltage waveforms, the minimum current observed is close to zero or slightly negative (-20 A).

7.3.3 High Speed Photographs

The high speed photographs show a plasma in violent motion. It is unfortunate that the V & I oscilloscope traces show a cyclic process taking place at about equal to, or slightly more frequently than, the maximum camera frame speed. Because of this, it is difficult to get a clear indication of what is taking place. For much of the time the arc is relatively long (> 2 cm) and so much of it is out of sight due to the restricted viewing angle.

It appears that an arc is formed directly between the electrodes. This arc rapidly expands outwards, at some point a new arc strikes and the process is repeated, see Fig. 19. The anode attachment wanders rapidly and probably continuously across the anode surface, covering the anode end and at times reaching as far as one anode diameter down the electrode, see Figure 20. This wandering is probably controlled by small amounts of easily ionisable material (e.g. Ca, Mg, Na etc.) that become exposed on the electrode surfaces. This is clearly shown in Figure 21, where a coal core anode is being used, with radial holes through the graphite shell every few centimetres. The holes get filled with coked coal, plus pyrolysis material and vent pyrolysis gases. The anode attachment can be seen to jump down onto the hole material for one frame and then to resume its wandering.

The cathode tends to be more 'stable', appearing to move in discrete jumps, depending on whether the arc is long or short.

Figure 19 : Repeating arc strike blow-out mode. 7·9 mm graphite anode, current 100 A nominal. time is downwards at 350 us between frames.

Figure 20: Anode attachment movement. nominal current 200 A 350 us between frames. Note spot cool-down rate.

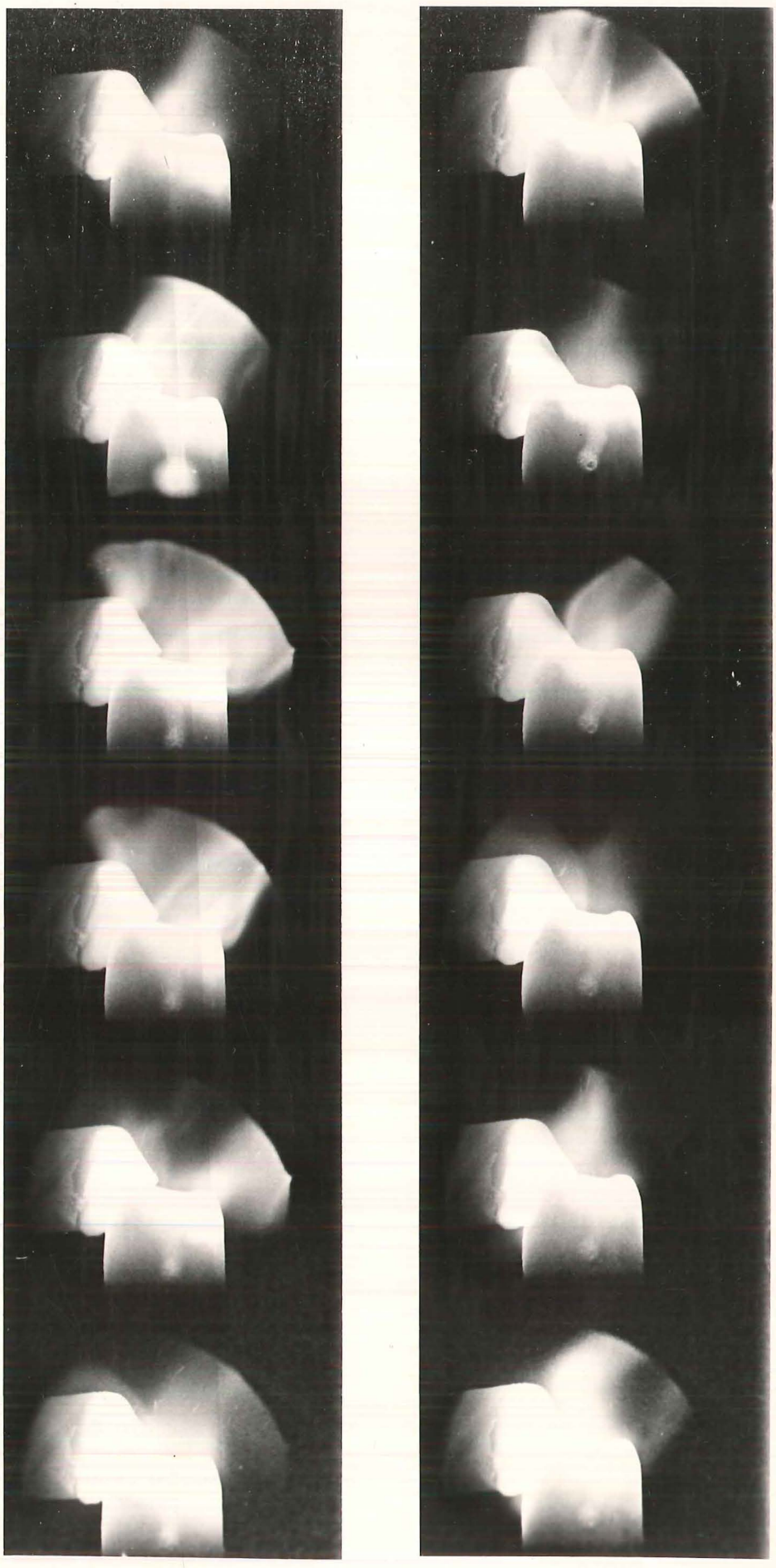

Figure 21: Anode spot attached to coal core vent hole.

The anode and cathode attachment spots appear to be similar in size (0.9 ± 0.2 mm diameter) Fig. 22. Assuming a current of 160 A, then the current density would be 25,000 A/cm^2. This is two orders of magnitude greater than current densities reported by Cobine[42] for a carbon arc (in air).

Examination of a number of films shows numerous examples of particles of graphite being ejected from both electrodes. This is particularly noticeable when the electrode surface has a macroscopic discontinuity on it, Figures 23a, b. (Presumably a section of the electrode becomes thinned and is then an unfavourable current conductor, so eventually it becomes undermined and ejected in a burst from the surface.) The size of particles observed is a few hundred microns. Their total contribution to the ablated carbon is no more than 5% (from material collected in the dust cyclone). So this does not result in a significant inefficiency or loss to the process; at least for graphite electrodes. This may not be the case for coal electrodes of low strength and high internal gas pressures.

7.3.4 Arc Attachment Spot Temperature

It can be readily seen that the arc attachments are at a somewhat higher temperature than the surrounding graphite (particularly when the anode attachment wanders onto the side of the electrode). Comparison of the radiance from the area close to the anode tip by imaging onto a thermopile, showed that it was almost uniform to about ½ the electrode diameter back from the tip, and that its brightness relative to the 3790 K standard arc indicated a temperature of 3950 ± 50 K. This is a mean temperature value. This assumes an emissivity which is the same as that of the standard arc, namely 0.99. However if the radiance is adjusted for $\varepsilon = 0.9 \pm 0.02$[43], then the surface temperature is 4055 ± 70 K. This value of the surface temperature is of special interest

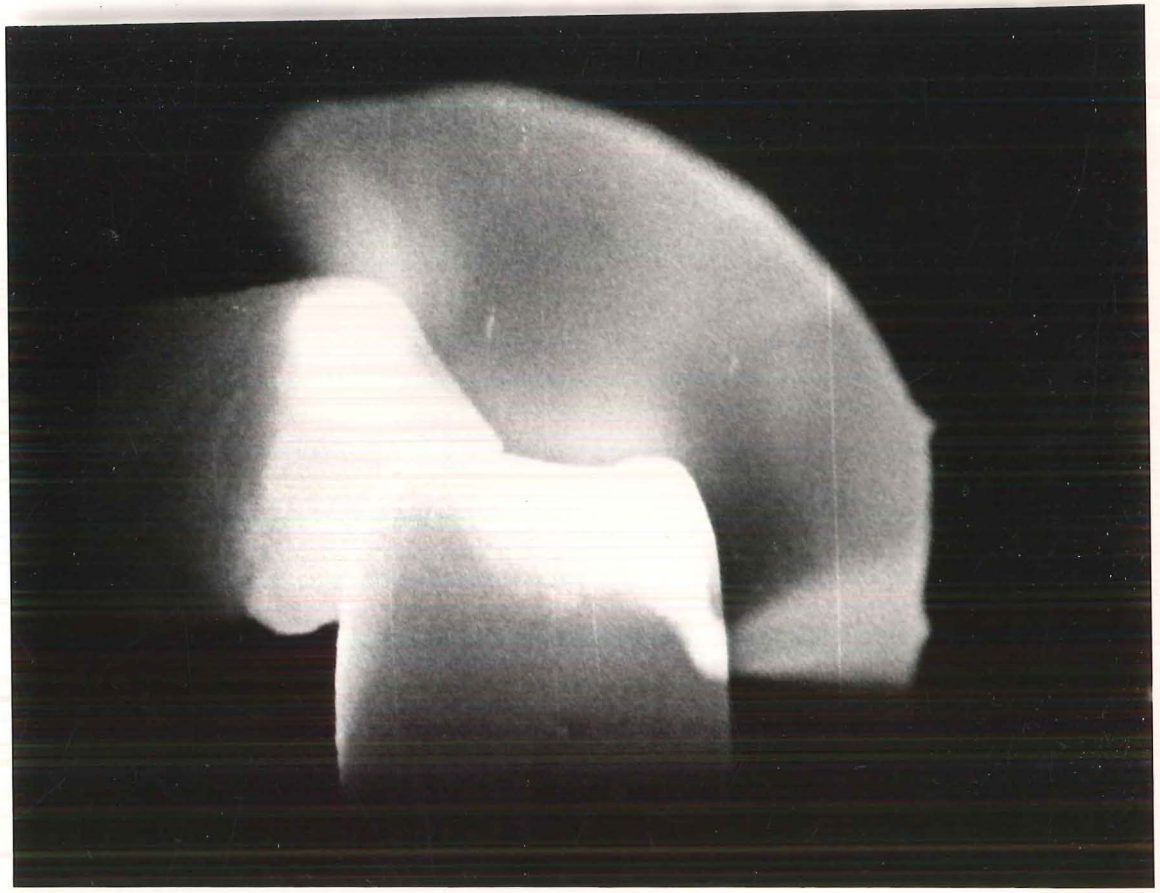

Figure 22: Anode arc attachment detail. 9·5 mm graphite electrode. Nominal current 200 A.

Figure 23: Particle mass loss from electrode surfaces. (350 us between frames)
[anode] [cathode]

as it neatly falls on the JANAF vapour pressure curve for carbon, at 1 bar. This curve has been experimentally verified by Lundell & Dickey[44] to 4600 K, by laser heating experiments. (It should be noted that Wilson and Spitzens' emissivity measurements[43] were made at temperatures up to 3400 K and 2900 K for Ll135P carbon and AGKSP graphite respectively. This still leaves uncertainty as to the true emissivity at ⩾ 3900 K, where the surface vapour pressure of carbon species is close to atmospheric[43].) The spectral emissivity of carbons is subject to intense debate. Schurer[45] has measured the spectral emissivity of carbons over the range 0.25 m to 1.7 μm. The spectral emissivity of the standard arc (3792 K) has a maximum emissivity over the visible of 0.99 ± 0.005, but decreases in the IR to 0.955 ± 0.01 at 1.7 μm. The radiance weighted mean emissivity would be about 0.97 ± 0.02. Schurer also measured the spectral emissivity of cold carbon anodes (fibres will be absent[90]), and found a more uniform emissivity, averaging 0.955 ± 0.02 over the range 0.25 - 1.7 μm. If these values are used then the corrected surface temperature is reduced back almost to the original 3950 K value - namely 3995 ± 70 K.
(The author makes the observation that there is a great need for reliable spectral emissivity values for carbons at or near the sublimation temperature with and without arcs on the surface, and which do not involve optical heating of the surface.) The peak temperature is what is of interest here. This can be estimated in two ways.

7.3.4.1 Measurement of spot temperature: Measurements were made of the relative spectral radiance of a 25 A graphite electrode in air, to the standard arc, using a medium quartz spectrophotometer and fast photomultiplier detector (rise time of the voltage follower and P.M. tube was less than 1 μs). A small area of the electrode surface (approx. 100 μm x 100 μm) was sampled by the detector. The output was

accumulated by the oscilloscope. From this, the envelope of peak brightness can be examined over a period of 50 seconds, and compared to the brightness of the standard arc. The peak spectral brightness was found to be twice that of the 3790 K radiation at 440 nm.

Using the Plack radiation function:-

$$E_\lambda = \frac{C_1}{(\lambda)^5 \left(e^{\frac{C_2}{\lambda T}} - 1\right)} \quad W\ m^{-2}\ m^{-1}$$

and taking the ratio of two spectral brightness values and a common wavelength:

$$\frac{E_{\lambda 1}}{E_{\lambda 2}} = \frac{e^{\frac{C_2}{\lambda T_2}} - 1}{e^{\frac{C_2}{\lambda T_1}} - 1} = 2 \pm 0.4$$

The error in the radiance ratio was estimated from the variation in the maximum spectral brightness envelope, over a period of time with the current and electrode gap as far as possible constant.

$T_2 = 3792$ K $\qquad \lambda = 440 \times 10^{-9}$ m

$C_2 = 0.01439$ mK

then T_1 is at least 4120 ± 100 K for $\varepsilon \lesssim 0.99$

7.3.4.2 Spot cool-down rate: The cool down time for ¼" D graphite anodes in air has been measured for a starting temperature of 3792 K[90]. By examining the high speed photographs, Figure 20, it can be seen that at least 5 frames (1.5 ms) are required for a hot anode spot to cool back to its background. If the background is at least 3850 K (the lowest surface brightness from the spectrophotometer trace of the anode of the 25 A air arc), and the graphite anode will cool by 350 K in 1.5 ms, then this would suggest that the spot temperature was at least 4200 K. It should be noted that the conductive cooling component of the hot anode spot back into the electrode bulk, is rather different compared to the

'standard' anode cooling mode. The hot anode spot can cool by radial conduction compared with almost pure axial cooling of the 'standard' anode. This value is in reasonable agreement with the previous estimate. In both calculations it has been assumed the surface emissivity is equal to that of the standard arc, namely $\varepsilon \simeq 1$.

Examination of the high speed photographs, Figures 20-23, shows that the cathode spot temperature is probably at least as hot as the anode, namely 4150 ± 100 K. This is consistant with the spectrophotometer investigation of anode and cathode spot brightnesses for 25 A, ¼" graphite electrodes in air, relative to the standard arc. This is also in general agreement with the cathode spot temperatures of a 20 A graphite-air arc measured by Hearne and Nixon[46], although they assumed an emissivity of 0.8.

7.3.5 Cathode Spot Current Density

If the cathode current density is estimated to be 25,000 A cm^{-2} Figure 19, and the electrode spot temperature is 4200 K, can this electron emission be accounted for by thermionic emission? Hearne and Nixon[46] calculated values for the graphite work function for their graphite-air cathode attachments. If a value of 4.5 eV is used, and using the Richardson-Dushman equation:

$$\dot{\gamma} = A T^2 \exp(-e\phi/KT)$$

where $\dot{\gamma}$ = current density in A cm^{-2}

A = constant = 120.4 A cm^{-2} K^{-2}

T = absolute temperature K

ϕ = thermionic work function

e = the electronic change

K = Boltzmann's constant

$$\dot{\gamma} = 120.4 \times 4200^2 \exp\left(\frac{-4.5 \times 1.602 \times 10^{-19}}{1.380 \times 10^{-23} \times 4200}\right)$$

$$= 2.12 \times 10^9 \times \exp(-12.44)$$

$$= 8406 \text{ A cm}^{-2}$$

Thus using a work function of 4.5 eV and a temperature of 4200 K, only 1/3 of the measured current density can be accounted for by thermal means. Cobine[47] notes that the work function can be reduced by the effect of local electric fields (e.g. positive ion space change of C^+ and H^+ at the cathode surface) and adsorbed gases on the surface (e.g. atomic H) and impurities (Na, Ca, K). An effective value of the work function required to produce the observed current density at 4200 K, would be 4.1 eV (a reduction of 0.4 eV).

7.4 Modelling of Observed Waveforms

An attempt will be made to explain the dynamic behaviour of the arc in terms of the available voltage, current and photographic data.

7.4.1. Arc Loop Expansion

An arc must be attached perpendicularly to its electrode surface due to the large electric fields present at the attachments. Thus when an arc forms across the gap of a right angled pair of electrodes, three distinct geometries can occur; concave upwards, concave downwards and concave both up and down.[48]

The curved arc column will be subject to the magnetic Lorentz force, due to the bunching of the magnetic flux on the inside of the curve relative to the outside. This force will cause the column to expand outwards from the electrodes. As a result the column will lengthen and become more strongly curved. Figure 19 shows this rather well. In the case of the arc starting concave downwards, the magnetic expansion force will be partially constrained by the opposing convection and bulk gas

flows. The concave upward case will be free to expand at a rate limited by the gas dynamic drag force of the hot arc column expanding into the colder surroundings. The rate of this expansion can be estimated by equating these two forces[48]. The force per unit length of the Lorentz force is given by:

$$\frac{dF}{dL} = -(3\ \mu_o\ i^2/16\ \pi\ R)\{1 - \frac{7}{18}\ (r_o/R)^2\}$$

where μ_o is the magnetic permeability of space

i is the current

R is the curve radius

r_o is the radius of the current carrying conductor

The drag force per unit length is given by:

$$\frac{dF}{dL} = C_D\ r_o\ \rho\ V^2$$

where C_D is the drag coefficient for a cylinder

ρ is the bulk gas density

V is the expansion velocity

Lack of required data for hydrogen arcs prevents this calculation being made in this case.

Equating these two forces, and using the values:

$i = 200$ A $\quad R = 1 \times 10^{-2}$ m $\quad r_o = 2 \times 10^{-3}$ m

$\rho = 3.7 \times 10^{-3}$ kg m^{-3} $\quad H_2$ at 4000 K (equilibrium)

$\mu_o = 4\pi \times 10^{-7}$ N A^{-2}

$C_D = 0.2$

The value of drag coefficient used by Wutzke et al.[48] will be used.

then $V = 447$ m sec^{-1} and for $R = 4 \times 10^{-3}$ m

$V = 675$ m sec^{-1}

If an arc loop is expanding radially at this rate, of order 0.5 mm μs^{-1} then the power required to sustain the expanding plasma loop is estimated to be:-

Volume of plasma formed per second

$= \pi \times (2 \times 10^{-3}\ m)^2 \times 500\ ms^{-1} \times 2\pi = 0.039\ m^3\ sec^{-1}$

Its mass will be (at 13,000 K; section 8.4.2).

$= 7.9 \times 10^{-4}\ kg\ m^{-3} \times 0.039\ m^3\ sec^{-1}$

$= 3.15 \times 10^{-5}\ kg\ sec^{-1}$

Specific enthalpy for hydrogen at equilibrium

13,000 K = 656 MJ kg^{-1} (70)

4,000 K = 263 MJ kg^{-1} (70)

Therefore power required $= 393 \times 10^6 \times 3.15 \times 10^{-5}$ W = 12.4 kW

If the input power to the reactor is 16 kW (80 V x 200 A), then at least 50% of this will be dissipated in the immediate vicinity of the electrodes (anode and cathode fall). Boumans[49] gives the combined anode and cathode fall voltage drop for a 10 amp air arc between pure graphite electrodes as 43 V. This presumably is for the stable arc, in which case the 'hissing' arc will have a combined fall voltage drop of about 8 V less[50]. It appears that such a process of magnetic expansion may be energy limiting, resulting in a drop in plasma temperature, resulting in an increasing plasma column resistance and decreasing current.

7.4.2 Voltage and Current Discontinuities

The discontinuities in the V and I waveforms could be the result of three envisaged processes.

(a) The arc column expands upwards rapidly under the influence of the Lorentz force. The column reaches sufficient length (4-6 cm) that the plasma hits the graphite chamber wall and is quenched. The reactor inner chamber usually has a uniform discoloured patch on its surface directly opposite the cathode-anode plane, suggesting abnormal

heating. There is no evidence under normal reactor operating conditions, that an arc strikes onto any part of the graphite lining. (If an arc is struck then the shell would be the anode, requiring a cathode-to-shell arc to form). The fastest likely quenching time would be if the arc column was expanding at 500 m/s under the Lorentz force with a column diameter of 4 mm, impinged directly onto the cold graphite surface (2000 - 3000 K). This time interval is 8 μs. This model is unlikely to account for the abrupt transition taking place in <2 μs.

(b) The arc column lengthens under magnetic, convective or bulk flow forces, until sufficient column resistance has been acquired, that a fresh arc can strike over between the electrodes. This model has two serious defects. The current must increase as the new arc strikes, so that $\frac{di}{dt}$ should be large and positive, and when combined with the inductance of the supply:

$$V_{arc} = V_{steady\ state} - L\frac{di}{dt}$$

A large negative voltage spike would be expected, but a large positive spike is observed. In addition it is hard to envisage a new arc striking at very low voltages (<50 V), where the transitions are usually observed. This model must also be rejected.

(c) If magnetic blowout occurs due to the energy limiting column expansion under the Lorentz force, then this process would result in a rapid reduction in current ($\frac{di}{dt} << 0$), producing a large positive voltage spike, which is what is observed. It is supported by the high speed photographs, which appear to show an arc interruption process occurring, Fig. 19.

However, it is difficult to see why arc blowout should suddenly occur during periods of steady state arc operation, or why

significant periods of steady state operation should exist. Once the voltage rises to > 150 V a new breakdown occurs and a new arc is formed. It is difficult to decide whether the gap breakdown is of the thermal or spark types. Because of the high electrode temperatures, significant thermionic emissions is assured favouring thermal breakdown. However a spark breakdown is suggested by the speed of breakdown, < 2 μs, and the often high breakdown voltage (> 350 V).

Crawford and Edels[51] note that only when the temperature is less than 2000 K can thermal ionisation be considered negligible, and it may be expected that breakdown will then be a function solely of gas density and gap length (a condition for spark breakdown).

Edels et al.[105] show that for graphite electrodes burning in free convection in air with 50 A for a few hundred milliseconds, have a recovery time of 1 ms before the voltage strength required for restriking reaches more than 200 V.

A spark breakdown seems unlikely, since a voltage recovery to 350 V in 1 μs is observed, unless hydrogen (or some other species) is able to remove all the positive ions about the electrode surfaces in the available time.

Once breakdown occurs the inductive energy is rapidly released (~50 μs) in the new arc, with the peak power being in the order of 10 times the average power.

7.4.3 Arc Voltage Less than Minimum Steady State

The minimum sustaining voltage for a carbon arc appears to be at least 35 V[50]. The arc voltage often drops from the steady state voltage (65V) down to zero or even some negative voltage (~-(20-30)V) in about 30-40 μs, figure 17. This must be a combined arc and inductive phenomena. For a sudden fall in voltage, $\frac{di}{dt} > 0$. Processes likely to produce this, are the growth of a second arc; a sudden reduction of the plasma column resistance

or the reduction of the cathode or anode fall voltages. A sudden increase in current is observed in the waveforms, Figures 18 a,b. The inductance of the saturable reactors is likely to depend on the current. However at zero current and 1000 Hz the circuit inductance appears to be 2.5 mH.

If the current increases by 0.1 A/μs then the voltage would be expected to fall by $-0.1 \times 10^6 \times \frac{2.5}{1000}$ V = -250 V.

It can be concluded that relatively small rates of change of current can produce substantial voltage swings, at low currents. If the arc column (which is assumed to be mostly hydrogen) encounters a high concentration of carbon vapour, this could significantly reduce the column resistance since the ionisation potential of carbon is 13.60 - 11.26 eV = 2.34 eV lower than hydrogen. Significant changes in cathode and anode fall voltages may occur when small concentrations of volatile, easily ionisable materials such as Na, are suddenly exposed at the electrode surfaces. This argument is strongly supported by the 'anodic hash' phenomenon[53].

It is believed in this phenomenon that an intense burst of ions are suddenly released at the anode surface. The effect of this is that the anodic sheath is virtually short-circuited by a plasma bridge and its voltage falls essentially to zero. Gradually the anode voltage is restored until the process repeats. When this is coupled with an inductive circuit a sudden increase in arc current and a sudden and substantial fall in the arc voltage would be expected. The rise time for the ion burst is in the microsecond region. This phenomenon may explain the negative voltage swings from steady state, but the fast voltage rise to ~350 V to 'restrike' cannot be accounted for.

It should be noted that the semi-conductor diodes of the power supply can pass large reverse currents for large negative $\frac{di}{dt}$ values (< -100 A μs^{-1}) as appears to be the case with this system, because they typically have a reverse recovery time of about 5 μs[52],

depending on the device and junction temperature.

7.5 Rate of Anode Attachment Movement

If it is assumed that the anode attachment moves over the electrode surface semi-continuously, then a lower limit can be placed on the rate of attachment movement by examination of the high speed photographs. This appears to be at least 1 cm in 300 μs i.e. at least 30 m s^{-1}. Finkelnburg[54] observes a rate of anode spot movement of 300 m s^{-1} for the high current carbon arc. He observed a current density in the attachment of 50,000 A/cm^2 which is within the likely experimental error of the value observed in this work. His velocity will be assumed to be more realistic. If the anode attachment has an equal probability of being at any point on the tip of the 9.5 mm diameter electrode (70 mm^2) and the spot diameter is 0.7 mm, then at 300 m s^{-1} it will cover the entire surface in 1/3000 s, i.e. 300 μs - which is approximately equal to the frame speed of the high-speed camera.

7.6 Bulk Surface or Arc Attachment Ablation

It is of fundamental interest in understanding the ablation of graphite, to decide whether the majority of the mass loss occurs in the arc attachment (which occupies only ~1% of the tip area at any instant) or whether ablation on the remaining 99% of the tip area dominates.

The free vaporization of graphites has been measured over a wide range of temperatures (2400 K - 4600 K) by Clarke and Fox, and Lundell and Dickey[55, 56, 44].

If an Arrhenius plot is made of these three sets of vaporization rate data, an excellent linear fit is obtained, linking Clarke & Fox's resistive heating in vacuum results to Lundell & Dickeys' laser results. See Appendix 5. (It appears reasonable to reject Lundell & Dickeys'

earlier supersonic jet heating results[44] due to doubts about the correct surface temperature.)

A plot of these results (vaporization rate per unit area versus temperature) is shown in Figure 24. Included on this plot are the measured ablation rates for a 280 A, 9.5 mm AGSR anode; namely 0.11 g s^{-1}. One point is based on the tip area at a temperature of 3950 K. The higher point is based on the arc attachment area (0.5 mm^2) and a spot temperature of 4200 K. Approximate error estimates have been included for both temperature and mass loss rate.

It can be seen that the tip vaporization rate is too low (by a factor of 3), whereas the arc spot vaporization rate is too great by a factor of about 3. It can be concluded, given the rather crude assumptions of mean temperature and area, that the ablation process on the anode can be accounted for by free vaporization at a combination of two temperatures.

This is significant because both Clarke & Fox's and Lundell and Dickey's vaporization results do not involve significant fractions of particle mass loss. (Clarke and Fox calculate that particle mass loss amounted to less than 1 part in 10^9 of the total mass loss rate). Therefore it appears that strong evidence (including visual and spectrographic) has been obtained which rules out significant mass loss by particle erosion. This result is in direct opposition to the work of Whittaker and Kinter[57] and Meyer and Lynch[58] who have shown that for graphite heated in vacuum to 3700 K or above, 90% of the mass loss is by particulate emissions.

Numerous carbon ablation models predict heats of vaporization of 20-30 MJ kg^{-1} and are supported by experimental data. See Baker[106] and Abrahamson et al.[107]. These heat of vaporization values are found to be between the estimated heats of vaporization of C_2 and C_3 (JANAF

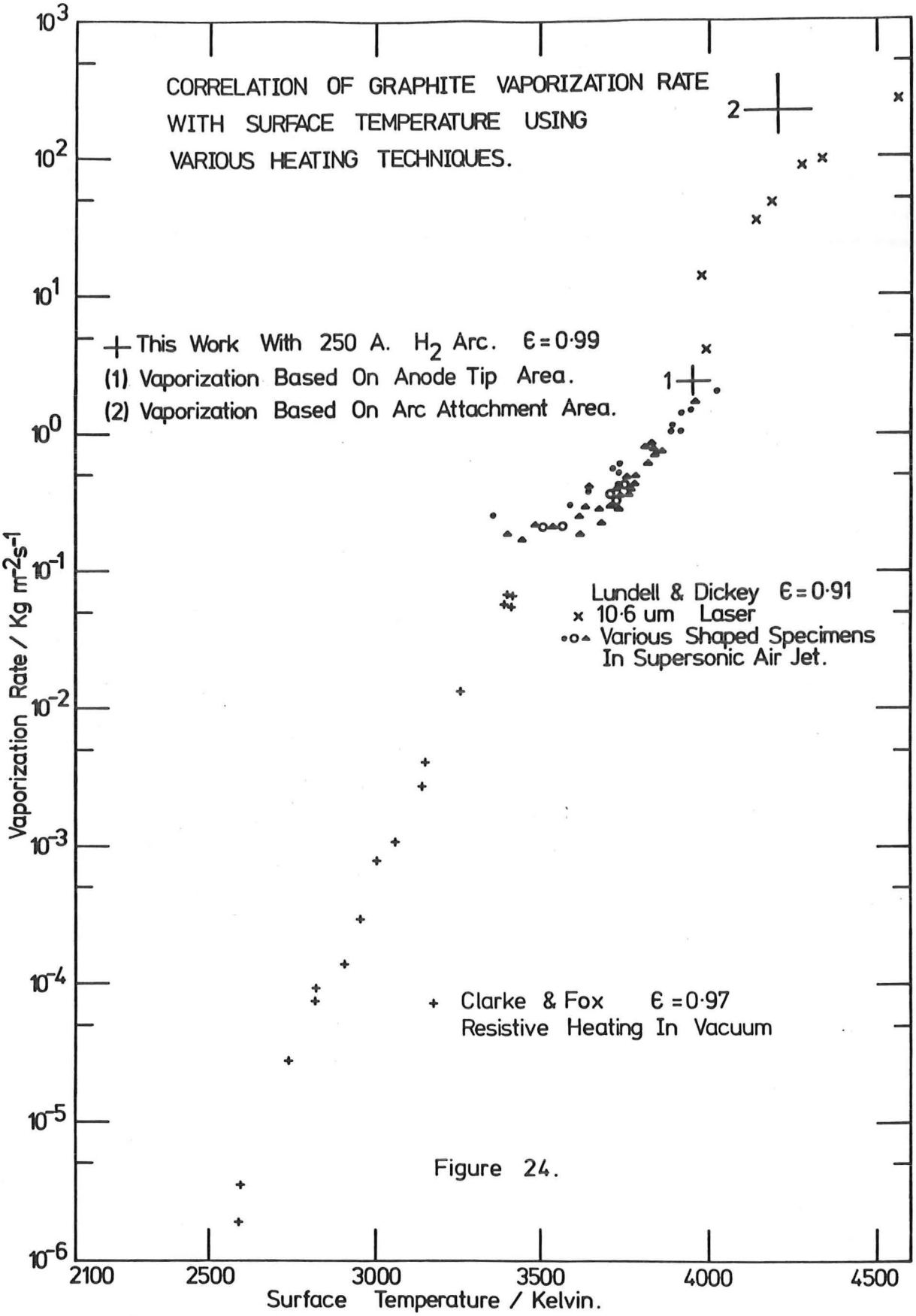
CORRELATION OF GRAPHITE VAPORIZATION RATE WITH SURFACE TEMPERATURE USING VARIOUS HEATING TECHNIQUES.
+ This Work With 250 A. H_2 Arc. $\epsilon = 0.99$
(1) Vaporization Based On Anode Tip Area.
(2) Vaporization Based On Arc Attachment Area.
Lundell & Dickey $\epsilon = 0.91$
× 10·6 um Laser
•o▲ Various Shaped Specimens In Supersonic Air Jet.
+ Clarke & Fox $\epsilon = 0.97$
Resistive Heating In Vacuum
Vaporization Rate / Kg $m^{-2}s^{-1}$
Surface Temperature / Kelvin.
10^3
10^2
10^1
10^0
10^{-1}
10^{-2}
10^{-3}
10^{-4}
10^{-5}
10^{-6}
2100
2500
3000
3500
4000
4500

Figure 24.

tables). This suggests that particle mass loss is insignificant in carbon ablation. The irreversible thermodynamic model of graphite sublimation developed by Baker[106] may resolve this conflict. This allows for a discontinuity of temperature and pressure to exist at the solid-vapour boundary. This predicts that the vapour region can become vapour saturated in carbon vapour species during ablation.

Much experimental and theoretical work is required to fully relate carbon ablation by radiation heating, to hypersonic heating and to arc heating.

7.7 Conclusions

The dynamic behaviour of the high current carbon-hydrogen arc, supplied via saturable reactors, has been probed with a 3200 fps camera and a storage oscilloscope. The arc has been found to be highly transient, with a mean period of a few kilohertz. Unfortunately without simultaneous voltage and current waveforms, combined with very fast photography (exposures of order of 1 μs), it is very difficult to observe accurately what is really taking place. It has been suggested that the observed phenomena are in part explained by arc blow-out and anodic hash . It has been established that the anode and cathode attachments are about 0.7 mm and 1.0 mm in diameter respectively. The anode attachment wanders over the electrode at a speed of order of 300 m s^{-1}. It is found that the anode attachment can reach down as far as one anode diameter back from the tip. This appears to be controlled by easily ionisable electrode impurities.

The anode temperature close to the tip appears to be about 3950 K and the arc attachment spot temperature about 200 K hotter. Uncertainty in emmissivity values tend to make these values lower limit estimates.

The ablation rate of the anode tip can be accounted for by the expected thermal vaporization rate of the bulk tip area and the arc attachment, at their respective temperatures. It appears that particle mass loss from the anode is not significant for the ablative-gasification of graphite in hydrogen.

8. SPECTROSCOPY OF THE CARBON HYDROGEN ARC

8.1 Summary

The visible and ultraviolet spectra of the carbon-hydrogen plasma were photographically recorded. The significant spectral features present were the hydrogen Balmer series, the C_2 Swan bands, carbon (neutral and ion) lines and numerous lines of impurity metals. The C_3 and CH molecular spectra were not detected.

It was estimated that the plasma for the 200 A arc has a temperature of 13,000 K and an electron concentration of 1×10^{23} m^{-3}. The C_2 molecular temperature gave values very much less than that of the plasma core. However the experimental data was very scattered, making the result rather tentative.

A thermopile was used to measure the averaged total plasma radiation, relative to the anode tip radiance.

With the integrated plasma radiation and the spectral plasma radiation, it was possible to carry out a radiation balance of all the known radiative processes present. Good agreement was obtained. This result placed low limits on any possible particulate carbon present in the plasma surrounding the anode tip.

The total energy radiated in the arc column amounts to only about $^1/_5$ of the column power dissipation.

8.2 Procedure

8.2.1 Films

The spectrum of the 200 A arc was obtained by focussing the beam from the 2.5 cm diameter reactor window onto the spectrograph with a 30 cm focal length lens. (Both the lens and reactor window were

Sl-UV grade silica). The lens was positioned such that the anode-plasma area was magnified approximately 1.5 times on the slit.

The spectrograph was a 1.5 m Baird-Atomic grating instrument with photographic recording. The spectrograph covers 370 nm - 740 nm in the first order with a dispersion of 1.5 nm/mm. The overlapping second order spectrum covers 185 nm - 370 nm at 0.75 nm/mm. A slit width of 32 μm was used for all spectra.

The films used were, Ilford FP4, for the visible, and Kodak SWR for the ultraviolet range. (FP4 provides a reasonable compromise between speed and granularity, as well as having a response far enough into the red to record the H_α line at 656 nm). The FP4 was developed in D76 at 1:3 dilution for 16.5 minutes at 20°C. The SWR film was used since it has negligible sensitivity at wavelengths greater than 450 nm. This enabled the UV spectrum between 240 nm and 370 nm to be recorded without the superimposed visible spectrum. No loss of sensitivity was suffered below 260 nm, since SWR film has a low gelatin content. Development was in D19, diluted 1:1 for 2 minutes at 20°C.

The shutter was a sectored disc, rotated by a synchronous motor. Exposures were; 0.1 seconds for FP4, and 1.5 seconds for SWR. When the visible spectrum was required a glass block was inserted into the beam to cut out the UV radiation.

All films were scanned on a Joyce-Loebl microdensitometer.

8.2.2 Film Calibration

(a) FP4: A tungsten strip lamp was focussed along the spectrograph slit. Optical alignment was checked by test exposures and adjusted until the most uniform slit illumination was obtained. The W-lamp was calibrated with two optical pyrometers (CED's and CD's) at

2270 ± 20°C. (No significant difference between the two instruments was observed over a wide range of strip temperatures, inspite of the pyrometers operating on different principles. The Chemistry Department device has a fixed field, with a variable filament current lamp to balance against the observed target. The Chemical Engineering Department device has a fixed intensity spot, with the observed beam being attenuated by neutral density filters to balance the target against the spot. The pyrometer reading was corrected for a 10% window reflection loss and an emissivity of 0.429 at 650 nm[59] to give a true strip temperature of 2850 ± 30 K.

A set of 0.75 s exposures were obtained using various combinations of neutral density filters, providing attenuations of 0, 0.2, 0.5, 0.7, 1.0, 1.2, 1.5 and 2.0 D. The optical density of a filter is related to the fractional transmission (T) by:-

$$D = \log_{10} \frac{1}{T}$$

All films were simultaneously developed. Calibration curves were obtained for the following wavelengths:- 656 nm, 619 nm, 563 nm, 516 nm, 490 nm and 438 nm.

The rotational C_2 spectra observed consists of lines spaced approximately 30 μm apart on the film. Closely spaced lines can lead to distortion of the film calibration curve, due to the Eberhard and other effects[60].

This was investigated by photographing a test grid of suitable spatial frequency with a camera using a shutter speed of 0.5 s and varying the aperature. The test target was illuminated by a narrow band interference filter, centred on the C_2 0-0 vibrational band head. (The adjacent 0-0 rotational band was to be analysed.) No significant effect was detected.

(b) SWR: An approximate calibration was obtained using the UV spectrum of a Hg lamp. Exposures of 1.5, 0.75, 0.5, 0.375, 0.25, and 0.125 seconds were obtained. Calibration plots were made with the 297 nm, 314 and 313 nm lines. The 253.7 nm line was too strong, relative to the others, since it always produced a density close to saturation.

8.2.3 Space and Time Averaging

The arc has been observed to switch on and off at a frequency of about 3 kHz (section 7.3). The spectrograph slit is aligned with the vertical anode image, in such a way that the spectrum of the anode tip and plasma immediately above could be observed. At an average (meter) current of 200 A during the exposure, at least 1000 cycles would occur with the current swinging through nearly 400 A for each cycle. High speed photography shows that between cycles the arc root may wander over the entire anode surface, so that during the exposure the arc will reside over the slit for only a fraction of the total time. Thus, the spectrum obtained of the plasma is a space and time averaged one.

8.3 Identification of Spectral Features

8.3.1 Visible Region

The visible spectrum is dominated by the C_2 Swan bands; heads being observed of the 0-2, 0-1, 0-0, 1-0, and 2-0 bands. The atomic hydrogen lines (Balmer H_α, H_β, H_γ and H_δ (extremely weak)), are present. The CN 0-0 band head is extremely weak - confirming that the reactor is essentially free of air.

The Na^oD, and $Ca^o422.67$ nm lines are present in absorption. No C^o or C^+ lines are detected in the visible. Two atomic lines appear at 396.7 nm and 400.1 nm. The former can be tentatively identified as Ca^+ at 396.85 nm (although a stronger Ca^+ line is absent at 393.37 nm).

The 400.1 nm line has not been identified.

The C_2 (0-1) Deslandres - D' Azambuja series at 410.23 nm is possibly present, but the (0-0) head is absent at 385.22 nm. The CH spectrum is notable by its absence at 431.42 nm (0-0). This band head is observable in the 10-20 A carbon-hydrogen arc which is contaminated by air. Gaydon[61] observes that, trace amounts of oxygen are required to either produce or excite CH. Two 'molecular' features at 476 nm and 477 nm have not been identified, even though they are present in the low current arc spectrum. Pearse and Gaydon[62] was examined for the following possible species with little success:- H_2, C_2, CH, CH^+, CN, C_3, $C_4H_2^+$ C_2^+, C_2^-, CH_2, CH_3, C_2H_2, CO, and CO^+. The 477.45 nm feature agrees well with the CH^+ (0-1) band at 477.59 nm, however the (0-0) band of CH^+ at 422.53 nm is absent. The molecular spectrum of H_2 is presumably present, but has not been identified[63] in this work.

8.3.2 Ultraviolet Region

The C_2 (1-0) band of the Deslandres - D' Azambuja system is present at 360.73 nm. Numerous vanadium and titanium lines (mostly ionised) were identified from NBS tables[64]. Several carbon lines (ionised and neutral) were identified[65, 66]. The C^o 247.8 nm line was by far the most intense.

The visible spectra is shown in figure (25) and the UV in figure (26 a, b, c).

8.4 Quantitative Interpretation of Spectra

It will be assumed in the following analysis that the plasma consists of a hot current-carrying column (of mostly atomic hydrogen, atomic carbon and their ions plus electrons) surrounded by cooler gases of molecular and atomic hydrogen, and carbon molecular species.

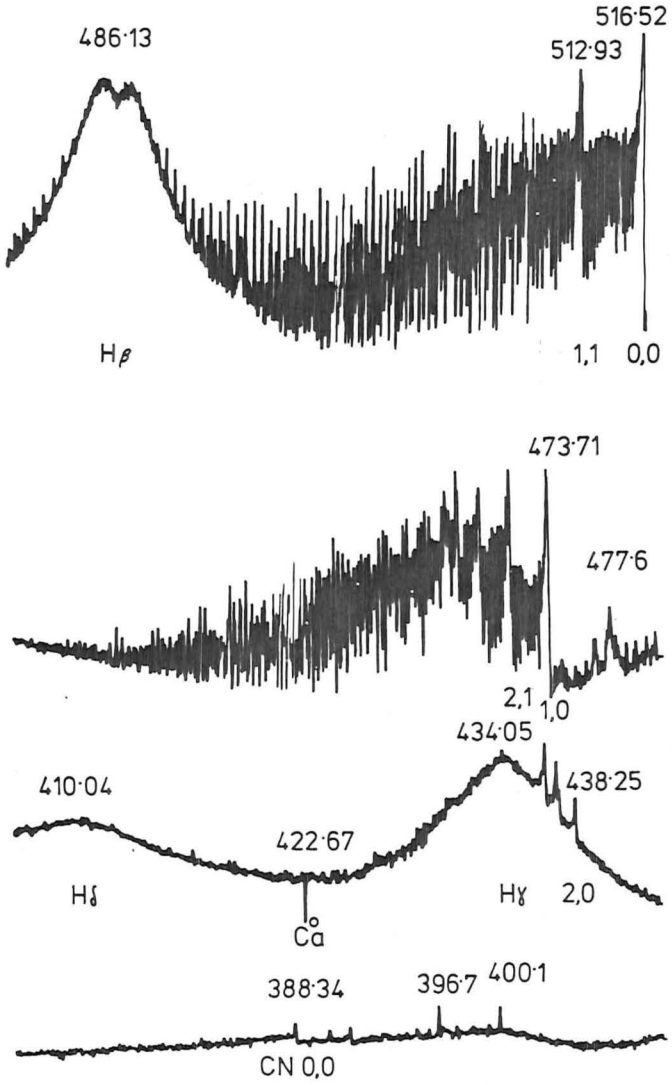

Visible Spectrum Of 200 Amp Carbon - Hydrogen Arc.

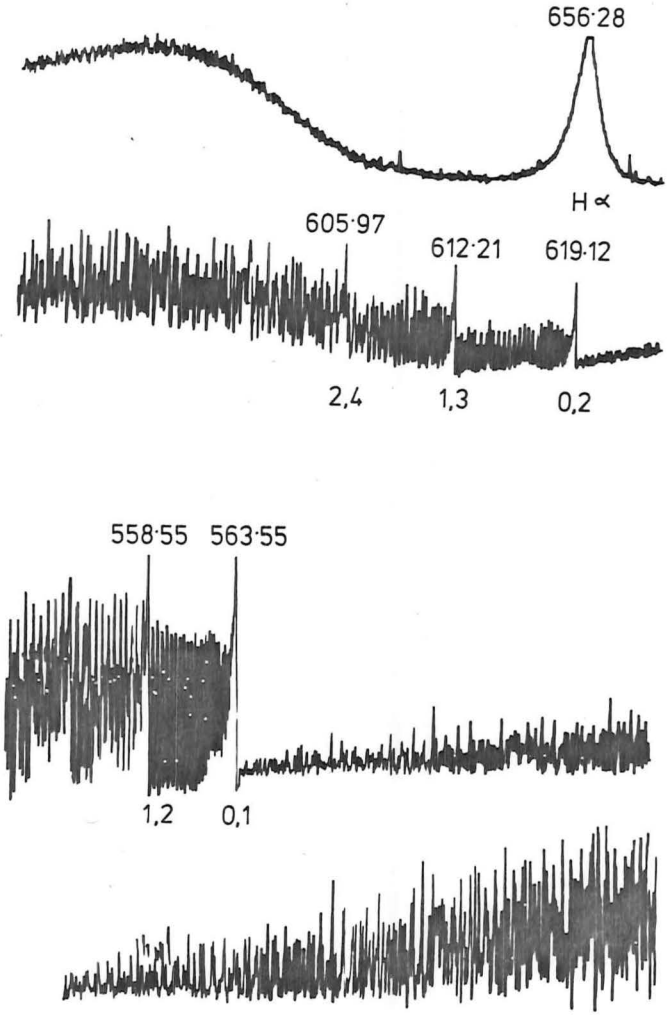

Figure 25.

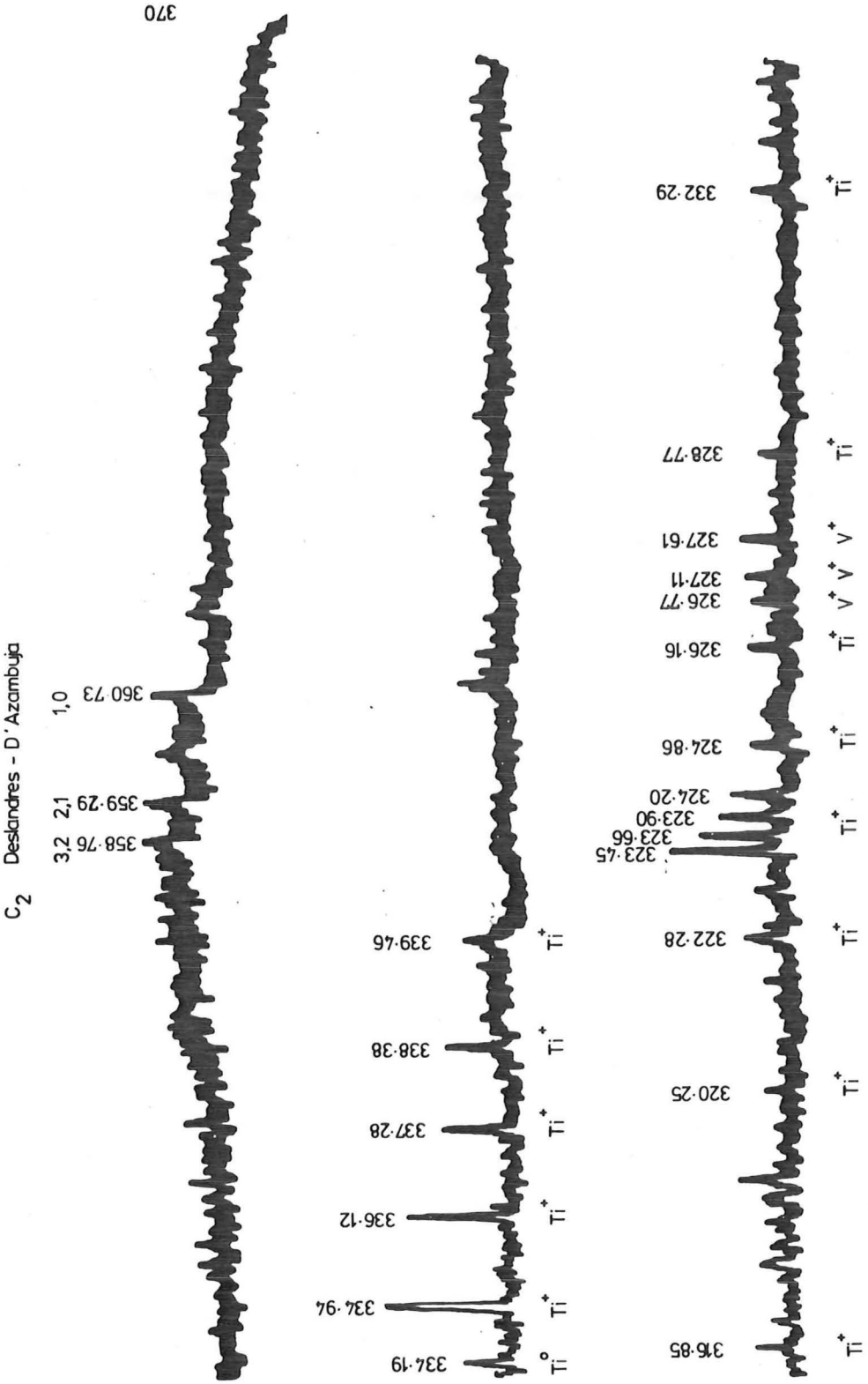

Ultraviolet Spectrum of 200 Amp. Carbon - Hydrogen Arc.

Figure 26 a.

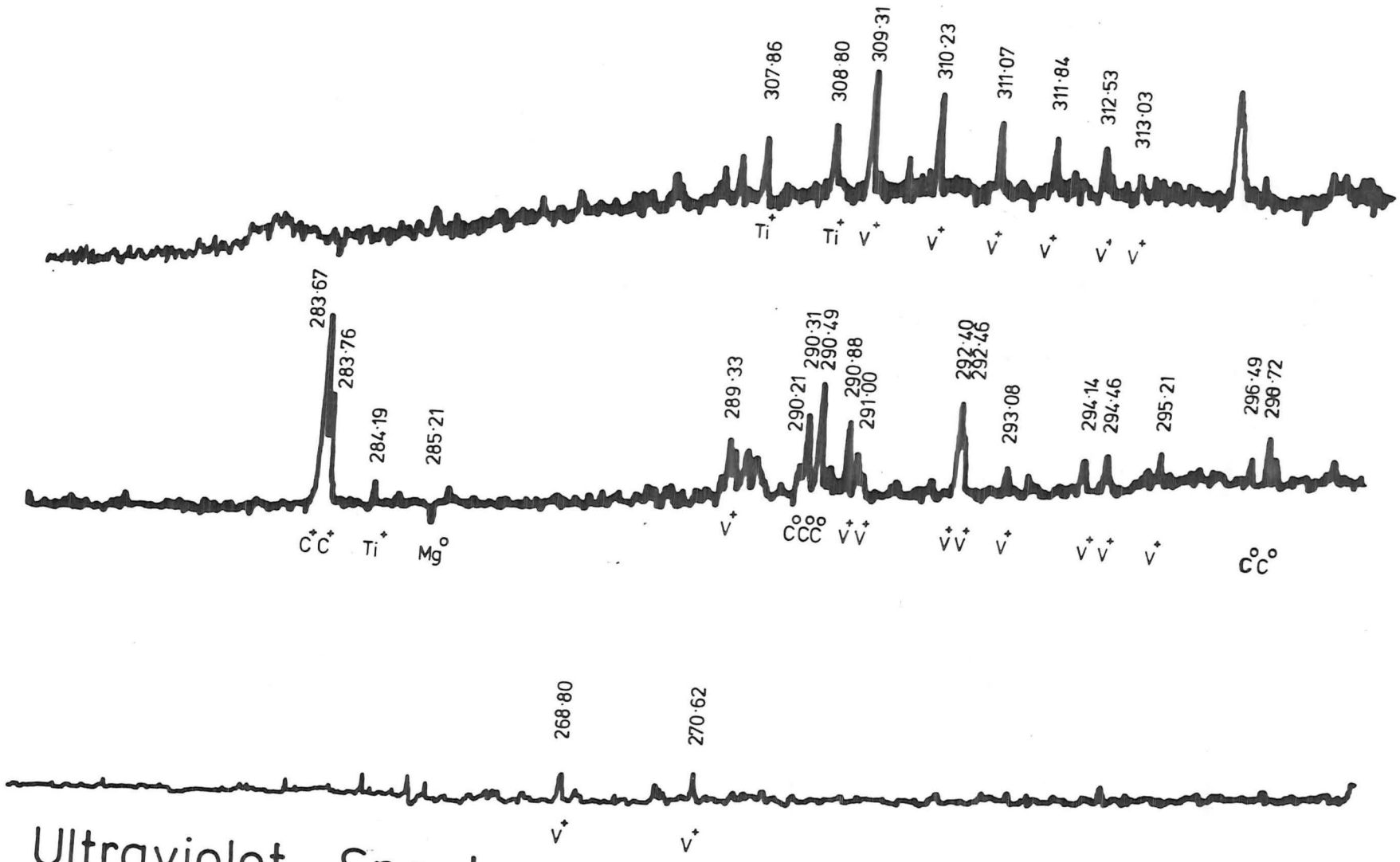

Ultraviolet Spectrum cont.

Figure 26 b.

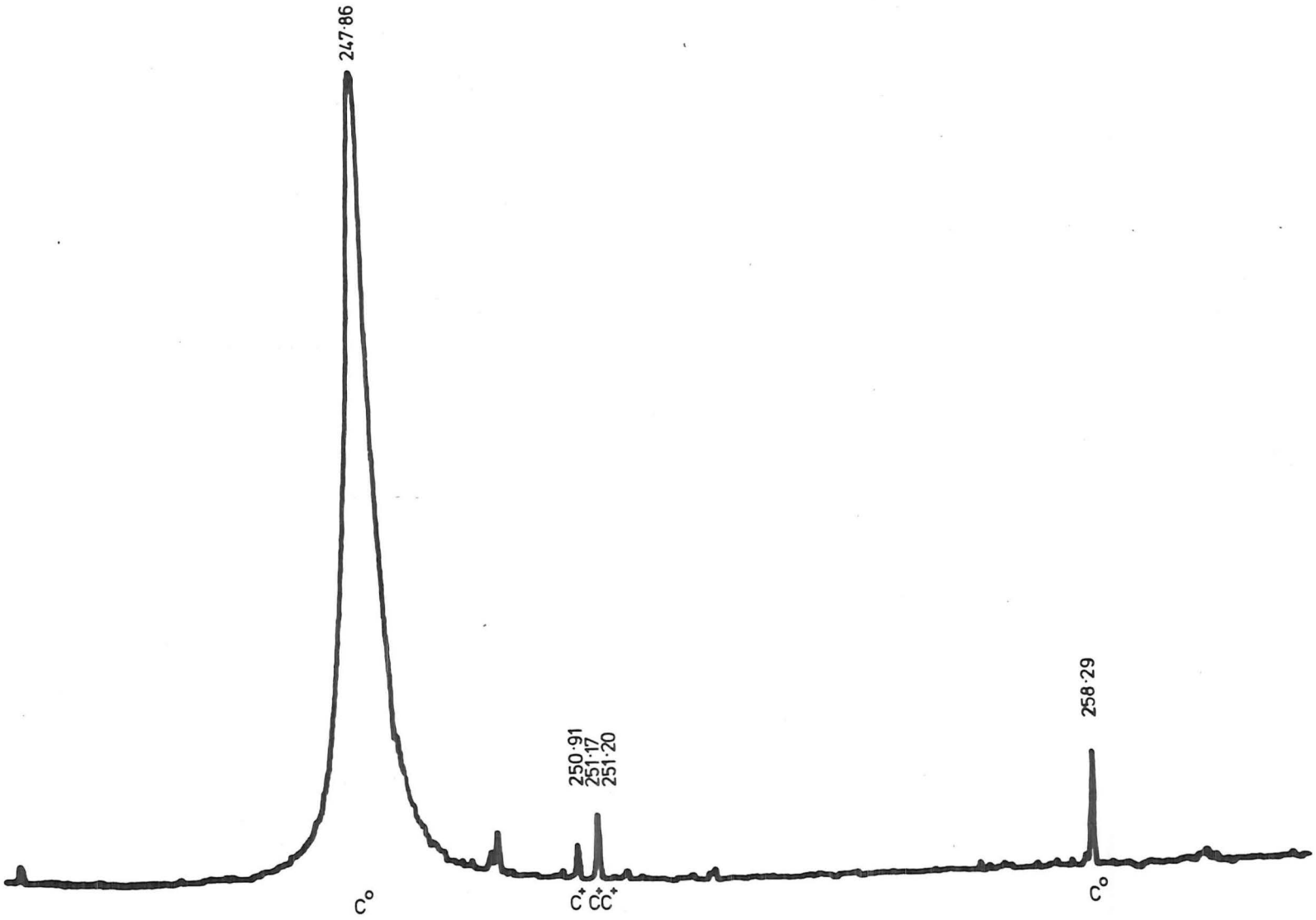

Ultraviolet Spectrum cont. Figure 26 c.

8.4.1 Electron Concentration

The electron concentration in the plasma can be estimated in two ways.

(a) The Stark effect causes the Balmer series to suddenly merge into a continuum.

Using the modified Inglis-Teller relation[67]:

$$\log_{10} N_c = 23.46 - 7.5 \log_{10} n$$

n = maximum quantum number observed

N_c = effective charged particle number density, cm^{-3}

For low temperatures ($< 10^5$ K/n), N_c = electron + ion concentrations, and assuming a pure hydrogen plasma then the electron concentration will be given by:

$$(Ne) = \frac{N_c}{2} .$$

The last Balmer line that is observed is the H_δ, for which n = 6, giving

$Ne = 2 \times 10^{17}$ cm^{-3}, valid for $T < 16{,}700$ K.

To get an idea of the coarseness of the result, using n = 7

$Ne = 0.65 \times 10^{17}$ cm^{-3}, valid for $T < 14{,}300$ K.

(b) Stark broadening of Balmer lines. The relative density profiles of the H_α, H_β, and H_γ lines are shown in figure (27). The H_β line has a ½ height width of 4.5 ± 1 nm. Using the graph in Huddlestone and Leonard[68], provides an electron concentration of $0.9 \pm 0.2 \times 10^{17}$ cm^{-3}. The H_γ line has a width of 7.5 ± 2 nm. Using data supplied in Huddlestone and Leonard[69], for a H_γ width of 4.0 nm, the electron concentration is 7.1×10^{16} cm^{-3} and scaling with the relation[67]:

$$\Delta\lambda_{\frac{1}{2}} \propto Ne^{2/3}$$

Microdensitometer profiles of Hydrogen Balmer lines.

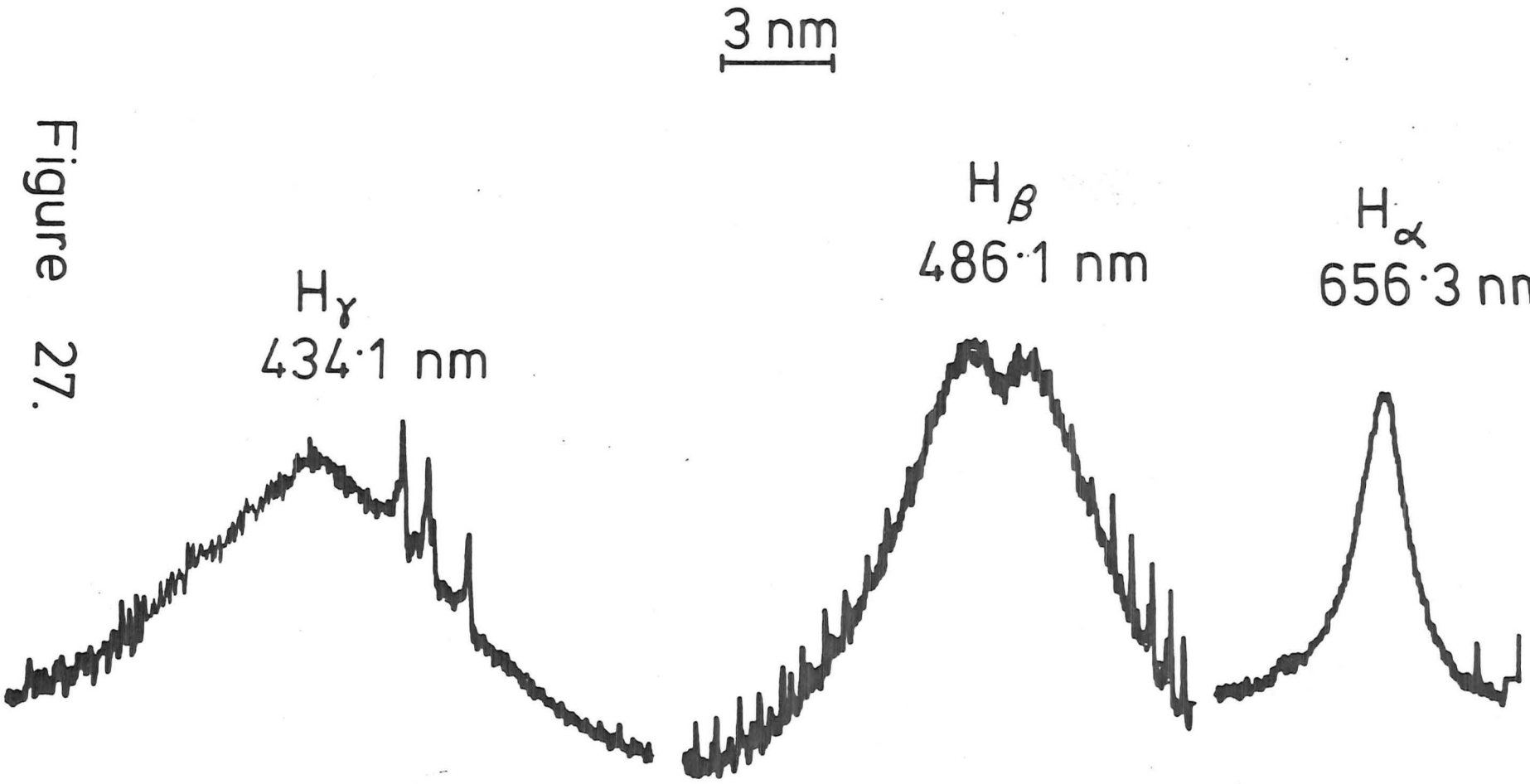

Figure 27.

where $\Delta\lambda_{\frac{1}{2}}$ is the half width at half height

and Ne is the electron concentration

then

$$\frac{7.5}{4.0} = \left(\frac{Ne}{7.1 \times 10^{16}}\right)^{2/3}$$

$$Ne = 1.8 \pm 0.8 \times 10^{17} \text{ cm}^{-3}$$

The three values show reasonable agreement, giving about 1×10^{23} electrons m^{-3}, and are summarized below:-

Table 6

Technique	Ne (m^{-3})
1. Series cut-off	$0.65 \times 10^{23} < Ne < 2 \times 10^{23}$
2. Stark broadening H_β	$0.9 \pm 0.2 \times 10^{23}$
3. Stark broadening H_γ	$1.8 \pm 0.8 \times 10^{23}$

8.4.2 Plasma Temperature

This can be estimated by several methods.

(a) If the electron concentration is used, and the following assumptions are made: 1. the plasma is pure hydrogen

2. the system is an ideal gas at a pressure of 1 bar

3. thermodynamic equilibrium exists in the plasma

then using equilibrium data for hydrogen[70] it is found that the electron concentration passes through a maximum at 18,000 K. Two temperatures are possible with an electron concentration of 1×10^{23} m^{-3}, namely 13,500 K and 37,000 K. The lower value is the more realistic.

(b) Using the ratio of intensities of the C^o 258.3 nm and C^+ 283.6 nm lines, Kroepelin and Hoffmann[71] provide a useful analysis of the C/H system. The large energy difference between the upper levels of these two lines provides a sensitive indication of temperature.

For $\frac{C^+}{C^o}$ intensity ratio = 3 ± 1

then the temperature is 13,000 ± 1000 K. They also show that for a C/H plasma with a molar C/H ratio approximately equal to 0.1, (our overall C/H ratio is between 0.2 and 0.05, but areas of the plasma may have carbon concentrations both considerably greater and lower than the overall mean), that the equilibrium concentration of C^o at 13,000 K is 1.6×10^{22} m^{-3} and for C^+ is 2.7×10^{22} m^{-3}.

With Ne = 1×10^{23} m^{-3} as found above, and assuming overall neutrality, then N_H+ = 7.3×10^{22} m^{-3}.
(Total particle density at 1 bar and 13,000 K for an ideal gas is 5.7×10^{23} m^{-3}.)

And so N_Ho would be by difference = 3.7×10^{23} M^{-3}.

Using the Saha equation on the hydrogen species concentrations,

for Te = 13,000 K

Ne = 1×10^{17} cm^{-3}

N_H+ = 7.3×10^{16} cm^{-3}

Then the N_Ho concentration (cm^{-3}) is given by[72]:

$$\log\left(\frac{N_H+ \, Ne}{N_Ho}\right) = -\chi_{H^oH^+} \Theta - \frac{3}{2} \log \Theta + 20.9366 + \log\left(\frac{2Q_H+}{Q_Ho}\right)$$

where χ is the ionisation potential in eV and equals 13.6 eV for hydrogen.

$\Theta = \frac{5040}{Te}$ where Te = 13,000 K

Q_H+ = partition function for H^+ = 1.0[72]

and Q_Ho = partition function for H^o = 2.0[72]

$$\log\left(\frac{N_H+ \, Ne}{N_Ho}\right) = -13.6 \times \frac{5040}{13,000} \; \frac{-3}{2} \log \frac{5040}{13,000} + 20.9366 + \log\left(\frac{2x1}{2}\right)$$

$$= 16.281$$

$$\frac{N_H + Ne}{N_H o} = 1.9 \times 10^{16} = \frac{7.3 \times 10^{16} \times 1 \times 10^{17}}{N_H o}$$

$$N_H o = 3.8 \times 10^{17} \text{ cm}^{-3}$$

which is very close to the ideal gas prediction.

The above assumption of a pure hydrogen plasma (at least away from the electrodes) is reasonable. Excellent agreement is achieved between these two temperature estimates.

The T_i^+ lines provide a further check on the temperature. Using the line ratio method[67] :-

$$\frac{I_1}{I_2} = \frac{g_{m1} A_1 \nu_1}{g_{m2} A_2 \nu_2} \exp\{-(E_{m1} - E_{m2})/KTe\}$$

where I is the line intensity W m^{-3}

g_m is the statistical weight of the upper state (m)

A is the transition probability in sec^{-1}

ν_1 is the line frequency

E_m is the energy of the upper state in Joules

Te is the electronic temperature in K

The appropriate spectroscopic values of g, A and E_m were obtained from NBS tables[73], and are tabulated in Appendix I.

Using T_i^+ lines which have the largest available difference in E_m:-

T_i^+ 326.160 nm E_m = 45,909 cm^{-1}

T_i^+ 339.458 nm E_m = 29,544 cm^{-1}

If $\frac{I_{326.160}}{I_{339.458}} = 1 \pm 100\%$

then Te = 6000 ± 1000 K

This is only half the previous estimates. Therefore using another pair:-

T_i^+ 328.77 nm $\quad E_m = 45{,}674\ cm^{-1}$

T_i^+ 338.376 nm $\quad E_m = 29{,}544\ cm^{-1}$

$$\frac{I_{328.77}}{I_{338.376}} = \frac{1}{1.5} \pm 50\% \qquad Te = 9050 \pm 1500\ K$$

A higher value is obtained but the consistency is poor. It should be noted that the values of the transition probabilities (A) may have an error in excess of ± 100%.[73] Several explanations of the above results are possible:-

1) Since the impurities Na, Ca, Mg, V and T_i presumably are derived from the electrodes, they must be released with the ablating carbon. The carbon vapour is emitted as a diffuse jet which may hardly interact with the main plasma column. Hence the carbon vapour and impurities may have a lower temperature.

2) Impurity inclusions in the electrodes may be emitted in sudden bursts as they become exposed. The impurities may be able to briefly reduce the plasma temperature due to their lower ionisation potentials.

8.4.3 Impurity Concentration in Plasma

An estimate of the T_i^+ concentration in the plasma column can be obtained by comparing the intensities of a suitable T_i^+ line to a C^+ line, and assuming a temperature of 13,000 K.

The absolute intensity of a spectral line is given by[67]:-

$$I_{mn} = A_{mn} (E_m - E_n)\, g_m \frac{N}{Q} \exp(-E_m/KTe)$$

where the terms are defined as above, except:

E_n is the energy level of the lower state in Joules

N is the number density in particles per m^3

Q is the internal partition function

The T_i^+ 338.376 nm line and the C^+ 283.67 nm line were used. Appropriate values of the constants were obtained from references[64, 65, 66]. Internal partition functions were obtained from Allen[72].

$$\frac{I_{mn}\ T_i^+}{I_{mn}\ C^+} = \frac{3.0}{5.6} \qquad \text{giving} \quad \frac{N_{T_i}^+}{N_{C^+}} = 4 \times 10^{-6}$$

It is unlikely that the T_i (or other metals) play any significant role in determining plasma temperature, or ion or electron concentrations. However, since all these metals have ionisation potentials far below carbon or hydrogen, they may still influence how the arc attachment moves over the electrode surfaces (where the gases are cooler).

8.4.4 Molecular Temperature

The ablated carbon vapour is believed to be mostly C_3 (at 4000 K). However no emission spectra of this molecule is observed (expected at 405 nm). Only the C_2 Swan system radiation can be used to provide any information on the excitation (temperature) of the carbon vapour.

8.4.4.1 C_2 Vibrational Temperature: The vibrational temperature of a molecule can be found by finding the slope $(\frac{1}{T})$ of the plot of $\ln\{I_{v'v''}/E^4_{v'v''}\ p(v', v'')\}$ against $G_{v'}/0.6925$ [67]

where $I_{v'v''}$ is line intensity

$E_{v'v''}$ is the energy difference of the transition $(v' \rightarrow v'')$

$p(v', v'')$ is the relative transition probability

$G_{v'}$ is the energy of the upper vibrational states (cm^{-1})

$$G_v = \omega_e(v + \tfrac{1}{2}) - \omega_e x_e(v + \tfrac{1}{2})^2 + \omega_e y_e(v + \tfrac{1}{2})^3$$

The vibrational constants for the C_2 A $^3\Pi g$ states were obtained from Herzberg[75].

Nicholls'[76] values of $p(v', v'')$ were used since they are 'smoothed' values of King's[77], who used the peak heights of the vibrational lines and used a grating spectrograph of 1.68 nm mm^{-1} dispersion (the instrument used for this work was 5 nm mm^{-1}). The (0,0), (0,1), (0,2), (1,0), (1,1), (1,2), (1,3), (2,1), and (2,0) band heads were used. Since the resolution is such that the overlapping rotational lines are partially resolved with the vibrational lines {(1,3), (1,2), (1,1), (2,1)}, the estimation of intensities is extremely difficult, see Figure 28 a,b,c,d. The results are plotted in Figure 29. The scatter in the results is such that a slope of best fit is difficult to place. An estimate gives a value of 6000 K, but the error is meaningless since a horizontal line (infinite temperature) could be fitted.

8.4.4.2: The C_2 Rotational Temperature: The C_2 rotational spectrum is sufficiently resolved to identify the P and R branches of the (1,0), (0,0), (0,1) and (0,2) bands[78, 79, 80]. The triplet structure of each line is not resolved, Figure 28 a,b,c,d.

The rotational temperature can be found by plotting

$$\ln(I_{j'}/S_{j'}) \text{ against } J'(J' + 1)$$

The slope is $-\frac{B_v}{KT}$ (67).

Here, $I_{j'}$ is the intensity of line j'

$S_{j'}$ is the strength factor for the state j',

B_v is the molecular coupling (81) constant given by:

$= Be - \alpha_e(v + \tfrac{1}{2}) + \ldots\ldots$

using Herzberg's values for the C_2 $A^3\Pi g$ state of Be = 1.7527 cm^{-1} and α_e = 0.01608 cm^{-1}(82), and so for the v' = 0 vibrational state;

$$B_v = 1.7446 \text{ cm}^{-1} = 3.46 \times 10^{-23} \text{ J}$$

Rotational - Vibrational Spectrum of C_2 (Swan band).

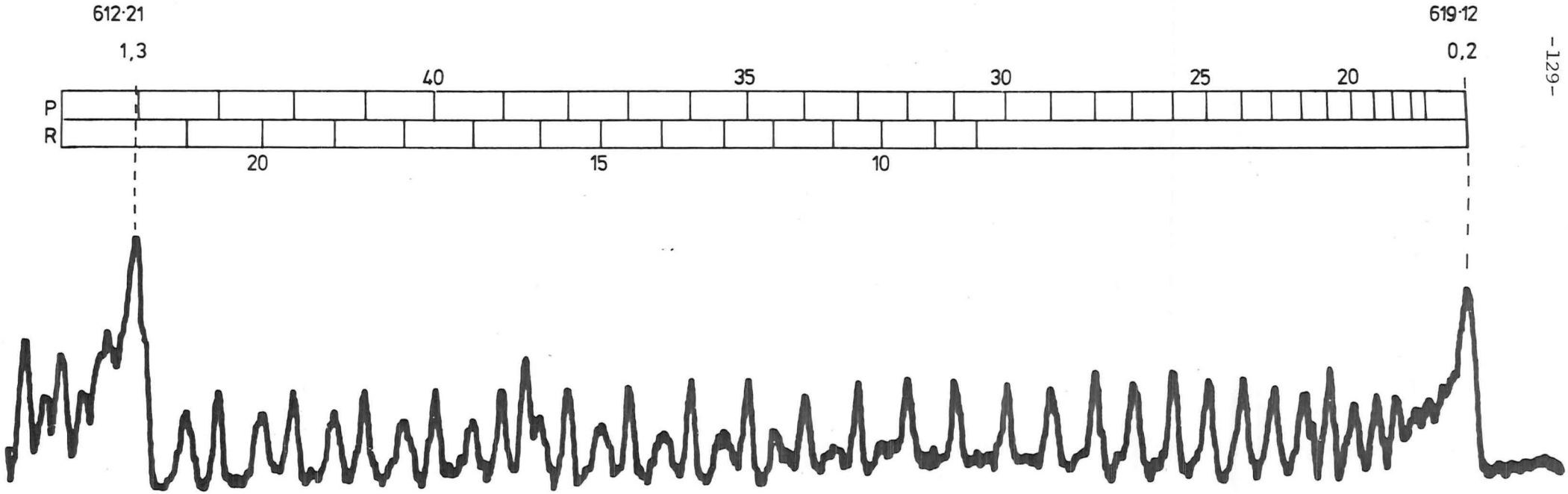

Figure 28 a.

Rotational C_2 Spectrum cont.

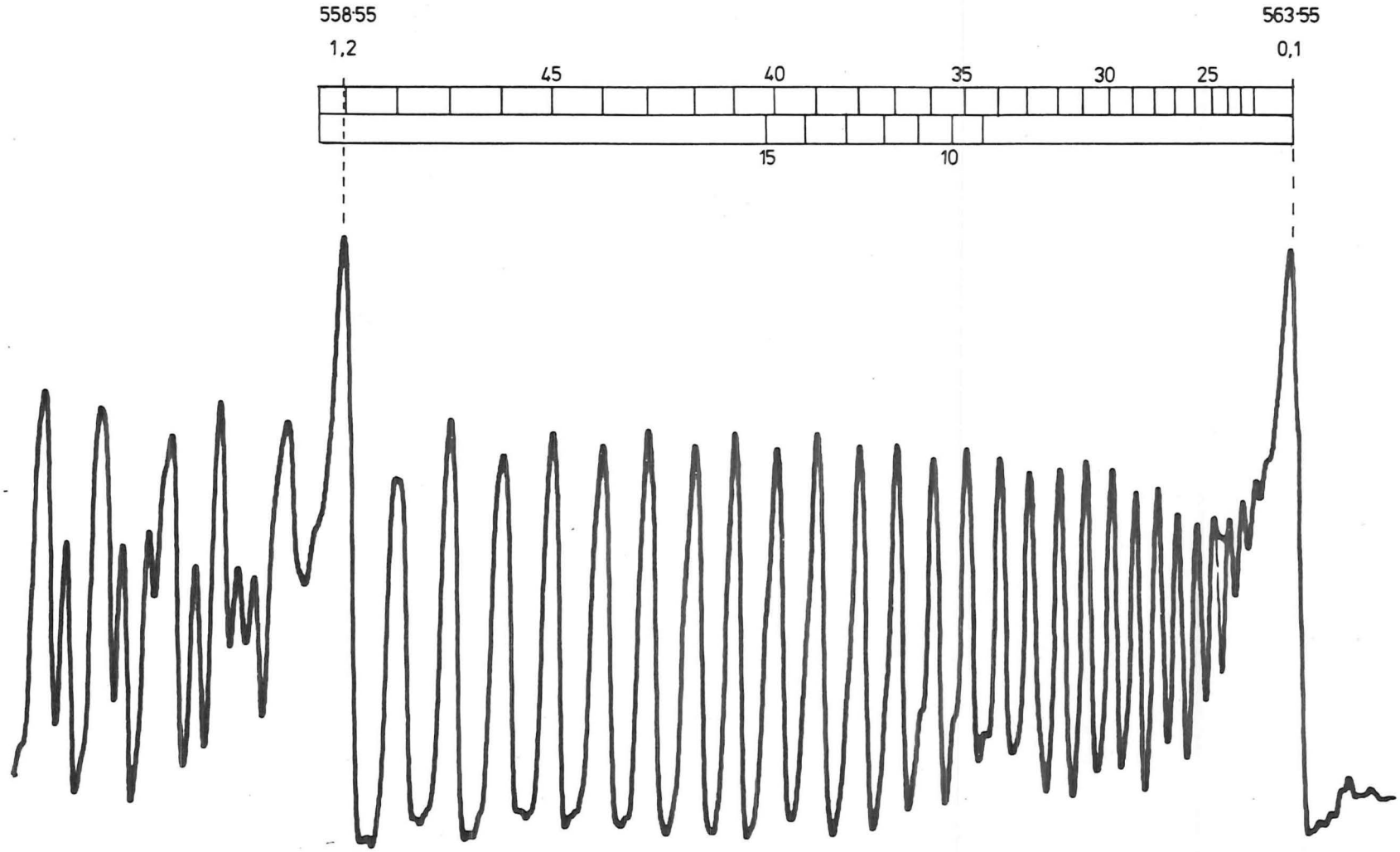

Figure 28 b.

Rotational C_2 Spectrum cont.

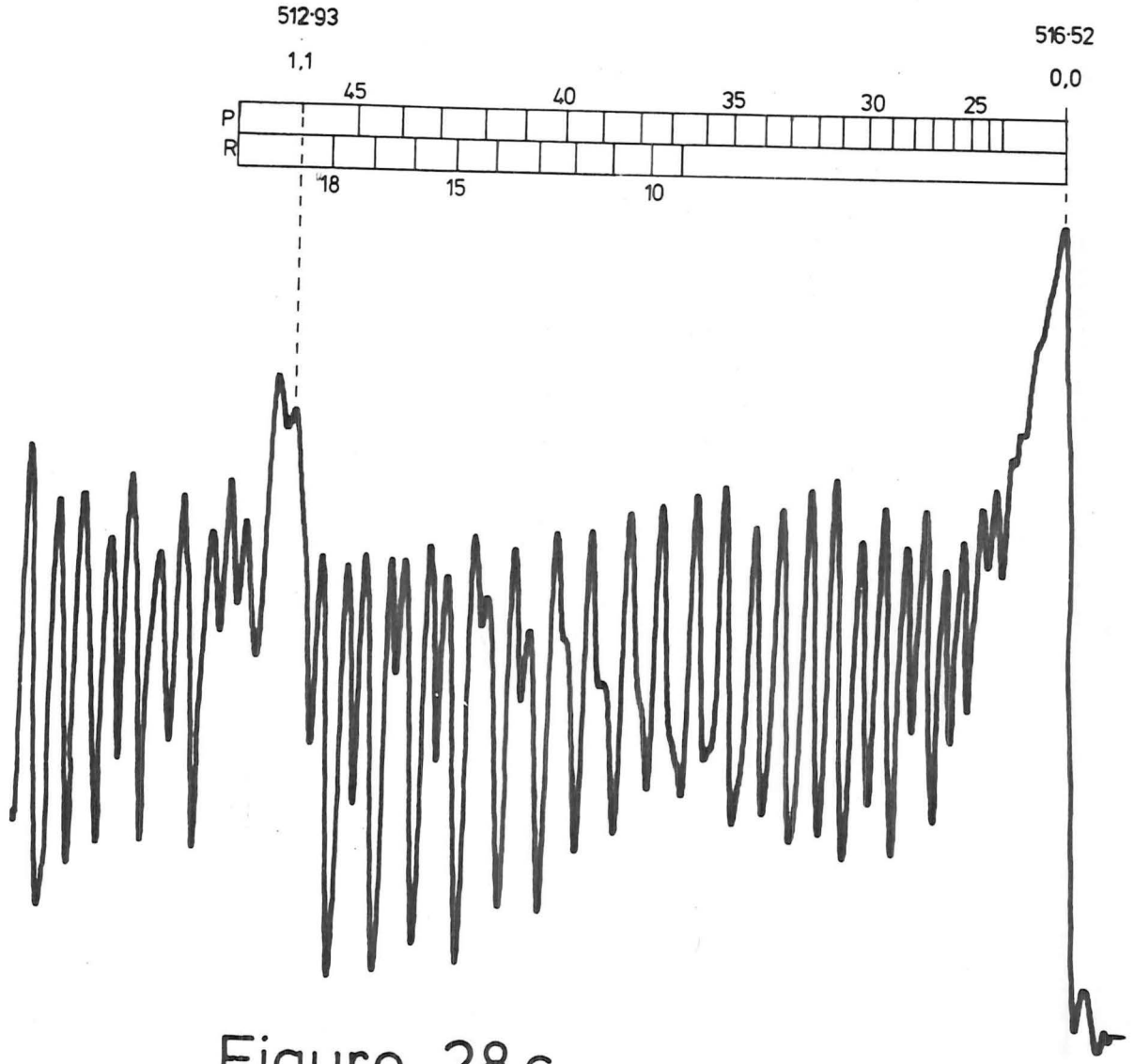

Figure 28c.

Rotational C_2 Spectrum cont.

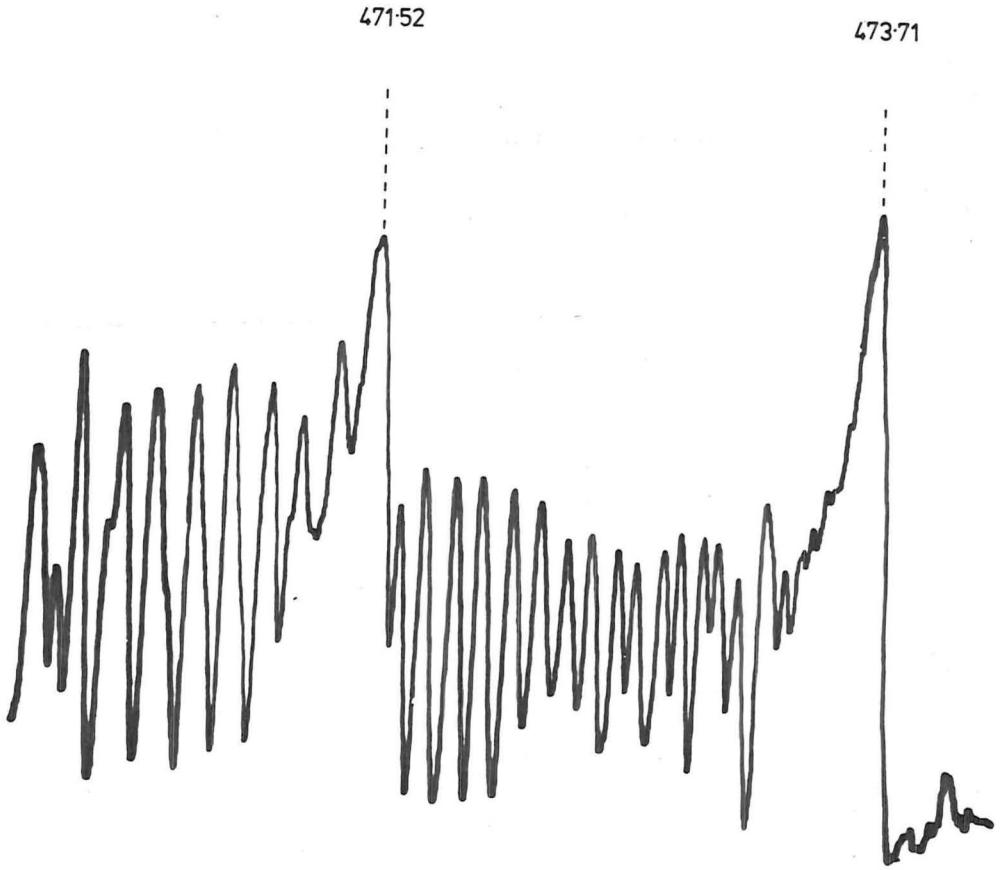

Figure 28 d.

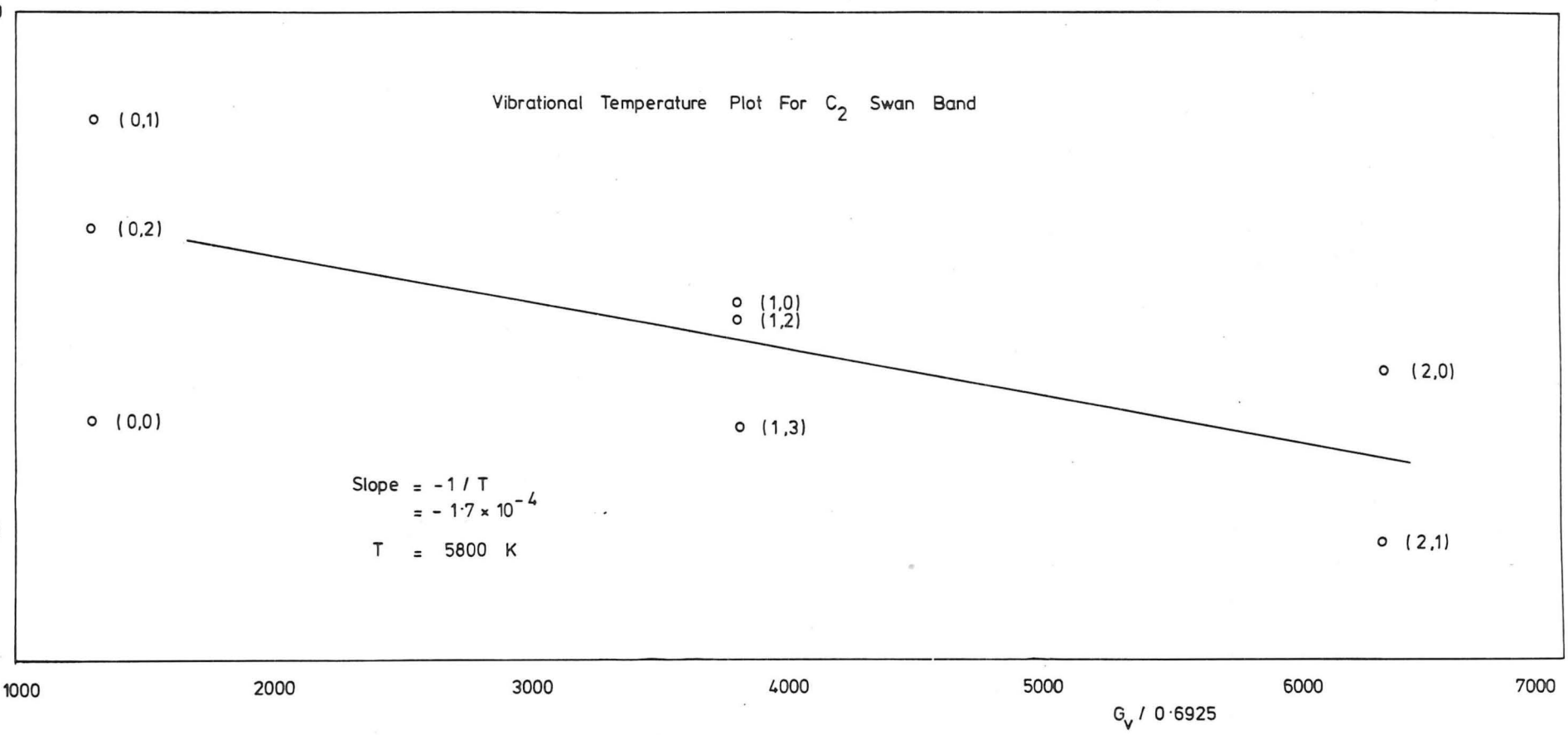
Vibrational Temperature Plot For C_2 Swan Band
0
- 1
- 2
$\ln (I_{v';v''} / E^4_{v';v''} . p(v';v''))$
(0,1)
(0,2)
(0,0)
(1,0)
(1,2)
(1,3)
(2,0)
(2,1)
Slope = - 1 / T
= - 1·7 × 10^{-4}
T = 5800 K
1000
2000
3000
4000
5000
6000
7000
G_v / 0·6925

Figure 29.

The wavelength interval of interest (P(46) to P(25)) is such that $\frac{1}{\lambda^4}$ varies only 2% over the interval, so that the frequency dependence of the rotational temperature plot can be ignored. The strength factors for the Swan system case $^3\Pi(b) \rightarrow {}^3\Pi(b)$ have been analysed by Budó [83]. However in the situation where the triplet splitting of the lines is not resolved, it is not clear what S_j, factors are appropriate. In this situation the Hönl-London formulae may be the most useful [84].

For the $^3\Pi - {}^3\Pi$ case $\Delta\Lambda = 0$, the Hönl-London factors are; for the P branch:

$$S_J^P = \frac{(J' + 1 + \Lambda')(J' + 1 - \Lambda')}{J' + 1}$$

and for the R branch:

$$S_J^R = \frac{(J' + \Lambda')\ (J' - \Lambda')}{J'}$$

Where J = rotational quantum number.
Λ = resultant orbital angular momentum quantum number.
(for the π state $\Lambda = 1$).

The results for the P branch are plotted in Figure 30. Once again a large amount of scatter is present, the experimental error could be at least ± 100%. The slope gives a rotational temperature of 3100 K.

For C_2H_2/O_2 flames at 1 bar C_2 rotational temperatures up to 6000 K have been measured [78].

It appears likely that the C_2 temperature is far less than the plasma column temperature. With the available data, little more can be concluded. The spatial profile of C_2 relative to the plasma axis would be most helpful in determining where the carbon is evolved. With a cylindrical steady arc column (both in magnitude and space), the Abel inversion could be used to show the radial C_2 profile is external to the hot arc column. Since the above conditions are far from being satisfied, the Abel inversion is unlikely to provide meaningful results.

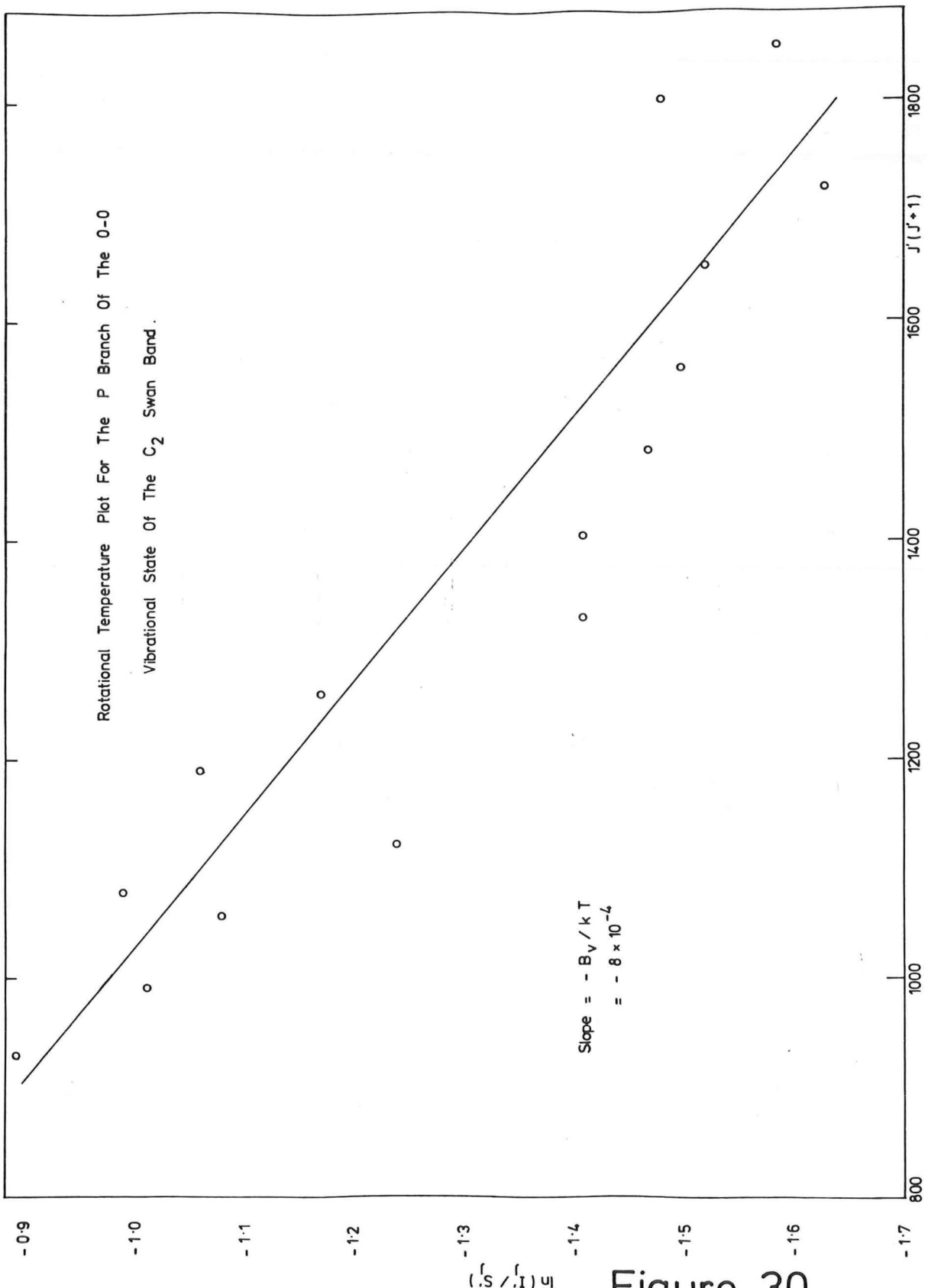
Rotational Temperature Plot For The P Branch Of The 0-0
Vibrational State Of The C_2 Swan Band.
Slope = $-B_v / kT$
$= -8 \times 10^{-4}$
$\ln(I'_J / S'_J)$
$J'(J'+1)$
-0·9
-1·0
-1·1
-1·2
-1·3
-1·4
-1·5
-1·6
-1·7
800
1000
1200
1400
1600
1800

Figure 30.

8.5 The Radiative Energy Balance

8.5.1 Procedure

The radiation from the reactor was imaged onto a Kipp and Zonen thermopile with a Sl UV lens (and window). By moving the thermopile in the vertical plane a small distance the relative radiances of the plasma immediately above the anode could be compared to that of the anode tip, for the same solid angle. The thermopile aperture had a diameter of 3 mm and the image was magnified 7 times. The transmission band width of the system was 180 nm to 3 μm.

It was found that the plasma intensity was 1/5 that of the anode tip. It will be assumed that the anode tip was at a black body temperature of 3950 K (section 7.3.4).

8.5.2 Individual Components of the Emitted Radiation

The arc column will be assumed to be at 13,000 K and have a diameter of 5 mm[88], and be composed of an equilibrium carbon-hydrogen plasma. The molar C/H ratio in the plasma is assumed to be the same as the mean overall C/H ratio for the reactor.

The absolute emission of a spectral line was given in section (8.4.3) and the spectroscopic constants are listed in Appendix I.

8.5.2.1 Atomic Carbon: The only significant line of carbon is the C^o line at 247.86 nm. If the C^o number density is 1.6×10^{22} m^{-3} for a C/H molar ratio of 0.09[71], then the volumetric emission (I_{mn}) is 2.5×10^9 $W\ m^{-3}$.

8.5.2.2 Atomic Hydrogen: Assuming an atomic hydrogen number density of 4×10^{23} m^{-3} then:-

for H_α $I_{mn} = 1.0 \times 10^9$ $W\ m^{-3}$

H_β $I_{mn} = 0.25 \times 10^9$ $W\ m^{-3}$

H_γ $I_{mn} = 0.1 \times 10^9$ $W\ m^{-3}$

The sum of the rest of the Balmer series $\simeq 0.2 \times 10^{9}$ W m^{-3}.

The Paschen and higher series up to 3 μm:

$$P_{\alpha} = 0.07 \times 10^{9} \text{ W m}^{-3}$$

(The contribution of the higher members of the Paschen series is estimated to total):-

$$\Sigma P_{\beta} \text{ and higher terms} \simeq 0.1 \times 10^{9} \text{ W m}^{-3}$$

8.5.2.3 Hydrogen Bremsstrahlung Radiation: Spectral Bremsstrahlung radiation for hydrogen is given by[67]:

$$B_{\lambda} = \{(2.68 \times 10^{13} \, p^{2})/\lambda^{2} \, Te^{5/2}\} \, e^{-(1.44 \times 10^{8})/\lambda Te} \text{ W m}^{-3} \, ^{o}\text{A}^{-1}$$

p is partial pressure of electrons in Pascals

Te is electronic temperature K

λ is wavelength in angstroms

Using p = 17,500 Pa, and Te = 13,000 K, then

$$B_{\lambda} = \frac{4.26 \times 10^{11}}{\lambda^{2}} \, e^{\frac{11077}{\lambda}}$$

$$B = \int_{1,800}^{30,000} \frac{4.26 \times 10^{11}}{\lambda^{2}} \, e^{\frac{-11,077}{\lambda}} \, d\lambda$$

integrating by the trapezoidal rule:

$$B \simeq 4 \times 10^{7} \text{ W m}^{-3}$$

8.5.2.4 Ratio of Recombination to Bremsstrahlung Intensity for H^{+} and electron recombination is given by the relationship[67]:

$$R = 3.16 \times 10^{5} \sum_{n1}^{n2} \frac{\exp(\chi_{n}/KTe)}{n^{3} \, Te}$$

where χ_{n} is the ionisation energy of the nth shell and Te is the electron temperature.

Table 7

Recombination Radiation Data

n	χ_n (eV)	χ_n (J)
2	13.60 - 10.2	5.44×10^{-19}
3	13.60 - 12.09	2.416×10^{-19}
4	13.60 - 12.75	1.36×10^{-19}
5	13.60 - 13.05	8.8×10^{-20}

For the case of recombination radiation between the Lyman series limit (91.2 nm) and the Balmer series limit (364.6 nm) and Te = 13,000 K

$$R = 3.16 \times 10^{5} \left(1.99 \times 10^{-4} + 1.1 \times 10^{-5} + 2.6 \times 10^{-6} \ldots\right) = 67$$

For the case between the Balmer series limit and the Paschen series limit (820 nm) and Te = 13,000 K

$$R = 3.16 \times 10^{5} \left(1.1 \times 10^{-5} + 2.6 \times 10^{-6} \ldots\right) = 4.3$$

Total recombination energy below 364.6 nm

$$I = 67 \times \int_{1800}^{3646} B\lambda \, d\lambda$$

$$= 67 \times 4.26 \times 10^{11} \times \int_{1800}^{3646} \frac{e^{\frac{-11077}{\lambda}}}{\lambda^2} \, d\lambda$$

$$= 67 \times 4.26 \times 10^{11} \times 4 \times 10^{-6} \text{ W m}^{-3}$$

$$= 1.1 \times 10^{8} \text{ W m}^{-3}$$

Total recombination energy between 364.6 nm and Paschen series limit

$$I = 4.3 \times \int_{3646}^{8203} B\lambda \, d\lambda$$

$$= 4.3 \times 4.26 \times 10^{11} \int_{3646}^{8203} \frac{e^{\frac{-11077}{\lambda}}}{\lambda^2} \, d\lambda$$

$$= 4.3 \times 4.26 \times 10^{11} \times 1.88 \times 10^{-5} \text{ W m}^{-3}$$

$$= 0.34 \times 10^{8} \text{ W m}^{-3}$$

The Recombination radiation beyond Paschen series will be considered negligible.

8.5.2.5 C_2 Molecular Radiation: The Planck mean absorption coefficient for C_2 is given as 0.5 cm^{-1} mole frac.$^{-1}$[85] at 5000 K and 1 bar. (The Planck mean absorption coefficient for C_3 is given as 2.0 cm^{-1} mole frac.$^{-1}$). The equilibrium mole fractions of C_2 and C_3 are estimated by Duff and Bauer[33]. For a C/H mole ratio of 0.1[71], pressure of 1 bar and temperature of 5000 K outside the arc column, C_2 = 3.5 x 10^{-3} molar fraction, and for C_3 = 1.5 x 10^{-4} mole fraction. (If C_2 radiation is not significant, C_3 radiation will be neglected, and is additionally justified by its absence on the observed spectrum.)

Therefore the Planck mean absorption coefficient for C_2 is:

$$K_p = 0.5\ cm^{-1}\ mf^{-1} \times 3.5 \times 10^{-3}\ mf \times 100\ cm\ m^{-1} = 0.175\ m^{-1}$$

The C_2 volumetric emission is given by[86]:

$$I_{C_2} = 4K_p\, e_b(T)\ W\ m^{-3}$$

where $e_b(T)$ is the black body radiance

and K_p is the Planck mean absorption coefficient

$$I_{C_2} = 4 \times 0.175\ m^{-1} \times 5.66 \times 10^{-8}\ W\ K^{-4}\ m^{-2} \times 5000^4\ K$$
$$= 2.5 \times 10^7\ W\ m^{-3}$$

This is small compared with other items and so C_3 radiation will be ignored.

8.5.2.6 The Total Volumetric Emission: The total radiative energy expected will be:

C^o	=	2.5 x 10^9 W m^{-3}
H_α	=	1.0 x 10^9 "
H_β	=	0.25x 10^9 "
H_γ	=	0.1 x 10^9 "
Σ H remainder	=	0.4 x 10^9 "

Bremsstrahlung = 4×10^{7} W m^{-3}

Recombination (total) = 1.4×10^{8} W m^{-3}

C_2 = 2.5×10^{7} W m^{-3}

Total = 4.455×10^{9} W m^{-3}

8.5.2.7 Anode Tip Radiation: The anode tip radiation will be given by:

$$I_{anode} = \int_{180\ nm}^{3.0\ \mu m} e_{\lambda b}\, d\lambda \text{ W } m^{-2} \text{ at } 3950 \text{ K}$$

(integrated over the window transmission)

where $e_{\lambda b}$ is the Planck radiation function. This relationship can be evaluated by using Kreith's chart[87].

Received radiation is 94% of total black body radiation, so that:

$$I_{anode} = 0.94 \times 5.66 \times 10^{-8} \times 3950^{4}$$
$$= 1.29 \times 10^{7} \text{ W } m^{-2}$$

The 'projected' plasma radiance is 1/5 of 1.3×10^{7} W m^{-2}, namely, 2.6×10^{6} W m^{-2}.

8.5.3 Moving Plasma Exposure Probability

Probability of the arc column residing over the spectrograph slit will be estimated.

In order to relate the absolute volumetric emission, calculated above, to the intensity measured by the thermopile, it is necessary to estimate the fraction of time the plasma column resides over the thermopile aperture. (High speed photographs have shown that the arc moves over a large area, relative to the anode.) This time fraction (or probability) will be estimated by determining the probability the plasma column is over the spectrograph slit. (Both the thermopile and spectrograph apertures

are small compared to the magnified image of arc column.) This will be done by comparing the mean emissive powers of the H_α, H_β and H_γ lines to the spectral emissive power of the anode tip at a black body temperature of 3950 K. The absolute emissive powers of each of the hydrogen lines has been estimated in the previous section. The optical geometry is such that a simple lens projects an image onto the spectrograph slit assembly. The solid angle of the rays captured is defined by the lens aperture.

8.5.3.1 The Anode: If the anode has a spectral emissive power of E_λ W m^{-2} m^{-1}, then the power captured by the lens solid angle is $E_\lambda \frac{\omega}{2\pi}$ W m^{-3}, where ω is the solid angle in steradians. If the image has a magnification, m, then the image brightness will be $E_\lambda \frac{\omega}{2\pi} \frac{1}{m^2}$ W m^{-2} m^{-1}.

8.5.3.2 The Plasma: The plasma has a volumetric emission coefficient of $\frac{I_{mn}}{4\pi}$ W m^{-3} sr^{-1}, and a solid angle ω is captured by the lens,

$$\frac{I_{mn}}{4\pi} \omega \text{ W } m^{-3}$$

The plasma column will be considered to be a 'flexible cylinder' of radius 2.5×10^{-3} m. This is consistent with the high speed photograph results and of other measurements of hydrogen arc columns[88]. The plasma emissive power captured by the lens per metre of arc is:

$$\frac{I_{mn}}{4\pi} \omega \pi r^2 \text{ W } m^{-1}$$

Assuming the plasma has a projected width equal to $\sqrt{\pi r^2}$, then the screen intensity

$$= \frac{I_{mn}}{4\pi} \omega \frac{\pi r^2}{\sqrt{\pi r^2}} \cdot \frac{1}{m^2} \text{ W } m^{-2}$$

If $\Delta\lambda_{\frac{1}{2}}$ is the line half width in m, then the mean spectral screen intensity

$$= \frac{I_{mn}}{\Delta\lambda_{\frac{1}{2}}} \frac{\omega}{4\pi} \cdot \frac{\pi r^2}{\sqrt{\pi r^2}} \cdot \frac{1}{m^2} \text{ W } m^{-2} \text{ } m^{-1}$$

then if P is the fraction of time the column resides over the slit, then:

$$\frac{\frac{I_{mn}}{\Delta\lambda_{\frac{1}{2}}} \frac{\omega}{4\pi} \cdot \frac{\pi r^2}{\sqrt{\pi r^2}} \cdot \frac{1}{m^2} \cdot P}{E_\lambda \frac{\omega}{2\pi} \cdot \frac{1}{m^2}} = \frac{\frac{I_{mn}}{\Delta\lambda_{\frac{1}{2}}} \cdot P \cdot \frac{\sqrt{\pi}\, r}{2}}{E_\lambda}$$

and is equal to:

$$\frac{\text{an integrated spectrum mean line intensity}}{\text{anode spectral intensity at } \lambda}$$

For $r = 2.5 \times 10^{-3}$ m, T_{plasma} = 13,000 K, 1 bar

Table 8: Hydrogen spectral and anode spectral data for slit probability.

	I_{mn} (W m^{-3})	$\Delta\lambda_{\frac{1}{2}}$ (m)	E_λ (W m^{-2} m^{-1})	$\frac{I_{mn}}{\Delta\lambda_{\frac{1}{2}}} \cdot \frac{\sqrt{\pi}}{2} \cdot r/E_\lambda$
H_α	1.0×10^{9}	1.0×10^{-9}	1.2×10^{13}	185
H_β	0.25×10^{9}	4.5×10^{-9}	7.2×10^{12}	17
H_γ	0.1×10^{9}	4.5×10^{-9}	5.5×10^{12}	7.1

8.5.3.3 Hydrogen Balmer/Anode Spectral Intensity Ratios:

The α, β and γ lines were integrated by dividing the α line into 16 slices 0.375 nm wide and the β and γ lines into 20 slices 0.75 nm wide.

The values of mean line spectral intensity to anode spectral intensity are:-

$$H_\alpha \qquad \frac{I_{\lambda mean}}{E_\lambda} = 12.0$$

$$H_\beta = 4.1$$

$$H_\gamma = 2.4$$

Therefore:

$$185 \times P_\alpha = 12 \qquad P_\alpha = 0.065$$

$$17 \times P_\beta = 4.1 \qquad P_\beta = 0.24$$

$$7.1 \times P_\gamma = 2.4 \qquad P_\gamma = 0.34$$

8.5.3.4 The Plasma-Slit Coincidence Probability. The thermopile aperture is 3.5 mm diameter compared to the slit width of 32 μm. However both are still small compared to the projected arc column (25 mm). Therefore P = 0.25 will be used for the probability the arc column resides over the thermopile aperture. This value is reasonable because the arc column of 5 mm diameter can move 1 to 2 cm either side of the vertical anode axis.

8.5.4 The Total Radiation Balance

The total estimated radiation emitted was 4.5×10^{9} W m^{-3}. Converting this to the projected intensity (W m^{-2}):

$$4.5 \times 10^{9} \times \frac{\sqrt{\pi}}{2} \times 2.5 \times 10^{-3} \times 0.25 \quad \text{W m}^{-2}$$

$$= 2.5 \times 10^{6} \text{ W m}^{-2}$$

The anode radiation was calculated in section (8.5.2.7) to be 1.29×10^{7} W m^{-2}, and the projected plasma intensity was measured as 1/5 of this, namely, 2.6×10^{6} W m^{-2}.

Therefore the agreement between the estimated total radiation and the total measured radiation is excellent and is much closer than the expected error.

8.6 Optically Thick H_α

The above analysis has assumed that the radiation from the 5 mm arc column is optically thin. This may not be so for the H_α and C^o (247 nm) lines.[113] (The low value of exposure probability for the H_α is a clue that this may not be so.) Since the 3950 K anode radiation is not recorded for the C^o line, it cannot be checked. For the H_α line, from experiment;

$$\frac{I_{\lambda mean}}{E_\lambda} = 12$$

The spectral radiance at 13,000 K and 656 nm (H_α line) for a black body plasma is:

$$E_{\lambda\alpha} = \frac{3.741 \times 10^{-16}}{(656 \times 10^{-9})^5 \left(e^{\frac{0.01439}{656 \times 10^{-9} \times 13000}} - 1\right)}$$

$$= 7.0 \times 10^{14} \text{ W m}^{-2} \text{ m}^{-1}$$

At 3950 K and 656 nm:

$$E_\lambda = 1.2 \times 10^{13} \text{ W m}^{-2} \text{ m}^{-1}$$

Therefore the expected ratio will be: (using P = 0.25)

$$\frac{E_{\lambda\alpha}}{E_\lambda} \cdot P = \frac{7 \times 10^{14} \times 0.25}{1.2 \times 10^{13}} = 14.6$$

as compared to 12 (measured). It can be concluded that the H_α line is an optically thick emitter. This provides further evidence that the plasma column temperature is close to 13,000 K. This also explains why the probability calculated for H_α was significantly lower than the H_β and H_γ values. The H_β and H_γ values are not likely to come from optically thick lines since the black body spectral radiances at these wavelengths will be greater, while the anode radiance and measured ratios are all smaller.

At 247 nm the ratio $\frac{E_{\lambda 13000 \text{ K}}}{E_{\lambda 3950 \text{ K}}}$ would be approximately 30,000, making an optically thick C^o line impossible to check.

8.7 Particulate Carbon Loss from the Anode

8.7.1 Carbon Arc in Air

When the carbon arc is operated with sufficient current density to cause significant ablation, an incandescent anode flame is observed when operating in air or inert gases[89]. This flame is believed to be caused by a stream of ablating carbon particles[91].

8.7.2 Carbon Arc in Hydrogen

In the case of our high current arc operating in hydrogen no such luminous flame phenomenon is observed, whether by visual appearance, fast colour photographs (1 ms exposure), high speed photographs (0.1 ms exposure), or by spectroscopic examination.

8.7.2.1 Radiation Profiles about the Anode Tip: The visible spectrum was scanned at a number of wavelengths so as to examine the spatial relationship of the spectral intensities in the neighbourhood of the anode tip-plasma interface. This was done at wavelengths corresponding to the maximum intensities of the H_α, H_β, C_2 0-2, and C_2 0-1 lines. The background intensity was obtained at a nearby wavelength that was free of discernible spectral features. See Figures (31, a, b, c,d). From the profiles, it can be seen how the anode black-body radiation falls off at the supposed anode tip, and also how the atomic hydrogen and C_2 concentrations behave around the anode tip. For both species, very little plasma radiation originates below the anode tip. This is consistent with the high-speed photographs, showing the arc attachment shooting down the anode for an insignificant proportion of the time. Therefore a temperature estimate of the anode tip region, relative to the Standard Arc, using the thermopile, is meaningful. It should be noted that the anode radiation decays very sharply at the anode tip (in less than 0.2 mm) to approximately 1/7 of the tip value for the H_α line. It can be concluded that any continuous radiation associated with particulate carbon around the anode tip contributes less than 1/7 of the tip intensity. However, all the background cannot be prescribed to particulate radiation. Sources of non-spectral radiation present which contribute to the background are, non-resolvable high order molecular lines of C_2 and H_2, reactor wall radiation ($\simeq$2000 K), Bremsstrahlung radiation, as well as stray light due to the exposure being taken in daylight.

Plate 1.

Close-up still photographs of High Intensity Carbon-Hydrogen Arc.

200 A nominal current with vertical 9·5 mm anode. Kodachrome 25 film, Takumar 50mm f4 macro lens at f 22, No. 1 extension ring, 2 Nikon 8X neutral density filters. shutter speed: left column, 1/1000s, right column, 1/500s.

Note anode grooves and variation of plasma colour, position and intensity.

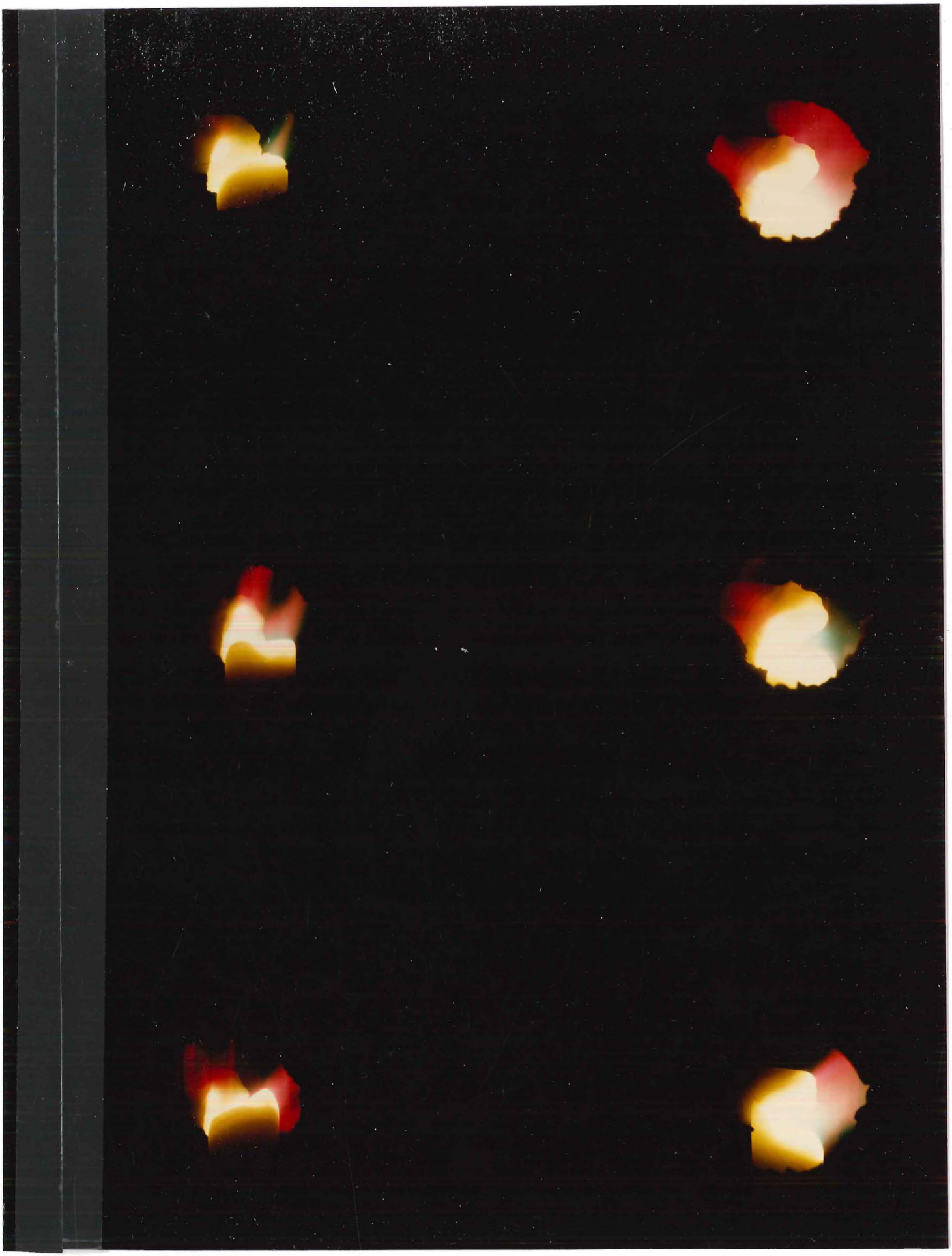

Anode - Plasma radiation profile at :

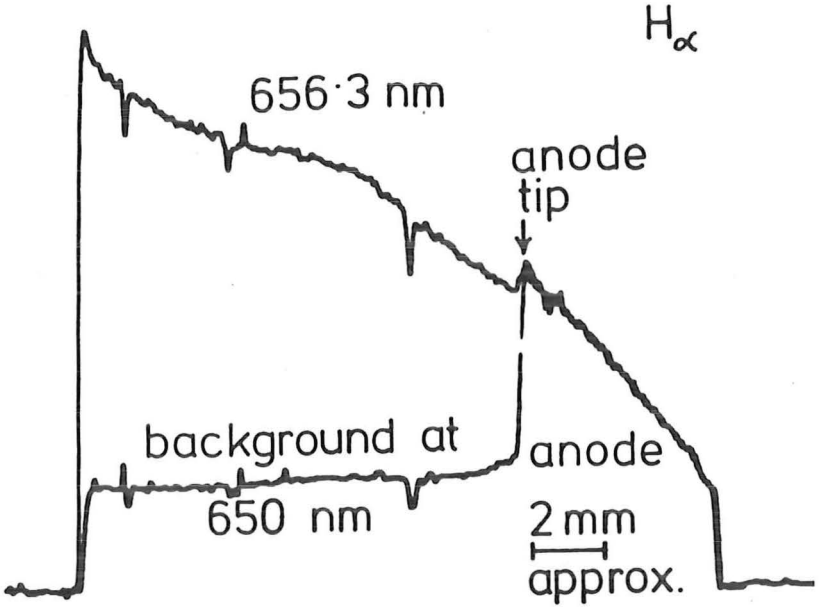

Figure 31a.

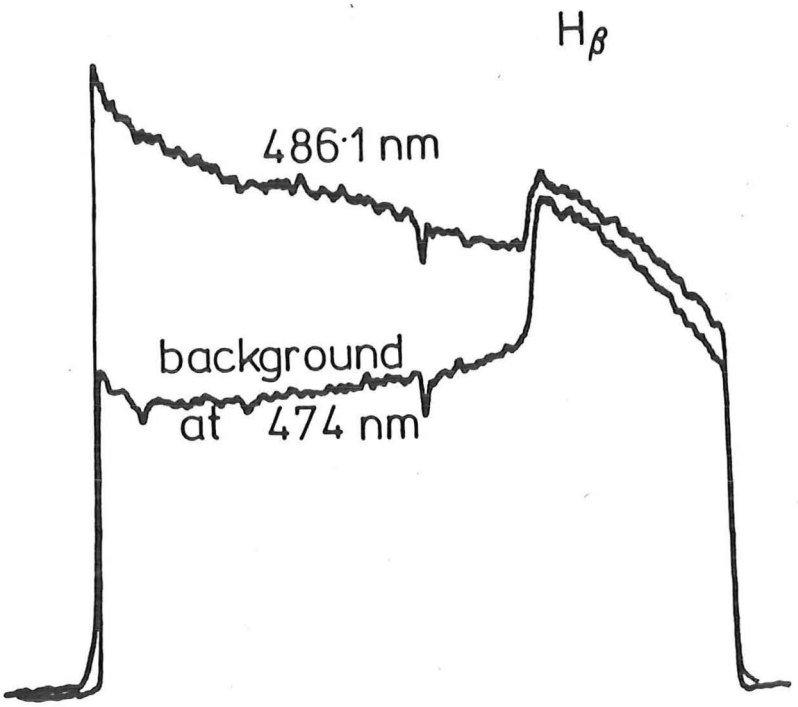

Figure 31b.

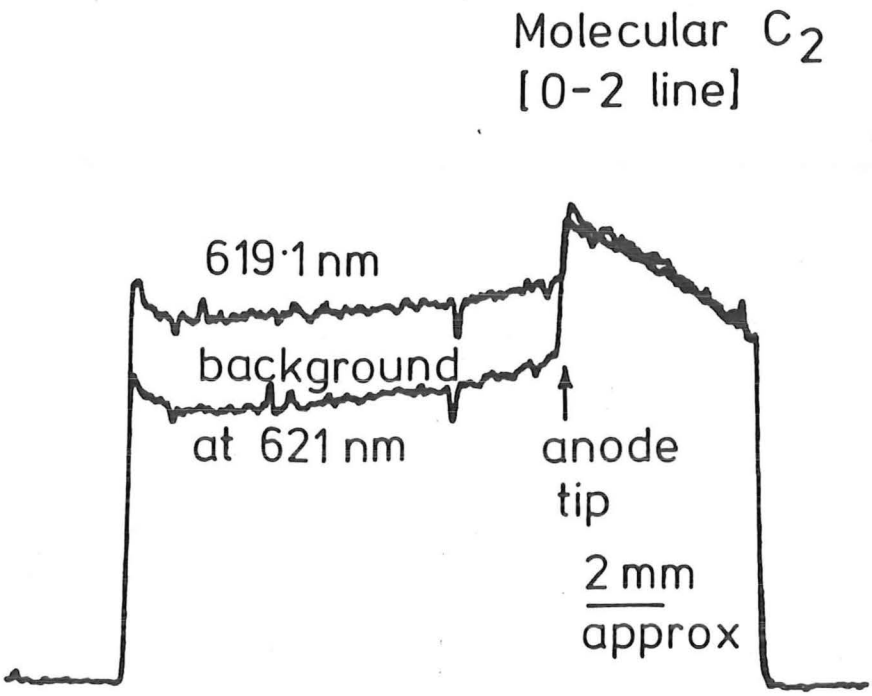

Figure 31 c.

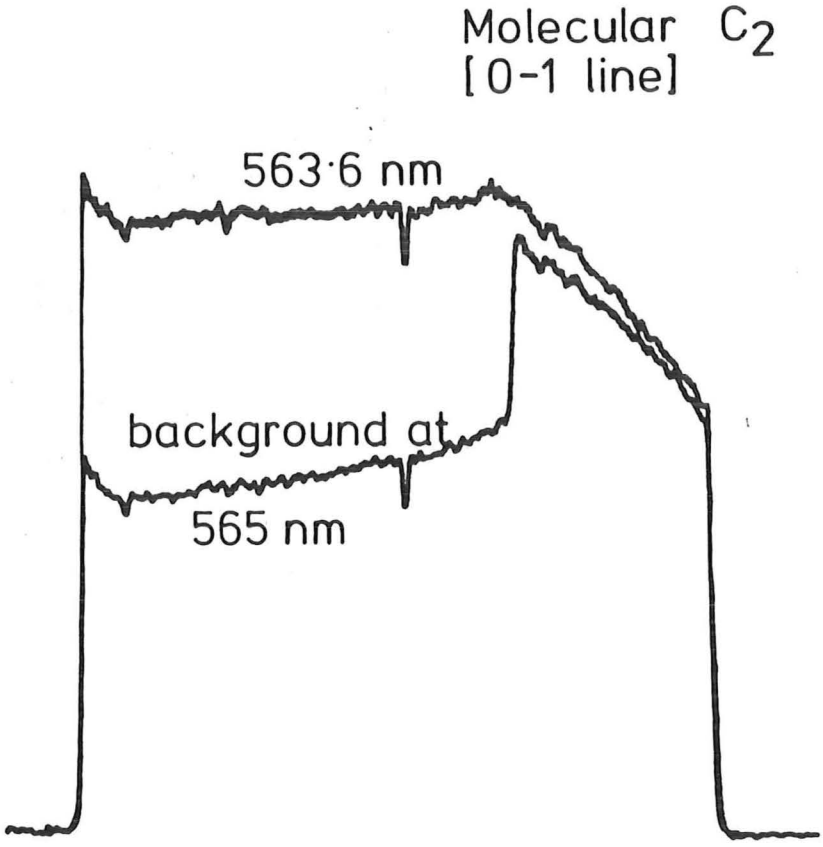

Figure 31 d.

It is also significant to notice that the C_2 profiles have almost constant intensities for about 5 mm beyond the anode (Figures 31, c and d). A very small amount of C_2 originates 1 to 2 mm back from the anode tip. This would be expected from carbon close to its sublimation temperature. The atomic hydrogen radiation starts sharply at the anode tip and increases to the edge of the spectrum, see Figure 31a. Figure 31b is not quite so convincing, but it should be noted that the H_β line is so wide that the anode radiance has changed significantly at the comparison wavelength.

The thermopile measurements will be used to place a limit on the amount of particulate carbon ejected more than a few 100 μm into the gas above the anode.

8.7.3 Quantitative Estimate of Particulate Radiation

The 7.9 mm diameter graphite anode operating at 286 A, ablates 1.1×10^{-4} kg/sec of carbon. It will be assumed that the temperature of this ablated material immediately above the anode surface is 4000 K and the stream is composed of 90% carbon vapour (C_3) and 10% particles. The particles are assumed to be 20 nm in diameter. (This is consistent with the author's transmission electron micrograph examination of the surface material of graphite and carbon anodes[90], the arguments of Abrahamson[91] and typical particle sizes found in hydrocarbon flames.[112])

The mean velocity of C_3 away from the anode face, (assuming an ideal gas), would be 19 m sec^{-1}. The particles (density 2000 kg m^{-3}) would be generated at the rate of 1.3×10^{15} sec^{-1}. The particle concentration would be 1.4×10^{18} m^{-3}. The radiant intensity of such a cloud is given by:

$$I = \int e_{\lambda b} (1 - e^{-a_\lambda S}) \, d\lambda \quad W\, m^{-2} \quad (92)$$

where $e_{\lambda b}$ is the Planck spectral intensity W m^{-2} m^{-1}, a_λ is the spectral

absorption coefficient, and S is the optical path length, which in this case will be assumed to be equal to the anode diameter, 8×10^{-3} m.

$$a_\lambda = E_\lambda A N$$

where E_λ is the spectral absorption efficiency factor

N is the particle density,

A is the particle cross sectional area.

Values of E_λ have been calculated by Wickramasinghe[93] for 20 nm carbon spheres. AN has the value 443 m^{-1}. Integrating over the optical system band width:

$$I = \int_{180\ nm}^{3.0\ \mu m} e_{\lambda b} \left(1 - e^{-443 \times 8 \times 10^{-3} E_\lambda}\right) d\lambda$$

Integration by the trapezoidal rule yields:

$$I = 7.1 \times 10^{6}\ W\ m^{-2}$$

The 3950 K anode radiance is:

$1.3 \times 10^{7}\ W\ m^{-2}$.

The total plasma radiation was measured as 1/5 of this, namely, $2.6 \times 10^{6}\ W\ m^{-2}$. If it is assumed that the particles are ejected from all over the anode tip, then the radiation from them will be independent of the sampling probability. But all of this ($2.6 \times 10^{6}\ W\ m^{-2}$) has been accounted for in the radiation balance, by atomic and molecular features, to an agreement of 10%. Therefore 10% particle loss is far too high a value, and 1% would be a realistic upper limit for particle mass loss from the anode and carried beyond 200 μm of the tip, see section (8.7.2.1).

8.8 Total Plasma Radiation Loss

The total radiative power loss from the plasma column in the arc will now be estimated.

reactor/ It was estimated above, that the total volumetric emission of radiation from the C/H plasma was 5×10^{9} W m^{-3}. If the plasma has a diameter of 5×10^{-3} m, then the power loss per metre is 98 kW m^{-1}. If an average arc length of 2 cm is assumed, then the total power radiated would be 1700 W, which is about one fifth of the total power dissipated in the arc column - 200 A x a plasma voltage drop of 40 V is $\simeq$ 8 kW.

8.9 Conclusions

The ultraviolet and visible spectrum of the carbon-hydrogen plasma consists of neutral and ionized lines of carbon, hydrogen Balmer lines, various metal impurity lines and the extensive C_2 Swan molecular bands. Molecular bands of CN are absent, confirming negligible air in the reactor. Molecular CH bands are absent, but no reasonable explanation can be provided, similarly C_3 bands are absent, even though they are a dominant species in a carbon-hydrogen equilibrium at 4000 K.

The 200 A arc has a core temperature of 13,000 K and an electron density of about 1×10^{23} m^{-3}. This is consistent with local thermodynamic equilibrium existing in the plasma. The spectral radiance of the plasma has been integrated over the range 190 - 3000 nm. Individual components of the spectrum have been quantitatively estimated and provide a satisfactory radiation balance. (By comparing the absolute emissive powers of the hydrogen Balmer lines to the 3950 K black body radiance of the anode tip at the same wavelengths, it was concluded that the plasma column resided over the spectrograph and thermopile apertures, 25% of the exposure time.)

The radiation balance provides additional strong evidence that carbon particles are consumed almost entirely (>99%) very close to the ablating anode tip in the case of the carbon-hydrogen arc.

The total plasma radiative power of 1700 W is approximately one-fifth of the total plasma dissipative power of about 8 kW.

9. CONCLUSIONS AND RECOMMENDATIONS

9.1 Ablation

The ablation of carbon materials has been studies in the Ward reactor over a wide range of currents (100-300 A) and current densities (1-15 A mm^{-2}). The power supply has the potential to provide probably in excess of 400 A. If it was decided to utilize the supply fully then a reactor would have to be designed which could dissipate about 30 kW of heat. The rectifier diode ratings would have to be carefully examined and extensive alterations could be required. Anodes of 7.95 mm diameter are the smallest that can be effectively joined end for end. This limitation would be crucial at high currents and high current densities.

Further ablation data would be used to improve Abrahamson and Davies'[107] estimates of enthalpy of vaporization, anode voltage drop, and thermal conductivity of carbon. However current densities of 15 A mm^{-2} (or more) may be academically useful, but are very unlikely to have industrial scale application. The constraint of resistive heating of the electrode precludes any process except extremely inefficient current densities of order 1 A mm^{-2}, if an ablating carbon electrode is used.

9.2 Coal Anodes

Extruded coal electrodes present immense difficulties. Their use cannot be considered until it is satisfactorily demonstrated that a rod of partially coked coal can be continuously heated and degassed to a temperature where graphitisation is rapid (in the order of minutes). If it can withstand the stresses of this treatment, it must still be strong enough to survive heating to 4000 K without fracturing or *significant* crumbling.

9.3 Graphite Sublimation Temperature in Hydrogen

The electrode tip temperature has been estimated (3900 - 4000 K, $\varepsilon = 1$). This could be usefully studied in far greater detail than has been possible in this work. Spectral examination of the tip radiance at a number of wavelengths, relative to the Standard Arc, would help to reduce the uncertainty of the sublimation temperature of graphite in hydrogen. See Appendix (IV) for details.

9.4 Arc Dynamics

The motion of the arc has been investigated to the limit of the department's measuring equipment available at the time. The origin of violent arc transients has only been speculated upon. If the phenomena is to be understood, simultaneous current and voltage (unfiltered) waveforms would be required. This requires a suitably fast storage oscilloscope. This data must be related to the visual behaviour of the arc. This can only be achieved by using a shutter speed more than ten times faster than the present high speed camera (100 μs). This would require the use of image converter devices.

9.5 Reactor Design

The temperature of the graphite reactor wall has not been properly investigated. It is desirable to maximise this. The ablation rate should be increased by re-radiation for a given current density. The rate of carbon deposition would probably be reduced, and the gas enthalpy into the quench increased. It may be possible to operate at substantially higher C/H ratios. These aspects have not been studied, and would require careful study if a larger scale reactor was ever envisaged.

It has been assumed by Abrahamson and Ward that a vertical anode reactor, with the gases travelling upwards, is the most logical. It is probable that arc stability would be increased by inverting the reactor. In the inverted configuration arc convective forces would be counteracted by the bulk gas flow. Higher gas rates should be possible without arc blow-out. This would require a major rethink on quenching systems.

A fluidised bed quench of novel design has been demonstrated. This device appears suitable for almost any application where rapid fluid cooling is required. It may be possible to operate the principle upside down (using a screw feeder to return the particles); thus removing a major constraint on its usefulness.

9.6 Spectroscopy

The rapid movement and current changes of the arc present major limitations to spectroscopic examination and interpretation. Further effort in plasma spectroscopy from the Ward reactor is probably not warranted in this Department.

9.7 Stockton Coal

The unique properties of Stockton No. 2 coal make it extremely promising for a chemical feedstock for acetylene production (a H/C molar ratio ~0.8, ash less than 0.5%, and high swelling number). The technical difficulties discussed above probably rule out its use for acetylene production in an electric arc process.

REFERENCES

1. Ward, R.A. The Production of Acetylene in a High-Intensity Electric Arc, University of Canterbury, Christchurch, 1974, 102p. (Ph.D. thesis; Chemical Engineering).

2. Baron, R.E. et al. Chemical Equilibrium in Carbon-Hydrogen-Oxygen Systems. MIT Press, p.46.

3. Touloukian, Y.S. Editor, the TPRC Data Series, Thermophysical Properties of Matter, Vol. 6, "Specific Heat", p.28 & 117. Plenum, New York, 1973.

4. Marchio, J.L. A Dual-Channel GC Technique for Mixtures of Permanent Gases and C_1-C_2 Hydrocarbons. J. Chrom. Sci. 9, 432, 1971.

5. Abrahamson, J. The Reactions of Coal in a High Intensity Electric Arc. University of Canterbury, Christchurch, 1971. (Ph.D. thesis; Chemical Engineering).

6. Gladisch, H. How Huels Makes Acetylene by DC Arc. Hydrocarbon Processing & Petroleum Refiner, 41, 6, 159, 1962.

7. Schulze, R.A. Du Pont Arc Acetylene Process. Chemistry & Industry, 45, 1539, 1968.

8. Maniero, D.A. et al. Electric Arc Heaters for High Temperature Chemical Processing. Westinghouse Engineer, May 1968, p.67.

9. Valibekov, Y.V. & Bolotov, G.M. An Investigation of the Process for Producing Acetylene. Int. Chem. Eng. 9, 4, 683, 1969.

10. Sennewald Von K. et al. Erzeugung von Acetylen durch thermische Spaltung von Kohlenwasserstoffen mittels hocherhitzten wasserstoffes. Chemie. Ing. Techn. 35, 1, 1, 1963.

11. Girardin, E.K. Private communication, Chemical Engineering Dept., University of Canterbury.

12. Nikolov, P.T. & Petrov, P.E. Application of Plasmas to the Synthesis of Nitrogen Compounds and Acetylene. Int. Chem. Eng. 16, 2, 229, 1976.

13. Davies, C.E. & Wiles, P.G. The Vaporization of Carbon in a High Intensity Electric Arc. Part I: Experimental. Departmental Report, Chemical Engineering, University of Canterbury, Christchurch, 1978.

14. Baddour, R.F. & Iwasyk, J.M. Reactions between Elemental Carbon and Hydrogen at Temperatures Above 2800 K. Ind. & Eng. Chem., Proc. Des. & Dev. 1, 3, 169, 1962.

15. Baddour, R.F. & Blanchet, J.L. Reactions of Carbon Vapour with Hydrogen and with Methane in a High Intensity Arc. Ind. & Eng. Chem., Proc. Des. & Dev. 3, 3, 258, 1964.

16. Davies, C.E. & Wiles, P.G. The Vaporization of Carbon in a High Intensity Electric Arc. Part II: Theoretical. Departmental Report, Chemical Engineering, University of Canterbury, Christchurch, 1978.

17. Carslaw, H.S. & Jaeger, J.C. Conduction of Heat in Solids, 2nd ed. Oxford University Press (1959), p191.

18. Mentel, J. The Influence of Vaporization Upon the Roots of a High Current Arc. I. Different Forms of Vaporization in the Arc Roots. App. Phys. 14, 273, 1977.

19. Palmer, H.B. The Formation of Carbon from Gases. Chapter 5 of The Chemistry and Physics of Carbon, Vol. 1, edited by P.L. Walker, Arnold, 1965.

20. Anderson, J.E. & Case, L.K. An Analytical Approach to Plasma Torch Chemistry. Ind. & Eng. Chem., Proc. Des. & Dev. 1, 3161, 1962.

21. Lieberman, M.L. Chemical Vapour Deposition of Carbon: A model to Relate Gas Phase Conditions to Structure of Deposit. Proc. 3rd Int. Conf. on Chemical Vapour Deposition, Utah, 1972.

22. Kreith, F. Principles of Heat Transfer, 2nd ed., Int. Textbook Co. 1965, Chapter 10.

23. Elliot, D.E. Private communication, University of Aston, Birmingham.

24. Forbes, B.A Fluidised Bed Quenching of a Low Pressure Gas, University of Canterbury, Christchurch, 1971 (B.E. project report, Chemical Engineering).

25. Squires, A.M. Gasifying Coal in High Velocity Fluidised Beds. Abs. Pap ACS Fuel, 20, 1973.

26. Squires, A.M. Private communication.

27. Touloukian et al. Editors, the TPRC Data Series, Thermophysical Properties of Matter, Vol. 2, Thermal Conductivity, Plenum, New York, 1973.

28. Paterson, S. The Heating or Cooling of a Solid Sphere in a Well-Stirred Fluid. Proc. Phys. Soc. 59, 50, 1947.

29. Babcock, J.A. Design Engineering of an Arc Acetylene Plant, Chem. Eng. Prog., 71, 3, 90.

30. Gehrmann, K. & Schmidt, H. Pyrolysis of Hydrocarbons using a Hydrogen Plasma. Proc. 8th World Petroleum Congress (Moscow), 4, 379, 1971.

31. Eisenklam, P. et al. Evaporation Rates and Drag Resistance of Burning Drops. 11th Symp. (Int) on Combustion, p.715, (1971).

32. Plooster, M.N. & Reed, T.B. Carbon-Hydrogen-Acetylene Equilibrium at High Temperatures J. Chem. Phys. 31, 66, 1957.

33. Duff, R.E. & Bauer, S.H. The Equilibrium Composition of the C/H System at Elevated Temperatures. U.S. Department of Commerce, 1961.

34. Lieberman, M.L. & Mark, J.L. Chemical Vapour Deposition of Carbon: Thermochemical Calculations of Equilibrium Gas Compositions. U.S. Department of Commerce, (1972).

35. Hooker, W.J. Shock Tube Studies of Acetylene Decomposition. 7th Symp. (Int) on Combustion, p.949, 1959.

36. Mar'yasin, I.L. & Nabutovskii, Z.A. Investigation of the Kinetics of the Pyrolysis of Acetylene in a Shock Tube. Translated from Kinetika i Kataliz, 11, 4, 856, 1970.

37. Liley, P.E. Transport Properties of Selected Elements and Compounds in the Gaseous State, Thermophysical Properties Research Centre, Purdue University, 1972, p22.

38. Balooch, M. & Olander, D.R. Reactions of Modulated Molecular Beams with Pyrolytic Graphite III Hydrogen. J. Chem. Phys. 63, 11, 4772, 1975.

39. JANAF Thermochemical Tables, 2nd ed. NSRDS - NBS37 Nat. Bur. Stand. Washington, 1970.

40. Clarke, J.T. & Fox, B.R. Reactions of Graphite Filaments with Hydrogen Above 2000 K. J. Chem. Phys. 46, 3, 827, 1967.

41. Geffe, P.R. Simplified Modern Filter Design. Iliffe Books, 1964, p136.

42. Cobine, J.D Gaseous Conductors. Dover Publications, New York (1958) p.301 & 344.

43. Wilson, R.G. & Spitzer, C.R. Visible and Near Infrared Emittance of Ablation Chars and Carbon. AIAA J. 6, 4, 665, 1968.

44. Lundell, J.H. & Dickey, R.R. Radiative Vaporization of Graphite in the Temperature Range of 4000 to 4500 K. Prog. Astro. & Aero. 56, 405, 1977.

45. Schurer, K. The Tungsten Strip Lamp and the Anode of the Carbon Arc as Radiometric Standards. University of Utrecht, Rotterdam (Ph.D. thesis, Physics, 1969).

46. Hearne, K.R. & Nixon, S.A Electrode Temperatures of Graphite and Carbon Arcs. Brit. J. Appl. Phys. (J. Phys. D) 2, 2, 413 , 1969.

47. Cobine, J.D. Gaseous Conductors. Dover Publications, N.Y. (1958) p.306.

48. Wutzke, S.A. et al. Symptomatic Behaviour of an Electric Arc with a Superimposed Flow. AIAA J. 6, 8, 1480, 1968.

49. Boumans, P.W.J.M. Theory of Spectrochemical Excitation. Hilger & Watts, 1966, p.40.

50. Cobine, J.D. Gaseous Conductors, Dover Publications, N.Y. (1958) p.293.

51. Crawford, F.W. & Edels, H. The Reignition Voltage Characteristics of Freely Recovery Arcs. Proc. IEE Lond. 107A, 202, 1960.

52. Philips Data Handbook: Recifier Diodes and Thyristors. SCIa-06-74.

53. Hoyaux, M.F. Arc Physics, p.172, Springer-Verlag, 1968.

54. Finkelnburg, W. The High Current Carbon Arc. FIAT Final Report 1052, Dept. of Commerce, Washington D.C. (about 1946) p.27.

55. Clarke, J.T. & Fox, B.R. Rate and Heat of Vaporization of Graphite above 3000 K. J. Chem. Phys. 51, 8, 3231, 1969.

56. Lundell, J.H. & Dickey, R.R. Ablation of ATJ Graphite at High Temperatures. AIAA J. 11, 2, 216, 1973.

57. Whittaker, A G. & Kinter, P.L. Particle Emission and Related Morphological Changes Occurring During the Sublimation of Graphitic Carbons. Carbon, 14, 5, 257, 1976.

58. Meyer, R.T. & Lynch, A.W. A Method for Determining the Vapour Phase Component of Carbon Mass Loss. Carbon, 12, 684, 1974.

59. de Vos, J.C. A New Determination of the Emissivity of Tungsten Ribbon. Physica, 20, 690, 1954.

60. Kodak Plates and Films for Science and Industry, 1st ed., No. P9, p.15.

61. Gaydon, A.G. The Spectroscopy of Flames, 2nd ed., Chapman and Hall, p.214-215.

62. Pearse, R.W.B. & Gaydon, A.G. The Identification of Molecular Spectra, 4th ed. Chapman & Hall.

63. Pearse, R.W.B. & Gaydon, A.G. The Identification of Molecular Spectra, 4th ed. Chapman & Hall, p.170.

64. Tables of Spectral Line Intensities. NBS Monograph 145, part 1 and 2, Department of Commerce, Washington D.C.

65. Atomic Transition Probabilities H Through Ne. NSRDS - NBS 4, Vol. 1, Department of Commerce, Washington D.C.

66. Selected Tables of Atomic Spectra. Atomic Energy Levels and Multiplet Tables NSRDS - NBS 3, section 3, Department of Commerce, Washington D.C.

67. Robinson, D. & Lenn, P.D. Plasma Diagnostics by Spectroscopic Methods. App. Opt. 6, 6, 983.

68. Huddlestone, R.H. & Leonard, S.L. Plasma Diagnostic Techniques, Academic Press, p.309.

69. Huddlestone, R.H. & Leonard, S.L. Plasma Diagnostic Techniques, Academic Press, p.274, 281.

70. Kubin, R.F. & Presley, L.L. Thermodynamic Properties and Mollier Chart for Hydrogen from 300 to 20,000 K. NASA SP-3002 (1964), p.41.

71. Kroepelin von H. & Hoffmann, K.U. Rechnerische Unterlagen zur spektroskopischen Temperaturbestimmung in Kohlenstoff-Wasserstoff-Plasmen aus dem Intensitätsverhätnis einer CII - und einer CI - Linie. Optik 22, 9, 599, 1965.

72. Allen, C.W. Astrophysical Quantities, 3rd ed. Athlone Press, 1973, p.34.

73. Experimental Transition Probabilities for Spectral Lines of Seventy Elements (1962). NBS Monograph 53. Department of Commerce, Washington, D C.

74. Handbook of Chemistry and Physics, 51st ed. Chemical Rubber Co. P.E56.

75. Herzberg, G. Molecular Spectra and Molecular Structure, I. Spectra of Diatomic Molecules, 2nd ed., p.513, van Nostrand, 1961.

76. Nicholls, R.W. The Interpretation of Intensity Distributions in the CN Violet, C_2 Swan, OH Violet and O_2 Schumann-Runge Band Systems by Use of their r-Centroids & Frank-Condon Factors. Proc. Phys. Soc. A. 69, 741, 1956.

77. King, R.B. Relative Transition Probabilities of the Swan Bands of Carbon. Astrophys. 108, 429, 1948.

78. Bulewicz, E.M. et al. Spectroscopic Studies of C_2, CH and OH Radicals in Low Pressure Acetylene and Oxygen Flames. Proc. Roy. Soc. A 315, 129, 1970.

79. Shea, J.D. The Structure of the Swan Bands. Phys. Rev. 30, 825, 1927.

80. Phillips, J.G. An Extension of the Swan System of the C_2 Molecule. Astrophys. 108, 434, 1948.

81. Herzberg, G. Molecular Spectra and Molecular Structure, I. Spectra of Diatomic Molecules. 2nd ed. von Nostrand, 1961, p.179.

82. Herzberg, G. Molecular Spectra and Molecular Structure, I. Spectra of Diatomic Molecules, 2nd ed. van Nostrand, 1961, p.513.

83. Budó von A. Intensitätsformeln für die Triplettbanden. Zeitschrift fur Physik. 105, 579, 1937.

84. Herzberg, G. Molecular Spectra and Molecular Structure, I. Spectra of Diatomic Molecules, 2nd ed. van Nostrand 1961, p.208.

85. Main, R.P. & Bauer, E. Opacities of Carbon-Air Mixtures at Temperatures from 3000 - 10,000 K. J. Quant. Spect. & Rad. Transfer, 6, 1, 1966.

86. Sparrow, E.M. & Cess, R.D. Radiation Heat Transfer, rev. ed. Brooks/Cole 1970, p.20.

87. Kreith, F. Principles of Heat Transfer, Int. Textbook Co., 1965, 2nd ed. p.208.

88. Eddy, T.L. Critical Review of Plasma Spectroscopic Diagnostics Via MTE. IEEE Trans. Plasma Science, PS-4, 2, 103, 1976.

89. Finkelnburg, W. The High Current Carbon Arc. FIAT Final Report 1052, Department of Commerce, Washington D.C. (about 1946) p.73.

90. Wiles, P.G. & Abrahamson, J. Carbon Fibre Layers on Arc Electrodes - I. Their Properties and Cool-Down Behaviour, Carbon 16, 341, 1978.

91. Abrahamson, J. Graphite Sublimation Temperatures, Carbon Arcs and Crystallite Erosion. Carbon 12, 111, 1974.

92. Siegel, R. & Howell, J.R. Thermal Radiation Heat Transfer, McGraw-Hill, 1972, p.720.

93. Wickramasinghe, N.C. Light Scattering Functions for Small Particles with Applications in Astronomy. Hilger 1973, p.494.

94. Hattenburg, A.T. Spectral Radiance of a Low Current Graphite Arc. Appl. Opt. 6, 95, 1967.

95. Bacon, R. Growth, Structure, and Properties of Graphite Whiskers. J. Appl. Physc. 31, 2, 283, 1960.

96. Ilford Manual of Photography, 5th ed. p.107, edited by Horder, A. Focal Press, 1958.

97. Hove J.E.
1st Industrial Carbon & Graphite Conference, London, 1958, p.501.

98. Perry, J.H. Chemical Engineers Handbook, 4th ed., McGraw-Hill, 1963, p.10-13.

99. Whittaker, A.G. Carbon: A New View of Its High-Temperature Behaviour. Science, 200, 763, 1978.

100. McGlashan, M.L. Physico-Chemical Quantities and Units. The Grammar and Spelling of Physical Chemistry. Royal Institute of Chemistry, Monograph No. 15, 1968, p.64-65.

101. Whittaker, A.G. The Controversial Carbon Solid-Liquid-Vapour Triple Point. Nature, 276, 5689, 695, 1978.

102. Arc-Coal Process Development. Period of performance, May 1966 to April 1972. R & D Report No. 34 - Final Report by Avco Corporation - Systems Division - for Office of Coal Research Dept. of the Interior, Washington DC 1972.

103. Davies, C.E., Pemberton, S & Abrahamson, J. The Extrusion of Stockton No. 1 Coal: to be published.

104. Wiles P.G. B.E. Project Report, Department of Chemical Engineering, University of Canterbury, 1973.

105. Edels, H., Whittaker, D., Evans, K.G. & Shaw, A.B. Experiments and Theory on Arc Reignition by Spark Breakdown. Proc. IEE 112, 12, 1965.

106. Baker, R.L. An Irreversible Thermodynamic Model for Graphite Sublimation in Radiation Environments. Prog. In Astro. & Aero. AIAA 64, 1979.

107. Abrahamson, J. et al. Erosion Rates of Graphite Anodes in High Current Arcs. To be published I. & E.C. Fundamentals.

108. Covington, M.A., Liu, G.N. & Lincoln, K.A. Free-jet Expansions from Laser-vaporized Planar Surfaces AIAA J. 15, 8, 1977.

APPENDIX 1

Spectroscopic Data

Species	Wavelength (nm)	g_K	A_{Ki} (sec^{-1})	E_{upper} (eV)	E_{lower} (eV)	Internal Partition Function Q
H^o						
Balmer						
H_α	656.28	18	4.41×10^7	12.09	10.2	2.0
H_β	486.13	32	8.42×10^6	12.75	"	"
H_γ	434.05	50	2.53×10^6	13.05	"	"
H_δ	410.17	72	9.73×10^5	13.22	"	"
H_ε	397.01	98	4.39×10^5	13.32	"	"
	388.90	128	2.2×10^5	13.39	"	"
	383.54	162	1.2×10^5	13.43	"	"
Paschen						
H_α	1,875.1	32	8.99×10^6	12.75	12.09	"
H_β	1,281.8	50	2.20×10^6	13.05	"	"
H_γ	1,093.8	72	7.78×10^5	13.22	"	"
H_δ	1,004.9	98	3.36×10^5	13.32	"	"
H	2,625.2	72	7.71×10^5	13.22	12.75	"
H	2,165.5	98	3.04×10^5	13.32	"	"
H^+	-	-	-	-	-	1.0
C^o	247.856	3	0.34×10^8	7.68	2.68	10.0
	258.39	3	8.6×10^3	7.48	2.68	10.0
	290.31	3	0.017×10^8	13.119	8.849	10.0
C^+	283.671	4	0.36×10^8	16.3343	11.964	6.0
	283.760	2	0.35×10^8	16.3329	11.964	"

	Wavelength	gA (sec^{-1})	E_{upper}	Q
T_i^+	326.160	186×10^8	5.70	83
	339.458	1.8×10^8	3.67	"
	328.77	77×10^8	5.67	"
	338.376	9.2×10^8	3.67	"

Various Physical Constants were obtained from McGlashan[100].

APPENDIX II

The Radiative Heat Loss from the Anode

Along the anode exists a very steep temperature gradient (from 4000 K at the tip, down to about 700 K immediately above the current contact, 7 cm below the tip). In order to measure the temperature profile accurately it is necessary to measure the total radiation at a particular point and accurately locate that point with respect to the tip.

A magnified image of the anode was projected onto the face of a Kipp and Zonen thermopile. By raising or lowering the thermopile on a lab jack the anode radiation could be sampled at any chosen point. The thermopile signal was recorded on a Yokagawa recorder to which an event marker was fitted. A camera was focused onto the thermopile screen. The camera flash contact was connected to the recorder event marker. When a reading was required, a photograph was taken of the anode image on the thermopile screen, and simultaneously the event marker fired, marking the precise thermopile signal for the particular point on the anode. Measurements were obtained at points from 1 mm to 10 mm down from the anode tip, for a 7.93 mm graphite rod carrying 220 A. The reactor window and lens were made of Sl UV grade silica which transmits all radiation between 190 nm and 3 μm.

The thermopile was calibrated by replacing the reactor anode with the crater of a 'standard' carbon arc. The precise optical geometry was retained, including any soot particles on the reaction window.

Since the window and lens do not transmit all the radiated power, a correction must be applied to the thermopile signal which depends on the *actual* point temperature. Thus in principle, an iterative procedure is required to find the true spot temperature. In practice the correction is not very sensitive to temperature, so that sufficient accuracy could

be obtained with one iteration.

Krieth[87] has a plot showing the fraction of radiation between $\lambda = 0$, to a given λ, and between $\lambda = 0$ to $\lambda = \infty$, for any wavelength λ and temperature. Since the standard arc has a temperature of 3792 K and an emissivity of 0.99[94], it was assumed that the anode had the same emissivity. (This results in a minimum estimate of the actual temperature. Should the uncertainty in the emissivity be as great as ±10% then once the fourth root of the radiance is obtained, the uncertainty at 4000 K is ±100 K.

The corrected results are plotted in Figure (A1). Between 1 mm and 10 mm the temperature profile is best represented by a straight line.

Total radiation loss from the anode

The power radiated from a differential element dA is given by:

$$dP = \varepsilon \sigma T^4 dA$$

where P is radiated power in Watts

ε is the emissivity (=0.99)

σ is the Stefan Boltzman constant

T is the temperature

If the anode is considered to be a uniform cylinder of radius r, and the temperature varies only in the longitudinal direction x, then dA can be considered to be a differential hoop around the cylinder:

$$dA = 2\pi r \, dx$$

$$P = \int_{\ell_1}^{\ell_2} 2\pi r \varepsilon \sigma T^4 \, dx$$

and since T(x) has been experimentally obtained viz: $T = 4093 - 193{,}000\, x$

$$P = 2\pi \times 0.004 \times 1 \times 5.8 \times 10^{-8} \int_{0.001}^{0.01} (4093 - 193{,}000)^4 \, dx$$

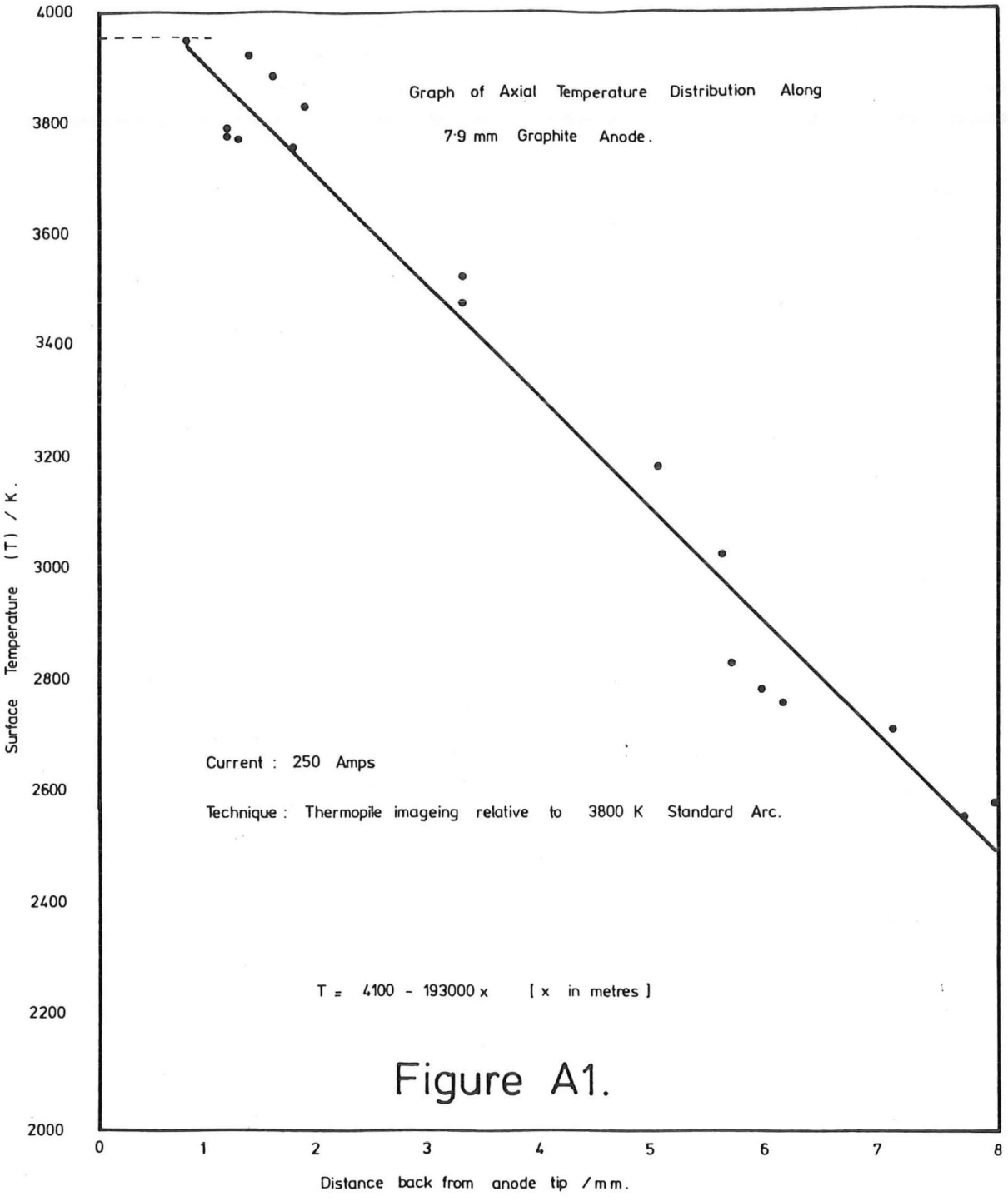
Graph of Axial Temperature Distribution Along
7·9 mm Graphite Anode.
Current : 250 Amps
Technique : Thermopile imageing relative to 3800 K Standard Arc.
T = 4100 - 193000 x [x in metres]
Surface Temperature (T) / K.
Distance back from anode tip / mm.
4000
3800
3600
3400
3200
3000
2800
2600
2400
2200
2000
0
1
2
3
4
5
6
7
8

Figure A1.

which on integration yields:

$$P = 1300 \text{ W}$$

then:

$$P_{tip + end} = \pi \times 0.004 \times 5.8 \times 10^{-8} \times 3950^4 (0.004 + 0.001 \times 2)$$

$$= 1060 \text{ W}$$

Total anode radiated power $\simeq$ 2400 W.

If a reactor wall temperature of 2500 K is allowed for, the power losses are about 800 W (along rod) and 745 W from the tip and end, totalling 1545 W.

The ohmic heating in a 10 mm length of 7.93 mm diameter rod would be:

$$i^2 \frac{\Omega \ell}{\pi r^2}$$

where Ω is the resistivity of graphite and is likely to be of order of 1×10^{-5} nm, hence for a current of 250 A:

power dissipated = 124 W.

Therefore the nett power that is supplied by conduction back from the anode tip is likely to be approximately 1400 W.

Carbon Vol. 16, pp. 341–349

0008-6223/78/1001-0341/$02.00/0

CARBON FIBRE LAYERS ON ARC ELECTRODES—I
THEIR PROPERTIES AND COOL-DOWN BEHAVIOUR

P. G. WILES and J. ABRAHAMSON†
Chemical Engineering Department, University of Canterbury, Christchurch, New Zealand

(*Received 7 December 1977*)

Abstract—A thick mat of fine fibres and crystallites has been found on the surfaces of graphite and carbon anodes after low current arc operation in nitrogen. Similar operation in air leaves no trace of the fibres. The dimensions and other properties have been studied by scanning and transmission electron microscopy. Radiance decays observed at the anode face of the "standard carbon arc" after rapid current cut-off have been studied over a range of wavelengths. The temperature drop at the surface is too rapid for bulk graphite cooling, as has been pointed out by Lozier and Null. Purely radiative and conductive-radiative cooling mechanisms in surface layers have been considered, and it is found that conduction through the fibre layer and a porous layer beneath the fibres controls the cooling rate for the first 100 μs.

1. INTRODUCTION

The radiance from the front face of the anode of a carbon arc has attracted much interest. When the carbon is pure, and the current is below a certain critical value of the order of ten amperes, it corresponds to a black-body temperature of close to 3800 K (at 1 atm), easily reproduced and almost independent of the current used. For these reasons, it is used as a secondary radiance standard, and the arc arrangement is called the "standard carbon arc."

It was natural in early work to identify the measured temperature with the sublimation temperature of carbon. This idea has been challenged by Abrahamson[1], who argues from many different experimental sources that the temperature is probably controlled by the vaporisation of very small carbon particles. If these particles were small enough, their surface contribution to the solid free energy would be large enough to lower the sublimation temperature several hundred Kelvins from the sublimation temperature of *bulk* carbon, thought to lie close to 4000 K, in keeping with other non-arc measurements (see [1]). Recently, Lozier and Null[2] have presented an analysis of the radiance decay observed from the anode face when a standard carbon arc is rapidly switched off. They interpreted their measurements of this decay, and other experimental work, in terms of two possible models:

(a) The existence of a loosely sitting or suspended layer of particles in front of the anode face proper. These particles were suggested to be about 150 nm in diameter compared to the 3 nm suggested by Abrahamson[1].

(b) The existence of a thin (5 μm depth) layer of poorly conducting carbon, covering the normal carbon surface.

Their analysis, which was kindly made available to us in full[3], favoured the layer model, but evidence supporting both models was found.

2. OBSERVATION OF FIBRES

Presumably many close investigations of the anode surface after it has cooled down, have been made in the past. Lozier and Null[3] at least, have looked at their surfaces and beneath them with optical and electron microscopy. Nothing significant beyond a loss of binder phase has been observed.

We ran our carbon arc in nitrogen and, after rapidly switching the current off, the anode cooled in nitrogen. We found mats of small fibres under a high resolution scanning electron microscope. These fibres were found on both graphite and carbon anodes, and were found on all anodes operated in nitrogen.

Two micrographs of the layers of fibres found on the high purity Union Carbide graphite SPK, and carbon L113SP, after cleaving the anode tip open from behind, are shown in Figs. 1 and 2, together with similar micrographs of anodes operated in air. The areas of fibres always corresponded with the blacker areas on the anode surface as seen by the eye, and in turn these areas corresponded with the bright area of arc attachment to the anode just before extinguishing the arc. We presume that operating the arc in nitrogen rather than air (as have previous investigators) preserved the fibres from oxidation during cooling. We must be careful, however, and argue from independent evidence that: (a), the fibres are unlikely to have been formed during the cooling (and condensation) period; and (b), the fibres exist during normal operation, even in air.

This independent evidence comes from the radiance transients observed during the cooling period after switching the arc off, and from the previous analysis by Abrahamson[1].

The fibres themselves will be closely described in a later paper on their structure, but it is sufficient to note here that they range in diameter from about 4 nm to

†To whom correspondence should be addressed.

(a)

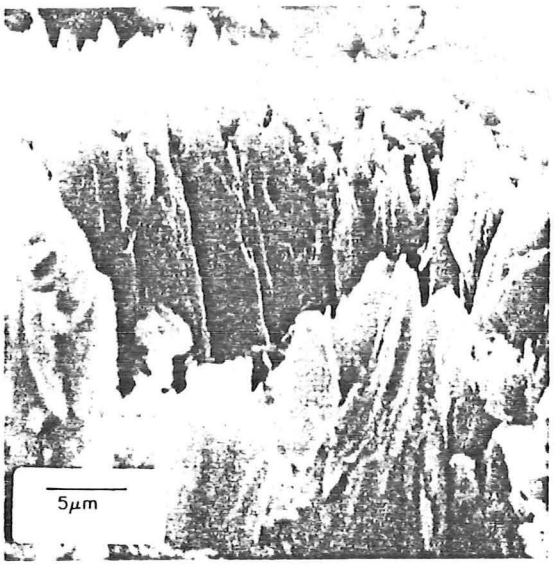

(b)

Fig. 1. Scanning electron micrographs of the surfaces of SPK graphite anodes after arc operation (11A) in (a) nitrogen, (b) air. The anodes were cut from the rear, and split open so that a relatively undisturbed section of the surface region could be examined.

(a)

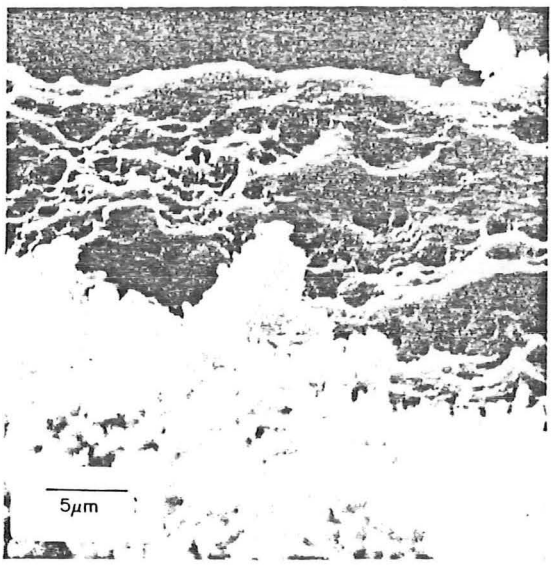

(b)

Fig. 2. Scanning electron micrographs of the surfaces of Union Carbide L113 SP carbon anodes after arc operation (9.5A) in (a) nitrogen, and (b) air. These specimens were similarly split from the rear. The darker area in focus in (b) shows the surface exposed to the arc, whereas the lighter area in (b) shows fractured interior carbon.

about 100 nm, with lengths up to 15 μm, and hold many small crystalline particles on them, especially around intersections of touching fibres. A transmission electron micrograph of the finer fibres on an SPK graphite anode, showing the attached particles, is given in Fig. 3. For carbon anodes, especially a Morganite carbon (see Table 1), the particles consituted much of the mass of the layer, and sometimes it was difficult to see the connecting fibres.

From the micrographs, estimates of the fraction of layer volume occupied by fibres were 1.5% for SPK graphite, and 1% for the Morganite carbon. In addition, another 1% was found in the form of particles collected either at the base of the fibres for the area of SPK anode (shown in Fig. 1) or on the fibres as shown in Fig. 2 (carbon) and Fig. 3 (graphite). An average diameter of 50 nm, spacing 300 nm, and density of 10^{13} m^{-2} of surface was estimated for the fibres on both graphite and carbon anodes. The distinct single particles on the Morganite carbon were about 20 nm average diameter and aggregated into clumps of 200–1000 (150–250 nm dia.). The particles on the graphite anodes were similarly sized and grouped. Some areas observed on a less pure graphite anode (Union Carbide CS) exhibited extensive branching of fibres.

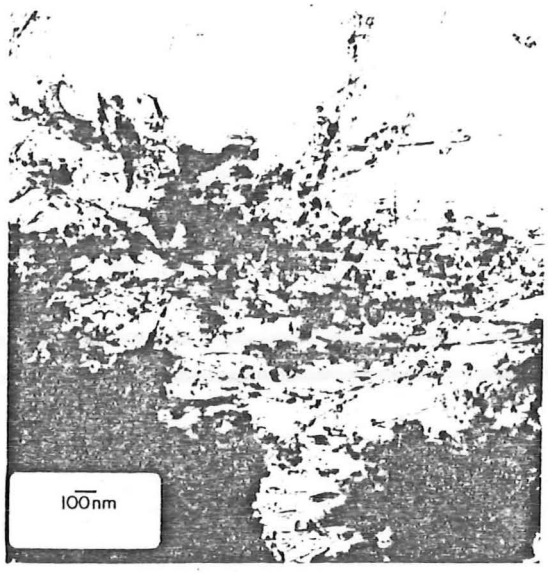

Fig. 3. A transmission electron micrograph of part of the fibre layer from an SPK graphite anode, after arc operation in nitrogen (11A current).

Table 1. Material specifications

	Anode graphite SPK	Anode carbon L113 SP	Anode carbon SG 305 E	Cathode Carbon
Dia. (mm)	6	6	6	6
Source	Union carbide	Union carbide	Morganite	Polaron
Total impurity (ppm)	<3	<6	<15	<50

N_2: (N.Z. Industrial gases) O_2 content 0.1% and H_2O dew point −60°C.

3. EXPERIMENTAL

The carbon arc was enclosed by a water-cooled jacket, with a hand-fed 6 mm dia. horizontal anode, and a hand-fed 6 mm dia. cathode arranged vertically. The 240 V power supply had a 1V peak-to-peak ripple at 11A. The anode and cathode impurities are detailed in Table 1, together with the nitrogen specification.

The arc was cut off by triggering a silicon controlled rectifier (SCR) so that the current was rapidly shunted around the arc. In this way the arc current dropped to zero in less than 3 μs.

Observations of the central region of the anode face were made through a 1.5 mm thick glass window with a Hilger and Watts medium quartz spectrophotometer E498. (When operating in air, this window was removed.) A square area of anode of about 40 μm × 40 μm was sampled by the spectrophotometer slit after focussing with an S1UV quartz lens. An RCA IP28 photomultiplier tube was used to detect the light. The tube/voltage follower/storage oscilloscope combination had a rise time of <3 μs, determined by a TTL pulse generator and light emitting diode. After making sure that the arc was burning stably within 0.5 A of its overload current (11 A for SPK, 9.5 A for L113SP), the SCR was triggered. The stored trace was photographed. The decay covers several decades in time, so the short and long time responses were taken separately. The linearity of the spectroscope/amplifier/oscilloscope combination with respect to intensity was checked with neutral filters and found to be within the experimental error over the range used (5%).

4. RESULTS

Radiance decays at several wavelengths were recorded for both SPK graphite anodes and L113 SP carbon anodes, operated in nitrogen or air. A typical oscilloscope trace is shown in Fig. 4, curve (a). Care was taken with anode radiance measurements in selecting spectral regions where the plasma radiance was negligible compared with that of the anode. The characteristic time for the radiance to drop to half its original value ranged from 80 μs at 260 nm to 1 ms at 540 nm, incidentally somewhat longer than the arc radiance half-life of 70 μs at similar wavelengths (monitored on both 400 nm CN and 460 nm C_2 bands transverse to the anode axis, about 1 mm out from the anode face, in air).

A somewhat less stable operation was found in nitrogen, than in air, in that the diffuse large arc attachment wandered about on the surface. This is presumably related to the fact that the anode face was larger for the same conditions in nitrogen, as the anode was not removed from the side by oxidation. Other workers have observed brief excursions to the unstable hissing mode when operating within 0.5 A of the overload current. We found that, if a momentary anode eruption (hiss) occurred only shortly (<1 s) before cutting off the current, then the decay was from a different value, and at least in those cases noted, deviated from the normal rate, as shown in Fig. 4, curve (b). It is evident that the surface condition was altered. These eruptions were more common with the carbon anodes.

A number of workers (see Ref. [3]) have established that the stable operating anode has a radiance closely approximated by a black-body radiator at 3800 K. We will use this reference point in presenting our radiance decays. We use the assumption that an effectively black radiation source is being observed at all times, and this is

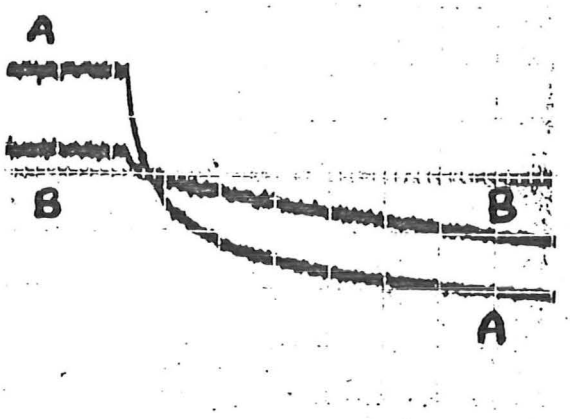

Fig. 4. Oscilloscope traces of spectral emissive power from a small central portion of an SPK anode, on an arbitrary scale. Wavelength 444 nm and time scale 100 μs/large division.

tested by noting the consistency among the temperatures calculated from different wavelengths.

If I_λ is the spectral emissive power at wavelength λ and time t, corresponding to a black-body temperature T, and $I_{\lambda 0}$ and $T_0 = 3800$ K are the values at time $t = 0$, then the temperature is easily found from the ratio of Planck emissive powers, R_λ, taken as a ratio from the oscilloscope traces;

$$\frac{I_\lambda}{I_{\lambda 0}} = R_\lambda = \frac{e^{C_2/\lambda T_0} - 1}{e^{C_2/\lambda T} - 1} \quad (1)$$

and since for our conditions, $e^{C_2/\lambda T} \gg 1$,

$$T = (1/3800 - \lambda \ln R_\lambda / C_2). \quad (2)$$

The temperatures thus calculated are plotted on Fig. 5 against a logarithmic scale of time. Figure 5(a) gives results for SPK graphite, and Fig. 5(b) results for L113 SP carbon, both in air and in nitrogen.

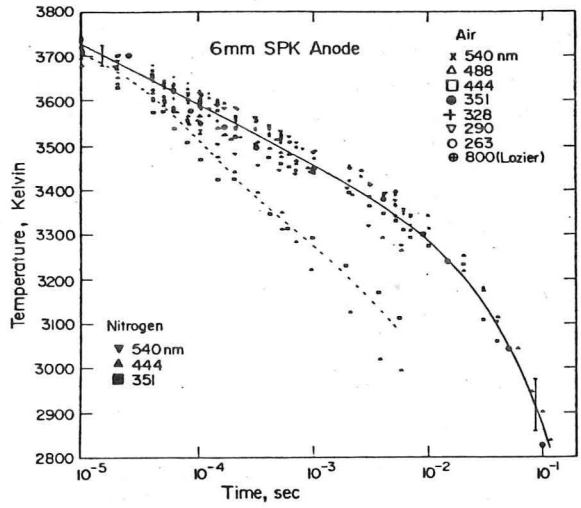

(a)

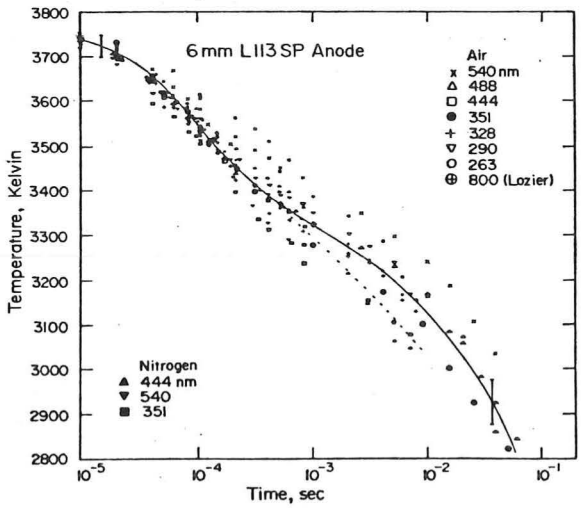

(b)

Fig. 5. Black-body surface temperatures during cool-down of (a) SPK graphite anodes, and (b) L113 SP carbon anodes, in air and nitrogen, as a function of time after the arc cut-off SCR was fired.

From Fig. 5, there appears to be no consistent variation of temperature estimate with wavelength, and so the anode face can be effectively represented by a black (or gray) body radiator at least up to 100 ms after arc cut-off. For the graphite, a difference can be seen between the cool-down curves in air and in nitrogen; this difference becoming significant compared to the scatter at about 100 μs. In contrast, there is little difference for the carbon.

5. DISCUSSION

Lozier and Null[3] measured cooling transients for the same graphite and carbon, both in air. Their results, also shown in Fig. 5, correspond closely to ours for the SPK graphite, but perhaps not so closely for the L113 SP carbon. Their determinations of T used a detector sensitive to $\lambda \simeq 800$ nm.

The model for the anode surface suggested by Abrahamson was that of a cloud of 3 nm particles suspended above a porous layer. The two models studied by Lozier and Null were separately (a), a suspended layer of particles about 150 nm in diameter; and (b), a poorly conducting (porous) layer. The fibrous mat observed in this work is a structure which could possibly cover the characteristics of all of these models. The fibres observed range in diameter from 10 nm or less to about 100 nm, and the suspended (adhering) particles were from 5 to 100 nm dia. A quick estimate of particle growth by condensation during cool-down, will satisfy any doubts that these particle and fibre dimensions are characteristic of those existing in the operating arc. One atmosphere of C_3 vapour at 3800 K has a density of 0.115 kg m^{-3}, and thus could only contribute 0.25% by mass to the observed fibre layer (density 40 kg m^{-3}).

It is easy to see that the fibres, if they exist on the surface while the arc is operating in nitrogen, can also exist while it is operating in air. Abrahamson[1] calculated from a gas diffusion/convection model of the anode net carbon vapour evolution, that the atmosphere (nitrogen, air) penetrates to within only about 100 μm of the surface. Within this distance, the gas phase should be almost solely carbon vapour. As the fibres extend only about 20–30 μm, there will be no difference in their surrounding atmosphere during arc operation, and hence their properties should be independent of the atmosphere. Indeed, operation of the standard arc in nitrogen has not shown a different radiance.

On cutting the current off, the oxygen will diffuse inward, oxidising and removing the fibrous layer. From the expression for the mean squared distance $\overline{x^2}$ travelled by a diffusing species with diffusivity D in time t,

$$\overline{x^2} = 2Dt \quad (3)$$

one can calculate a representative time for the start of chemical attack on the fibres by oxygen. For $\sqrt{(\overline{x^2})} = 100\ \mu$m, and $D = 1.0 \times 10^{-3}$ m^2 s^{-1} (see Ref. [1]), $t = 5\ \mu$s. This represents the minimum time for oxygen attack, not allowing for the finite rate of oxidation. It is thus reasonable that the observed difference between the air

and nitrogen cooling curves should have resulted from oxidation of the fibrous layer, since the time to when a difference was found was larger than this (~100 μs). This interpretation, and the conclusion in the following discussion that the cool-down curves are consistent with the existence of the fibrous layer at least back to 10 μs after cut-off, both argue for the existence of the fibres very shortly after cut-off. It is difficult to imagine the fibres being built up over 10 μs, and so one is led to the conclusion that they are present during the arc operation.

Cool-down models

Lozier and Null found some good evidence for their suspended (or loosely sitting) particle layer model. They were able to closely match the reflectance of the operating surface over a range of wavelengths if they assumed a layer of particles of diameter 160 nm. This success encourages us to consider the particle model seriously even for the fibre layer—the heat transfer through the layer for this model will be almost solely by radiative transfer from particle to particle (or fibre section to fibre section). Viskanta and Bathla[4] have found numerical solutions to the transient radiative cooling of a slab of semi-transparent non-conducting medium of thickness 2L, and by making a mathematical approximation in the radiative transfer equation, Chan and Cho[5] were able to find a successful analytical solution to the same problem. They related the dimensionless temperature $U = T/T_0$ to a dimensionless time $t^* = n^2\sigma T_0^3 K_e t/\rho c$ and a dimensionless optical depth τ/τ_L by the solution

$$U(\tau, t^*) = \{1 + 6t^*(E_2(\tau + \tau_L) + E_2(\tau_L - \tau))\}^{-1/3} \quad (4)$$

where T_0 = initial (uniform) temperature of slab, n = real part of the refractive index of the slab medium, σ = Stefan–Boltzmann constant, K_e = linear absorption coefficient, t = time, ρ = density of absorbing cloud, c = specific heat capacity, $\tau = \int_0^x K_e\,dx$, $\tau_L = \tau(x = L)$, x = distance measured from the centre of the slab, $2L$ = thickness of slab, and $E_2(\tau) = \int_0^1 \exp(-\tau/\mu)\,d\mu$.

Our problem with the fibre layer is one where the layer is optically thick. (For particles as small as 20 nm, absorption is proportional to total volume of carbon, and so K_e = Rayleigh factor × volume fraction carbon = $5 \times 10^6\,m^{-1} \times 2 \times 10^{-2} \simeq 1 \times 10^5\,m^{-1}$ through layer.† Thus $\tau_L = K_e L = 1 \times 10^5\,m^{-1} \times 15 \times 10^{-6}\,m = 1.5$, i.e. optically thick to the centre of the layer). Thus the effective depth into the layer, x_m, from where we measure an average temperature by pyrometer, is in the range $0 < x_m < L$. In this case, $E_2(\tau_m + \tau_L) \ll E_2(\tau_L - \tau_m)$ and we can ignore the radiative interaction with the other side of the slab (which in our case is exchanging with a somewhat cooler rear bulk carbon surface), and apply Chan and Cho's solution to the observed U (τ_m, t^*). Collecting terms together which are expected to be constant during a cool-down,

$$U\,(\text{observed}) = (1 + At)^{-1/3} \quad (5)$$

where A is a constant $= 6\,n^2\sigma T_0^3 K_e E_2(\tau_L - \tau_m)/\rho c$.

We have attempted to fit this relationship to the temperature-time experimental plots, and found that the second derivative of temperature is much too high. Figure 6 shows an example arbitrarily fitted at 3700 K for $t = 10\,\mu$s, where the constant $A = 8 \times 10^3\,s^{-1}$. If one calculates A using the properties of the fibre layer‡ ($n = 1.01$, $\rho = 40\,kg\,m^{-3}$, and $\tau_L - \tau_m = 1.5 - 0.7 = 0.8$) then $A = 4.5 \times 10^3\,s^{-1}$, which gives a single point match a little later but fits the experimental points no better ($T_s = 3745$ K for $t = 10^{-5}$ s, $T_s = 3360$ K for $t = 10^{-4}$ s). It is evident that the radiative model does not adequately account for the cooling behaviour beyond about 10 μs, if at all.

Another model for the surface is that of a conducting layer covering the anode, with a lower conductivity/thermal diffusivity than the anode. Lozier and Null have interpreted their cooling curves up to 50 μs in terms of the cooling of the front surface by conduction through such a layer, together with a radiative loss from the front. By approximating this radiative loss to a convective type loss (a coefficient times a temperature difference), they were able to solve the resulting linear boundary condition problem in the simple form

$$T_s(t) = T_s(0) - 2(R_0 + F_0)\left(\frac{t}{\pi k c \rho}\right)^{1/2} \quad (6)$$

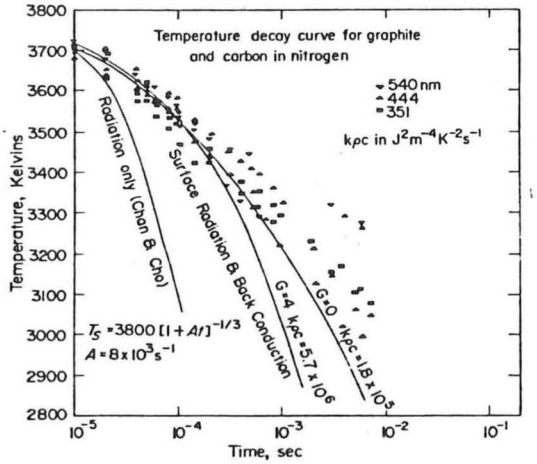

Fig. 6. Black-body surface temperatures during cool-down in nitrogen, as in Fig. 5, together with radiation and conduction-radiation models of layer cooling.

†In the limit of small spheres, Mie scattering gives the Rayleigh factor as $(36\pi/\lambda)[nk/((n^2 - k^2 + 2)^2 + 4n^2k^2)]$, where the complex refractive index $\bar{n} = n - ik$ (see Ref. [6]). Twitty and Weinman[7] review the measured values for n and k for graphite at different wavelengths. Using the range of values they report, the Rayleigh factor is calculated to vary between 2 and 11 × $10^6\,m^{-1}$ over the wavelength range of 3800 K radiation. An effective mean value is about $5 \times 10^6\,m^{-1}$.

‡n of the layer can be calculated from n of graphite by using the definition of molar refraction R, which is a property of 1 mole of graphite atoms.

$$R = \frac{n^2 - 1}{n^2 + 2} \cdot \frac{M}{\rho}$$ where M = molecular weight and ρ = density.

Finding R for graphite ($n = 2$, $\rho = 2000\,kg\,m^{-3}$) and using the same R for the layer but with $\rho = 40\,kg\,m^{-3}$, $n = 1.01$. $E_2(0.8) = 0.20$ from Abramowitz and Stegun[8].

where $T_s(t)$ is the surface temperature at time t, $R_0 = \sigma\epsilon T_s^4(0)$ is the radiated flux at time zero, F_0 is the conducted flux into the anode at time zero, k is the layer conductivity, and c, ρ refer to the layer specific heat capacity and density respectively.

By assuming a value for F_0 (derived from an energy balance over the anode surface in which the accurately measured R_0 and a less accurately known anode voltage drop was used), the initial part of the observed cooling curve was adjusted to eqn (6) by choosing a suitable $kc\rho$.

The values of $kc\rho$ found by Lozier and Null were 25 to 50 times smaller than those of the bulk electrode, supporting the existence of a low conductivity layer. However, for the case $F_0 = 0$, Lozier and Null's analysis, when compared with Jaeger's more accurate series solution[9], gives too steep a temperature drop. It was thought desirable in the more useful case of $F_0 > 0$, to calculate more accurate solutions for the surface temperature.

The integral method used by Goodman and described by Ozisik[10] yields the following integral

$$\theta^2 = \frac{3}{2}\int_1^U \frac{(U-1)(G+U^4) - 2(U-1)^2U^3}{(G+U^4)^3}\,dU \quad (7)$$

where $U = T_s(t)/T_s(0)$, $G = F_0/R_0$, and

$$\theta = \left(\frac{\sigma\epsilon T_s^3(0)t^{1/2}}{kc\rho}\right).$$

The solution to this integral is compared in Fig. 7 with eqn (6), which can be recast as

$$U = 1 - 2(1+G)\theta/\sqrt{\pi}. \quad (8)$$

It can be seen that, for higher G ratios, Lozier and Null's square root of time relationship (eqn 8) is quite close to the more accurate eqn (7), and can be safely used. We have taken Lozier and Null's value of $G = 4$, derived from an effective anode voltage drop of 38 V (the maximum likely, giving the maximum G) and have matched the $G = 4$ curve with the experimental points in Fig. 6 by choosing $kc\rho = 5.7 \times 10^6\ \mathrm{J^2\,m^{-4}\,K^{-2}\,s^{-1}}$. One can see more success in modelling the cool-down curve with this than with the radiative transfer model, but even so, after 200 μs the experimental points begin to deviate sharply from the conduction model. This can be seen more clearly in Fig. 7, where the envelope of experimental points has been transposed from Fig. 6 using the above value of $kc\rho$.

The integral method used to obtain the eqn (7) is based on a thermal diffusion thickness δ and provides an estimate of the penetration of the thermal disturbance into the layer at any time, as shown in Fig. 8(a).

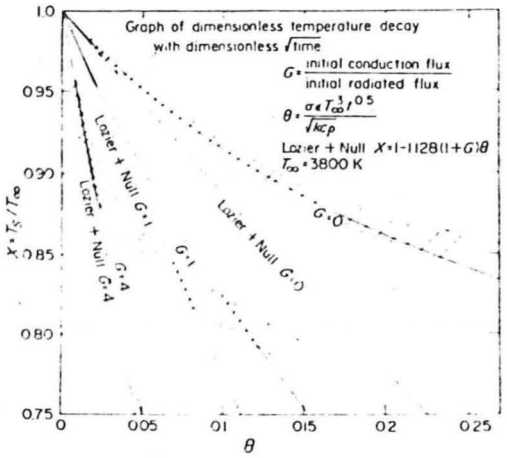

Fig. 7. Surface temperatures from Fig. 6 represented by a hatched band, on a plot of dimensionless temperature vs dimensionless (time)$^{1/2}$. Note the departure of experiment from Lozier and Null's straight lines, for the case $G = 4$, and even from the more accurate solutions (unlabelled) of the semi-infinite slab cooling problem.

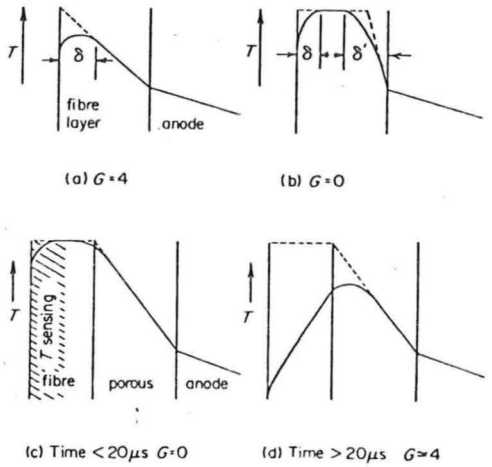

Fig. 8. Temperature profiles with distance into the anode for successively used layer models and initial conditions, (a) fibre/bulk $G = 4$, (b) fibre/bulk $G = 0$, (c) fibre/porous/bulk $G = 0$, time $< 20\ \mu$s, (d) fibre/porous/bulk $G \simeq 4$, $20\ \mu\mathrm{s} <$ time $< 100\ \mu$s.

$$\delta = \frac{3k\{T_s(0) - T_s(t)\}}{F_0 + \sigma\epsilon T_s^4(t)}. \quad (9)$$

As soon as the thermal wave generated by the arc shut-off reaches the back face of the low conductivity layer, the physical problem is no longer that of a semi-infinite body of constant properties, as assumed for the derivation of eqn (7). Shortly after this discontinuity is reached, the surface temperature will begin to show some modification from the curves calculated above. If we set $\delta = 30\ \mu$m, the maximum observed thickness of the fibre layer, and assume an effective fibre layer $k = 1.3\ \mathrm{W\,m^{-1}\,K^{-1}}$† the corresponding time from eqn (9) is 200 μs. This coincides with the time in Fig. 6 when deviation of points from the eqn (7) curve becomes noticeable. (The corresponding $T_s/T_0 = 0.89$ on Fig. 7.) Thus the later deviation is explainable as an influence of the higher $kc\rho$ of the interior anode material (e.g. 2.8 ×

†The cross sectional area for fibres is 0.01 m^2 per m^2 of anode surface. Taking the fibre conductivity to be that for annealed pyrolytic graphite along the basal plane at 2700 K (180 W m^{-1} K^{-1} from Null *et al.*[11]), adjusted for temperature to 3700 K by Kelly's inverse proportionality[12], then the fibre layer conductivity is $k = 180 \times 0.01 \times 2700/3700 = 1.3\ \mathrm{W\,m^{-1}\,K^{-1}}$.

$10^8\,J^2\,m^{-4}\,K^{-2}\,s^{-1}$ for an extruded fine grain graphite up to 2800 K[13]). This is essentially Lozier and Null's argument also, although theirs was semi-quantitative. They interpreted the long-time behaviour by means of a second $t^{1/2}$ cooling curve based on the interior $kc\rho$.

Using our knowledge of the fibre layer properties, we can now check the feasibility of the thermal condition—radiation model by estimating $kc\rho$ for the layer. For $k = 1.3\,W\,M^{-1}\,K^{-1}$ and $\rho = 0.02 \times 2000 = 40\,kg\,m^{-3}$ as above, and $c = 2.1\,kJ\,kg^{-1}\,K^{-1}$ from JANAF tables in this temperature range[14], $kc\rho = 1.1 \times 10^5\,J^2\,m^{-4}\,K^{-2}\,s^{-1}$. This is a factor of 50 too low. The conductivity is based on the maximum possible graphite conductivity (stress annealed pyrolytic) but ignores the presence of particles on the fibres, and this may increase k by perhaps 100%. At the most, another 100% increase could possibly be made with ρ, but this still leaves over an order of magnitude difference to be explained. We must conclude that the conduction-radiation model applied either to the fibre layer or the bulk anode cannot explain the observed radiance decay after cutting off the arc.

The problem here is that both models—radiative transfer within the layer, and conduction within the layer—predict too rapid a measured temperature drop after arc cut-off. For a given temperature gradient within the layer, we can at least determine which of the two transport mechanisms will dominate. The Rosseland optically thick relationship for heat transfer q_R is

$$q_R = -\frac{4}{3}\sigma\frac{dT^4}{d\tau}. \tag{10}$$

For a temperature drop from 3800 to 3700 K across the layer ($\tau = 3.0$), $q_R = 0.5\,MW\,m^{-2}$. In comparison for the same temperature drop, the conductivity of $1.3\,W\,m^{-1}\,K^{-1}$ calculated above gives a conducted transfer of $4\,MW\,m^{-2}$. From this it is seen that the conducted flux will dominate, and temperatures will be controlled by this mechanism. Lozier and Null[3] in their Appendix B1 have ignored any opacity in the layer in allowing the whole layer to radiate to the surroundings, but it can be seen from $\tau = 3$ and the relationship of τ to the emittance: $\epsilon = 1 - e^{-\tau}$, that this is not a good approximation.

A better approximation for the case of no opacity would be to allow 1/3 of the layer to cool ($\tau = 1$), and the cooling rate

$$\frac{dT_s}{dt} = \frac{\epsilon\sigma T_s^4}{c\rho l} = 11.5 \times 10^6\,\frac{J}{m^2 s}$$

$$\times \frac{m^3\,K}{2.1 \times 40 \times 10^3\,J \times 10 \times 10^{-6}\,m} = 1.4 \times 10^7\,K\,s^{-1}.$$

This will be applicable at the very start of cool-down, when temperature gradients may be small (see below). In fact the average observed cool-down rate over the first 10 μs is approximately $10^7\,K\,s^{-1}$.

Two possible factors in slowing the measured temperature drop must be examined:

(a) Condensation of carbon vapour, with release of the high latent heat of evaporation,

(b) Heating from the hot arc gas.

The atmosphere of carbon vapour within the fibre layer at the moment of arc cut-off will condense as the layer cools. For example, cooling from 3800 to 3600 K will condense about 0.9 of the vapour (taken to be 1 atm of C_3, at 3800 K due to surface energy effects). With the latent heat of vaporisation of C_3 being 750 kJ mol^{-1} and the vapour density $3.2\,mol\,m^{-3}$ at 3800 K, 1 atm, the available energy is $0.9 \times 3.2 \times 750 \times 10^3 \times 30 \times 10^{-6} = 65\,J\,m^{-2}$ of layer area. This is about 10% of the sensible energy involved in cooling the fibres and particles of the layer through the same temperature range ($500\,J\,m^{-2}$). Thus it appears that a slowing of the temperature drop rate by 10% might be possible due to condensation.

However, the vapour will be subjected to pressure gradients during cooling and may not condense where it was generated. The solid surface of the anode behind the layer is expected to have thermodynamic properties and hence an equilibrium vapour pressure appropriate to bulk graphite (probably less than 0.01 atm even for T = 3800 K). There will be rapid condensation on this face, and a bulk movement of vapour through the layer towards the face. This in turn will bring in gas from the arc, which is much hotter than the layer, and will heat at least the front portion. (From Brinkman[15], the rotational temperature (CN bands) of the arc gas is close to 6500 K. We have found a half life for the CN 400 nm band intensity of 70 μs, which means that the temperature will still be above 5500 K after this time.) A calculation of the sensible energy of 1 atm of nitrogen from 6000 to 4000 K, together with the association energy of $2N \rightarrow N_2$ for these temperatures, gives an energy influx into the layer of $15\,J\,m^{-2}$ of surface, assuming that the carbon vapour is totally replaced by nitrogen. This maximum value for the heating due to the arc gases is still negligible compared with the sensible energy change of the cooling layer, and one can ignore both the arc gas effect and the carbon vapour condensation when looking for major influences on the observed temperature.

The conduction of energy within the layer remains the dominant mechanism during cool-down, except perhaps for the first few μs. It is the condition of the layer at the beginning of cool-down which needs to be examined. We will argue in a later paper that, during steady-state operation of the arc, the dominant mechanism for energy transfer through the layer is by evaporation/condensation of carbon vapour, with only small temperature gradients. We will now make the approximation that temperature gradients through the fibre layer are zero at arc cut-off. The solution to this new transient problem has already been given; it is that described by the integral eqn (7) and drawn in Fig. 7, for no initial conduction flux, or $G = 0$. If one fits the cool-down temperatures found in nitrogen to the $G = 0$ curve over the initial portion of the curve (as shown in Fig. 7) by adjusting $kc\rho$, a value $kc\rho = 1.8 \times 10^5\,J^2\,m^{-4}\,K^{-2}\,s^{-1}$ is obtained. This is close enough to the $kc\rho = 1.1 \times 10^5\,J^2\,m^{-4}\,K^{-2}\,s^{-1}$ calculated for the fibre layer from electronmicroscopy for the difference to be merely due to errors in k or ρ.

This success in matching $kc\rho$ from the geometry of the fibre layer and from the cool-down experiments is tempered with a realisation of the time over which the conduction model should be valid. Equation (9) gives the thermal diffusion thickness δ for the thermal wave advancing through the layer from the front face, as shown in Fig. 8. The time for δ to reach the other side of the layer, ($\delta = 30\,\mu$m) using the $kc\rho$ found above, is only 10 μs. The time for the measured radiance to be appreciably affected by this discontinuity in the inward travelling wave may be several times 10 μs, but also there will be a thermal wave travelling outwards towards the observer. As shown in Fig. 8(b) the steady state temperature profile is taken as approximately flat across the fibre layer at 3800 K, with a steep gradient down to the bulk anode surface temperature. At arc cut-off the layer will be cooled by the anode surface and one can conservatively approximate the problem to that of cooling a body initially at uniform temperature T_i, with one face suddenly brought down to temperature T_{0A} at time $t = 0$, with exact solution (10)

$$\frac{T - T_i}{T_{0A} - T_i} = 1 - \operatorname{erf}\left(\frac{x}{\sqrt{(4 \propto t)}}\right) \qquad (11)$$

where x = distance in from the face, $\propto$ = thermal diffusivity and $T = T(x, t)$. Using the calculated properties of the layer in eqn (11), the temperature of the midpoint of the layer is lowered 50% towards T_{0A} in 15 μs, this resulting in 10% lowering of the observed temperature from the front. Thus the $G = 0$ curve from Fig. 7 cannot be strictly applied for times after about 10 μs, which includes all except the first measured temperatures. As can be seen in Fig. 7, however, the extrapolation back to the steady state temperature $T_0 = 3800$ K ($X = 1$) is acceptable, and the reasonable value of $1.8 \times 10^5\,J^2\,m^{-4}\,K^{-2}\,s^{-1}$ found from this can be taken as the property of the fibre layer. If the atmosphere is air, this has not been oxidised appreciably by 10 μs.

We cannot interpret the reminder of the cool-down curves in terms of the fibre layer alone, and yet the $kc\rho = 5.7 \times 10^6\,J^2\,m^{-4}\,K^{-2}\,s^{-1}$ obtained with the maximum feasible G ($G = 4$) is still much less than that of the bulk anode materials. Inspection of the Figs. 1–4 shows a region under the fibre layer, which is more porous than the parent anode material. This is difficult to see with the carbon anodes, but clearly with the graphite anode, cool-down in air leaves a severely etched deep layer below where the fibre layer had been, and cool-down in nitrogen still leaves deep eroded spaces between grains. Euler[16] observed steep temperature profiles over a layer 40 to 70 μm thick on operating anodes, from 3800 K down to 3500 K as described by Lozier and Null[3]. Using Lozier and Null's value of 35 MW m^{-2} for the steady state energy flux into a graphite anode, we calculate a thermal conductivity of $8\,W\,m^{-1}\,K^{-1}$ for Euler's layer. We believe that this porous layer controls the observed temperatures during cool-down from 10 μs to about 200 μs, and that it can be identified with the material *beneath* the fibre layer, rather than the latter. If the fibre layer exists during cool-down, the observed temperature (that of the front half of the fibres) will lead the temperature of the porous layer behind, as observed in Fig. 5(a) (difference between nitrogen and air curves). If one takes the $kc\rho = 5.7 \times 10^6\,J^2\,m^{-4}\,K^{-2}\,s^{-1}$ as a rough measure of the properties of a combination of the fibre layer with the layer behind, then using Euler's k, $\rho \simeq 350\,kg\,m^{-3}$. This is reasonable from the micrographs, both for a combination of fibre and moderately eroded layers (in nitrogen), or for a more severely eroded layer (in air).

These properties of the combined layer ($k = 8\,W\,m^{-1}\,K^{-1}$, thickness 70 μm) (graphite anodes) are consistent with the limit to which the model applies. Using eqn (9) again, the corresponding time for δ to reach 70 μm is 50 μs. Thus it is reasonable that large deviations from the layer model should occur after 200 μs, as shown in Figs. 6 and 7. After this time, Lozier and Null[3] have suggested that the properties of the bulk anode control, and we accept this as likely.

One puzzling observation remains. There is little difference between the cool-down curves of the carbon anodes in air and in nitrogen. At first this might indicate no influence of the fibre layer on the surface temperature. However, the porous carbon layer beneath the fibre layer may well be etched by air sufficiently to lower its conductivity again so that the loss of the fibre layer by oxidation is compensated for.

6. CONCLUSIONS

1. The possibility of small carbon particles influencing the optical properties of the anode of the "standard carbon arc", suggested by Abrahamson[1], has been strikingly confirmed by the discovery of fibres and particles on the anode face.

2. Whereas the observation of the fibrous layer after cool-down depends on the presence or absence of oxygen, the existence and properties of the layer at arc operating temperatures will be independent of the atmosphere, for it is surrounded by carbon vapour during arc operation.

3. An effectively black-body radiation is observed during cool-down from 3800 to 2800 K, and this is supported by the fine scale and optical thickness of the fibre layer.

4. In nitrogen (as distinct from in air) surface temperatures during cool-down were very similar for both carbon and graphite anodes. Thus the relevant properties of the fibre layers appear to be independent of the parent material. Indeed they appear similar under the electron microscope.

5. A radiative energy transfer through the fibre layer cannot control the surface temperature in competition with conduction, except perhaps in the first few μs.

6. Heating of the fibre layer by condensation of carbon vapour and by an inward drift of hot arc gas will have only a small effect on the layer temperature, and then only within the first 10 μs.

7. Conduction back into the anode, together with radiation from the front face, provides a reasonable explanation of the transients if one notes that the anode face is composed of a fibre layer, a porous layer, and the

normal density anode beneath. Observed surface temperatures are controlled variously for different times:

(a) $0 < t < 20\ \mu$s: Fibre layer control (conduction with perhaps radiative transfer)—A $kc\rho$ is found which agrees with that calculated for the fibre layer, provided a uniform temperature exists within the fibre layer at $t = 0$.

(b) $20\ \mu s < t < 100\ \mu$s: Fibre layer and porous layer control—Using an initial conducted flux and hence temperature profile, a $kc\rho$ was found which was appropriate for this combination.

(c) $100\ \mu s < t < 10$ ms: Fibre, porous layers and bulk control—Largely determined by bulk properties, as Lozier and Null[3] have suggested.

Acknowledgements—We are grateful for valuable discussion, and stimulation from Dr. W. W. Lozier. We would like to thank Dr. L. A. Erasmus and Dr. B. L. Rhoades for help on the electron microscopes, the Mechanical Engineering Department at Canterbury for the use of their JEOL 35 SEM, the Christchurch Clinical School for the use of their JEOL 100B TEM, and the Chemistry Department at Canterbury for the loan of their spectrophotometer. One of us (P.G.W.) was supported during this work by a grant from the Mineral Resources Sub-Committee of the N.Z. University Grants Committee. Anodes were kindly given to us by Dr. R. Bacon of Union Carbide, and by the Morganite Co., U.K.

REFERENCES

1. J. Abrahamson, *Carbon* **12**, 111 (1974).
2. W. W. Lozier and M. R. Null, In *Extended Abstracts 13th Biennial Carbon Conf*, Irvine, California, July 1977.
3. W. W. Lozier and M. R. Null, *Carbon* **16**, 311 (1978).
4. R. Viskanta and P. S. Bathla, *Z. Angew. Math. Phys.* **18**, 353 (1967).
5. S. H. Chan and D. H. Cho, *Trans. Am. Nuclear Soc.* **21**, 323 (1975).
6. R. Siegel and J. R. Howell, *Thermal Radiation Heat Transfer*, p. 717. McGraw-Hill, New York (1972).
7. J. T. Twitty and J. A. Weinman, *J. Appl. Meteorol.* **10**, 725 (1971).
8. M. Abramowitz and I. A. Stegun, *Handbook of Mathematical Functions*, p. 248. N.B.S. Appl. Maths Series 55 (1964).
9. J. C. Jaeger, *Proc. Cambridge Phil. Soc.* **46**, 634 (1950).
10. M. N. Özisik, *Boundary Value Problems of Heat Conduction*, p. 321. International Textbook, Scranton, Penn. (1968).
11. M. R. Null, W. W. Lozier and A. W. Moore, *Carbon* **11**, 81 (1973).
12. B. T. Kelly, *High Temp.-High Pressure* **5**, 133 (1973).
13. M. R. Null and W. W. Lozier, *Paper I-D.* Proceedings of 5th Conference on Thermal Conductivity (1965).
14. *JANAF Thermochemical Tables*, 2nd Edn. NSRDS-NBS37 Nat. Bur. Stand., Washington (1970).
15. H. Brinkman, Ph.D. Thesis (1937) in P. W. J. M. Boumans *Theory of Spectrochemical Excitation*, p. 152. Hilger & Watts, London (1966).
16. J. Euler, *Ann. Phys.* **11**, 203 (1953).

APPENDIX III(a)

Supplement to paper 'Carbon Fibre Layers on Arc Electrodes I'[90]

a.1 Circumstantial Evidence

The fibre layer observed when the standard carbon arc was operated in nitrogen instead of air, was described in the above paper. It was argued that this layer was present during arc operation by way of the transient cooling behaviour.

Additional circumstantial evidence will be presented which helps to confirm this view.

A fibre layer has been found on the carbon cathode crater (when present), of a type which is quite different when compared to the anode layer, see plate (A1 a b c d). It is difficult to see how distinctly different layers could form on each electrode if their growth occurred during the cool-down period.

Bacon[95] operating a carbon arc in argon at about 90 bars and in the high current mode was able to deposit most of the anode ablated carbon onto the cathode surface, in the form of a continuously growing rod. When this deposit was broken open it was found to be full of graphite whiskers up to 10 mm in length. Since the deposit was continuously produced at close to the sublimation temperature, it is clear that the whiskers were produced continuously at the electrode surface temperature. Furthermore, Bacon's whiskers, although 1000 times longer than those observed above, have a microstructure very similar to the observed anode whiskers.

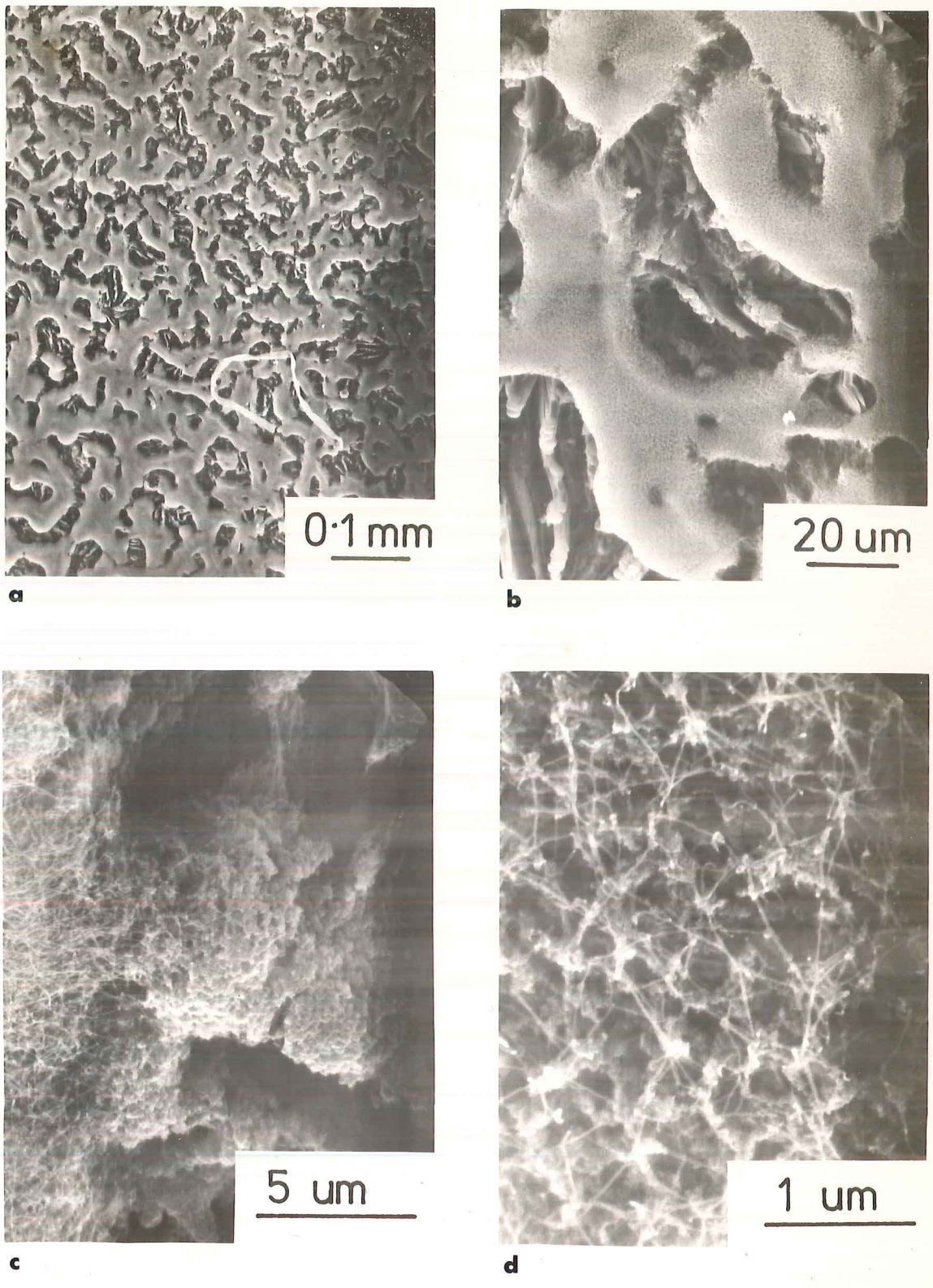

Plate A1 SEM micrographs showing details of carbon whisker deposits on a graphite cathode crater (37 A.). Note apparent random track caused by the arc attachment.

It is suggested that the low current arc is a classic case of field ionisation, where the ions are generated at the very high field strength at the whisker tips. Indeed, for the same current, the low current arc voltage is about 10 V greater than for the high current arc[50].

The sudden change from the low to the high current arc when the current is increased is possibly due to the whisker tips being eroded by the plasma at a greater rate than the whiskers can grow. The layer is destroyed forcing the arc attachment to change to thermal ionization.

a.2 Looking for Whisker Growth after Arc Cutoff (an attempt)

Photographs were taken of a SPK anode approximately 5 ms before the arc current was short circuited by firing a silicon controlled rectifier (SCR). Similarly photographs were taken of the anode approximately 5 ms after the current was reduced to zero. In each case a comparison photograph was taken when the anode had cooled to near ambient temperature. A series of 0.71 mm diameter holes were drilled through the anode so as to provide fixed reference points for the measurement of the anode front face. The arc (11A) was run in nitrogen to prevent oxidation during the cool-down period.

Using this technique it was hoped to be able to measure the position of the anode surface relative to the fixed reference hole, just before and just after cutoff, to an accuracy of ± 5μm. The fibre layer is known from SEM studies to be about 10 μm thick. If a significant and consistent difference occurred, the distance after cool-down being greater than while burning, then evidence for layer growth during cool-down would have been obtained.

a.2.1 Experimental

Diagrams of the electronic circuitry are shown in figures (A2 and A3). The SCR was fired by the camera FP flash contact via a TTL one shot variable delay, and appropriate circuitry. In this way the current could be reduced to zero in 3 μs at any chosen period between 0.3 ms to 35 ms after the camera FP contact switch closed.

Subsidary experiments were performed with an Asahi Pentax Spotmatic camera, Tektronix storage oscilloscope and the variable delay unit. By delaying the scope sweep and using suitable sweep speeds, it was found that a 15 ms delay occurred between the FP contact closing and the start of travel of the leading shutter blind. Also it was found that the leading shutter blind took another 15 ms to cross the film field. (The effect of using different shutter speeds is that the trailing shutter blind moves behind the leading blind with a time delay corresponding to the required exposure).

Thus by using appropriate delays it was found to be possible to photograph the anode tip a few milliseconds before and after the arc was extinguished.

The accurate photographing of a carbon anode tip at 3800 K at a distance of 8 cm presents difficulties of exposure, halation and possible flare effects. The Spotmatic body was used in conjunction with a Takumar 50 mm f4 macro lens, a Hoya R(25A) red filter and a Nikon 8X neutral density filter. The film used was extremely fine grained Kodak 5069. The film has a panchromatic response to 650 nm, and when combined with the R(25A) filter (cut off below 580 nm), gave a spectral window which avoided almost all the molecular emissions but had maximum sensitivity to 3800 K Planck radiation. (By eliminating the plasma background the maximum edge sharpness could be obtained.) A lens aperture of f11 was used. This was a compromise between maximum depth of field

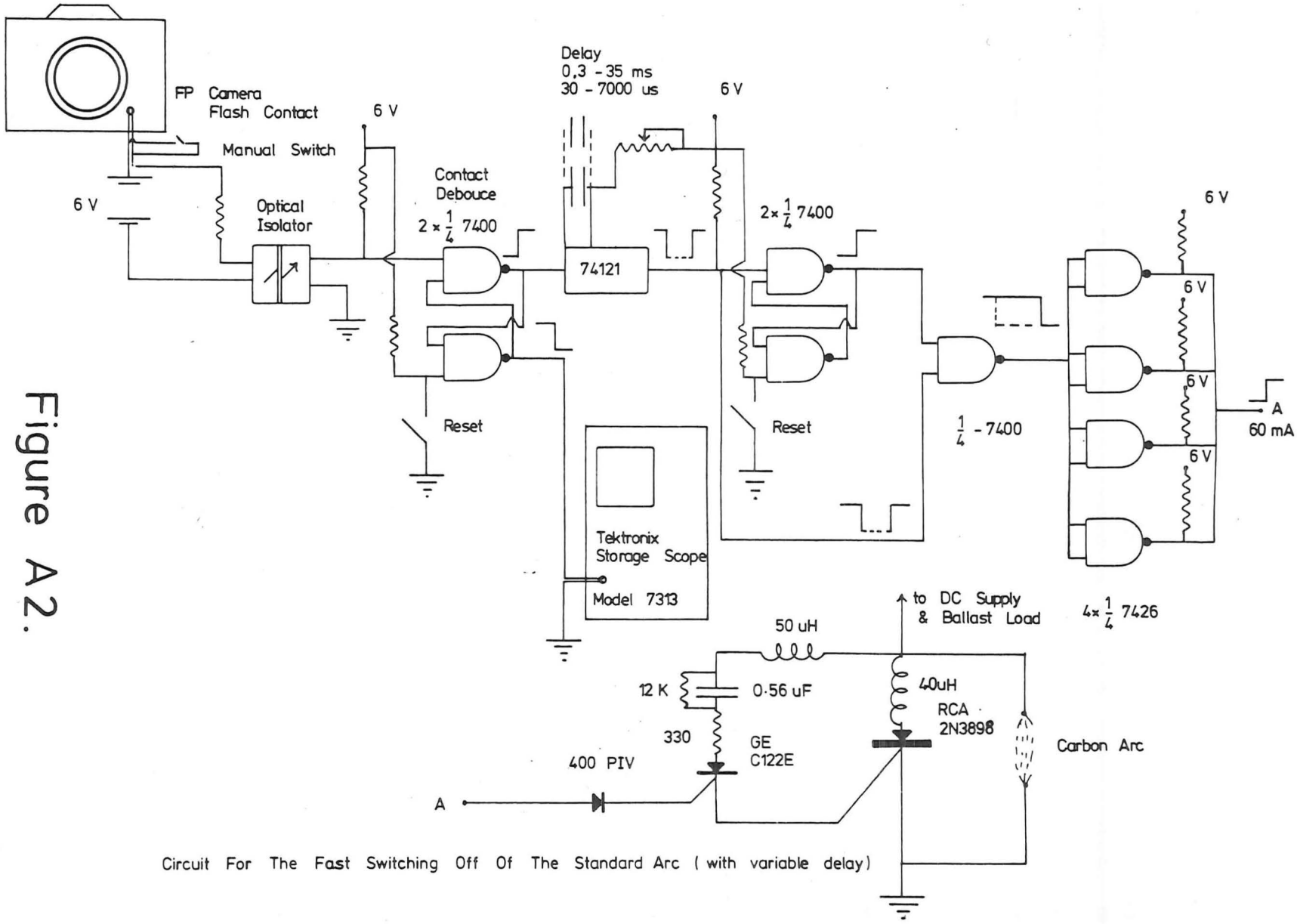

Figure A2.

Circuit For The Fast Switching Off Of The Standard Arc (with variable delay)

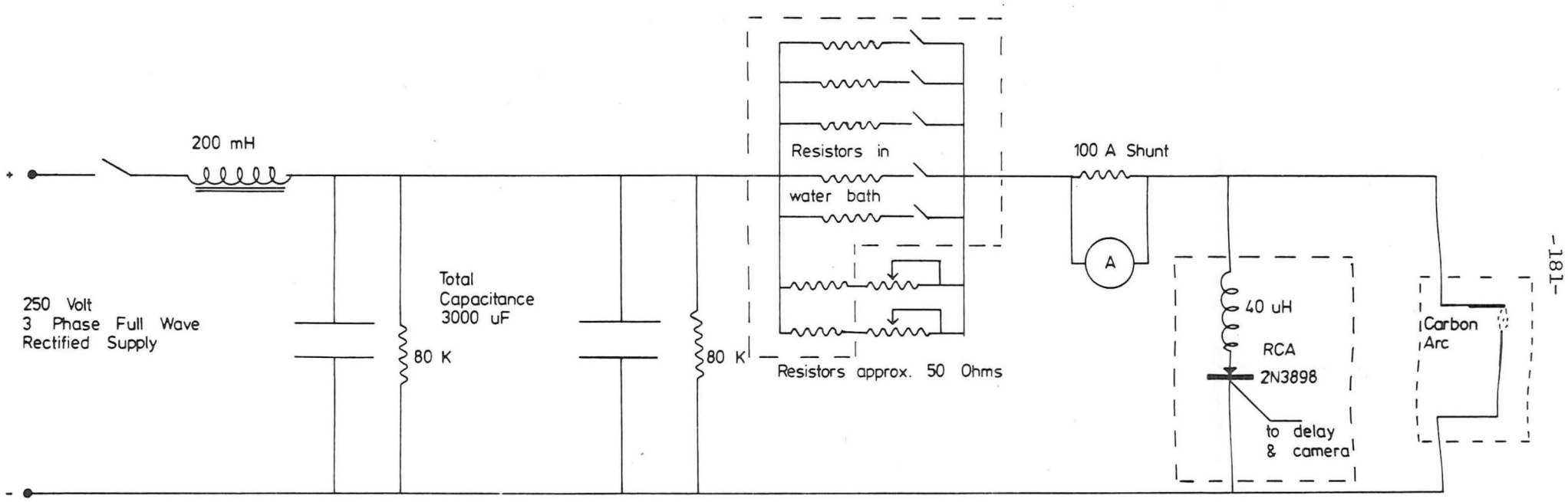

Power Supply For Standard Arc. (5 - 40 Amp.)

Figure A 3.

and diffraction limiting at large f numbers. An exposure of 1 ms was required for the anode while hot. To photograph the cold anode supplementary illumination was required. An Aldis projector with 1 kW bulb was placed in front of the anode, but offset towards the camera side so that both the anode tip and reference hole were illuminated. The projector beam was focussed with a simple lens to a spot less than 1 cm diameter on the tip area. The cold anode required an exposure of 40 s to obtain a similar film density when photographed through the above optics. A diagram of the apparatus is shown in figure A4.

The arc was allowed to burn in the normal low current (11A) mode, using 6 mm SPK anodes, in air until one of the reference holes approached the tip. The chamber was closed and the nitrogen was admitted. If an exposure of the burning anode was required, a 1 ms exposure was taken with a delay of 25 ms. If an exposure just after cutoff was required a 2 ms exposure with a delay of 10 ms was used.

The film was developed in D19 for 2.5 minutes with continuous agitation. The films were scanned on a Joyce-Loebl microdensitometer using a mechanical magnification of 50 times.

9.2.2 Results and Discussion

Analysis of eight pairs of photographs showed that no detectable difference in the position of the anode face relative to a fixed hole, before or after cutoff, was present to an experimental uncertainty of ± 20 μm, see figures A5(a) and A5(b). This uncertainty, which is at least four times too big to be able to detect with any certainty the effect being sought, was due to constraints on the anode geometry and the limiting optical sensitivity of the microdensitometer. With these limitations present no effects of insufficient depth of field, flare, halation, and diffraction were detected.

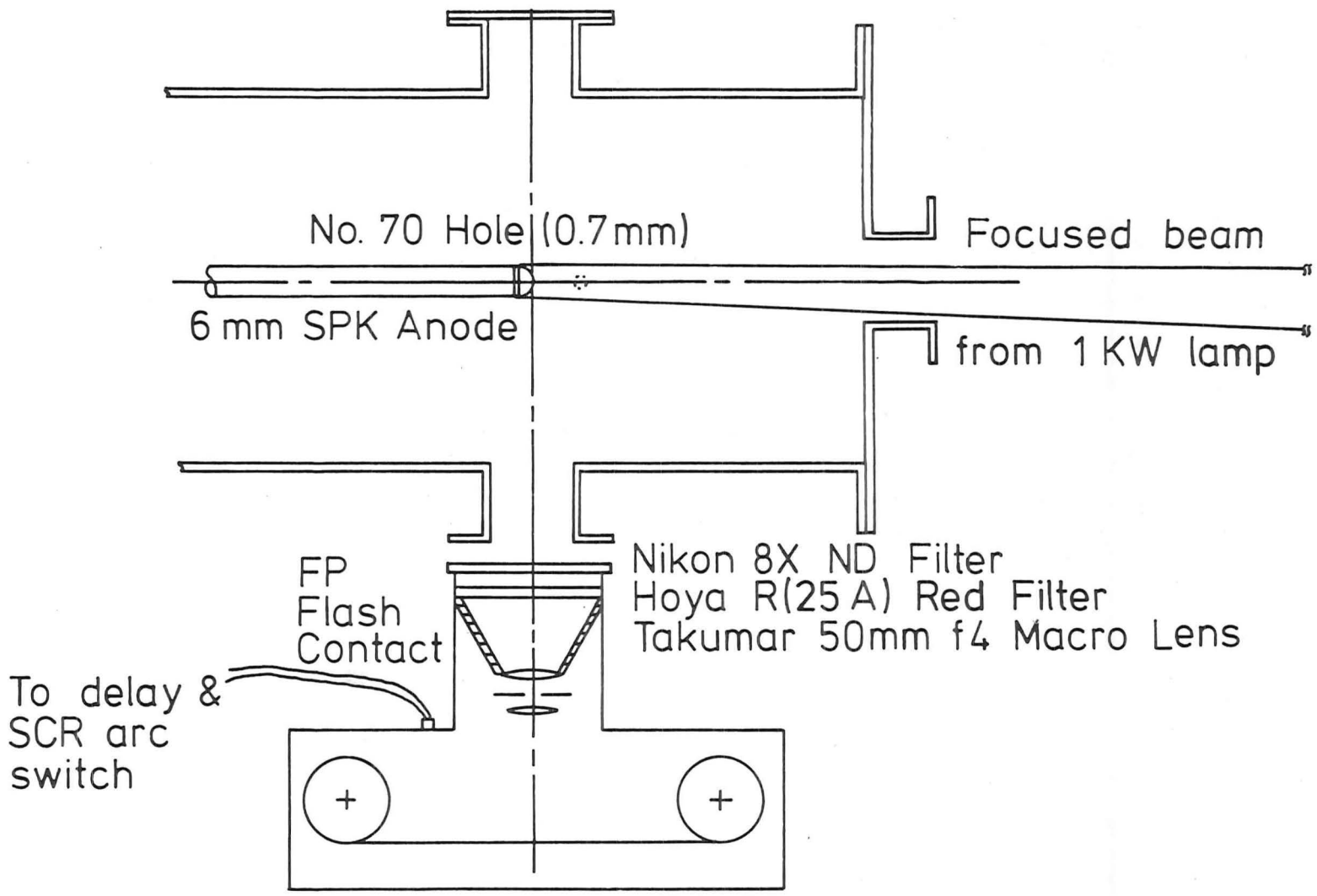

Experiment to detect whisker growth on the anode of the standard arc. Figure A4.

Location of Anode face : 5 ms before and after arc cut-off, with respect to the cold anode. [Superimposed microdensitometer traces.]
Standard Arc conditions : 11 A , 6 mm SPK anode, nitrogen atmosphere .

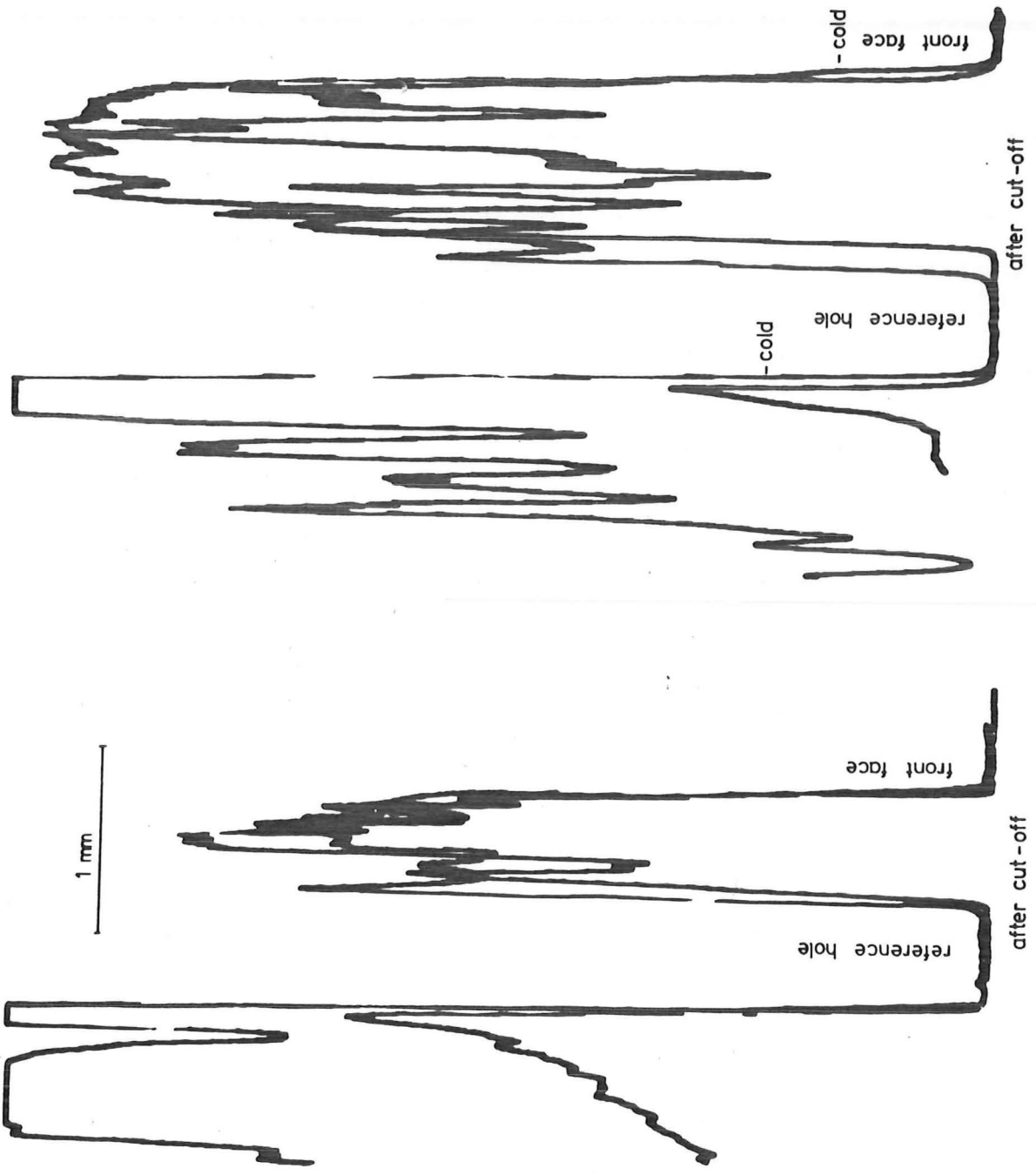

Figure A5(a).

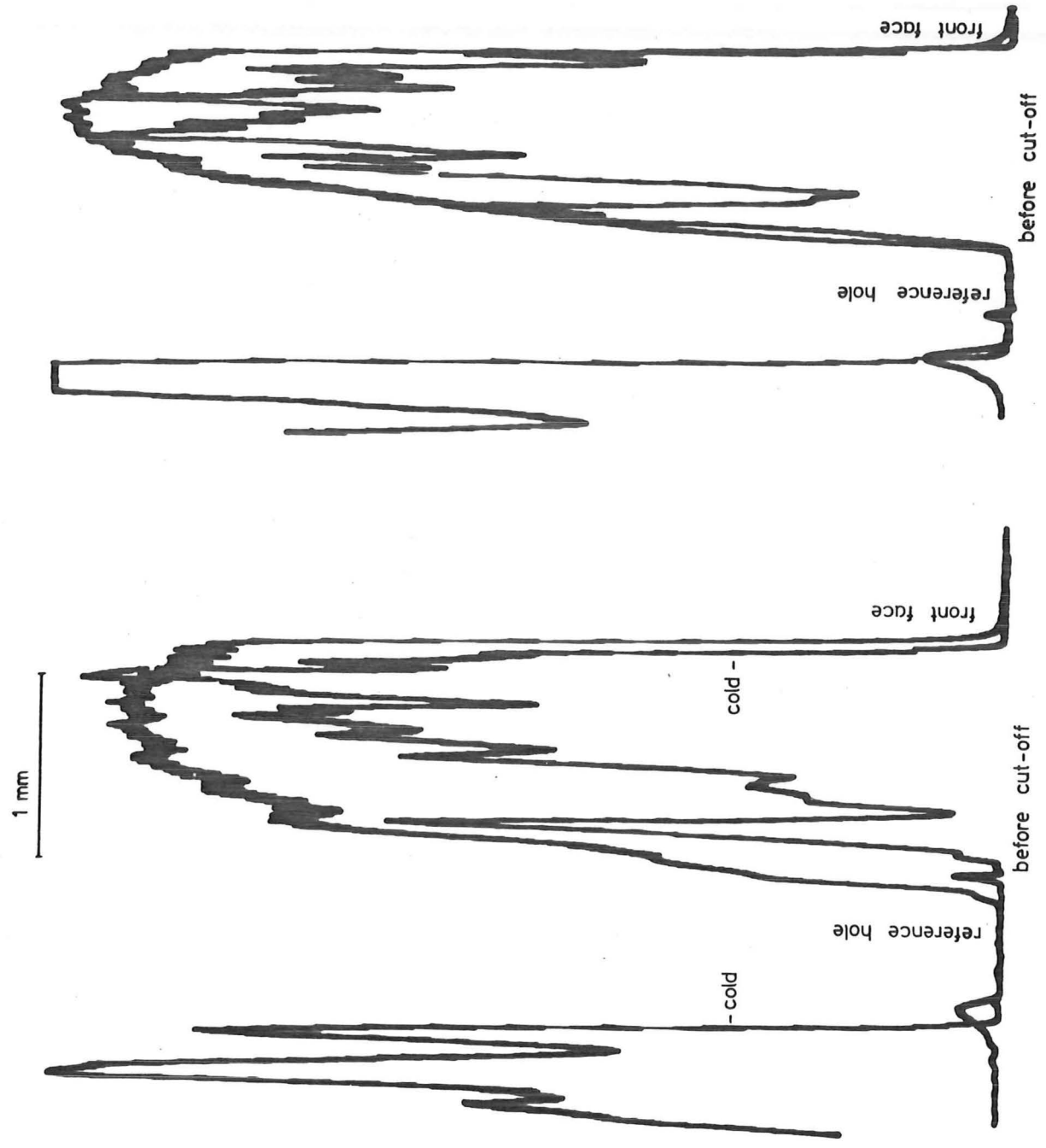
front face
before cut-off
reference hole
front face
cold -
before cut-off
reference hole
- cold
1 mm

Figure A5(b).

Depth of Field

The anode face is not in the same plane as the entrance of the reference hole.

Total depth of field is given by[96]:

$$TDF = 2c\ N\ \left(\frac{m + 1}{m^2}\right)$$

where TDF is the total depth of field in mm

c is the allowable circle of comparison in mm

N is the lens f number

m is the image magnification

For $c = \frac{1}{100}$ mm $\quad m = 0.5 \quad N = 11$

TDF = 1.3 mm which is just acceptable.

Thermal Expansion

Thermal expansion is going to alter the distance between the anode surface and reference hole, when hot and cold. If it is assumed that the average temperature while hot is 3300 K between the measuring points then a contraction of 1.5% can be expected when ambient temperature is reached[97]. This amounts to 15 μm per millimetre.

Contraction while cooling during exposure of the hot electrode

Since about 2 ms is required for the shutter blind to travel from the anode face image to the reference hole image, bulk contraction of the whole electrode (up to 20 cm long) may cause a significant distortion between the two measuring points.

If the mean rod temperature is 500°C and the combined convective and radiative heat transfer coefficient from it is 57 W m^{-2} K^{-1}[98], then it can be shown that the change in the rod length is of the order of 0.03 μm in 2 ms.

If the end is considered to be 2500 K for a length of 10 mm then the experimental cooling curves show that a temperature drop of the order of 100 K is possible in 2 ms. This will result in a contraction of 5 μm[90].

Thus it appears that the experimental accuracy obtained is not controlled by thermal distortion, but by the sensitivity of the measuring instrument and the 'graininess' of the graphite.

APPENDIX IV

The Sublimation Temperature of Graphite

The sublimation temperature of graphite has been argued for probably a century. As noted in Chapter 7, section (7.3.4.1), there is much speculation still as to the correct emissivity at 3800 K and above. The author's discovery of carbon whiskers on the surface of the standard arc while operating complicates the emissivity problem once again[90].

The other major argument is what type of heating most reliably reaches the sublimation temperature. Superheating and surface pressure are problems using laser heating. Resistive heating can be subject to superheating and mechanical collapse of the test-piece. Heating of the surface by supersonic plasma jets appears to result in incorrect temperature determinations, see figure A6. It is suggested here that the high intensity arc could provide useful data on the problem of sublimation temperature determination. Since the electrode surface (tip) is heated only at a local spot which randomly covers the surface, bulk superheating is unlikely to occur; i.e. the heated anode spot can relax back to the free sublimation temperature before being reheated by the arc root.

It is interesting to observe that the lowest surface radiance of a 6 mm SPK anode at 25 A (relative to the 3800 K standard arc), when observed at 440 nm with a spectrophotometer with a fast rise-time photomultiplier, gives a temperature ($\varepsilon = 0.99$) of 3910 K. When this is compared to the thermopile results from the tip of the 200 - 250 A anode, giving a temperature of 3950 $\pm$ 50 K ($\varepsilon = 0.99$), the similarity is important.

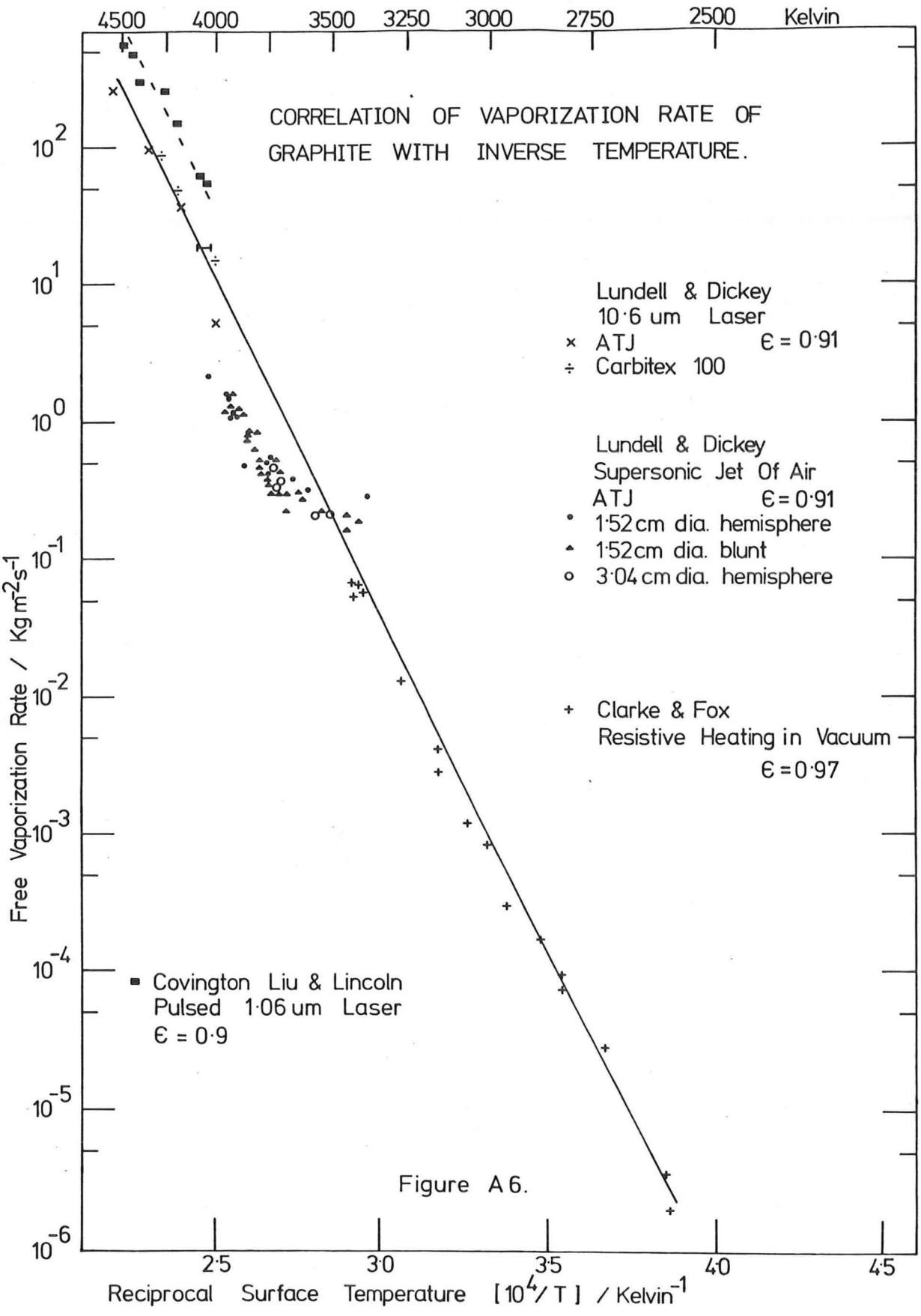
4500
4000
3500
3250
3000
2750
2500
Kelvin
CORRELATION OF VAPORIZATION RATE OF GRAPHITE WITH INVERSE TEMPERATURE.
Lundell & Dickey
10·6 um Laser
× ATJ ϵ = 0·91
÷ Carbitex 100
Lundell & Dickey
Supersonic Jet Of Air
ATJ ϵ = 0·91
• 1·52 cm dia. hemisphere
▲ 1·52 cm dia. blunt
o 3·04 cm dia. hemisphere
+ Clarke & Fox
Resistive Heating in Vacuum
ϵ = 0·97
■ Covington Liu & Lincoln
Pulsed 1·06 um Laser
ϵ = 0·9
Free Vaporization Rate / Kg m⁻² s⁻¹
10²
10¹
10⁰
10⁻¹
10⁻²
10⁻³
10⁻⁴
10⁻⁵
10⁻⁶
2·5
3·0
3·5
4·0
4·5
Reciprocal Surface Temperature [10⁴/T] / Kelvin⁻¹

Figure A 6.

If the anode voltage drop in the high intensity arc mode is independent of current, then in the 250 A case the anode heating is of the order of 10 times as great as the 25 A electrode. It is suggested that the arc free surface of the high amperage anode is extremely close to the required temperature. The correct emissivity of the surface remains in doubt.

If the above argument is accepted then the emissivity problem could be removed by drilling a number of uniformly spaced small holes almost through the anode. If the electrode tip was focussed onto a spectrophotometer and photomultiplier unit in such a way that as a radial anode hole was about to be consumed at the tip, the radiation from it was imaged onto the spectrophotometer slit, then the black-body radiance could be measured. By obtaining data at a number of wavelengths which are void of plasma interference, the black-body temperature would be obtainable.

APPENDIX V

The Free Vaporization of Graphite

Clarke & Fox[55] have obtained much useful data on the vaporization of electrically heated graphite filaments, in vacuum over the temperature range 2400 - 3500 K. Their surface temperatures were based on emissivity values listed below:

		ε
2800 K	ε_λ 0.65 μm	0.89
3000 K		0.92
3200 K		0.94
3400 K		0.95
3800 K - standard arc		0.97

They found a linear relationship when the vaporization rate data was graphed on an Arrhenius type plot. This provided an activation energy of 900 KJ $mole^{-1}$, see figure A6. The maximum vapour pressure they obtained was 1 mm Hg (as C_2). They observed microparticles being ejected from the surface but showed that this did not exceed 1 part in 10^9 of the mass loss rate. They concluded that the data was best represented by the majority of the vapour being C_2.

In Lundell and Dickey's earlier work on ATJ graphite vaporization[56], they used a supersonic jet of arc heated air to heat their specimens. This technique presents difficulties in measuring the surface temperature, and at low vaporization rates deciding on the oxidation rate of the specimens. An emissivity of 0.91 was used throughout.

Lundell and Dickey did a new study[44], using the intense heating of a continuous 30 kW CO_2 laser. Both polycrystalline graphite (ATJ) and pyrolytic graphite bars were drilled by the laser beam. Their

analysis required the condition of sonic flow in the ablating cavity. An emissivity of 0.90 was used throughout. The highest temperature reached was 4555 K at a total vapour pressure of 11.4 bars. They assumed that C_3 was the dominant vapour species.

An Arrhenius plot of these three works shows the interesting result that Clarke and Fox's linear fit can be extended over 8½ decades, see figure A6. It can be seen that the supersonic jet ablation results do not fit satisfactorily with the later laser results.

The effect of a change of emissivity of 0.91 to 0.95 on the temperature of Lundell & Dickey's results is shown by the error bar. The effect is small. It is interesting to notice in the laser heating results that no difference is detectable between the ATJ and Carbitex 100 carbons. The lowest of the laser heating data points can be neglected as the authors state that the heating intensity was not sufficient to reach sonic flow and therefore the analysis is invalid for that particular point. Also included on the graph are the results of Covington, Liu and Lincoln[108], who used a pulsed neodymium laser to produce sonic jets from the ablating carbon surface. It is significant to note that their work covers the range explored by Lundell and Dickey, and that the slope of the data points matches the Lundell and Dickey slope. However there is a displacement of the data by a factor of 3 times in terms of ablation rate, or approximately 200 K in temperature from the Lundell and Dickey - Clarke and Fox correlation. It is possible that the pulsed heating technique of Covington et al. allowed fracturing and break-up of the surface into solid particles. However it is more likely that their surface temperature estimates are in error. The total radiance from the specimen was recorded using a silicon photo-diode.

Interference filters were used to attenuate the 1.06 μm laser line from the photo-diode. An emissivity of 0.9 was used for the specimen surfaces (ATJ graphite, vitreous and pyrolytic carbon). The surface irradiation was 9×10^{9} W m^{-2} while the surface thermal (4000 K) radiance would be 1.5×10^{7} W m^{-2}. The authors concede that their temperature data was 'limited'. It seems likely that their estimated thermal radiance could be low by 10 - 20% which would account for the possible discrepancy of 200 K.

It appears that there is no evidence for particle mass loss in the laser results, because of the agreement between the two carbons and the fit with Clarke and Fox's data. The activation energy is approximately 945 KJ $mole^{-1}$ and that the mass loss rate is given by:

$$\dot{m} = 2.2 \times 10^{13} \exp(-945/RT \text{ (KJ/mol)}) \text{ kg } m^{-2} \text{ } s^{-1}$$

This linear correlation would appear to eliminate any possibility of a phase change (to the liquid state or any other) of the bulk material, as suggested by Whittaker[99, 101] at around 0.2 bar (and 3800 K).

Whittaker argues[101] that Lundell and Dickey's[44] ablation results do not show the effects of phase changes to high temperature forms of carbon (carbynes), and finally melting, because at least 2-3 seconds at 3800 K are required for the conversion (80-90%) of the graphite to the carbyne form. Using the ablation data presented above, it is found that for 7.9 or 9.5 mm anodes, and at currents of 150-200 A that there is at least 2 seconds residence time for the material to be in excess of 3800 K. Therefore the anode tip should be predominantly carbyne; and melting, according to Whittaker, should occur. It would then be expected that the vaporization would significantly depart from the solid graphite free vaporization rates. With sufficient residence time available for the claimed phase changes, reliable

temperatures of the anode tip greater than 3800 K (3950 K and $\varepsilon = 0.99$), provide additional doubt on Whittaker's claims.

Appendix VI

14th BIENNIAL CONFERENCE ON CARBON. INSERT FOR PAGES 254 - 255

STRUCTURE OF CARBON FIBRES FOUND ON CARBON ARC ANODES

J. Abrahamson, P.G. Wiles
Chemical Engineering Department, University of Canterbury, Christchurch, New Zealand.

B.L. Rhoades
Mechanical Engineering Department, University of Canterbury, Christchurch, New Zealand.

1. Introduction

Wiles and Abrahamson (1) have described the thick mat of fine fibres and crystallites which they found on graphite and carbon anodes, following low current arc operation in nitrogen at atmospheric pressure. By considering the conditions during the cooling down period after switching the arc off, they concluded that (a) the fibres and crystallites could not have been formed by condensation after switch-off, and (b) the fibres and crystallites must exist during arc operation, surrounded by a carbon vapour atmosphere, irrespective of the gas the arc is operated in. Operation in air removes them by oxidation once the arc is cut off. We describe here some details of crystallographic structure, and indicate possible mechanisms of growth.

2. Fibre Structure

Selected-area electron diffraction of the larger fibres (>12 nm dia.) showed evidence of a multiple crystal structure. Figure 1 shows a diffraction pattern of a single fibre of 13 nm dia. The bright (00.2) and (00.4) spots lie perpendicular to the fibre axis, and arise from the sides of the fibre where the graphite basal layers come into approximate alignment with the beam. The inner and outer rings of spots, (10.0) and (11.0) spots respectively, are generated from the central section of the fibre where the basal layers are approximately normal to the beam. Eight hexagonal networks are noted, and as the beam is diffracted at both the front and the rear of the fibre, giving mirror image spots, this fibre consists of four layers of crystalline material wrapped together, but successively rotated by about 5° in the basal plane.

Smaller fibres show a single crystal structure. Figure 2 shows a diffraction pattern from a 5 nm dia fibre. Fibres of this size showed a single pattern of (10.0) spots, although weak, and results from a limited number of these fibres indicate that the [210] growth direction lies along the fibre axis. Strong [002] reciprocal lattice streaking is found in all patterns, indicating variations in C spacing. Of much interest is the distinct splitting of the (00.2) spots indicating two distinct C spacings. Average C spacings determined from five fibres 5 nm to 16 nm dia were 0.333 and 0.350 nm, with an approx. error of ± 0.0015 nm. Also strong [002] streaking is shown in Figure 3, which is a diffraction pattern from the cluster of several hundred particles shown in Figure 4. Close inspection of Figure 3 also shows some separation of (002) spots, indicating that radius of curvature effects cannot account altogether for the distinct C spacings.

Electronmicroscopy

Figure 5 shows a fibre tip with successively shed layers near the tip, first single layers at A and B, and approximately six layers at C. The hollow core visible towards the tip is characteristic of these smaller fibres.

Discussion

It is expected that the basal layers are very loosely held together at 3800K (2), and molecular carbon species can penetrate deep into fibres and particles. On cooling, trapped interstitials are likely, and the larger C spacing may be the result of propping by larger interstitials. We are checking this proposition by some molecular orbital calculations.

It is of interest to find out whether the high electric field at the anode is necessary for the formation of fibres. We are checking this by a resistive heating experiment.

Givargizov and Babasian (3) have outlined the possibility of fibres being formed on vaporising crystals by a two-dimensional solid-liquid-vapour (SLV) mechanism. The presence of carbon liquid at atmospheric pressure is predicted by Whittaker (4) who places the triple point at 0.2 atm., 3800K. The existence of fine fibres at 1 atm., 3800K argues against this, but a small amount of liquid may still have been present. We are investigating the formation of fibres at pressures below 0.2 atm.

References

1. Wiles, P.G. and Abrahamson, J. Carbon 16 (1978) 341.

2. Abrahamson, J. Carbon 11 (1973) 337.

3. Givargizov, E.I. and Babasian, P.A. J.Cryst. Growth 37 (1977) 129.

4. Whittaker, A.G., Kintner, P.L., Nelson, L.S. and Richardson, N. Paper presented in 12th Carbon Conference, Pittsburgh, 1975.

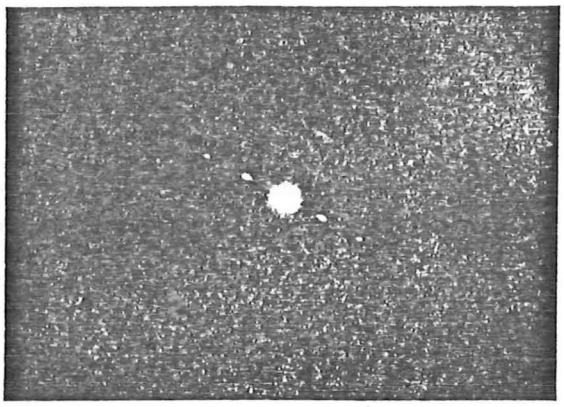

Figure 1. Diffraction pattern of a 13 nm dia fibre found on a 6 mm dia spectroscopically pure carbon anode after low current operation in nitrogen.

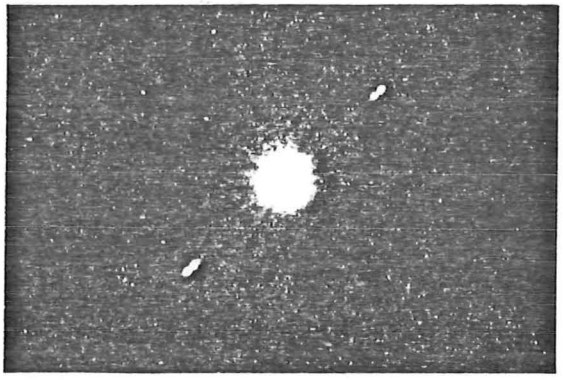

Figure 2. Diffraction pattern of a 5 nm dia fibre found under same conditions as Fig.1. (pattern enlarged to show detail)

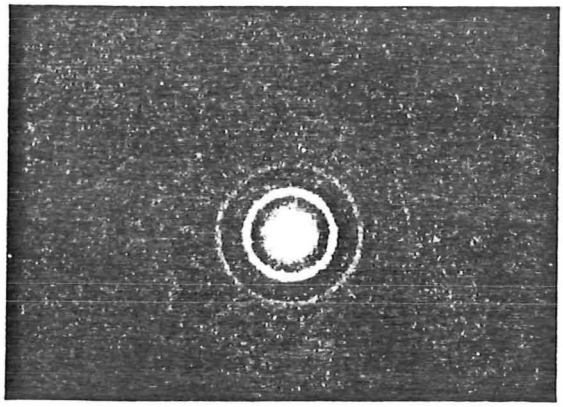

Figure 3. Diffraction pattern of fibres and particles shown in Fig.4.

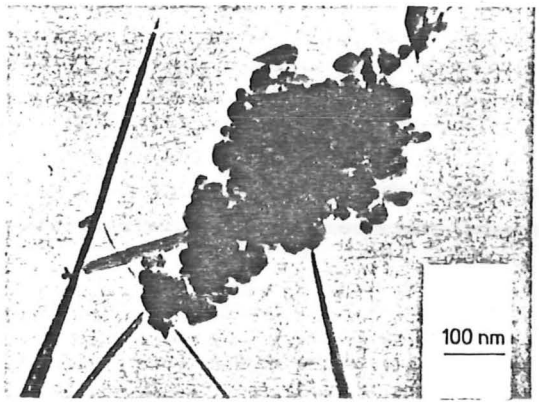

Figure 4. A cluster of carbon particles attached to fibres, from same sample as Fig.1.

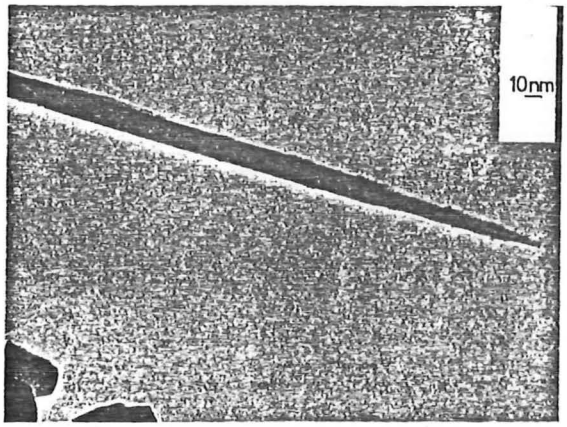

Figure 5. An enlarged view of the fibre tip seen in Fig.4.

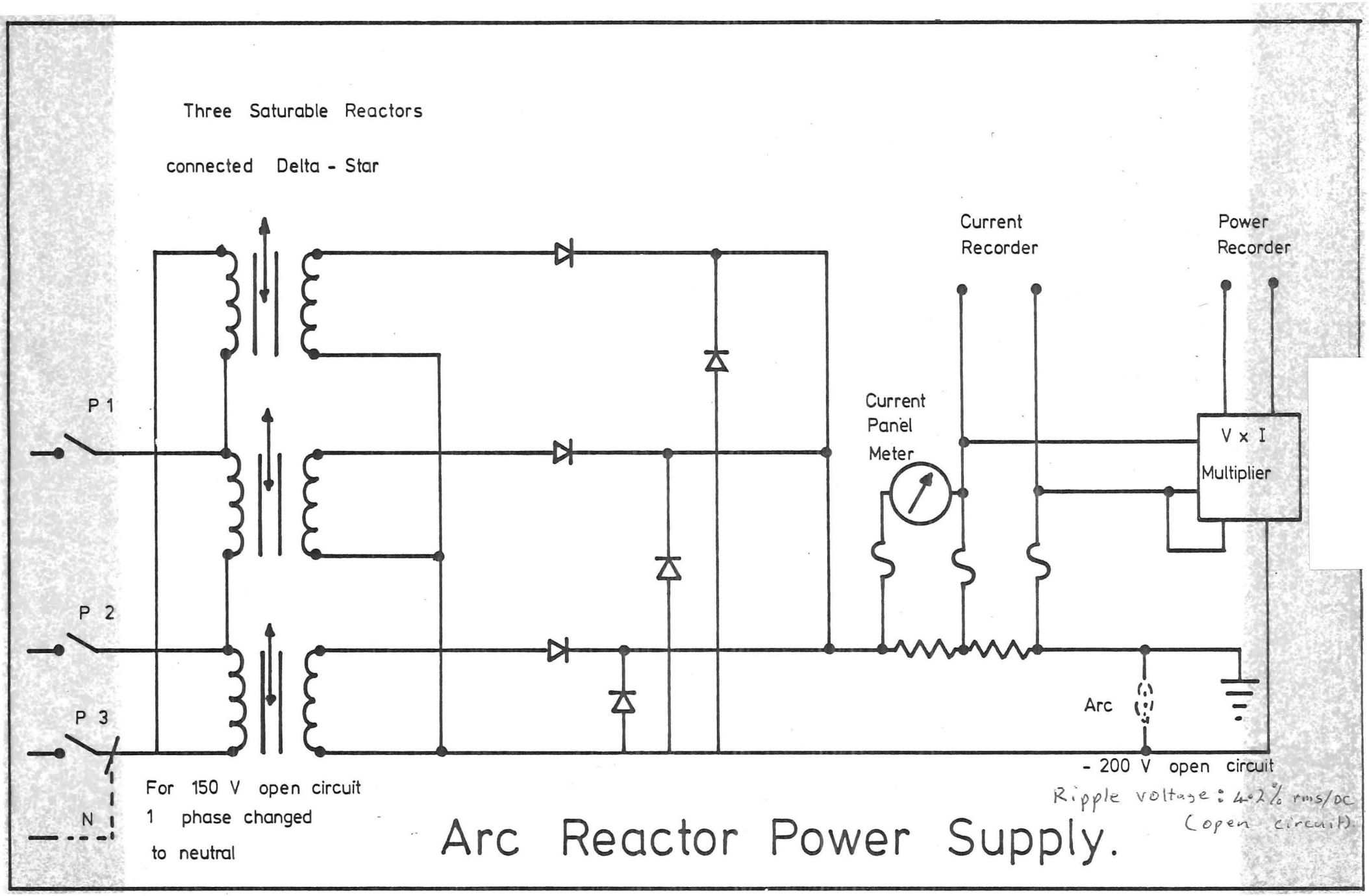
Three Saturable Reactors
connected Delta - Star
P 1
P 2
P 3
N
For 150 V open circuit
1 phase changed
to neutral
Current
Recorder
Power
Recorder
Current
Panel
Meter
V x I
Multiplier
Arc
- 200 V open circuit
Ripple voltage: 4·2% rms/DC
(open circuit).
Arc Reactor Power Supply.